



Delft University of Technology

High-frame-rate volumetric ultrasound imaging using dedicated arrays and deep learning

Ossenkoppele, B.W.

DOI

[10.4233/uuid:904477fe-5ac7-41a9-806a-f6178f8ba11c](https://doi.org/10.4233/uuid:904477fe-5ac7-41a9-806a-f6178f8ba11c)

Publication date

2023

Document Version

Final published version

Citation (APA)

Ossenkoppele, B. W. (2023). *High-frame-rate volumetric ultrasound imaging using dedicated arrays and deep learning*. [Dissertation (TU Delft), Delft University of Technology].
<https://doi.org/10.4233/uuid:904477fe-5ac7-41a9-806a-f6178f8ba11c>

Important note

To cite this publication, please use the final published version (if applicable).
Please check the document version above.

Copyright

Other than for strictly personal use, it is not permitted to download, forward or distribute the text or part of it, without the consent of the author(s) and/or copyright holder(s), unless the work is under an open content license such as Creative Commons.

Takedown policy

Please contact us and provide details if you believe this document breaches copyrights.
We will remove access to the work immediately and investigate your claim.

HIGH-FRAME-RATE VOLUMETRIC ULTRASOUND IMAGING USING DEDICATED ARRAYS AND DEEP LEARNING

HIGH-FRAME-RATE VOLUMETRIC ULTRASOUND IMAGING USING DEDICATED ARRAYS AND DEEP LEARNING

Dissertation

for the purpose of obtaining the degree of doctor
at Delft University of Technology
by the authority of the Rector Magnificus, prof.dr.ir. T.H.J.J. van der Hagen,
chair of the Board for Doctorates
to be defended publicly on
Wednesday, 28 June 2023 at 17:30 o'clock

by

Boudewine Willemine OSSENKOPPELE

Master of Science in Mechanical Engineering,
Delft University of Technology, the Netherlands,
born in Amersfoort, the Netherlands.

This dissertation has been approved by the promotores.

Composition of the doctoral committee:

Rector Magnificus,	chairperson
Prof.dr.ir. N. de Jong,	Delft University of Technology, promotor
Dr.ir. M.D. Verweij,	Delft University of Technology, promotor
Dr.ir. R.J.G. van Sloun,	Eindhoven University of Technology, promotor

Independent members:

Prof.dr.ir. A.C. Schouten,	Delft University of Technology
Prof.dr.ir. M. Mischi,	Eindhoven University of Technology
Dr. G.W. McLaughlin,	Yorlabs, USA
Dr. J.C. van Gemert,	Delft University of Technology
Prof.dr. B. Rieger,	Delft University of Technology, reserve member



This research is part of the 3D-ICE project with project number 14279 of the Open Technology Programme which is partly financed by the Dutch Research Council (NWO).

Keywords: ultrasound, 3D, ICE, high-frame-rate, matrix transducer array, deep learning, beamforming

Printed by: Proefschrift Specialist

Cover by: Boudewine Ossenkoppele & Proefschrift Specialist, image generated with Midjourney

Copyright © 2023 by B.W. Ossenkoppele

ISBN 978-94-6366-701-2

An electronic version of this dissertation is available at
<http://repository.tudelft.nl/>.

CONTENTS

Summary	ix
Samenvatting	xi
1 Introduction	1
1.1 Medical Ultrasound Imaging	2
1.1.1 Ultrasound	2
1.1.2 Imaging	2
1.2 High-frame-rate ultrasound	3
1.2.1 Application of HFR: Measuring muscle stretch	5
1.3 High-frame-rate volumetric ultrasound	5
1.3.1 Application of 3D HFR: 3D intracardiac echography for EWI	7
1.3.2 Application of 3D HFR: contrast-enhanced ultrasound	8
1.4 Deep learning for ultrasound signal processing	9
1.5 Thesis outline	10
References	11
2 Imaging Scheme for 3-D High-Frame-Rate Intracardiac Echography	17
2.1 Introduction	19
2.1.1 Clinical Background	19
2.1.2 EWI Imaging	19
2.1.3 High-Frame-Rate 3-D ICE	20
2.1.4 Data Rate Reduction by Micro-Beamforming	20
2.1.5 3-D ICE Imaging Scheme Design	22
2.2 Materials and Methods	22
2.2.1 Imaging Scheme Design: Parameters	22
2.2.2 Steerable Fan-Shaped Transmit Beam	23
2.2.3 Angular Weighted Averaging	23
2.2.4 Simulation Setup	23
2.2.5 Numerical Phantoms	24
2.2.6 Evaluation Criteria	25
2.3 Results	26
2.3.1 Imaging Scheme Optimization	26
2.3.2 Imaging Performance Evaluation	28
2.3.3 Discussion and Conclusion	33
2.4 Appendix A Fan-Shaped Transmit Beam Generation	36
References	37

3 An 8 x 9 Matrix Transducer with Transceiver ASIC for HFR 3D-ICE	41
3.1 Introduction	43
3.2 System Design	45
3.2.1 Overview	45
3.2.2 Architecture	47
3.2.3 Hybrid ADC	48
3.2.4 Datalink	50
3.3 Experimental Results	51
3.3.1 Electrical Measurements	53
3.3.2 Acoustis Measurements	56
3.4 Conclusion	59
References	59
4 An Ultrasound Matrix Transducer for HFR 3D-ICE	63
4.1 Introduction	65
4.2 Materials and Method	67
4.2.1 Design choices	67
4.2.2 Imaging scheme	68
4.2.3 ASIC implementation	69
4.2.4 Transducer fabrication	70
4.2.5 Acoustic characterization	71
4.2.6 High-frame-rate 3D imaging	72
4.3 Results	72
4.3.1 Transmit characterization	72
4.3.2 Receive characterization	74
4.3.3 Pulse-echo measurements	74
4.3.4 Imaging	76
4.4 Discussion	77
4.5 Conclusions	78
References	79
5 Improving lateral resolution in 3D imaging with ABLE	83
5.1 Introduction	85
5.2 Materials and Methods	88
5.2.1 Network architecture	88
5.2.2 Training set-up	90
5.2.3 Training data acquisition	91
5.2.4 Training data preparation	92
5.2.5 Comparison to other beamformers	92
5.2.6 Algorithmic complexity	94
5.2.7 Evaluation criteria	95
5.3 Results	96
5.3.1 Performance comparison modified ABLE - training data	101
5.3.2 Performance comparison ABLE - receptive field size	102

5.4	Discussion	104
5.5	Conclusions	106
5.6	Appendix: Network Architectures	106
	References	107
6	Neural MAP and ABLE for 3-D Contrast Ultrasound with a Sparse Array	111
6.1	Introduction	113
6.2	Methods	115
6.2.1	Sparse spiral array	115
6.2.2	Imaging scheme	115
6.2.3	Simulation data for training and evaluation	115
6.2.4	<i>In vitro</i> data acquisition	116
6.2.5	<i>In vivo</i> data acquisition	116
6.2.6	Beamforming with Adaptive beamforming by deep learning	116
6.2.7	Beamforming with Neural MAP	117
6.2.8	Beamformers for comparison: DAS and SC	119
6.2.9	Training procedure	120
6.2.10	CEUS and ULM Processing pipeline	120
6.2.11	Evaluation process and metrics	122
6.3	Results	123
6.3.1	Simulation: separation of microbubbles	123
6.3.2	Simulation: image of microbubble clouds	124
6.3.3	Simulation: localization	124
6.3.4	<i>In vitro</i> experiment: helical tube	126
6.3.5	<i>In vivo</i> experiment: chicken embryo	130
6.4	Discussion and conclusion	130
	References	132
7	Discussion and recommendations	137
7.1	A high-frame-rate 3D-ICE transducer for EWI	137
7.1.1	Electromechanical wave imaging	137
7.1.2	High-frame-rate 3D-ICE catheter	138
7.2	Deep learning-based beamforming for 3D US	140
	References	142
A	System identification of ankle joint dynamics with plane-wave ultrasound	145
A.1	Introduction	146
A.2	Method	147
A.2.1	Experiment 1: Continuous	148
A.2.2	Experiment 2: Transient	148
A.2.3	Data processing	149
A.3	Results	150
A.3.1	Experiment 1: Continuous	150
A.3.2	Experiment 2: Transient	151
A.4	Discussion	152
	References	153

Acknowledgements	155
Curriculum Vitæ	157
List of Publications	159

SUMMARY

Ultrasound imaging at high-frame-rates (>500 Hz) enables novel clinical ultrasound applications. At the same time, imaging the inherently 3D structures of the body in 3D enables an improved visualization of relevant phenomena compared to a 2D image slice. However, realizing high-quality high-frame-rate volumetric ultrasound imaging is challenging. Keeping the cable count and data rate of the transducer device at a realistic level without sacrificing image quality to an undesirable extend means that dedicated design with carefully chosen trade-offs is required and powerful processing of the received signals is desired. This thesis aims to develop high-frame-rate volumetric ultrasound with dedicated transducer design and explores the use of deep learning-based beamforming to achieve high-image-quality 3D imaging. Specifically, the first part of this thesis focuses on the design, realization and testing of an high-frame-rate 3D intracardiac echography (3D-ICE) transducer. The second part of the thesis concentrates on the use of deep learning in the image reconstruction process to improve image quality of volumetric ultrasound, first specifically for miniature ultrasound probes such as a catheter-based 3D-ICE probe and then for a sparse ultrasound array.

The background and motivation of this thesis are introduced in Chapter 1, including a background on high-frame-rate ultrasound and the existing approaches to realize 3D ultrasound imaging. Chapter 2 proposes an imaging scheme and transducer element layout to realize a 3D-ICE probe capable of imaging at a 1000 Hz, using seven steered fan-shaped beams and 1-D micro-beamforming to reduce the channel count. The element size is chosen such that sufficient area for integrated circuitry is available. Simulations are used to motivate trade-offs in the central frequency, micro-beamformer size and transmit divergence angles. Finally, a design is proposed that is suitable for electromechanical wave imaging of atrial fibrillation. In Chapter 3 a first proof of concept transducer is presented. A matrix of 8×9 PZT elements is fabricated on an ASIC, which includes high-voltage transmitters, analog front-ends, micro-beamforming and in-probe digitization. Acoustic and electronic measurements are performed, demonstrating among other things, the transmit and receive functionality at a frame rate of 1000 Hz, a sufficient dynamic range for ICE imaging and the ability to perform 3D imaging with a needle phantom. Chapter 4 presents a subsequent prototype 3D-ICE transducer. The full intended elevational size was realized and transmit control enabled imaging with seven steered diverging transmit beams, signals were micro-beamformed to the same pre-steering directions. Acoustic measurements showed that the 288 elements in the prototype had an average measured transmit frequency of 5.5 MHz and a measured -6 dB single-way bandwidth of 60%. The elements had a uniform sensitivity, with 92% of the elements having a sensitivity within the same 3 dB range. Finally, imaging experiments demonstrated the prototype's ability to achieve 3D imaging with a large field of view and at a 1000 Hz.

Chapter 5 proposes to use Adaptive Beamforming by deep LEarning (ABLE) in com-

bination with training targets generated by a large aperture array, to improve the lateral resolution of volumetric images generated with miniature matrix transducers. Taking into account the use of micro-beamforming in miniature matrix arrays, ABLE was modified to extend its receptive field across multiple voxels. The method improved lateral resolution both quantitatively and qualitatively. It was shown that image quality is improved compared to that achieved by existing Delay-and-Sum, Coherence Factor, Filtered-Delay-Multiplication-and-Sum and Eigen-Based Minimum Variance beamformers. Furthermore, only in silico data was needed to train the network, making the method easily implementable in practice.

In Chapter 6 deep learning-based beamforming is used to improve the image quality of contrast enhanced ultrasound images acquired with a sparse spiral array. Two types of deep learning-based beamforming are investigated: ABLE and a novel deep learning-based beamformer termed neural maximum-a-posteriori (neural MAP) beamforming. The neural networks are trained on simulated data. Neural MAP and ABLE qualitatively improved resolution compared to delay-and-sum (DAS) and spatial coherence (SC) beamforming on the simulated and in vivo data. Ultrasound localization microscopy (ULM) images were created from the images formed by the different beamforming methods. When localizing in silico microbubbles neural MAP showed the best performance followed by ABLE, SC and DAS. Finally, a discussion of the achievements and limitations of the work in this thesis is presented along with recommendations for future work in Chapter 7.

SAMENVATTING

Echografische beeldvorming met hoge beeldfrequenties (>500 Hz) maakt nieuwe klinische toepassingen van echografie mogelijk. Tegelijkertijd maakt het in 3D afbeelden van de inherent 3D-structuren van het lichaam een verbeterde visualisatie van relevante verschijnselen mogelijk in vergelijking met een 2D-beeldplak. Het realiseren van hoogwaardige volumetrische echografie beelden met hoge framesnelheid is echter een uitdaging. Om het aantal kabels en de datatransmissiesnelheid van de echotransducent op een realistisch niveau te houden zonder de beeldkwaliteit ongewenst ver in te perken is een toepassingsspecifiek ontwerp met zorgvuldig gekozen trade-offs nodig en is een krachtige verwerking van de ontvangen signalen gewenst. Dit proefschrift heeft tot doel volumetrische echografie met een hoge framesnelheid en hoge beeldkwaliteit te realiseren door toepassingsspecifiek transducerontwerp en het gebruik van deep learning in het beeldreconstructieprocess. Het eerste deel van dit proefschrift richt zich specifiek op het ontwerp, de realisatie en het testen van een 3D intracardiale echografie (3D-ICE) transducent met een hoge framesnelheid. Het tweede deel van het proefschrift richt zich op het gebruik van deep learning in het beeldreconstructieproces om de beeldkwaliteit van volumetrische echografie te verbeteren, eerst specifiek voor miniatuur echoapparaten zoals een 3D-ICE-katheter en vervolgens voor een transducent met een patroon van schaars verspreide elementen.

De achtergrond en motivatie van dit proefschrift wordt geïntroduceerd in Hoofdstuk 1, met o.a. een beschrijving van het opnemen van echografie beelden met een hoge beeldsnelheid en de bestaande benaderingen om 3D echografie te realiseren. Hoofdstuk 2 presenteert een beeldvormingsstrategie en transducent indeling voor het realiseren van een 3D-ICE-katheter welke in staat is om met 1000 Hz beelden te vormen door het gebruik van zeven gestuurde waaiervormige bundels en 1-D microbundelvorming om het aantal kanalen te verminderen. De grootte van de elementen is zo gekozen dat er voldoende ruimte voor geïntegreerde schakelingen beschikbaar is en simulaties worden gebruikt om compromissen in de centrale frequentie, de grootte van de microbundelvormer en de zenddivergentiehoeken te motiveren. Ten slotte wordt een ontwerp voorgesteld dat geschikt is voor het in beeld brengen van de elektromechanische golven bij atriumfibrillatie. In Hoofdstuk 3 wordt het eerste prototype van de transducent gepresenteerd. Een matrix van 8 x 9 PZT-elementen wordt gefabriceerd op een ASIC, welke hoogspanningszendcircuits, analoge front-ends, micro-bundelvorming en anloog-naar-digitaalomzetting integreert. Er worden akoestische en elektronische metingen uitgevoerd, waarbij onder meer de zend- en ontvangstfunctionaliteit bij een framesnelheid van 1000 Hz, een voldoende dynamisch bereik voor ICE-beeldvorming en 3D-beeldvorming van een naaldfantoom worden gedemonsteerd. Hoofdstuk 4 presenteert een volgend prototype van een 3D-ICE-transducer. De volledige beoogde grootte in de elevatierichting werd gerealiseerd en controle over de bundelvorming van de uitgezonden golf maakt het mogelijk gestuurde divergerende golven te zenden en de ont-

vangen signalen werden verwerkt met microbundelvorming in dezelfde stuurrichtingen. Akoestische metingen toonden aan dat de 288 elementen in het prototype een gemiddeld gemeten zendfrequentie hadden van 5.5 MHz en een -6 dB (eenrichtings) bandbreedte van 60%. De elementen hebben een uniforme gevoeligheid, waarbij 92% van de elementen een gevoeligheid heeft welke binnen hetzelfde bereik van 3 dB ligt. Ten slotte toonden experimenten aan dat het prototype in staat is om 3D-beeldvorming te bereiken met een groot blikveld en bij 1000 Hz.

Hoofdstuk 5 presenteert het gebruik van Adaptive Beamforming by deep LEarning (ABLE) in combinatie met trainingsdoelen gegenereerd door een transducent met grote aperture, om de laterale resolutie van volumetrische beelden gegenereerd met miniatuur matrix-transducenten te verbeteren. Rekening houdend met het gebruik van microbundelvorming in miniatuur matrix-transducenten, werd ABLE aangepast om zijn receptieve veld over meerdere voxels uit te breiden. De methode verbeterde de laterale resolutie zowel kwantitatief als kwalitatief. Er werd aangetoond dat de beeldkwaliteit verbeterd is in vergelijking met die van bestaande Delay-and-Sum, Coherence Factor, Filtered-Delay-Multiplication-and-Sum en Eigen-Based Minimum Variance bundelvormers. Bovendien was alleen *in silico* data nodig om het neurale netwerk te trainen, waardoor de methode eenvoudig in de praktijk kon worden geïmplementeerd.

In Hoofdstuk 6 wordt op deep learning gebaseerde bundelvorming gebruikt om de beeldkwaliteit te verbeteren van contrastversterkte echo beelden verkregen met een transducent waarvan de elementen in een spiraal patroon schaars over het aperture zijn verspreid. Er worden twee soorten op deep learning gebaseerde bundelvorming onderzocht: ABLE en een nieuwe op deep learning gebaseerde bundelvormer genaamd neural maximum-a-posteriori (neural MAP) beamforming. De neurale netwerken worden getraind op gesimuleerde data. Neural MAP en ABLE verbeterden de resolutie kwalitatief in vergelijking met Delay-and-Sum (DAS) en Spatial Coherence (SC) bundelvorming op de gesimuleerde en *in vivo* gegevens. Ultrasone lokalisatiemicroscopie (ULM) beelden werden gemaakt op basis van de beelden gevormd door de verschillende bundelvorm-methodes. Neural MAP presteerde het best in het lokaliseren van *in silico* microbellen gevuld door ABLE, SC en DAS. Ten slotte wordt in hoofdstuk 7 een besprekking van de verworvenheden en beperkingen van het werk in dit proefschrift gepresenteerd en wor-den aanbevelingen voor toekomstig werk gedaan.

1

INTRODUCTION

1.1. MEDICAL ULTRASOUND IMAGING

1.1.1. ULTRASOUND

Ultrasound is the most widely used medical imaging modality [1] due to its relatively low cost and portability compared to X-ray, CT and MRI and its lack of ionizing radiation. It is used both in a wide variety of medical specialties and in many phases of medical treatment, from making initial diagnoses to the planning of procedures, during interventions and to follow-up on treatment success. In medical ultrasound imaging, high-frequency acoustic waves are used to visualize structural or physiological properties of tissues and organs.

Sound waves are sent by the ultrasound transducer, which transforms electrical energy into acoustic energy and vice versa. Typically, this conversion between electrical and acoustical energy is accomplished with piezoelectric material, although capacitive micromachined ultrasound transducers (CMUTs) are becoming more widely used. The acoustic wave that is transmitted into the tissue is partially reflected when it encounters a tissue boundary where there is a difference in acoustic impedance. Acoustic impedance is a material property that is defined as the product of its density and speed of sound. The reflected acoustic energy is received by the transducer array, which converts it to electrical signals. The relatively small differences in the acoustic impedance of soft-tissues mean that the reflection coefficient is small enough to let enough energy propagate to deeper tissues. How deep the energy can propagate into the tissue depends on the frequency of the ultrasound pulse. Lower frequencies are attenuated less and can thus propagate further. In medical ultrasound typically frequencies between 1 and 15 MHz are used.

1.1.2. IMAGING

TRANSMIT BEAMFORMING

Steering and focusing of the ultrasound beam to acoustically illuminate a specific direction and depth can be realized by using an array of small transducer elements (size in the order of a wavelength) and exciting the elements with specific electronic delays to control the interference pattern in the desired way. This way, a steered beam can be generated using a linearly increasing delay pattern perpendicular to the steering direction, a concave delay pattern can be used to focus the beam and a convex delay pattern to defocus/diverge (see Figure 1.1). The shape of the transmitted beampattern can be further influenced by applying apodization, meaning that a weighting function is applied to the aperture by exciting elements with a different amplitude. Apodization is mainly employed to reduce the negative effect of additional off-axis energy in the beampattern, called sidelobes or secondary lobes, which reduces the image quality. This process of modifying the shape, direction and/or focus of the transmit beam is called transmit beamforming.

RECEIVE BEAMFORMING

After a pulse of acoustic energy has been transmitted into the medium and the transducers have received the reflected acoustic energy from the medium, the received time domain signals still need to be transformed into the spatial map of acoustic reflectivity that forms the ultrasound image. This is possible with a similar beamforming process as

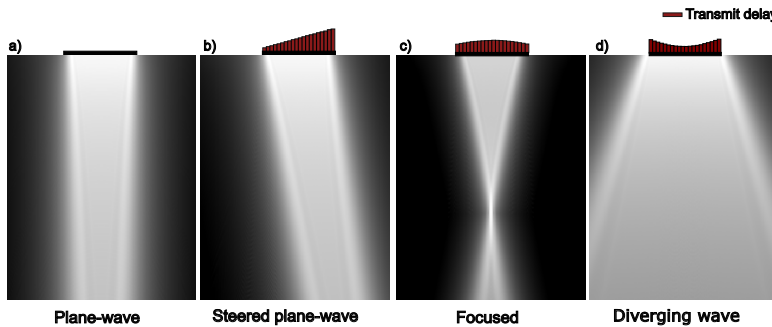


Figure 1.1: Schematic representation of the transmit delays needed to generate a) plane-wave, b) steered plane-wave, c) focused transmit and d) diverging wave transmit.

in transmit. For each position in the image, the time that an acoustic wave travels from this point to each element of the transducer array can be calculated. Based on this travel time, delays can be applied to the received signals of all elements, such that the signals originating from this focal point are aligned in time. In receive it is possible to store the data and then focus on each point in the image, which is called dynamic focusing. After focusing the signals to the desired spatial location, the final step in the receive beam-forming process is to combine the signals. The simplest and conventional method to do this is to coherently sum the signals after the delays are applied, this is referred to as the Delay-And-Sum (DAS) method.

Often data-independent apodization weights are applied before summing the signals to reduce the effect of unwanted energy received from sidelobes. However, this comes at the cost of resolution, as such the setting of such static apodization weights is a trade-off. More advanced data-dependent methods for weighting the received signals have been developed to improve image quality. For example, by exploiting the coherence of the signal or by determining apodization weights based on the received data to suppress unwanted off-axis signals.

POST-PROCESSING

After a spatial map of acoustic reflectivity is obtained through the beamforming step, several post-processing steps are taken. These can for example include band-pass filtering to improve the image quality. Finally, the envelope of the image is taken and signals are compressed into a logarithmic scale for display.

1.2. HIGH-FRAME-RATE ULTRASOUND

From the 1970s when medical ultrasound imaging appeared, images were acquired in a line-by-line fashion, based on the way echolocation is done [2]. Meaning, a narrow, focused, transmit pulse is send and backscattered echoes are reconstructed along the depth of this line. Next, a focused beam is transmitted at a small lateral distance with respect to the previous transmit. The backscattered echoes for this next transmit are then acquired, resulting in another reconstructed line in the image (see Figure 1.2 a)). Historically, this was done by mechanically translating/rotating the transducer and later

by electronic switching and delaying of transducer array elements [2]. This process is then repeated until the full image is acquired, for a 2D image typically 64 to 512 times [3]. This way of imaging means that the rate at which images are acquired (FR) does not only depend on the imaging depth (z) and the speed of sound (c), but also on the number of lines (N_{lines}) that are used to reconstruct the image:

$$FR = \frac{c}{2N_{\text{lines}}z}. \quad (1.1)$$

For an image depth of 10 cm acquired with 128 lines, this would mean that 60 images can be acquired every second.

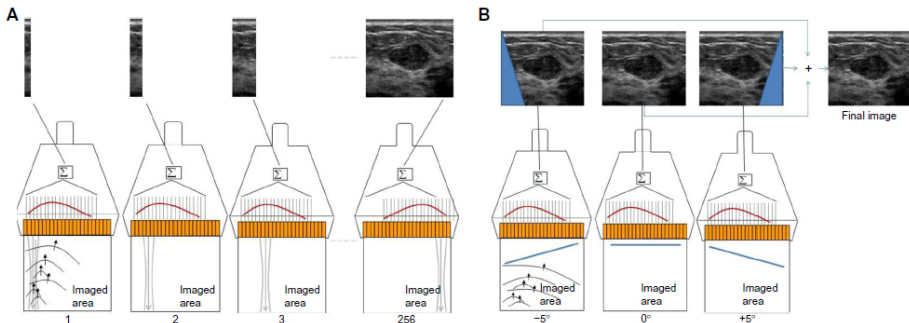


Figure 1.2: a) Conventional focused imaging where the image is insonified line-by-line and b) ultrafast ultrasound imaging. Reproduced from Bercoff [3], Published in Ultrafast Ultrasound Imaging, Ultrasound Imaging - Medical Applications, Prof. Oleg Minin (Ed.), under CC BY-NC-SA 3.0 license. Available from: <http://dx.doi.org/10.5772/19729>.

Methods to realize higher frame rate imaging by building up multiple or all image lines in parallel from a single transmit, have been proposed as early as the 1970s. Building up a full image at an ultrafast frame rate from a single unfocused transmit that covers a wide imaging region was already proposed in 1977 [4]. However, ultrafast imaging over a large field of view in an in vivo clinical setting was only realized around 30 years later [5, 6]. In the meantime methods to capture and process in parallel not all but just a couple of neighboring image lines from a single slightly defocused transmission had been proposed and validated in vivo [7]. Multiline processing of 2-16 lines was implemented in clinical systems to increase the frame rate. However, these systems were still built on a serialized architecture and to bring the full parallel processing of a complete image to commercial machines, there were two technological bottlenecks [3]. First, this huge volume of raw ultrasound data must be transferred from the transducer to the processing unit at rates of several GigaBytes/s and then, the data needs to be processed fast enough for real-time clinical use. The development of fast numerical links and powerful GPUs made this possible. As a result, the number of lines in the image is no longer limiting the frame rate, which becomes:

$$FR_{\text{ultrafast}} = \frac{c}{2z} \quad (1.2)$$

Thus the same image of 10 cm depth can be acquired at 7700 Hz instead. Of course, the lack of transmit focus impacts the image quality, reducing image contrast and resolu-

tion. However, image quality can be improved by sending multiple tilted plane waves [8] or diverging waves [9] and coherently summing the acquired images, such that the transmit focusing process is rebuilt virtually. There is thus a trade-off between the maximum frame rate that is achieved and the image quality, through the number of transmit angles that is used to acquire the image. Nonetheless, the same image quality as that of line-by-line acquisition can be achieved at a frame rate that is around 5-10 times higher [8]. This development from line-by-line to ultrafast ultrasound imaging is considered a paradigm shift. The higher frame rate that was now achievable made it possible to measure motion of tissue, blood and contrast agents at kHz framerates and thereby inspired the development of completely novel clinical applications for ultrasound imaging [10]. These clinical applications include, among others, shear wave elastography [11-13], functional imaging of the brain [14, 15], high-resolution vector flow imaging [16, 17], ultrafast contrast imaging [18, 19] and electromechanical wave imaging [20]. With high-frame-rate¹ (HFR) ultrasound it is also possible to visualize the fast contraction of skeletal muscles [21].

1.2.1. APPLICATION OF HFR: MEASURING MUSCLE STRETCH

Effective treatment of movement disorders requires a thorough understanding of human limb control. Joint dynamics can be assessed using robotic manipulators and system identification. However, due to tendon compliance, joint angle and muscle length are not proportional. As a result, the measured joint angle does not directly reflect the muscle stretch. Plane-wave ultrasound imaging can be used to reach the frame rates required to capture the fast movements of the muscle and can thereby be used to investigate the dynamic relation between ankle joint angle and muscle fiber stretch. In Appendix A [22], it is shown that using plane-wave ultrasound, it is feasible to measure muscle stretch during motor control experiments with transient and small continuous ankle joint motions. Furthermore, with this measurement, it was possible to draw conclusions on the proportional behavior of muscle lengthening and ankle angle during different tasks and perturbation types.

1.3. HIGH-FRAME-RATE VOLUMETRIC ULTRASOUND

When trying to measure very fast muscle stretching with a 2D image, the reliability of the measurement is reduced by the fact that it is difficult to keep the same muscle region in the narrow imaging slice of the ultrasound transducer. This is illustrative of the fact that capturing the movement of a 3D structure with a 2D image has inherent limitations. Because the global muscle stretch of the contraction of the lower leg muscle has a relatively clear direction and symmetry, it can still be captured quite well with 2D imaging. However, the use of 2D images becomes an increasing problem when capturing more complex 3D movements such as the flowing of contrast agents in 3D vessel structures or induced and natural shear wave propagation in the heart. However, realizing 3D ultrasound imaging at kHz frame rates is challenging. Mechanical or freehand scanning of a volume with a probe that has a 1D array of transducer elements (see Fig.1.3), as is used for 2D imaging, is not an option, because the process is too slow to realize the desired

¹In this thesis, the term 'high-frame-rate' is used for frame rates $\geq 500\text{Hz}$.

high-frame-rates.

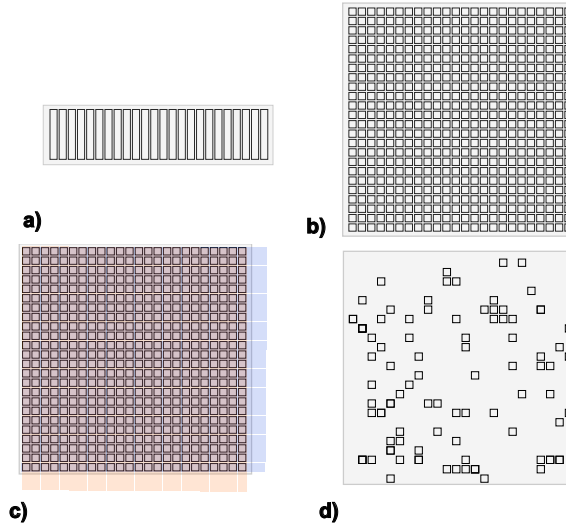


Figure 1.3: a) 1-D linear array probe. b) 2-D matrix array. c) Row-column array. d) 2-D random sparse array.

Instead, 2D transducer arrays are used for fast 3D imaging. Having an array of elements that extends in two dimensions instead of one, allows focusing and beamforming along all three spatial directions. Although extending an $N \times 1$ transducer array to an $N \times N$ matrix array is conceptually a straightforward step, the practical challenge to realize it is complex. Individually controlling each element of an $N \times N$ element array requires N^2 electronic connections. For such a high level of interconnection and processing, the resulting large volume of data poses a great challenge. Simply reducing the number of elements by reducing the size of the array is undesirable, because of the resulting loss in lateral resolution. At the same time, simply increasing the spacing of elements in the array to above half a wavelength is undesirable, because the resulting grating lobes in the beampattern can result in artifacts in the image [2]. As a result, different transducer designs have been proposed and developed that approach the data rate and interconnection challenge of high-frame-rate volumetric ultrasound in different ways.

Sparse arrays are designed to reduce the number of elements that need a direct connection to the mainframe of the ultrasound system, while maintaining a large aperture size as desired for a good lateral resolution, by sparsely rather than fully covering the aperture with elements. Various ways of distributing the elements across the aperture of sparse arrays have been proposed [23–26] to mitigate as much as possible the increased unwanted secondary lobes and reduced transmit uniformity, which form important downsides of sparse arrays. Sparse arrays can maintain the flexibility to employ different transmit schemes, such as focused, plane, and diverging wave transmission, although care should be taken to realize an acceptable level of transmit uniformity [27]. However, the reduced SNR of sparse arrays is a limitation that makes their use less suitable for many applications.

Row-column arrays try to both keep a large aperture size and maintain the element count of a fully populated array, while reducing the number of required electrical connections from $N \times N$ to $N \times 2$, by using a cross-electrode (see Fig 1.3) [28–30]. Compared to a sparse element distribution this is favorable for maintaining SNR. However, image quality loss still results from not being able to focus in azimuth and elevation simultaneously. Furthermore, the cross-electrode results in a reduced flexibility in transmit imaging schemes. Imaging can only be done in a rectilinear region in front of the array [28] and realizing imaging with a footprint wider than that of the array, as is required for example in cardiac applications, is challenging. Solutions such as curved arrays or doubly curved acoustic lenses have been proposed, but some of their downsides include their inflexibility and fabrication difficulties [31].

An alternate approach to have a fully populated array is to manufacture the array on top of an Application Specific Integrated Circuit (ASIC), which can then reduce the channel count before sending signals to the back-end system through multiplexing and/or pre-beamforming of the data from small groups of elements. The ASIC electronics can also include pulsers for ultrasound transmission and it will take care of amplification of the received echoes to increase the robustness of the signal transmission to the imaging system. The specific advantages and disadvantages of the different types of transducer designs for volumetric ultrasound imaging, make them specifically suited for one range of ultrasound applications while making them less suited for applications that emphasize other demands. Thereby making a transducer design that is dedicated to the application necessary.

1.3.1. APPLICATION OF 3D HFR: 3D INTRACARDIAC ECHOGRAPHY FOR EWI

Visualization of the heart with ultrasound can be done from three different vantage points, each requiring a different type of ultrasound transducer. In transthoracic echocardiography (TTE), the heart is visualized by placing a transducer on the chest wall, between the patient's ribs. The reflections from the ribs and lungs and attenuation from the skin and fat tissue between the heart and the probe have a negative impact on the image quality. In transesophageal echocardiography (TEE), the heart is visualized from the patients esophagus by a miniature ultrasound probe. The closer distance to the heart enables the use of higher frequency probes, thereby improving the spatial resolution of the cardiac images. Thirdly, echocardiography can be performed from inside the heart, using an even smaller intracardiac echocardiography (ICE) device that is mounted at the tip of a catheter to be passed into the heart chambers, see Fig. 1.4. ICE is widely used in guiding interventional cardiovascular procedures [32].

The desire for enhanced visualization with 3D images has led to the development of ICE probes for volumetric imaging. The use of matrix arrays is desired over the use of rotated linear arrays to realize real-time frame rates. However, since the cabling of an ICE probe needs to fit in a catheter shaft whose diameter is usually limited to less than 3 mm, this results in an especially acute element connection challenge. Several 3D-ICE designs have been proposed that solve this challenge for real-time imaging [33–35]. However none of these can achieve high-frame-rate volumetric imaging.

A high-frame-rate volumetric 3D-ICE device would enable novel imaging modes, specifically it could enable electromechanical wave imaging (EWI) [20, 36, 37] for the

mapping of atrial fibrillation [38]. Atrial fibrillation is the abnormal beating of the atrial chambers of the heart. It is the most common type of sustained cardiac arrhythmia and causes a major increase in the risk of stroke [39]. Atrial fibrillation can be treated by ablating the arrhythmogenic sources. 2D-ICE is currently already used to guide the ablation catheter and monitor the ablation process [40]. With high-frame-rate 3D-ICE, it would also be possible to use the device for the generation of a 3D map of the electromechanical activation of the heart by measuring the cardiac deformation [20, 36, 37, 41–43]. This ultrasound technique is called electromechanical wave imaging, after the tight coupling between the electrical excitation of the cardiac muscle cells and their resulting mechanical contraction and its wave-like spreading over the cardiac wall. The electromechanical activation map could be used to determine the correct location for ablation treatment.

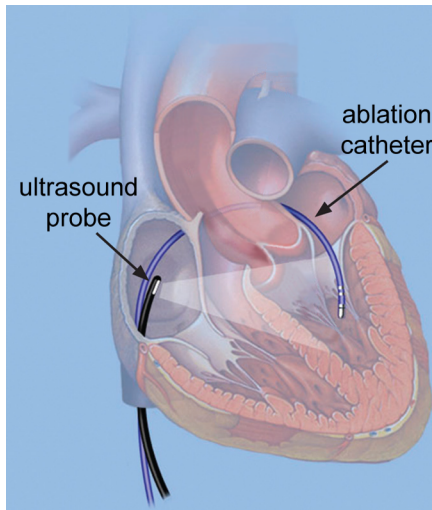


Figure 1.4: ICE-catheter positioned in the atrium.

1.3.2. APPLICATION OF 3D HFR: CONTRAST-ENHANCED ULTRASOUND

Contrast-enhanced ultrasound (CEUS) is an ultrasound modality where contrast agents are administrated into the bloodstream to enhance the sensitivity of the ultrasound image to blood flow. Pioneering work on contrast agents for ultrasound took place between the 1960-1980s [44]. The development of stable microbubble (MB) contrast agents and contrast-specific imaging modes resulted in the increased application of CEUS [45]. MBs consist of a gas core encapsulated in a lipid/protein/synthetic shell material [46]. The large impedance mismatch between gas inside a MB and the surrounding blood results in a high backscattering intensity and thereby increased signal-to-noise ratio [47, 48]. CEUS is currently successfully used in the clinic for the visualization of the macro- and micro-vasculature and the perfusion of tissues. Through the visualization of the vasculature structure and tissue perfusion, CEUS can be used for the diagnosis of various diseases and pathologies, including the characterization of liver and breast lesions [44],

[48–51], as well as the monitoring of therapy responses and the assessment of interventional procedures such as ablation [52].

Pathological modifications of microvascular structure and hemodynamic patterns are important indicators to diagnose and assess various diseases and pathologies. However, the resolution of conventional CEUS images are inherently limited by the wavelength. While using an increased center frequency improves the resolution, this reduces the achievable penetration depth. Therefore, even though the increased backscattering intensity of the microbubbles improves the visualization of microvessels, a detailed map of the microvasculature cannot be distinguished from a conventional CEUS image when vessels are separated by distances smaller than the diffraction limit.

SUPER-RESOLUTION ULTRASOUND LOCALIZATION MICROSCOPY

Super-resolution Ultrasound Localization Microscopy (ULM) is an emerging technique that can realize contrast-based ultrasound imaging at a resolution beyond the diffraction limit [53, 54]. Inspired by optical super-resolution microscopy, the center of isolated microbubbles are localized with sub-wavelength precision and the localized bubble positions are tracked over time to form vascular maps, see Fig. 1.5. Typically, a 10 times better spatial resolution can be achieved with ULM compared to CEUS images [55]. Although ULM could potentially provide a better alternative to CEUS in clinical areas where the microvasculature is depicted, there are still several technical and practical barriers to its clinical application [56].

Volumetric imaging is highly desired for CEUS and ULM to provide a 3D map of the vasculature and to allow for the correction of out-of-plane motion. At the same time, high frame rates are desirable for the effective application of post-processing filters and motion compensation and to reduce acquisition time.

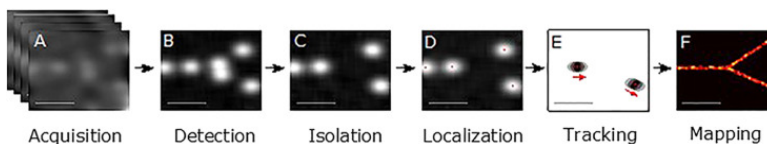


Figure 1.5: Illustration of a general processing pipeline for super-resolution ultrasound imaging. Image from Chistensen-Jeffries et al. [53]. A) Acquisition and beamforming of the image. B) Detecting micro-bubbles. C) Removal of microbubbles that cannot be separated due to too much overlap of the signals. D) Localizing the center of the MBs. E) Tracking the MBs across multiple frames. F) Constructing either a map of microbubble density or velocity.

1.4. DEEP LEARNING FOR ULTRASOUND SIGNAL PROCESSING

Very successful applications of deep learning in imaging include the fields of image segmentation and classification. In the medical imaging field, the main focus of applications of deep learning was initially also on segmentation and classification tasks [57]. More recently, attention also turned towards solving inverse problems, i.e. estimating parameters from (imperfect) observations, such as denoising and improving the process of reconstructing images [58, 59]. This is also the case for ultrasound imaging, where

deep learning techniques have been applied along various stages of the signal processing chain [60].

To realize high-frame-rate volumetric ultrasound imaging, compromises that come at the cost of image quality are often necessary to reach the desired frame rate and realize a realistic channel count. For miniature ultrasound devices, the constraints can be even stronger leading to larger trade-offs in image quality. Therefore, realizing a more powerful processing of the received signals through deep learning techniques could play an important role in realizing high-quality high-frame-rate volumetric ultrasound.

1.5. THESIS OUTLINE

High-frame-rate volumetric ultrasound is desired for many applications. However, when developing ultrasound devices capable of HFR 3D imaging, reducing the channel count and data rate to feasible levels without reducing image quality below what is required for the desired applications is a major challenge. The application of the device must be kept in mind to make the right trade-offs. Still, compromises which negatively impact image quality are sometimes unavoidable, increasing the interest in the application of signal processing methods that improve image quality. The goal of this thesis is to develop high-frame-rate volumetric ultrasound imaging through dedicated transducer design and explore how deep learning-based beamforming of the transducer signals can further help achieve this goal. The first part of this thesis focuses on the design, realization, and testing of an ultrasound transducer prototype for high-frame-rate 3D intracardiac echography with the aim of not just providing 3D guidance during interventional procedures, but specifically to enable mapping of the electromechanical wave propagation. The second part of the thesis focuses on using deep learning-based beamforming to improve image quality in high-frame-rate volumetric imaging for contrast imaging with sparse array probes and for miniature ultrasound probes such as ICE transducers. This thesis has the following outline:

Chapter 2 describes the development of a transducer layout and imaging scheme that enables volumetric imaging with a sufficient frame rate and image quality for intracardiac electromechanical wave imaging, while reducing the data rate to realistic values. A 1D micro-beamforming approach is used to achieve the channel count and data reduction, while the shape and size of the transmit beam are optimized to suppress grating-lobes that would cause image artifacts resulting from the micro-beamforming. The spacing of transducer elements is chosen with space for dedicated electronics in mind and the divergence and central frequency of the array are optimized to achieve a high axial resolution for EWI while suppressing secondary axial pressure waves arising from diverging wave transmission with a relatively large element spacing. This simulation-based chapter shows a promising ICE design for EWI, where the catheters channel count constraint can be satisfied given a further on chip channel count reduction of a factor 4. **Chapter 3** presents the first 3D-ICE prototype consisting of a matrix of a limited number of piezoelectric transducer elements integrated on a dedicated ASIC that provides the required electronics including pulsers, analogue-to-digital conversion, micro-beamforming and a further channel reduction through time-division multiplexing. The functionality of the prototype transducer was shown with electronic measurements, acoustic measurements and an imaging experiment. **Chapter 4** shows the design and fabri-

cation of a follow-up 3D-ICE prototype of the full intended elevational size and with full transmit control, allowing the realization of steered diverging waves that form an essential part of the imaging strategy for EWI. Acoustical measurements characterize the transducers transmit and receive behavior and the high-frame-rate 3D imaging capability is shown.

Chapter 5 addresses the reduced lateral resolution that miniature ultrasound probes with small apertures face. The use of Adaptive Beamforming by deep LEarning (ABLE) in combination with training targets generated by a larger aperture array is proposed. The receptive field of the beamformer is extended across multiple voxels to deal with the focussing errors introduced by micro-beamforming methods often employed in matrix arrays. Only simulated training data was required to quantitatively and qualitatively improve lateral resolution.

Spiral arrays are an attractive option to realize contrast-enhanced volumetric ultrasound due to their relatively low cable count, data rate and cost. Although their transmit efficiency and receive sensitivity is lower compared to fully populated arrays, the high reflectivity of microbubbles makes this less of a concern in contrast-enhanced imaging. However, other downsides compared to fully populated matrix arrays remain. The variation of magnitude and pulse shape within the emitted field is higher and the high-amplitude secondary lobes of a sparse array can cause artifacts and reduce contrast during beamforming. At the same time, the unfocused transmit beams needed for high-frame-rate imaging also negatively impact resolution. In **Chapter 6** we examine the use of deep learning-based beamformers to improve image quality of 3D contrast ultrasound images acquired with a sparse spiral array. ABLE beamforming and a novel deep learning-based beamformer, neural MAP, which allows incorporation of prior information into the beamforming process, are compared to two existing beamforming techniques. Localization performance for super-resolution imaging is also examined for in silico and in vivo data. ULM images acquired with the different beamformers are presented. Finally, **Chapter 7** discusses the findings of this thesis as well as recommendations for future work.

REFERENCES

- [1] C. F. Dietrich, C. B. Sirlin, M. O’Boyle, Y. Dong, and C. Jenssen, “Editorial on the Current Role of Ultrasound”, *Applied Sciences*, vol. 9, no. 17, 2019. DOI: [10.3390/app9173512](https://doi.org/10.3390/app9173512).
- [2] T. L. Szabo, *Diagnostic ultrasound imaging: inside out*. Academic press, 2004.
- [3] J. Bercoff, “Ultrafast Ultrasound Imaging”, in *Ultrasound Imaging*, I. V. Minin and O. V. Minin, Eds., Rijeka: IntechOpen, 2011, ch. 1. DOI: [10.5772/19729](https://doi.org/10.5772/19729).
- [4] C. Bruneel, R. Torguet, K. Rouvaen, E. Bridoux, and B. Nongaillard, “Ultrafast echotomographic system using optical processing of ultrasonic signals”, *Applied Physics Letters*, vol. 30, no. 8, pp. 371–373, 1977. DOI: [10.1063/1.89436](https://doi.org/10.1063/1.89436).
- [5] J. Bercoff, S. Chaffai, M. Tanter, L. Sandrin, S. Catheline, M. Fink, J. Gennisson, and M. Meunier, “In vivo breast tumor detection using transient elastography”, *Ultrasound in medicine & biology*, vol. 29, no. 10, pp. 1387–1396, 2003. DOI: [https://doi.org/10.1016/S0301-5629\(03\)00978-5](https://doi.org/10.1016/S0301-5629(03)00978-5).
- [6] M. Couade, M. Pernot, M. Tanter, E. Messas, A. Bel, M. Ba, A.-A. Hagège, and M. Fink, “Ultrafast imaging of the heart using circular wave synthetic imaging with phased arrays”, in *2009 IEEE International Ultrasonics Symposium*, IEEE, 2009, pp. 515–518. DOI: [10.1109/ULTSYM.2009.5441640](https://doi.org/10.1109/ULTSYM.2009.5441640).
- [7] D. P. Shattuck, M. D. Weinschenker, S. W. Smith, and O. T. von Ramm, “Explososcan: A parallel processing technique for high speed ultrasound imaging with linear phased arrays”, *The Journal of the Acoustical Society of America*, vol. 75, no. 4, pp. 1273–1282, 1984. DOI: [10.1121/1.390734](https://doi.org/10.1121/1.390734).

[8] G. Montaldo, M. Tanter, J. Bercoff, N. Benech, and M. Fink, "Coherent plane-wave compounding for very high frame rate ultrasonography and transient elastography", *IEEE transactions on ultrasonics, ferroelectrics, and frequency control*, vol. 56, no. 3, pp. 489–506, 2009. DOI: [10.1109/TUFFC.2009.1067](https://doi.org/10.1109/TUFFC.2009.1067).

[9] J. Provost, C. Papadacci, J. E. Arango, M. Imbault, M. Fink, J. L. Gennisson, M. Tanter, and M. Pernot, "3D ultrafast ultrasound imaging in vivo", *Physics in Medicine and Biology*, vol. 59, no. 19, p. L1, 2014. DOI: [10.1088/0031-9155/59/19/L1](https://doi.org/10.1088/0031-9155/59/19/L1).

[10] M. Tanter and M. Fink, "Ultrafast imaging in biomedical ultrasound", *IEEE Transactions on Ultrasonics, Ferroelectrics, and Frequency Control*, vol. 61, pp. 102–119, 1 2014. DOI: [10.1109/TUFFC.2014.6689779](https://doi.org/10.1109/TUFFC.2014.6689779).

[11] L. Sandrin, B. Fourquet, J.-M. Hasquenoph, S. Yon, C. Fournier, F. Mal, C. Christidis, M. Ziol, B. Poulet, et al., "Transient elastography: a new noninvasive method for assessment of hepatic fibrosis", *Ultrasound in medicine & biology*, vol. 29, no. 12, pp. 1705–1713, 2003. DOI: [10.1016/j.ultrasmedbio.2003.07.001](https://doi.org/10.1016/j.ultrasmedbio.2003.07.001).

[12] J. Bercoff, M. Tanter, and M. Fink, "Supersonic shear imaging: a new technique for soft tissue elasticity mapping", *IEEE transactions on ultrasonics, ferroelectrics, and frequency control*, vol. 51, no. 4, pp. 396–409, 2004. DOI: [10.1109/TUFFC.2004.1295425](https://doi.org/10.1109/TUFFC.2004.1295425).

[13] M. Tanter, J. Bercoff, A. Athanasiou, T. Deffieux, J.-L. Gennisson, G. Montaldo, M. Muller, A. Tardivon, and M. Fink, "Quantitative assessment of breast lesion viscoelasticity: initial clinical results using supersonic shear imaging", *Ultrasound in medicine & biology*, vol. 34, no. 9, pp. 1373–1386, 2008. DOI: [10.1016/j.ultrasmedbio.2008.02.002](https://doi.org/10.1016/j.ultrasmedbio.2008.02.002).

[14] E. Macé, G. Montaldo, I. Cohen, M. Baulac, M. Fink, and M. Tanter, "Functional ultrasound imaging of the brain", *Nature methods*, vol. 8, no. 8, pp. 662–664, 2011. DOI: [10.1038/nmeth.1641](https://doi.org/10.1038/nmeth.1641).

[15] B.-F. Osmanski, C. Martin, G. Montaldo, P. Lanièce, F. Pain, M. Tanter, and H. Gurden, "Functional ultrasound imaging reveals different odor-evoked patterns of vascular activity in the main olfactory bulb and the anterior piriform cortex", *Neuroimage*, vol. 95, pp. 176–184, 2014. DOI: [10.1016/j.neuroimage.2014.03.054](https://doi.org/10.1016/j.neuroimage.2014.03.054).

[16] J. Udesen, F. Gran, K. L. Hansen, J. A. Jensen, C. Thomsen, and M. B. Nielsen, "High frame-rate blood vector velocity imaging using plane waves: Simulations and preliminary experiments", *IEEE transactions on ultrasonics, ferroelectrics, and frequency control*, vol. 55, no. 8, pp. 1729–1743, 2008. DOI: [10.1109/TUFFC.2008.858](https://doi.org/10.1109/TUFFC.2008.858).

[17] K. L. Hansen, J. Udesen, F. Gran, J. A. Jensen, and M. B. Nielsen, "In-vivo examples of flow patterns with the fast vector velocity ultrasound method", *Ultraschall in der Medizin-European Journal of Ultrasound*, vol. 30, no. 05, pp. 471–477, 2009. DOI: [10.1055/s-0028-1109572](https://doi.org/10.1055/s-0028-1109572).

[18] O. Couture, E. Dransart, S. Dehay, F. Nemati, D. Decaudin, L. Johannes, and M. Tanter, "Tumor delivery of ultrasound contrast agents using Shiga toxin B subunit", *Molecular imaging*, vol. 10, no. 2, pp. 7290–2010, 2011. DOI: [10.2310/7290.2010.00030](https://doi.org/10.2310/7290.2010.00030).

[19] O. Couture, M. Fink, and M. Tanter, "Ultrasound contrast plane wave imaging", *IEEE transactions on ultrasonics, ferroelectrics, and frequency control*, vol. 59, no. 12, pp. 2676–2683, 2012. DOI: [10.1109/TUFFC.2012.2508](https://doi.org/10.1109/TUFFC.2012.2508).

[20] J. Provost, W.-N. Lee, K. Fujikura, and E. E. Konofagou, "Imaging the electromechanical activity of the heart in vivo", *Proceedings of the National Academy of Sciences*, vol. 108, no. 21, pp. 8565–8570, 2011. DOI: [10.1073/pnas.1011688108](https://doi.org/10.1073/pnas.1011688108).

[21] T. Deffieux, J. L. Gennisson, M. Tanter, M. Fink, and A. Nordez, "Ultrafast imaging of in vivo muscle contraction using ultrasound", *Applied Physics Letters*, vol. 89, 18 2006. DOI: [10.1063/1.2378616](https://doi.org/10.1063/1.2378616).

[22] B. W. Ossenkoppele, L. Wei, B. Luijten, H. J. Vos, N. De Jong, R. J. Van Sloun, and M. D. Verweij, "3-D contrast enhanced ultrasound imaging of an in vivo chicken embryo with a sparse array and deep learning based adaptive beamforming", in *2022 IEEE International Ultrasonics Symposium (IUS)*, IEEE, 2022, pp. 1–4. DOI: [10.1109/IUS54386.2022.9957383](https://doi.org/10.1109/IUS54386.2022.9957383).

[23] M. Bernal, B. Cunitz, D. Rohrbach, and R. Daigle, "High-frame-rate volume imaging using sparse-random-aperture compounding", *Physics in Medicine and Biology*, vol. 65, no. 17, 2020. DOI: [10.1088/1361-6560/ab9372](https://doi.org/10.1088/1361-6560/ab9372).

[24] O. Martínez-Graullera, C. J. Martín, G. Godoy, and L. G. Ullate, "2D array design based on Fermat spiral for ultrasound imaging", *Ultrasonics*, vol. 50, no. 2, pp. 280–289, 2010. DOI: [10.1016/j.ultras.2009.09.010](https://doi.org/10.1016/j.ultras.2009.09.010).

[25] A. Ramalli, S. Harput, S. Bezy, E. Boni, R. J. Eckersley, P. Tortoli, and J. D'Hooge, "High-frame-rate tri-plane echocardiography with spiral arrays: From simulation to real-time implementation", *IEEE*

Transactions on Ultrasonics, Ferroelectrics, and Frequency Control, vol. 67, no. 1, pp. 57–69, 2020. DOI: [10.1109/TUFFC.2019.2940289](https://doi.org/10.1109/TUFFC.2019.2940289).

[26] L. Wei, E. Boni, A. Ramalli, F. Pool, E. Noothout, A. F. Van Der Steen, M. D. Verweij, P. Tortoli, N. De Jong, *et al.*, “Sparse 2-D PZT-on-PCB Arrays With Density Tapering”, *IEEE Transactions on Ultrasonics, Ferroelectrics, and Frequency Control*, vol. 69, no. 10, pp. 2798–2809, 2022. DOI: [10.1109/TUFFC.2022.3204118](https://doi.org/10.1109/TUFFC.2022.3204118).

[27] L. Wei, G. Wahyulaksana, B. Meijlink, A. Ramalli, E. Noothout, M. D. Verweij, E. Boni, K. Kooiman, A. F. Van Der Steen, *et al.*, “High Frame Rate Volumetric Imaging of Microbubbles Using a Sparse Array and Spatial Coherence Beamforming”, *IEEE Transactions on Ultrasonics, Ferroelectrics, and Frequency Control*, vol. 68, no. 10, pp. 3069–3081, 2021. DOI: [10.1109/TUFFC.2021.3086597](https://doi.org/10.1109/TUFFC.2021.3086597).

[28] C. E. Morton and G. R. Lockwood, “Theoretical assessment of a crossed electrode 2-D array for 3-D imaging”, in *IEEE Symposium on Ultrasonics*, 2003, IEEE, vol. 1, 2003, pp. 968–971. DOI: [10.1109/ULTSYM.2003.1293560](https://doi.org/10.1109/ULTSYM.2003.1293560).

[29] C. E. Demore, A. W. Joyce, K. Wall, and G. R. Lockwood, “Real-time volume imaging using a crossed electrode array”, *IEEE transactions on ultrasonics, ferroelectrics, and frequency control*, vol. 56, no. 6, pp. 1252–1261, 2009. DOI: [10.1109/TUFFC.2009.1167](https://doi.org/10.1109/TUFFC.2009.1167).

[30] C. H. Seo and J. T. Yen, “A 256 x 256 2-D array transducer with row-column addressing for 3-D rectilinear imaging”, *IEEE transactions on ultrasonics, ferroelectrics, and frequency control*, vol. 56, no. 4, pp. 837–847, 2009. DOI: [10.1109/TUFFC.2009.1107](https://doi.org/10.1109/TUFFC.2009.1107).

[31] H. Bouzari, M. Engholm, C. Beers, M. B. Stuart, S. I. Nikolov, E. V. Thomsen, and J. A. Jensen, “Curvilinear 3-D Imaging Using Row-Column-Addressed 2-D Arrays With a Diverging Lens: Feasibility Study”, *IEEE Transactions on Ultrasonics, Ferroelectrics, and Frequency Control*, vol. 64, no. 6, pp. 978–988, 2017. DOI: [10.1109/TUFFC.2017.2687521](https://doi.org/10.1109/TUFFC.2017.2687521).

[32] S. S. Kim, Z. M. Hijazi, R. M. Lang, and B. P. Knight, “The use of intracardiac echocardiography and other intracardiac imaging tools to guide noncoronary cardiac interventions”, *Journal of the American College of Cardiology*, vol. 53, no. 23, pp. 2117–2128, 2009. DOI: [10.1016/j.jacc.2009.01.071](https://doi.org/10.1016/j.jacc.2009.01.071).

[33] D. Wildes, W. Lee, B. Haider, S. Cogan, K. Sundaresan, D. M. Mills, C. Yetter, P. H. Hart, C. R. Haun, *et al.*, “4-D ICE: A 2-D Array Transducer with Integrated ASIC in a 10-Fr Catheter for Real-Time 3-D Intracardiac Echocardiography”, *IEEE Transactions on Ultrasonics, Ferroelectrics, and Frequency Control*, vol. 63, no. 12, pp. 2159–2173, 2016. DOI: [10.1109/TUFFC.2016.2618602](https://doi.org/10.1109/TUFFC.2016.2618602).

[34] R. Fontes-Carvalho, F. Sampaio, J. Ribeiro, and V. Gama Ribeiro, “Three-dimensional intracardiac echocardiography: a new promising imaging modality to potentially guide cardiovascular interventions”, *European Heart Journal-Cardiovascular Imaging*, vol. 14, no. 10, pp. 1028–1028, 2013. DOI: doi.org/10.1093/eihci/jet047.

[35] M. Alkhouri, T. Simard, A. M. Killu, P. A. Friedman, and R. Padang, “First-in-Human Use of a Novel Live 3D Intracardiac Echo Probe to Guide Left Atrial Appendage Closure”, *Cardiovascular Interventions*, vol. 14, no. 21, pp. 2407–2409, 2021. DOI: [10.1016/j.jcin.2021.07.024](https://doi.org/10.1016/j.jcin.2021.07.024).

[36] J. Provost, W. Lee, K. Fujikura, and E. E. Konofagou, “Electromechanical wave imaging of normal and ischemic hearts *in vivo*”, *IEEE transactions on medical imaging*, vol. 29, no. 3, pp. 625–635, 2009. DOI: [10.1109/TMI.2009.2030186](https://doi.org/10.1109/TMI.2009.2030186).

[37] J. Grondin, D. Wang, C. S. Grubb, N. Trayanova, and E. E. Konofagou, “4D cardiac electromechanical activation imaging”, *Computers in biology and medicine*, vol. 113, p. 103382, 2019. DOI: doi.org/10.1016/j.combiomed.2019.103382.

[38] M. Soozande, B. W. Ossenkoppele, Y. Hopf, M. A. P. Pertijs, M. D. Verweij, N. De Jong, H. J. Vos, and J. G. Bosch, “Imaging Scheme for 3-D High-Frame-Rate Intracardiac Echography: A Simulation Study”, *IEEE Transactions on Ultrasonics, Ferroelectrics, and Frequency Control*, vol. 69, no. 10, pp. 2862–2874, 2022. DOI: [10.1109/TUFFC.2022.3186487](https://doi.org/10.1109/TUFFC.2022.3186487).

[39] J. Jalife, O. Berenfeld, and M. Mansour, “Mother rotors and fibrillatory conduction: A mechanism of atrial fibrillation”, *Cardiovascular Research*, vol. 54, no. 2, pp. 204–216, 2002. DOI: [10.1016/S0008-6363\(02\)00223-7](https://doi.org/10.1016/S0008-6363(02)00223-7).

[40] J. Sra and M. Akhtar, “Mapping Techniques for Atrial Fibrillation Ablation”, *Current Problems in Cardiology*, vol. 32, no. 12, pp. 669–767, 2007. DOI: [10.1016/j.cpcardiol.2007.09.002](https://doi.org/10.1016/j.cpcardiol.2007.09.002).

[41] M. Pernot and E. E. Konofagou, “Electromechanical imaging of the myocardium at normal and pathological states”, in *IEEE Ultrasonics Symposium, 2005.*, IEEE, vol. 2, 2005, pp. 1091–1094. DOI: [10.1109/ULTSYM.2005.1603040](https://doi.org/10.1109/ULTSYM.2005.1603040).

1

- [42] E. E. Konofagou and J. Provost, "Electromechanical wave imaging for noninvasive mapping of the 3D electrical activation sequence in canines and humans *in vivo*", *Journal of Biomechanics*, vol. 45, no. 5, pp. 856–864, 2012. DOI: doi.org/10.1016/j.jbiomech.2011.11.027.
- [43] J. Provost, S. Thiébaut, J. Luo, and E. E. Konofagou, "Single-heartbeat electromechanical wave imaging with optimal strain estimation using temporally unequispaced acquisition sequences", *Physics in Medicine & Biology*, vol. 57, no. 4, p. 1095, 2012. DOI: [10.1088/0031-9155/57/4/1095](https://doi.org/10.1088/0031-9155/57/4/1095).
- [44] S. B. Feinstein, B. Coll, D. Staub, D. Adam, A. F. Schinkel, F. J. Ten Cate, and K. Thomenius, "Contrast enhanced ultrasound imaging", *Journal of Nuclear Cardiology*, vol. 17, no. 1, pp. 106–115, 2010. DOI: [10.1007/s12350-009-9165-y](https://doi.org/10.1007/s12350-009-9165-y).
- [45] H.-X. Xu, H. P. Weskott, J.-B. Liu, and R.-Q. Zheng, "Contrast-Enhanced Ultrasound", *BioMed Research International*, vol. 2015, pp. 1–2, 2015. DOI: [10.1155/2015/865028](https://doi.org/10.1155/2015/865028).
- [46] W. K. Chong, V. Papadopoulou, and P. A. Dayton, "Imaging with ultrasound contrast agents: current status and future", *Abdominal Radiology*, vol. 43, no. 4, pp. 762–772, 2018. DOI: [10.1007/s00261-018-1516-1](https://doi.org/10.1007/s00261-018-1516-1).
- [47] C. Dietrich, M. Averkiou, M. Nielsen, R. Barr, P. Burns, F. Calliada, V. Cantisani, B. Choi, M. Chammas, *et al.*, "How to perform Contrast-Enhanced Ultrasound (CEUS)", *Ultrasound International Open*, vol. 04, no. 01, E2–E15, Jan. 2018. DOI: [10.1055/s-0043-123931](https://doi.org/10.1055/s-0043-123931).
- [48] P. G. Ranganath, M. L. Robbin, S. J. Back, E. G. Grant, and D. T. Fetzer, "Practical advantages of contrast-enhanced ultrasound in abdominopelvic radiology", *Abdominal Radiology*, vol. 43, no. 4, pp. 998–1012, 2018. DOI: [10.1007/s00261-017-1442-7](https://doi.org/10.1007/s00261-017-1442-7).
- [49] P. S. Sidhu, V. Cantisani, C. F. Dietrich, O. H. Gilja, A. Saftoiu, E. Bartels, M. Bertolotto, F. Calliada, D. A. Clevert, *et al.*, "The EFSUMB guidelines and recommendations for the clinical practice of contrast-enhanced ultrasound (CEUS) in Non-Hepatic Applications: Update 2017 (Long Version)", *Ultraschall in der Medizin*, vol. 39, no. 2, e2–e44, 2018. DOI: [10.1055/a-0586-1107](https://doi.org/10.1055/a-0586-1107).
- [50] C. F. Dietrich, C. P. Nolsoe, R. G. Barr, A. Berzigotti, P. N. Burns, V. Cantisani, M. C. Chammas, N. Chaubal, B. I. Choi, *et al.*, "Guidelines and Good Clinical Practice Recommendations for Contrast Enhanced Ultrasound (CEUS) in the Liver – Update 2020 – WFUMB in Cooperation with EFSUMB, AF-SUMB, AIUM, and FLAUS", *Ultraschall in der Medizin - European Journal of Ultrasound*, vol. 41, no. 05, pp. 562–585, Jul. 2020. DOI: [10.1055/a-1177-0530](https://doi.org/10.1055/a-1177-0530).
- [51] J. Wang, R. Zhao, and J. Cheng, "Diagnostic accuracy of contrast-enhanced ultrasound to differentiate benign and malignant breast lesions: A systematic review and meta-analysis", *European Journal of Radiology*, vol. 149, no. January, p. 110219, 2022. DOI: [10.1016/j.ejrad.2022.110219](https://doi.org/10.1016/j.ejrad.2022.110219).
- [52] R. Kessner, D. A. Nakamoto, V. Kondray, S. Partovi, Y. Ahmed, and N. Azar, "Contrast-Enhanced Ultrasound Guidance for Interventional Procedures", *Journal of Ultrasound in Medicine*, vol. 38, no. 10, pp. 2541–2557, 2019. DOI: [10.1002/jum.14955](https://doi.org/10.1002/jum.14955).
- [53] K. Christensen-Jeffries, O. Couture, P. A. Dayton, Y. C. Eldar, K. Hynynen, F. Kiessling, M. O. Reilly, G. F. Pinton, G. Schmitz, *et al.*, "Super-resolution Ultrasound Imaging", *Ultrasound in Medicine and Biology*, vol. 46, no. 4, pp. 865–891, Apr. 2020. DOI: [10.1016/j.ultrasmedbio.2019.11.013](https://doi.org/10.1016/j.ultrasmedbio.2019.11.013).
- [54] O. Couture, B. Besson, G. Montaldo, M. Fink, and M. Tanter, "Microbubble ultrasound super-localization imaging (MUSLI)", in *2011 IEEE International Ultrasonics Symposium*, IEEE, 2011, pp. 1285–1287. DOI: [10.1109/ULTSYM.2011.6293576](https://doi.org/10.1109/ULTSYM.2011.6293576).
- [55] Y. Desailly, J. Pierre, O. Couture, and M. Tanter, "Resolution limits of ultrafast ultrasound localization microscopy", *Physics in Medicine and Biology*, vol. 60, pp. 8723–8740, 22 2015. DOI: [10.1088/0031-9155/60/22/8723](https://doi.org/10.1088/0031-9155/60/22/8723).
- [56] H. Yi, M. R. Lowerison, P. Song, and W. Zhang, "A review of clinical applications for super-resolution ultrasound localization microscopy", *Current Medical Science*, vol. 42, no. 1, pp. 1–16, 2022. DOI: [10.1007/s11596-021-2459-2](https://doi.org/10.1007/s11596-021-2459-2).
- [57] M. T. McCann, K. H. Jin, and M. Unser, "Convolutional neural networks for inverse problems in imaging: A review", *IEEE Signal Processing Magazine*, vol. 34, no. 6, pp. 85–95, 2017. DOI: [10.1109/MSP.2017.2739299](https://doi.org/10.1109/MSP.2017.2739299).
- [58] A. Lucas, M. Iliadis, R. Molina, and A. K. Katsaggelos, "Using deep neural networks for inverse problems in imaging: beyond analytical methods", *IEEE Signal Processing Magazine*, vol. 35, no. 1, pp. 20–36, 2018. DOI: [10.1109/MSP.2017.2760358](https://doi.org/10.1109/MSP.2017.2760358).
- [59] G. Wang, J. C. Ye, K. Mueller, and J. A. Fessler, "Image reconstruction is a new frontier of machine learning", *IEEE transactions on medical imaging*, vol. 37, no. 6, pp. 1289–1296, 2018. DOI: [10.1109/TMI.2018.2833635](https://doi.org/10.1109/TMI.2018.2833635).

[60] R. J. G. Van Sloun, R. Cohen, and Y. C. Eldar, "Deep learning in ultrasound imaging", *Proceedings of the IEEE*, vol. 108, no. 1, pp. 11–29, 2019. DOI: [10.1109/jproc.2019.2932116](https://doi.org/10.1109/jproc.2019.2932116).

2

IMAGING SCHEME FOR 3-D HIGH-FRAME-RATE INTRACARDIAC ECHOGRAPHY: A SIMULATION STUDY

This chapter has been published as:

Mehdi Soozande, Boudewine W. Ossenkoppele, Yannick Hopf, Michiel A.P. Pertijs, Martin D. Verweij, Nico de Jong, Hendrik J. Vos, Johan G. Bosch, Imaging Scheme for 3-D High-Frame-Rate Intracardiac Echography: A Simulation Study, IEEE Transactions on Ultrasonics, Ferroelectrics, and Frequency Control, vol. 69, no. 10, pp. 2862-2874, 2022.

2

Atrial fibrillation (AF) is the most common cardiac arrhythmia and is normally treated by RF ablation. Intracardiac echography (ICE) is widely employed during RF ablation procedures to guide the electrophysiologist in navigating the ablation catheter, although only 2-D probes are currently clinically used. A 3-D ICE catheter would not only improve visualization of the atrium and ablation catheter, but it might also provide the 3-D mapping of the electromechanical wave (EW) propagation pattern, which represents the mechanical response of cardiac tissue to electrical activity. The detection of this EW needs 3-D high-frame-rate imaging, which is generally only realizable in tradeoff with channel count and image quality. In this simulation-based study, we propose a high volume rate imaging scheme for a 3-D ICE probe design that employs 1-D micro-beamforming in the elevation direction. Such a probe can achieve a high frame rate while reducing the channel count sufficiently for realization in a 10-Fr catheter. To suppress the grating-lobe (GL) artifacts associated with micro-beamforming in the elevation direction, a limited number of fan-shaped beams with a wide azimuthal and narrow elevational opening angle are sequentially steered to insonify slices of the region of interest. An angular weighted averaging of reconstructed subvolumes further reduces the GL artifacts. We optimize the transmit beam divergence and central frequency based on the required image quality for EW imaging (EWI). Numerical simulation results show that a set of seven fan-shaped transmission beams can provide a frame rate of 1000 Hz and a sufficient spatial resolution to visualize the EW propagation on a large 3-D surface.

2.1. INTRODUCTION

2.1.1. CLINICAL BACKGROUND

The heart pumps blood with a rhythm determined by a group of pacemaking cells in the sinoatrial node. These cells generate an action potential that depolarizes cardiomyocytes. This action potential triggers the adjacent cells and propagates along the cardiac wall to generate global contraction. The conduction properties of cardiomyocytes and electrical pathways can be changed by normal aging or certain diseases, which leads to various types of arrhythmias. Atrial fibrillation (AF) is the most common cardiac arrhythmia and is the major cardiac precursor of stroke [1]. AF can be treated by RF ablation. A high-resolution 3-D anatomical mapping of electrical activity is required for localizing sources generating AF to plan the ablation procedure [2, 3]. A key feature of AF is its irregularity in time and space. Because the patterns of atrial activation change on a beat-to-beat basis, a series of consecutive activation maps is needed to cover the spatiotemporal variation in activation [4]. Intracardiac electroanatomical mapping is widely exploited to generate a 3-D surface map of atrial electrical activity [5].

2.1.2. EW IMAGING

Electrical excitation of cardiomyocytes is followed by a transient contraction after about 20-40 ms [6]. The electrical excitation is passed to neighboring cells and propagates along the atrial wall as a reaction-diffusion wave with a velocity of 0.5-2 m/s [7]. A high correlation between electrical and resulting mechanical activations has been reported in several studies [8-11] and this activation propagates as a wave-like phenomenon over the atrial wall: the electromechanical wave (EW). EW imaging (EWI) was introduced and has been developed by the group of Konofagou [7, 12-19] as a noninvasive ultrasound-based imaging method to map the electromechanical activations in the heart. Recent studies demonstrated a high correlation between the cardiac electrical activity and its consequent EW for healthy and arrhythmic cases in a simulation study [16], in the left ventricular wall [17, 18], atrial wall [15], and also in the walls of all four chambers [20].

EWI is accomplished in a two-stage process on ultrasound data [12-15]. In the first stage, tissue strain is estimated, commonly by a cross-correlation technique, along the axial direction on consecutive RF signals that are acquired at a motion-estimation rate (500-2000 Hz) [19]. In the second stage, EW onset is estimated by measuring the time at which the axial incremental strain departs from or crosses zero at a given pixel. We intend to image the propagation of the EW wavefront with a spatiotemporal resolution suitable for the identification of local electrophysiological phenomena. Since the EW velocities are in the order of 0.5-2 m/s and the desired spatial resolution is in the order of millimeters, we aim at a volume rate of 1000 Hz and a lateral resolution of 2-5 mm.

Current EWI can provide single-beat 2-D maps of the electromechanical wavefront (i.e., a cross-sectional image with activation times) with a lateral resolution of <5 mm. Since the EWs propagate throughout the entire heart, volumetric imaging is desirable to fully visualize their patterns. In previous studies, several 2-D images were acquired and processed separately. Then, a pseudo-3-D map was generated by combining these 2-D maps through ECG gating [20] and spatial interpolation. Recently, Grondin et al. [21] used a transthoracic matrix transducer to achieve 3-D EWI of the entire heart from

the apical view. The narrow intercostal space and channel count limitations restricted their transducer size to 9.6 mm x 9.6 mm. In consequence, the lateral resolution was limited, to 5.8 at 40 mm. For the atria that are located much deeper (>10 cm), the lateral resolution will be lower. It would be interesting to see whether a higher resolution can improve strain mapping and reduce local inaccuracies in the EW patterns, especially in the atria.

2

2.1.3. HIGH-FRAME-RATE 3-D ICE

Using an intracardiac echography (ICE) transducer can drastically reduce the required imaging depth for atrial EWI compared to the transthoracic apical view. Moreover, the possibility of using a higher central frequency compared to transthoracic transducers allows a higher spatial resolution in the atrial regions. Nowadays, ICE is widely exploited for RF ablation procedures to guide the electrophysiologists in septal puncture and to navigate the ablation catheter. However, this is limited to low-frame-rate 2-D-ICE. Several 3-D-ICE designs have been proposed [22–24], but these are not capable of imaging at high frame rates. A high-frame-rate 3-D ICE probe, in addition to delivering at least the functionality of conventional 2-D ICE, could provide a single-beat 3-D EW map. However, high-frame-rate 3-D ultrasound imaging introduces several challenges, including handling a high data rate generated by a large number of elements. Moreover, high volume rate allows just a few transmissions to illuminate the total volume, so a diverging wave transmission scheme is required. Possibilities for compounding are limited, and thus, SNR will be relatively low [25]. Furthermore, an intracardiac catheter imposes additional constraints on the transducer size, cable count, and power dissipation. Therefore, data reduction and an educated choice of design tradeoffs are crucial for high-frame-rate 3-D ICE.

2.1.4. DATA RATE REDUCTION BY MICRO-BEAMFORMING

Micro-beamforming is a well-established method to reduce the channel count while preserving the image quality and SNR for volumetric imaging [26, 27]. In this method, element signals in a subaperture are mutually delayed and summed to form a single micro-beamformed signal from a predefined-steered-direction. The entire region of interest can thus be imaged by steering the subapertures to a sequence of different directions in, potentially, both azimuth and elevation, and implementing a parallel beamforming technique at the back-end system [28–30]. Since the final beamforming is based on the received data from subapertures with a relatively large effective pitch, grating lobes (GLs) can occur. Using relatively narrow transmit beams that are steered to the presteering directions can reduce the GL artifacts. Hence, a significant number of such narrow beams should be utilized to preserve the image quality [26]. Thus, increasing the number of elements per subaperture reduces the channel count but also reduces the achievable volume rate or field of view.

Wildes et al. [22] developed a 2-D transducer consisting of 60 x 14 elements with application-specific integrated electronics for volumetric ICE based on a 10-Fr (3.3 mm) catheter. A 2-D micro-beamforming approach was used to reduce the total receive channel count to 48 (along with power, transmit, and auxiliary signals leading to a total of 88 connections). Their method provided an imaging sector of 90° x 60° x 8 cm with a spa-

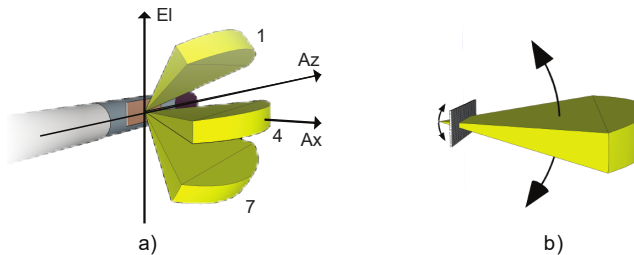


Figure 2.1: (a) Schematic representation of the proposed side-looking transducer mounted in an intracardiac catheter. Azimuth (Az), elevation (El), and axial (Ax) directions are indicated on the corresponding axes. A set of three out of seven fan-shaped beams steered to different directions in elevation is shown to illustrate the transmit scheme. (b) Fan-shaped transmit beam is generated from a virtual source behind the transducer.

tial resolution of $1.7 \text{ mm} \times 4.9 \text{ mm}$ (azimuth x elevation) at a depth of 50 mm. They concluded that the achieved spatial resolution was sufficient for atrial imaging. To suppress the GLs formed by micro-beamforming, narrow beams were used in transmission, which limited the frame rate to 30 vol/s [22].

Implementing a 1-D (i.e., a $1 \times N$ subaperture) rather than a 2-D micro-beamformer introduces the GLs only in the direction in which the micro-beamforming is implemented. Therefore, the transmit beams need to be narrow only in the corresponding direction. Consequently, a 1-D micro-beamforming could provide a relatively high volume rate 3-D imaging by employing a set of fan-shaped diverging transmit beams that are narrow in the micro-beamforming direction and wide in the perpendicular direction (see Fig. 2.1). These asymmetric fan-shaped beams can cover a large volume of interest with a limited number of transmissions. These fan-shaped beams can be generated by a dual virtual source similar to the method proposed by Chen et al. [31] or a single virtual source behind a rectangular transducer, as shown in Fig. 2.1(b). Since a dual virtual source approach generates a curved transmit fan beam, it is less appropriate to be combined with a micro-beamforming approach. Therefore, we use a single virtual source approach in this study.

The size of the 1-D micro-beamformer should be chosen such that the needed reduction in channel count is achieved, while GL levels are kept sufficiently low. In the design of the high-frame-rate 3-D ICE many tradeoffs need to be made to realize an imaging scheme that satisfies the requirements for EWI while remaining within the constraints on transducer size and cable count, resulting from the small catheter size. Furthermore, the elements will be mounted on a pitch-matched application-specific integrated circuit (ASIC) containing all the required electronics, including high-voltage pulsers, low-noise amplifiers, time-gain compensation circuits, ADCs, and micro-beamformers, which are necessary to realize the proposed method [27, 32, 33].

The minimum pitch of the transducer elements is limited to $160\mu\text{m} \times 160\mu\text{m}$ by the area required for the designed electronics.

In this study, we did not consider electronic noise and ultrasonic attenuation in the simulations since we are assuming that they are not limiting factors on the clutter and PSF image quality parameters we are studying here. They have been considered in the electronics design procedure [33] to achieve the desired imaging depth. Although these

electronics design choices put some limits on the transducer layout and the imaging scheme as mentioned in Sections I and II, fully describing these choices is out of the scope of this article.

2

2.1.5. 3-D ICE IMAGING SCHEME DESIGN

In this study, we develop a novel imaging scheme for high-frame-rate 3-D ultrasound imaging with a matrix intracardiac catheter as sketched in Section I-D and optimize the transducer design and imaging scheme for intracardiac EWI. The main goal is to enable volumetric imaging with a sufficient frame rate and image quality for EWI while reducing the data rate to realistic values. The proposed method consists of implementing a 1-D micro-beamforming in the elevation direction to reduce the data rate. By combining this with the transmission of fan-shaped beams, a high-frame-rate is enabled, while GLs in the elevation direction are suppressed. The proposed method achieves further reduction of the GL artifacts and improved contrast to noise ratio (CNR) by implementing angular-weighted coherent compounding. We will discuss the optimization of the imaging scheme (transmit frequency, microbeamformer size, and transmit beam divergence) to achieve the desired channel count reduction while providing a sufficient frame rate and image quality for EWI. Finally, we evaluate the proposed imaging scheme in a series of simulations. The novelty of this work lies in an imaging scheme optimized for dedicated integrated circuitry to realize high-frame-rate 3-D ICE suitable for EWI.

2.2. MATERIALS AND METHODS

2.2.1. IMAGING SCHEME DESIGN: PARAMETERS

We strive for a 3-D ICE design with a frame rate of 1000 Hz, an imaging depth of 10 cm, an opening angle of $70^\circ \times 70^\circ$, and a lateral resolution of 5 mm to be able to realize the 3-D EWI of the left atrium from the right atrium.

For a depth of 10 cm, the pulse repetition frequency (PRF) is limited to 7.7 kHz by the round-trip travel time of the ultrasound waves assuming a speed of sound of 1540 m/s. Therefore, a maximum number of seven transmissions are available to acquire the entire region of interest, and we will always use this number of transmissions in our scheme.

We base the design of the matrix transducer on a 10-Fr intracardiac catheter, which limits the transducer size to 3 mm in the elevation direction [see Fig. 2.1(a)] and the number of cables to a maximum of 100 [22, 34]. The aperture of the matrix array is rectangular, with the shortest axis perpendicular to the ICE probe shaft. We consider square elements with a pitch of 160 μm , imposed by the area needed for the pitch-matched application-specific electronics [32]. Choosing such a large pitch (50%-80% of the wavelength for the assumed frequency range of 5-8 MHz) introduces GLs in image reconstruction and also secondary waves in diverging wave transmission. To counteract these, we optimize the central frequency in the given range to suppress the secondary waves. In addition, an angular weighting function is applied to a conventional delay and sum to reduce the GLs. Based on the chosen pitch and catheter size constraints, we consider a matrix array of 18x64 elements.

The imaging scheme consisting of steered fan-shaped diverging transmit beams will be used with 1-D micro-beamforming in the elevation direction and acquisition of all

element-level signals in the azimuthal direction. Furthermore, angular weighted coherent compounding will be used to reduce GL levels. Transducer size, pitch, number of transmissions, and imaging depth are fixed in this study, whereas the other features are optimized in a simulation study.

2.2.2. STEERABLE FAN-SHAPED TRANSMIT BEAM

A single virtual source was used to generate the desired fan-shaped beam. In this approach, the beam divergence in azimuth and elevation is not independent. First, we determined the virtual source location based on the transducer size and desired beam divergence in the elevational direction, and then, the effective transducer size in azimuth was determined to achieve the required beam divergence in that direction (see Appendix I).

2.2.3. ANGULAR WEIGHTED AVERAGING

A voxel-based delay and sum is proposed to reconstruct an intermediate full volumetric image corresponding to each transmission. Since only a narrow region is insonified in the elevation direction for each transmission, reconstructing regions far from this transmission direction only adds noise to intermediate images. In addition, the receive beam profile contains strong GLs at directions corresponding to the large effective pitch associated with the micro-beamformer size [26]. Hence, the final volumetric image is obtained by applying angular weighting functions to the intermediate images in order to suppress the noise and GLs in noninsonified regions and also improve the image quality by coherent compounding of overlapping regions using

$$I(R, \Theta_r, \varphi) = \sum_{i=1}^7 W(\Theta_r, \Theta_i) \sum_{m=1}^{N_{\mu\text{BF}}} \sum_{n=1}^{N_{\text{Az}}} S_{m,n}(t - \sigma_i - \sigma_{m,n}) \quad (1)$$

where $I(R, \Theta_r, \varphi)$ is the reconstructed RF sample in a spherical coordinate system, $W(\Theta_r, \Theta_i)$ is the weighting function (as shown in Fig. 2.2) corresponding to the transmit direction Θ_i , $S_{m,n}$ is the micro-beamformed signal of a subgroup at the elevation position m and azimuthal position n in the transducer array, $\sigma_i(R, \Theta_r, \varphi)$ is the transmit delay, $\sigma_{m,n}(R, \Theta_r, \varphi)$ is the receive delay, and Θ_i is the transmit/presteering direction.

Fig. 2.2 shows the angular weights as a function of the reconstruction line direction for different transmission directions. To avoid abrupt changes in image intensity, the angular weights have some overlap with their neighboring transmissions [33].

2.2.4. SIMULATION SETUP

The simulation study consists of three steps. First, the azimuthal beam divergence and central frequency in a range of 20° - 45° and 5-8 MHz, respectively, are mutually optimized to provide an acceptable tradeoff among the imaging opening angle, transmit beam quality, and spatial resolution. Transmit beam quality in diverging wave imaging is known to be susceptible to the occurrence of so-called axial lobes or secondary pulses [35, 36], related to imperfect signal cancellation of late-arriving element signals from arrays with pitch larger than half a wavelength. Since the quality of the transmitted wave is very important for our image quality, we will first investigate and optimize the

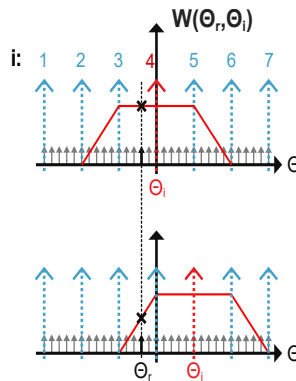


Figure 2.2: Applied weights $W(\theta_r, \theta_i)$ as a function of the reconstruction elevation direction θ_r for different transmit beams. Blue arrows show all transmission directions and red arrow shows the current transmission direction with its corresponding angular weighting function. Black arrows show the reconstruction directions and the bold black arrow shows an example of receive line with its corresponding weights (black cross) when the transmit direction is θ_i .

temporal profile of the transmitted diverging wave in our simulations.

Second, transmit beam divergence in elevation will be determined based on GL artifacts and the intensity uniformity between transmissions. Finally, the image quality will be evaluated for a micro-beamformer size ranging between 1 (no micro-beamforming) and 4 to achieve an acceptable tradeoff between the desired image quality and data rate reduction. The imaging parameters are summarized in Table 2.1. All simulations are performed in Field II [37].

2.2.5. NUMERICAL PHANTOMS

STATIC PHANTOM:

A 3-D numerical phantom, a cube with an edge length of 100 mm containing hyperechoic and hypoechoic spherical regions with diameters of 2, 4, 6, and 10 mm, highly reflective points and background point scatterers with an average density of $0.2/\lambda$, has been used in Field II simulations. The relatively low point scatterer density is chosen to limit simulation time for this large-size cubic phantom and the high number of transducer elements. In addition, a single-point scatterer at a depth of 50 mm is simulated to determine the point spread function (PSF).

BEATING LEFT ATRIUM

To evaluate the proposed high-frame-rate imaging scheme in a dynamic environment, a spherical shell with an outer diameter of 50 mm and a thickness of 3 mm has been simulated mimicking a left atrium. The center of the sphere is at an axial distance of 50 mm, equivalent to imaging the left atrium from the center of right atrium. A circumferentially propagating wave has been introduced to this phantom by applying a radial thickening with an amplitude of 10 mm/s (10 $\mu\text{m}/\text{frame}$). The atrial thickening initiates from a single point and propagates omnidirectionally along the atrial wall with a velocity of 2 m/s [7]. A cross section of the beating left atrium numerical phantom is shown in Fig. 2.3.

Table 2.1: Imaging Parameters

Parameters	Value
Transducer size	2.88 mm x 10.24 mm
Pitch	160 μm x 160 μm
Kerf	20 μm
Number of elements	18x64
Micro-beamformer size	1-4 elements*
Imaging depth	10 cm
Frame rate	> 1000 Hz
Transmit beam	Steerable Fan beam
Number of transmission	7
Transmission beam (azimuth)	Direction: 0°; divergence: 20°-45°*
Transmission beam (elevation)	Direction: -30° to 30°; step:10°;
divergence:	10.7°, 12.5°-20°*; step: 2.5°
Central frequency	5-8 MHz*
Sampling frequency	4xcentral frequency
Transmit apodization	2-D Tukey window with cosine fraction 0.2

* These parameters are evaluated within the given ranges to optimize the imaging scheme.

We use 1-D axial cross correlation (two cycles Tx pulse, 20-sample I/Q) to estimate the frame-to-frame tissue displacement. Since simulating a 3-D numerical phantom with a matrix array in Field II is very time consuming, we limit our simulations to only three pairs of consecutive volumetric datasets acquired at an interval of 1 ms within each pair (i.e., mimicking a frame rate of 1000 Hz). The consecutive pairs of datasets have been simulated for three time points, $t = 0, 10$, and 20 ms to show the concept of EWI. The final map of tissue displacement (actually displacement over 1 ms in the direction of the ultrasound beam, so the axial tissue velocity component) has been generated by applying an image intensity-based mask to the displacement data to only visualize the atrial wall. In addition, another mask based on tissue displacement has been applied to the displacement map to exclude nonmoving tissue.

2.2.6. EVALUATION CRITERIA

The performance of various combinations of transmission and micro-beamforming schemes has been evaluated, as assessed by the widths of PSF at -6 dB (azimuthal and elevational resolutions), the sidelobe level, the GL level, and the CNR. The sidelobe level is defined as the peak level of the highest sidelobe compared to the main lobe in dB, and the GL level is defined as the peak level at the theoretically expected GL direction. These two were measured by imaging only one scatterer in the field of view. The CNR is calculated using [38]

$$CNR = \frac{\mu_s - \mu_c}{\sqrt{(\sigma_s^2 + \sigma_c^2)/2}} \quad (2)$$

where μ_s and μ_c are the mean amplitudes and σ_s and σ_c are the standard deviation

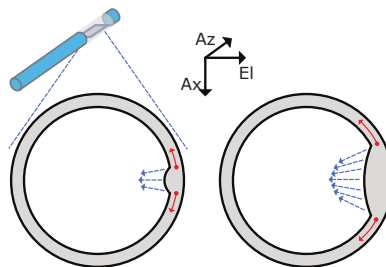


Figure 2.3: Schematic cross sections of the 3-D left atrium numerical phantom (radius 50 mm and thickness 3 mm). Left: wave is introduced as a radial wall thickening (blue arrows). Red arrows show the circumferential electromechanical wavefront propagation direction. Right: wavefront propagation after 10 ms (thickness/excursions not to scale).

of the gray levels in the speckle and anechoic cyst regions, respectively, of the 3-D numerical phantom.

Imaging with a limited number of diverging beams and micro-beamforming may result in angle-dependent changes in image characteristics. To evaluate these effects, a lateral shift-variance plot (LSV-plot) [35] is used. An LSV-plot is constructed for a given imaging system by imaging a point scatterer shifting laterally. For each lateral position, a PSF is calculated and stacked to the other PSFs to form a 2-D image. The entire image is normalized to its maximum value and plotted in a decibel scale. If there is little position dependence, the plot will be invariant along the diagonal; otherwise, deviating structures will be visible revealing the nature of the position dependence. In this study, a point scatterer at a distance of 50 mm from the center of the transducer is shifted along the elevation direction from -45° to 45° with a step of 1° to create the LSV-plot.

2.3. RESULTS

2.3.1. IMAGING SCHEME OPTIMIZATION

TRANSMIT CENTRAL FREQUENCY AND AZIMUTHAL DIVERGENCE ANGLE

When evaluating the transmitted diverging waves, we found significant secondary pulse levels in the transmitted time signals. In Fig. 2.4(a) where the envelope of the transmit pulse is shown for all azimuth angles, it can be seen that the secondary pulse is present over a large range of the opening angle and gets longer for larger angles, following the primary short pulse after a few microseconds. Fig. 2.4(b) shows the transmit pulse generated by a transducer with a 45° divergence and 7.5-MHz center frequency in a point 50 mm from the transducer, at an angle of 40° .

We evaluated how the pulse shape depended on the beam divergence and transmit central frequency. The level of the secondary pulse has been measured at points located on a spherical surface with a radius of 50 mm ranging from -45° to 45° in both azimuth and elevation directions. The maximum of the secondary pulses measured in different directions is shown in Fig. 2.5(a) as a function of central frequency and beam divergence. The function has a triangular local minimum region in the frequency band of 5.3-7.5 MHz and the azimuthal beam divergence of 25° - 45° . Any local minimum close to the

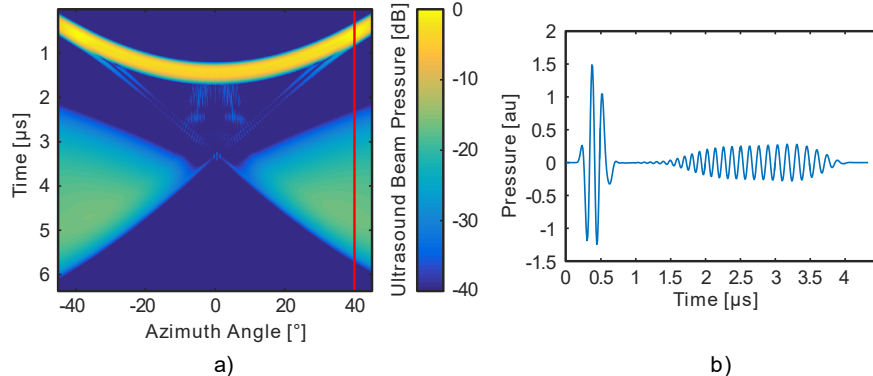


Figure 2.4: Transmitted pressure profile of a diverging wave as a function of time and azimuth angle at typical imaging depth of 50 mm, $f = 7.5$ MHz, and divergence = 45° . (a) Envelope of the pressure from -45° to 45° (red line indicates the position of the point used to acquire the 1-D signal in (b)). (b) Time-domain pressure signal at 40° azimuth. The secondary pulse is observed as a longer pulse with lower amplitude compared to the main pulse.

triangle hypotenuse will achieve low secondary pressure levels for a relatively high central frequency and opening angle. To show the effect of these secondary pulses, images of point scatterers made with transmit beams with different secondary pressure levels are reconstructed. Fig. 2.5(b) shows that the larger secondary pulse [corresponding to the black dot in Fig. 2.5(a)] will interact with the scatterers to show prominent secondary echoes of scatterers (arrows), whereas in Fig. 2.5(c), where the transmit beam has a lower secondary-pulse pressure level [corresponding to the white dot in Fig. 2.5(a)], the secondary echoes are almost invisible. We choose a central frequency of 6 MHz and an azimuthal beam divergence of 35° and these values will be used as bases for the rest of simulations.

ELEVATIONAL BEAM DIVERGENCE AND INTENSITY RIPPLE:

With the proposed transducer size and the chosen azimuthal beam divergence of 35° , the single virtual source technique can provide an elevational beam of 10.7° . The transmit beam profile for this elevational beam divergence is shown in Fig. 2.6, which shows an intensity ripple over elevational angle of -3.6 dB. To reduce this ripple, we would need to increase elevational beam divergence. To achieve the wider elevational beam divergences of 12.5° , 15° , 17.5° , and 20° , the effective number of elements in azimuth was reduced from 64 to 56, 47, 41, and 36 elements, respectively. This azimuthal apodization was needed to maintain the 70° azimuth opening angle when bringing the virtual focus closer to the probe for more elevational divergence. The intensity ripples between two adjacent transmissions are listed in Table 2.2 for different elevational beam divergences as a measure of nonuniformity. The results show a lower intensity ripple for broader beam, which indicates more uniform image intensity along the elevation direction.

ELEVATIONAL BEAM DIVERGENCE AND GLs:

In the next step, the effect of elevational beam divergence on the GL level has been evaluated. The GL directions for a micro-beamformer size of 2, 3, and 4 are 53° , 32° , and 24° ,

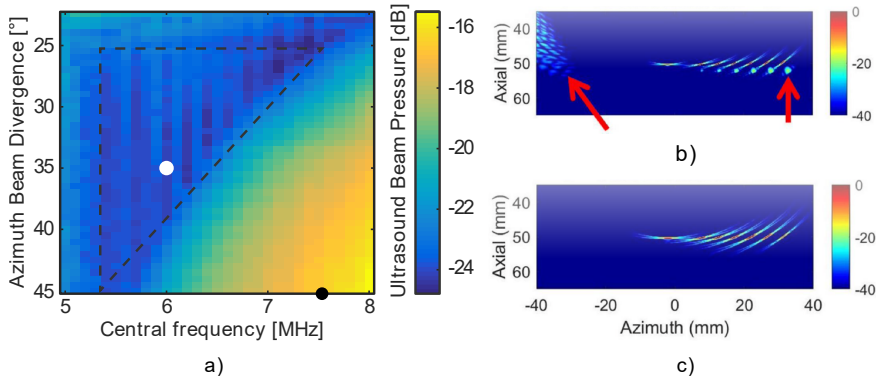


Figure 2.5: (a) Maximum of secondary pressure peaks as a function of central frequency and azimuthal beam divergence. Reconstructed images based on a fully sampled array for a central frequency and azimuthal beam divergence of (b). $f=7.5$ MHz and $\varphi_{az}=45^\circ$ [black point in (a)] and (c). $f=6$ MHz and $\varphi_{az}=35^\circ$ [white point in (a)]. Red arrows show the secondary reflection and GL caused by poor destructive interference of waves transmitted from each individual element.

respectively, at the chosen frequency of 6 MHz. The acoustic pressure at GL directions has been compared for elevational beam divergence of 10.7° , 12.5° , 15° , 17.5° , and 20° . Fig. 2.7 shows that increasing the transmission elevational beam divergence intensifies the GL levels. An elevational beam divergence of 10.7° , which is the narrowest possible divergence, with a beam separation of 10° , provides the lowest GL level and highest SNR at the cost of some nonuniformity in image intensity. We chose the elevational beam divergence of 10.7° and used this value in the remainder of the simulations. With this elevational divergence, the set of steerable fan-shaped beams provides an imaging field of view of 70° (width of insonified region at -3 dB) in the elevation direction.

2.3.2. IMAGING PERFORMANCE EVALUATION

The angular weighted coherent compounding approach is evaluated for a micro-beamformer of 2-4 elements by reconstructing images of a single-point scatterer. Applying the proposed angular weighting function reduces the GL level to a value that we will refer to as the GL residual (GLR). Fig. 2.8(a) shows the effect of using angular-weighted coherent compounding compared to uniform coherent compounding for a micro-beamformer

Table 2.2: Transmit Beam Profile Nonuniformity Measured by the Intensity Ripple Between Two Consecutive Transmissions

Elevational beam divergence	Intensity ripple (dB)
10.7° (possible minimum)	-3.6
12.5°	-3.3
15°	-2.4
17.5°	-1
20°	-0.4

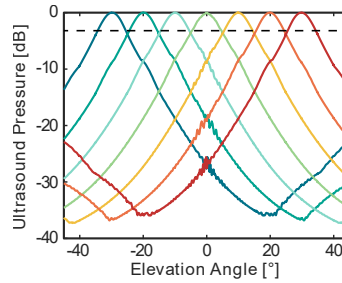


Figure 2.6: Transmit beam profile in the elevation direction for an elevational beam divergence of 10.7° . The horizontal dashed line shows an intensity ripple level of -3.6 dB.

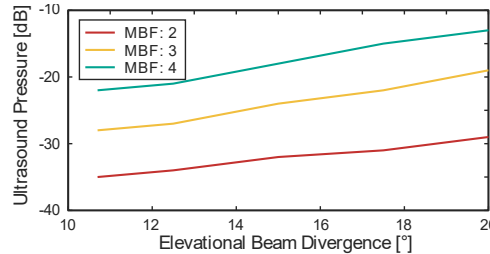


Figure 2.7: Transmit pressure at GL directions, normalized to transmit pressure at main lobe for different beam divergences.

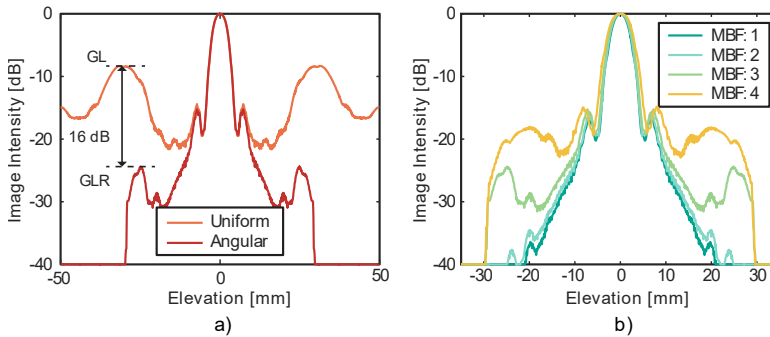


Figure 2.8: (a) PSF in the elevational direction, for a single-point scatterer at 50 mm depth which is reconstructed by uniform coherent compounding and reconstructed by angular-weighted coherent compounding. GL level and GL residual level are shown for uniform coherent compounding and angular-weighted compounding, respectively. (b) PSF for angular-weighted compounding for different micro-beamformer sizes and elevational beam divergence of 10.7° .

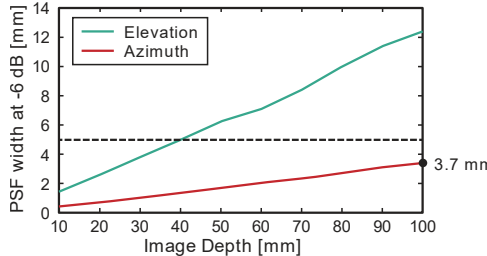


Figure 2.9: Lateral resolution as a function of depth in azimuth and elevation directions for a micro-beamformer size of three elements. The horizontal dashed line indicates the desired lateral resolution for EWI.

size of three elements. This angular weighted coherent compounding reduces the GL levels by 28, 16, and 13 dB for micro-beamformer sizes of 2, 3, and 4, respectively. Elevational PSFs for angular-weighted compounding for different micro-beamformer sizes are shown in Fig. 2.8(b). The width of PSF at -6 dB is shown in Fig. 2.9 for different imaging depths in both azimuthal and elevational directions.

The spatial variance of the proposed imaging scheme in the elevation direction is evaluated by an LSV-plot. Fig. 2.10(a) shows the LSV-plot for micro-beamforming size 3. Although the effect of the seven transmit beams is visible as nonuniform image intensity in this plot, the lateral resolution, sidelobe level, and GL levels are fairly diagonally uniform. In addition to lateral shift variability, the LSV-plot was used to compare the proposed angular weighting function with the conventional triangular weighting function [35]. Since the proposed method compounds a high number of transmissions to reconstruct a single receive line, the LSV-plot is more diagonally uniform and has a narrower main lobe. However, it produces higher clutter around the main lobe, as shown in Fig. 2.10.

The numerical tissue-mimicking phantom has been imaged to evaluate the image quality in terms of CNR for various micro-beamformer sizes. The clutter level is increased in hypoechoic regions by increasing the micro-beamformer size [see Fig. 2.11(a)-(d)], which reduces the CNR in both elevation and azimuth planes, as shown in Fig. 2.11(e). Narrow transmission beams with a large separation angle cause nonuniform image intensity along the elevation direction, as expected from Fig. 2.6. Fig. 2.11(a) and (b) shows that the axial resolution (estimated at 0.8 mm) is not affected by the microbeamforming, as expected, and seems sufficient with respect to the atrial wall thickness.

HIGH-FRAME-RATE IMAGING OF A BEATING ATRIUM PHANTOM:

A rendered volumetric image of the beating left atrial numerical phantom has been generated with a micro-beamformer size of three elements and is shown in Fig. 2.12. A quarter of the top hemisphere has been removed to show the wall thickness in azimuthal, elevational, and c -plane. We can clearly see the spherical object mimicking left atrium. The atrial wall appeared thicker in the elevational direction, which is caused by the lower elevational resolution. A combination of fan-shaped transmit beams and the proposed weighting function successfully suppressed the GLs and no obvious GL is visible. However, nonuniform image intensity is rather visible in the elevation direction.

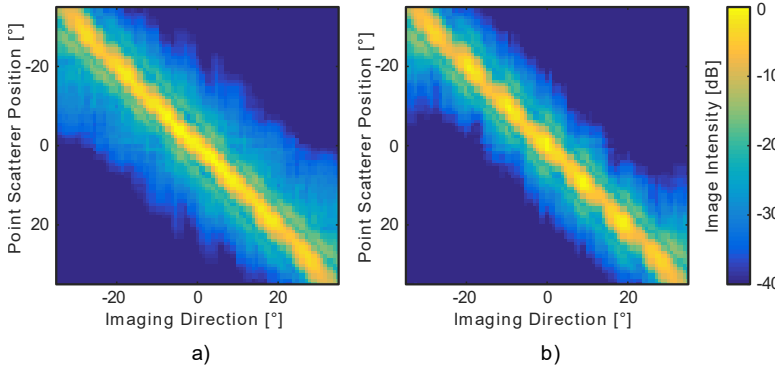


Figure 2.10: LSV-plot of a single-point scatterer at different positions ranging from -35° to 35° in the elevation direction, which is reconstructed by (a) proposed weighting function and (b) triangular weighting function.

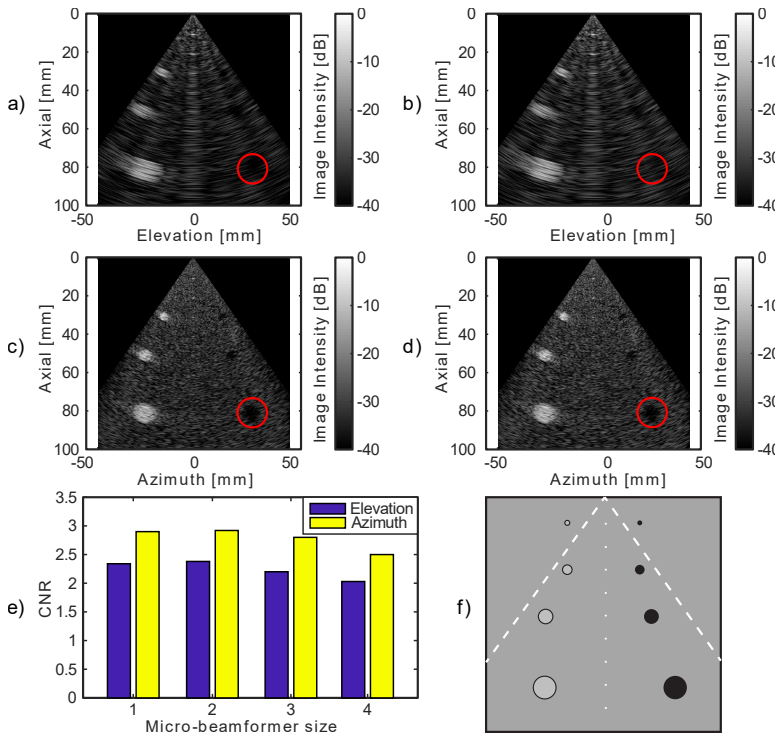


Figure 2.11: Reconstructed images of a tissue-mimicking phantom in (a) elevation direction for a fully sampled array, (b) elevation direction for a micro-beamformer size of three elements, (c) azimuth direction for a fully sampled array, and (d) azimuth direction for a micro-beamformer size of three elements. Red circles show hypoechoic regions where the CNR was calculated. (e) CNR in azimuth and elevation for different micro-beamformer sizes. (f) Schematic representation of tissue-mimicking phantom, rotated to (a) and (b) elevation or (c) and (d) azimuth plane.

Fig. 2.12(a)-(c) shows the tissue displacement maps on three orthogonal planes, namely, azimuthal, elevational, and c -plane, which were calculated at $t = 1$, 11, and 21 ms. The EW has initiated from a point shown by the blue arrow in Fig. 12(a) and propagated omnidirectionally on the atrial surface. Fig. 2.12(b) and (c) shows the propagation of the EW at 11 and 21 ms after the wave generation. The electromechanical wavefront is clearly visible and the color gradient indicates the radial strains. The EW map was masked by an intensity-based mask derived from the B -mode images. There is no unwanted motion detection on other parts of the region of interest. The red arrow in Fig. 2.12(c) shows a region where the radial motion is purely perpendicular to the ultrasound wave axial direction. Therefore, the 1-D axial cross-correlation technique could not detect this displacement.

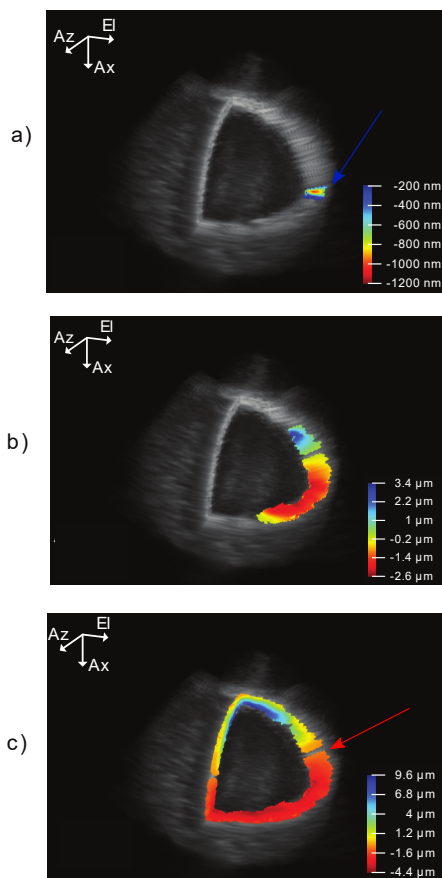


Figure 2.12: Tissue frame-to-frame axial displacement map corresponding to EW propagation at (a) $t = 1$ ms, (b) $t = 11$ ms, and (c) $t = 21$ ms plotted on orthogonal planes. The blue arrow on (a) shows the initial point of EW and the red arrow on (c) shows the location at which the displacement is perpendicular to the ultrasound axial direction and cannot be estimated. The probe is located left side of the atrium at 50-mm distance. Please note that the color scale represents axial displacement over 1 ms, so a displacement of 10 μm is equivalent to an axial velocity component of 10 mm/s.

2.3.3. DISCUSSION AND CONCLUSION

In this study, we have proposed a novel imaging scheme for high-frame-rate 3-D ultrasound imaging with a matrix intracardiac catheter. The main goal is to enable volumetric imaging with a sufficient frame rate and image quality for EWI while reducing the data rate to realistic values. The proposed method consists of three main parts: 1) implementing 1-D micro-beamforming in the elevation direction to reduce the data rate; 2) transmitting fan-shaped beams to suppress GLs in the elevation direction while providing a high frame rate; and 3) angular-weighted coherent compounding to further reduce the GL artifacts and improve CNR.

The transducer consists of 64×18 elements with a pitch of $160 \mu\text{m}$, which is larger than half of the wavelength at 5-8 MHz, giving rise to spatial aliasing. Generating a diverging wave from an array with such pitch can lead to a secondary, trailing, pulse as a result of poor destructive interference of the signals from the adjacent elements-see Fig. 2.4. This secondary pulse will also interact with scatterers, leading to secondary reflections in the reconstructed images and thus increased axial clutter levels [36], as shown in Fig. 2.5(b). Such axial lobes were previously reported by Rodriguez-Molares et al. [39] for coherent plane wave compounding. They theoretically analyzed the secondary-pulse formation and proved that late-arriving transmit waves lead to delayed echoes that render as axial lobes. They showed that in a densely sampled array (pitch $<\lambda/2$), late-arriving signals will cancel each other out, which reduces the axial lobe level. In this work, we reduce the secondary pulse level by carefully choosing the central frequency and azimuthal beam divergence for the given array configuration [see Fig. 2.5(a)].

We intend to image the EW wavefront propagation in 3-D with sufficient spatial resolution by employing a high volume rate of 1 kHz. This is sufficient for local motion estimation over the whole volume, but previous research on EWI [19] suggests that while a local motion detection rate of 0.5-2 kHz is required, a slower rate might be sufficient for the motion sampling (the generation of the strain maps), leaving room for more lenient interleaved spatial interrogation. Provost et al. [19] reported that a mapping rate of 120 Hz would suffice since the highest frequency content of the EW would be around 50 Hz. However, since we operate at higher spatial resolution and the EW is a complex reaction-diffusion wave, we are not sure that this bound is valid in our situation. Therefore, we preferred to pursue the full 1-kHz volume rate. Furthermore, this also opens the way to other high-frame-rate applications such as shear wave elastography and ultrafast Doppler.

A high ultrasound frequency was preferred to achieve a sufficient lateral resolution for EWI. On the other hand, a large opening angle was needed to capture the entire left atrium. As shown in Fig. 2.5, a central frequency of 6 MHz and an azimuth opening angle of 35° will result in a low secondary-pulse pressure level. Furthermore, at these values, small variations in the fabrication process and delay quantization frequency will not have large effects on the secondary pressure level.

The elevational beam divergence is subject to a tradeoff between the image intensity uniformity, SNR, and GL levels. A wider transmission reduces image intensity nonuniformity but also generates a higher acoustic pressure in the GL direction. Since we use a single virtual source method, the effective aperture size in the azimuthal direction must be reduced to generate divergences larger than the smallest realizable divergence of 10.7° .

Consequently, wider elevational divergence reduces SNR.

To achieve a high SNR and low GL levels, we selected a divergence of 10.7° in the elevation direction. This leads to a nonuniform image intensity in the elevation direction. This nonuniformity is not expected to influence the performance of the proposed method for EWI since the tissue displacement is measured in the axial direction. Nonuniformity of the transmitted power in the B-mode can be compensated for by applying a weighting function to the reconstructed images. However, this corrects the nonuniform image intensity at the cost of producing a nonuniform SNR.

By using a dual virtual source technique similar to that proposed by Chen et al. [31], the dependence between the azimuthal and elevational beam divergence can be avoided such that all aperture sizes can be used. However, we found that using a dual source was an unsuitable solution for our design since beams appeared to curve in the elevation direction when steering to large angles, which decreases the overlap between the transmit beam directions and the micro-beamforming presteering direction.

The proposed set of steerable fan-shaped beams can insonify a region of $70^\circ \times 70^\circ$, which is sufficient to cover the entire left atrium from the center of the right atrium, as shown in Fig. 2.12.

Fig. 12 shows a rendered volumetric image of the left atrium. Since the lateral resolution is lower in elevation, the atrial wall seems to be thicker in this direction in comparison to the azimuthal direction. The image intensity nonuniformity caused by narrow transmit beams in elevation is visible as darker traces. In addition, there are some artifacts at lower depths that are caused by high clutter level of the proposed method, as shown in Fig. 10(a). The high clutter levels are mainly caused by implementing 1-D micro-beamforming in elevation, as shown in Fig. 8(b). This can reduce the tissue displacement estimation accuracy. Hence, more advanced beamforming techniques, such as minimum variance and clutter suppression techniques, might be further used to improve the motion estimation and EW tracking.

In this study, we have evaluated the imaging performance of the proposed method in a series of simulations in which we tried to mimic the *in vivo* situation. However, there are more practical challenges, which could not be investigated in these simulations. For instance, signal-to-noise ratio or detecting EWI onset in the presence of noise, motion, and anisotropic tissue scattering are important *in vivo* challenges, which should be evaluated extensively in *in vitro*, *ex vivo*, and/or *in vivo* studies.

The tissue motion has been estimated by 1-D cross correlation and shown in Fig. 2.12(a)-(c). The atrial wall thickening has been successfully shown as a radial gradient in the frame-to-frame displacement map. However, this is only a limited and highly simplified proof of principle of the EW onset detectability. The EW onset is usually tracked by finding a zero crossing on strain rate data. Since only three pairs of high-frame-rate volumes have been simulated in this study, a full map of EW is not generated. Nevertheless, the EW onset is clearly visible on the tissue displacement maps. The EW approximately propagated one eighth of the sphere circumference at 10 ms, which is equal to a velocity of 2 m/s. These intermediate results show the general imaging performance of the proposed method and its potential for EWI, although this remains to be confirmed by more realistic simulations and shown in experiments.

The proposed method provides an azimuthal lateral resolution smaller than 3.7 mm

on the entire imaging depth (10 cm), which is likely sufficient for EWI [7]. The diameter of the targeted 10-Fr catheter limits the transducer size to 3 mm in the elevation direction, leading to a poorer lateral resolution in this direction. Therefore, at depths beyond 40 mm, the resolution in the elevation direction exceeds 5 mm. The results show that the proposed method outperforms the state of the art on 3-D ICE in terms of frame rate [22]. Moreover, previous works on pseudo-3-D EWI showed that 2-4 planes already provided additional information for EWI of the atrium [14, 20] to reconstruct a volume by spatial interpolation. Our proposed method provides a volume consisting of 12 planes in the elevation direction (natural divergence of transducer at 6 MHz is 6°), which can thus provide even more 3-D details. In addition, the proposed method acquires the 3-D EW at a single heartbeat, which is more suitable than ECG-gated 3-D EWI for mapping cardiac arrhythmia. With this increase in 3-D detail, the proposed design has the potential to improve the accuracy of electromechanical activation mapping and to detect smaller and nonperiodic arrhythmogenic sources.

In this study, we have focused on EWI for mapping AF. However, recent studies showed that EWI can be useful for mapping other cardiac conduction system abnormalities and arrhythmia such as atrial flutters [18] or accessory pathways in patients with the Wolf-Parkinson-White syndrome [13].

Many aspects are still unclear regarding EWI. The relation between electrical activation and mechanical contraction is determined by a combination of biochemical and mechanical interactions of partially unknown properties. Especially in cases of nonuniformities or pathology, this relation will be very complex. Whether the mechanical response alone can be used for patient-specific diagnosis remains to be shown. Nevertheless, measuring the mechanical response with high spatiotemporal resolution is important to gain insight here.

A practical probe implementation requires channel-count reduction since the number of elements far exceeds the number of cables that can be accommodated. A 1-D micro-beamforming scheme reduces the data rate by a factor equal to the number of elements per subaperture. We have shown that a data rate reduction by a factor of 2 results in negligible image quality loss. A micro-beamformer size of 3 or 4 introduces some imaging artifacts. The PSF analysis has shown that the elevational resolution changes negligibly by increasing the micro-beamformer size to 3 but increases from 6.1 to 7 mm by utilizing a micro-beamformer of four elements at 50-mm imaging depth. Fig. 8(b) shows an increase of 16 and 22 dB in residual GL level for a micro-beamformer of three and four elements, respectively.

The channel count is reduced from 1152 (the number of elements) by a factor corresponding to the micro-beamformer size. Since a 10-Fr intracardiac catheter with a diameter of 3.3 mm limits the number of data transferring channels to around 100 micro-coaxial cables [34], the total reduction factor should be at least 12 to account for additional control signals and power supplies. A further on-chip reduction by at least a factor of 4 is thus required to reduce the channel count sufficiently. This can be achieved by methods such as analog time-division multiplexing [40], in-probe digitization combined with digital multiplexing [30, 32], or coding of the digitized signal [41].

In conclusion, the results show a feasible solution for intracardiac 3-D EWI. The 1-D micro-beamforming approach, in combination with on-chip channel-count reduction,

can sufficiently reduce the data rate for transfer over a 10-Fr intracardiac catheter, while the proposed fan-shaped transmit beams and weighted averaging function preserve the image quality. The proposed method has the potential to offer single-beat 3-D EWI of the left atrium.

2.4. APPENDIX A FAN-SHAPED TRANSMIT BEAM GENERATION

To calculate a set of delays required for generating the desired beam, first, a virtual source location was determined based on beam divergence, transducer size, and steering direction in elevation; then, the transducer effective size in azimuth was determined based on the virtual source location and azimuthal beam divergence (see Fig. 2.13).

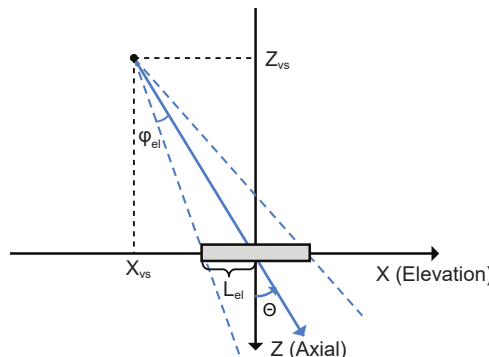


Figure 2.13: Generating a fan-shaped transmitting beam with a divergence of φ_{el} in elevation and steered to θ using a virtual source behind the transducer.

The virtual source location was calculated by

$$\begin{cases} X_{vs} = -\text{sign}(\theta) \frac{L_{el} \tan|\theta|}{\tan|\theta| - \tan(|\theta| - \varphi_{el})}; & Z_{vs} = \frac{X_{vs}}{\tan(\theta)} \theta \neq 0 \\ X_{vs} = 0; & Z_{vs} = \frac{L_{el}}{\tan(\theta)} \theta = 0 \end{cases} \quad (3)$$

where θ is the steering angle with a counterclockwise direction from the axial direction, φ_{el} is the beam divergence in elevation from a center line to a -6 dB contour, and L_{el} is half of the transducer size in elevation. The Y -coordinate value of the virtual source was always 0 because there was no transmit beam steering in the azimuth dimension. Having the virtual source location, the effective transducer size in azimuth was calculated by

$$L_{az} = R_{vs} \tan(\varphi_{az}); \quad R_{vs} = \sqrt{X_{vs}^2 + Z_{vs}^2} \quad (4)$$

where L_{Az} is half of the effective aperture size in azimuth and ϕ_{az} is the beam divergence in azimuth from a center line to a 6-dB contour.

REFERENCES

[1] J. Jalife, O. Berenfeld, and M. Mansour, "Mother rotors and fibrillatory conduction: A mechanism of atrial fibrillation", *Cardiovascular Research*, vol. 54, no. 2, pp. 204–216, 2002. DOI: [10.1016/S0008-6363\(02\)00223-7](https://doi.org/10.1016/S0008-6363(02)00223-7).

[2] M. Haïssaguerre, D. C. Shah, P. Jaïs, M. Hocini, T. Yamane, I. Deisenhofer, S. Garrigue, and J. Clémenty, "Mapping-guided ablation of pulmonary veins to cure atrial fibrillation", *The American journal of cardiology*, vol. 86, no. 9, K9–K19, 2000. DOI: [doi.org/10.1016/S0002-9149\(00\)01186-3](https://doi.org/10.1016/S0002-9149(00)01186-3).

[3] A. Yaksh, L. J. van der Does, C. Kik, P. Knops, F. Oei, P. C. van de Woestijne, J. A. Bekkers, A. J. Bogers, M. A. Allessie, *et al.*, "A novel intra-operative, high-resolution atrial mapping approach", *Journal of Interventional Cardiac Electrophysiology*, vol. 44, no. 3, pp. 221–225, 2015. DOI: doi.org/10.1007/s10840-015-0061-x.

[4] M. Allessie and N. de Groot, "CrossTalk opposing view: Rotors have not been demonstrated to be the drivers of atrial fibrillation", *The Journal of physiology*, vol. 592, no. Pt 15, p. 3167, 2014. DOI: [10.1113/jphysiol.2014.271809](https://doi.org/10.1113/jphysiol.2014.271809).

[5] J. Sra and M. Akhtar, "Mapping Techniques for Atrial Fibrillation Ablation", *Current Problems in Cardiology*, vol. 32, no. 12, pp. 669–767, 2007. DOI: [10.1016/j.cpcardiol.2007.09.002](https://doi.org/10.1016/j.cpcardiol.2007.09.002).

[6] H. Ashikaga, B. A. Coppola, B. Hoppenfeld, E. S. Leifer, E. R. McVeigh, and J. H. Omens, "Transmural dispersion of myofiber mechanics: implications for electrical heterogeneity in vivo", *Journal of the American College of Cardiology*, vol. 49, no. 8, pp. 909–916, 2007. DOI: doi.org/10.1016/j.jacc.2006.07.074.

[7] E. E. Konofagou and J. Provost, "Electromechanical wave imaging for noninvasive mapping of the 3D electrical activation sequence in canines and humans *in vivo*", *Journal of Biomechanics*, vol. 45, no. 5, pp. 856–864, 2012. DOI: doi.org/10.1016/j.jbiomech.2011.11.027.

[8] E. McVeigh, O. Faris, D. Ennis, P. Helm, and F. Evans, "Electromechanical mapping with MRI tagging and epicardial sock electrodes", *Journal of electrocardiology*, vol. 35, no. Suppl, p. 61, 2002. DOI: [10.1054/jelc.2002.37156](https://doi.org/10.1054/jelc.2002.37156).

[9] O. P. Faris, F. J. Evans, D. B. Ennis, P. A. Helm, J. L. Taylor, A. S. Chesnick, M. A. Guttman, C. Ozturk, and E. R. McVeigh, "Novel technique for cardiac electromechanical mapping with magnetic resonance imaging tagging and an epicardial electrode sock", *Annals of Biomedical Engineering*, vol. 31, no. 4, pp. 430–440, 2003. DOI: [10.1114/1.1560618](https://doi.org/10.1114/1.1560618).

[10] B. T. Wyman, W. C. Hunter, F. W. Prinzen, and E. R. McVeigh, "Mapping propagation of mechanical activation in the paced heart with MRI tagging", *American Journal of Physiology - Heart and Circulatory Physiology*, vol. 276, no. 3 45-3, pp. 881–891, 1999. DOI: [10.1152/ajpheart.1999.276.3.h881](https://doi.org/10.1152/ajpheart.1999.276.3.h881).

[11] F. R. Badke, P. Boinay, and J. W. Covell, "Effects of ventricular pacing on regional left ventricular performance in the dog", *American Journal of Physiology - Heart and Circulatory Physiology*, vol. 7, no. 6, 1980. DOI: [10.1152/ajpheart.1980.238.6.h858](https://doi.org/10.1152/ajpheart.1980.238.6.h858).

[12] M. Pernot and E. E. Konofagou, "Electromechanical imaging of the myocardium at normal and pathological states", in *IEEE Ultrasonics Symposium, 2005.*, IEEE, vol. 2, 2005, pp. 1091–1094. DOI: [10.1109/ULTSYM.2005.1603040](https://doi.org/10.1109/ULTSYM.2005.1603040).

[13] L. Melki, C. S. Grubb, R. Weber, P. Nauleau, H. Garan, E. Wan, E. S. Silver, L. Liberman, and E. E. Konofagou, "Localization of accessory pathways in pediatric patients with Wolff-Parkinson-White syndrome using 3D-rendered electromechanical wave imaging", *JACC: Clinical Electrophysiology*, vol. 5, no. 4, pp. 427–437, 2019. DOI: [10.1016/j.jacep.2018.12.001](https://doi.org/10.1016/j.jacep.2018.12.001).

[14] P. Nauleau, L. Melki, E. Wan, and E. Konofagou, "A 3-D rendering algorithm for electromechanical wave imaging of a beating heart", *Medical physics*, vol. 44, no. 9, pp. 4766–4772, 2017. DOI: doi.org/10.1002/mp.12411.

[15] J. Provost, A. Costet, E. Wan, A. Gambhir, W. Whang, H. Garan, and E. E. Konofagou, "Assessing the atrial electromechanical coupling during atrial focal tachycardia, flutter, and fibrillation using electromechanical wave imaging in humans", *Computers in biology and medicine*, vol. 65, pp. 161–167, 2015. DOI: [10.1016/j.combiomed.2015.08.005](https://doi.org/10.1016/j.combiomed.2015.08.005).

[16] J. Provost, V. Gurev, N. Trayanova, and E. E. Konofagou, "Mapping of cardiac electrical activation with electromechanical wave imaging: an in silico-in vivo reciprocity study", *Heart Rhythm*, vol. 8, no. 5, pp. 752–759, 2011. DOI: doi.org/10.1016/j.hrthm.2010.12.034.

[17] J. Provost, W.-N. Lee, K. Fujikura, and E. E. Konofagou, "Imaging the electromechanical activity of the heart in vivo", *Proceedings of the National Academy of Sciences*, vol. 108, no. 21, pp. 8565–8570, 2011. DOI: [10.1073/pnas.1011688108](https://doi.org/10.1073/pnas.1011688108).

[18] J. Provost, V. T.-H. Nguyen, D. Legrand, S. Okrasinski, A. Costet, A. Gambhir, H. Garan, and E. E. Konofagou, "Electromechanical wave imaging for arrhythmias", *Physics in Medicine & Biology*, vol. 56, no. 22, p. L1, 2011. DOI: [10.1088/0031-9155/56/22/F01](https://doi.org/10.1088/0031-9155/56/22/F01).

[19] J. Provost, S. Thiébaut, J. Luo, and E. E. Konofagou, "Single-heartbeat electromechanical wave imaging with optimal strain estimation using temporally unequispaced acquisition sequences", *Physics in Medicine & Biology*, vol. 57, no. 4, p. 1095, 2012. DOI: [10.1088/0031-9155/57/4/1095](https://doi.org/10.1088/0031-9155/57/4/1095).

[20] A. Costet, E. Wan, E. Bunting, J. Grondin, H. Garan, and E. Konofagou, "Electromechanical wave imaging (EWI) validation in all four cardiac chambers with 3D electroanatomic mapping in canines in vivo", *Physics in Medicine & Biology*, vol. 61, no. 22, p. 8105, 2016. DOI: [10.1088/0031-9155/61/22/8105](https://doi.org/10.1088/0031-9155/61/22/8105).

[21] J. Grondin, D. Wang, C. S. Grubb, N. Trayanova, and E. E. Konofagou, "4D cardiac electromechanical activation imaging", *Computers in biology and medicine*, vol. 113, p. 103 382, 2019. DOI: doi.org/10.1016/j.combiomed.2019.103382.

[22] D. Wildes, W. Lee, B. Haider, S. Cogan, K. Sundaresan, D. M. Mills, C. Yetter, P. H. Hart, C. R. Haun, et al., "4-D ICE: A 2-D Array Transducer with Integrated ASIC in a 10-Fr Catheter for Real-Time 3-D Intracardiac Echocardiography", *IEEE Transactions on Ultrasonics, Ferroelectrics, and Frequency Control*, vol. 63, no. 12, pp. 2159–2173, 2016. DOI: [10.1109/TUFFC.2016.2615602](https://doi.org/10.1109/TUFFC.2016.2615602).

[23] R. Fontes-Carvalho, F. Sampaio, J. Ribeiro, and V. Gama Ribeiro, "Three-dimensional intracardiac echocardiography: a new promising imaging modality to potentially guide cardiovascular interventions", *European Heart Journal—Cardiovascular Imaging*, vol. 14, no. 10, pp. 1028–1028, 2013. DOI: doi.org/10.1093/eihci/jet047.

[24] M. Alkhouri, T. Simard, A. M. Killu, P. A. Friedman, and R. Padang, "First-in-Human Use of a Novel Live 3D Intracardiac Echo Probe to Guide Left Atrial Appendage Closure", *Cardiovascular Interventions*, vol. 14, no. 21, pp. 2407–2409, 2021. DOI: [10.1016/j.jcin.2021.07.024](https://doi.org/10.1016/j.jcin.2021.07.024).

[25] G. Montaldo, M. Tanter, J. Bercoff, N. Benech, and M. Fink, "Coherent plane-wave compounding for very high frame rate ultrasonography and transient elastography", *IEEE transactions on ultrasonics, ferroelectrics, and frequency control*, vol. 56, no. 3, pp. 489–506, 2009. DOI: [10.1109/TUFFC.2009.1067](https://doi.org/10.1109/TUFFC.2009.1067).

[26] P. Santos, G. U. Haugen, L. Lovstakken, E. Samset, and J. D'Hooge, "Diverging Wave Volumetric Imaging Using Subaperture Beamforming", *IEEE Transactions on Ultrasonics, Ferroelectrics, and Frequency Control*, vol. 63, no. 12, pp. 2114–2124, 2016. DOI: [10.1109/TUFFC.2016.2616172](https://doi.org/10.1109/TUFFC.2016.2616172).

[27] C. Chen, Z. Chen, D. Bera, E. Noothout, Z. Y. Chang, M. Tan, H. J. Vos, J. G. Bosch, M. D. Verweij, et al., "A pitch-matched front-end ASIC with integrated subarray beamforming ADC for miniature 3-D ultrasound probes", *IEEE Journal of Solid-State Circuits*, vol. 53, no. 11, pp. 3050–3064, 2018. DOI: [10.1109/JSSC.2018.2864295](https://doi.org/10.1109/JSSC.2018.2864295).

[28] S. A. Scampini, *Microbeamforming transducer architecture*, US Patent App. 11/576,401, Oct. 2008.

[29] J. D. Larson III, *2-D phased array ultrasound imaging system with distributed phasing*, US Patent 5229933, Jul. 1993.

[30] D. Bera, F. van den Adel, N. Radeljic-Jakic, B. Lippe, M. Soozande, M. A. Pertijs, M. D. Verweij, P. Kruizinga, V. Daeichin, et al., "Fast Volumetric Imaging Using a Matrix Transesophageal Echocardiography Probe with Partitioned Transmit-Receive Array", *Ultrasound in Medicine and Biology*, vol. 44, no. 9, pp. 2025–2042, 2018. DOI: [10.1016/j.ultrasmedbio.2018.05.017](https://doi.org/10.1016/j.ultrasmedbio.2018.05.017).

[31] Y. Chen, L. Tong, A. Ortega, J. Luo, and J. D'hooge, "Feasibility of multiplane-transmit beamforming for real-time volumetric cardiac imaging: A simulation study", *IEEE transactions on ultrasonics, ferroelectrics, and frequency control*, vol. 64, no. 4, pp. 648–659, 2017. DOI: [10.1109/TUFFC.2017.2651498](https://doi.org/10.1109/TUFFC.2017.2651498).

[32] G. Gurun, C. Tekes, J. Zahorian, T. Xu, S. Satir, M. Karaman, J. Hasler, and F. L. Degertekin, "Single-chip CMUT-on-CMOS front-end system for real-time volumetric IVUS and ICE imaging", *IEEE transactions on ultrasonics, ferroelectrics, and frequency control*, vol. 61, no. 2, pp. 239–250, 2014. DOI: [10.1109/TUFFC.2014.6722610](https://doi.org/10.1109/TUFFC.2014.6722610).

[33] Y. Hopf, B. Ossenkopppele, M. Soozande, E. Noothout, Z.-Y. Chang, C. Chen, H. Vos, H. Bosch, M. Verweij, et al., "A Pitch-Matched ASIC with Integrated 65V TX and Shared Hybrid Beamforming ADC for

Catheter-Based High-Frame-Rate 3D Ultrasound Probes”, in *2022 IEEE International Solid- State Circuits Conference (ISSCC)*, vol. 65, 2022, pp. 494–496. DOI: [10.1109/ISSCC42614.2022.9731597](https://doi.org/10.1109/ISSCC42614.2022.9731597).

[34] W. Lee, S. F. Idriss, P. D. Wolf, and S. W. Smith, “A miniaturized catheter 2-D array for real-time, 3-D intracardiac echocardiography”, *IEEE transactions on ultrasonics, ferroelectrics, and frequency control*, vol. 51, no. 10, pp. 1334–1346, 2004. DOI: [10.1109/TUFFC.2004.1350962](https://doi.org/10.1109/TUFFC.2004.1350962).

[35] T. Hergum, T. Bjastad, K. Kristoffersen, and H. Torp, “Parallel beamforming using synthetic transmit beams”, *IEEE transactions on ultrasonics, ferroelectrics, and frequency control*, vol. 54, no. 2, pp. 271–280, 2007. DOI: [10.1109/TUFFC.2007.241](https://doi.org/10.1109/TUFFC.2007.241).

[36] Y. Zhang, Y. Guo, and W.-N. Lee, “Ultrafast ultrasound imaging using combined transmissions with cross-coherence-based reconstruction”, *IEEE Transactions on Medical Imaging*, vol. 37, no. 2, pp. 337–348, 2017. DOI: [10.1109/TMI.2017.2736423](https://doi.org/10.1109/TMI.2017.2736423).

[37] J. Jensen, “Field: A program for simulating ultrasound systems”, in *10th Nordic-Baltic Conference on Biomedical Imaging*, vol. 34, Supple, 1996, pp. 351–353.

[38] M. Van Wijk and J. Thijssen, “Performance testing of medical ultrasound equipment: fundamental vs. harmonic mode”, *Ultrasonics*, vol. 40, no. 1-8, pp. 585–591, 2002. DOI: [10.1016/S0041-624X\(02\)00177-4](https://doi.org/10.1016/S0041-624X(02)00177-4).

[39] A. Rodriguez-Molares, J. Avdal, H. Torp, and L. Løvstakken, “Axial lobes in coherent plane-wave compounding”, in *2016 IEEE International Ultrasonics Symposium (IUS)*, IEEE, 2016, pp. 1–4. DOI: [10.1109/ULTSYM.2016.7728520](https://doi.org/10.1109/ULTSYM.2016.7728520).

[40] Q. Liu, C. Chen, Z. Chang, C. Prins, and M. A. P. Pertijs, “A mixed-signal multiplexing system for cable-count reduction in ultrasound probes”, in *2015 IEEE International Ultrasonics Symposium (IUS)*, IEEE, 2015, pp. 1–4. DOI: [10.1109/ULTSYM.2015.0141](https://doi.org/10.1109/ULTSYM.2015.0141).

[41] Z. Chen, M. Soozande, H. J. Vos, J. G. Bosch, M. D. Verweij, N. de Jong, and M. A. P. Pertijs, “Impact of Bit Errors in Digitized RF Data on Ultrasound Image Quality”, *IEEE Transactions on Ultrasonics, Ferroelectrics, and Frequency Control*, vol. 67, no. 1, pp. 13–24, 2019. DOI: [10.1109/TUFFC.2019.2937462](https://doi.org/10.1109/TUFFC.2019.2937462).

3

AN 8 X 9 PZT MATRIX TRANSDUCER WITH PITCH-MATCHED TRANSCEIVER ASIC FOR HIGH-FRAME-RATE 3D INTRACARDIAC ECHOCARDIOGRAPHY

This chapter is based on the publication:

Yannick M. Hopf, Boudeleine W. Ossenkoppele, Mehdi Soozande, Emile Noothout, Zu-Yao Chang, Chao Chen, Hendrik J. Vos, Johan G. Bosch, Martin D. Verweij, Nico de Jong, Michiel A. P. Pertijs, A Pitch-Matched Transceiver ASIC With Shared Hybrid Beamforming ADC for High-Frame-Rate 3-D Intracardiac Echocardiography, IEEE Journal of Solid-State Circuits, vol. 57, no. 11, pp. 3228- 3242, 2022.

3

In this chapter, a prototype PZT matrix transducer with application-specific integrated circuit (ASIC) for 3-D, high-frame-rate ultrasound imaging is presented. The design is the first to combine element-level, high-voltage (HV) transmitters and analog front-ends, subarray beamforming, and in-probe digitization in a scalable fashion for catheter-based probes. The integration challenge is met by a hybrid analog-to-digital converter (ADC), combining an efficient charge-sharing successive approximation register (SAR) first stage and a compact single-slope (SS) second stage. Application in large ultrasound imaging arrays is facilitated by directly interfacing the ADC with a charge-domain subarray beamformer, locally calibrating interstage gain errors and generating the SAR reference using a power-efficient local reference generator. Additional hardware-sharing between neighboring channels ultimately leads to the lowest reported area and power consumption across miniature ultrasound probe ADCs. A pitch-matched design is further enabled by an efficient split between the core circuitry and a periphery block, the latter including a datalink performing clock data recovery (CDR) and time-division multiplexing (TDM), which leads to a 12-fold total channel count reduction. A prototype of 8 x 9 elements was fabricated in a TSMC 0.18- μ m HV BCD technology and a 2-D PZT transducer matrix with a pitch of 160 μ m, and a center frequency of 6 MHz was manufactured on the chip. The imaging device operates at up to 1000 volumes/s, generates 65-V transmit pulses, and has a receive power consumption of only 1.23 mW/element. The functionality has been demonstrated electrically as well as in acoustic and imaging experiments.

3.1. INTRODUCTION

Several cardiovascular conditions can be addressed using minimally invasive interventions, including the treatment of cardiac arrhythmia through electrophysiology and catheter ablation, trans-catheter valve replacement, closure of atrial septal defects, and occlusion of the left atrial appendage [1, 2]. Real-time guidance of these interventions is traditionally achieved through fluoroscopy. However, this is associated with a low resolution of soft tissue and exposure of the patient and the physician to harmful ionizing radiation [3].

Ultrasound imaging can alleviate these disadvantages. But simply obtaining images of the heart from outside the body with a hand-held probe, in a so-called transthoracic echocardiogram (TTE), suffers from a limited acoustic window through the chest and requires a dedicated operator [4]. It is possible to obtain unobstructed, high-resolution ultrasound images from within the body by imaging from the esophagus in a trans-esophageal echocardiography (TEE) procedure or from within the heart in an intracardiac echocardiography (ICE) procedure [5]. The latter can often work on the same local anesthesia as the actual intervention as opposed to the, more risky, general anesthesia required for working from the esophagus. This has made ICE one of the most commonly applied ultrasound tools for minimally invasive cardiac interventions [4].

Until recently, a drawback of ICE probes was their limitation to 2-D images. This was mostly due to the integration and wiring challenge posed by the larger transducer matrix that is generally required for 3-D imaging [6]. The probes are limited to a diameter of around 3 mm to enable accessing the heart through the vascular system, as shown in an example with entry from the inferior vena cava in Fig. 3.1(a). Within this space, the transducer array has to be accommodated at the tip and all external connections in the shaft. To enhance the visualization for the physician, 3-D images were initially created from either manual [7] or motorized [8] rotation of 1-D transducer arrays, sacrificing real-time imaging capability or resulting in very low frame rates. In [9], a helical 1-D array was applied instead, enabling 3-D imaging at higher frame rates at the cost of a limited elevation opening angle of just 22°. The class of forward-looking, ring-shaped probes [10], [11] showed a similar issue in being able to provide 3-D images but only for a small volume ahead of the device and therefore not being applicable for the full range of procedures. A way to achieve a sufficient field of view and imaging rate is provided with the advanced integration of 2-D transducer arrays in the catheter tip. However, the problem is that for individual connection from each transducer element to an imaging system outside the body, the interconnect becomes limiting to the array size, resulting in insufficient image quality [12–14].

Subarray beamforming has recently been investigated as an approach to interface large arrays, such as the approximately 1000 elements of a typical 3-D ICE device [6, 15]. The method shifts part of the receive beamforming, usually applied in the imaging system, into the catheter in the form of delay-and-sum operations on the received signals of a subarray [16]. This effectively reduces the number of connections needed inside the catheter shaft as only the combined signal is transmitted. However, it does not provide the raw data of the full array and introduces focusing errors [17]. These result in increased grating and sidelobe levels as well as broadening of the main beam, all negatively impacting image quality. Narrower transmit beams can be used to mitigate these

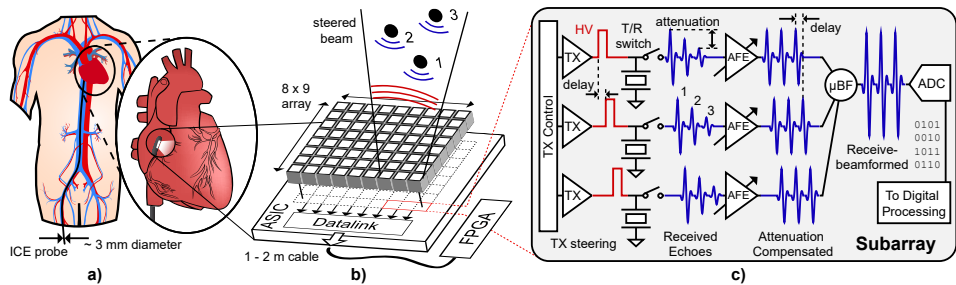


Figure 3.1: (a) Example of an ICE procedure with catheter entry from the inferior vena cava and imaging of the left ventricle from the right atrium. (b) Transducer matrix array integration overview. (c) Schematic of a 1x3-element subarray including transmit (TX) and receive circuitry.

effects but require more acquisitions per volume, ultimately leading to a trade-off between subarray size, with related channel count reduction, and achievable frame rate [18].

A reduction in frame rate leads to worse motion tracking and can prevent the use of upcoming imaging modes like high-frame-rate blood flow or electromechanical wave imaging [19], which offer more diagnostic potential to physicians but require about 1000 volumes/s. A method to manage the impact on frame rate while still offering cable count reduction is provided by multiplexing multiple channels onto one cable in analog or digital form. Analog multiplexing has been demonstrated in the time [20, 21] and frequency [22] domains but is constrained by the limited bandwidth across the commonly applied micro-coaxial cables and suffers from channel-to-channel crosstalk [23]. Digital time-domain multiplexing (TDM), on the other hand, has been shown to benefit from better tolerance to crosstalk, interference, and noise [15]. The availability of digital receive signals in the catheter moreover opens the possibility for future cointegration with emerging image processing such as data reduction with machine-learned compression [24, 25] or adaptive beamforming [26]. A major benefit of multiplexing lies in the compatibility with subarray beamforming, as has been shown in digital beamforming of element-level signals [27–29] and analog beamforming with subsequent digitization and TDM [29–31]. While the former requires an analog-to-digital converter (ADC) per element, the subarray area available for the latter makes the scheme more feasible for large arrays.

Both ways, current digital ICE probe designs still suffer from large ADCs. This expresses itself in the reported designs not being able to match the element-level circuitry to the transducer pitch [28, 31], a requirement for a scalable system, or the associated silicon area requirement making cointegration with adequate transmit circuitry impossible [15, 32, 33]. These transmitters need to excite the transducer elements with high-voltage (HV) pulses to obtain sufficient signal-to-noise ratio (SNR) for around 10-cm imaging depth, requiring the use of HV transistors with large isolation rings [6].

A scalable application-specific integrated circuit (ASIC) with a cointegrated $160\mu\text{m} \times 160\mu\text{m}$ transducer array is presented [34]. While [15] has already shown a large channel count reduction through the combination of subarray beamforming and digital TDM with a beamforming ADC, the presented converter was too big to be able to include transmitters. Moreover, its associated subarray size of 3x3 elements precludes frame

rates on the order of 1000 volumes/s. To address these issues, this chapter presents a novel hybrid beamforming ADC, consisting of an efficient charge-sharing successive approximation register (SAR) first stage and a compact single-slope (SS) second stage. The ADC architecture achieves the smallest reported power consumption and area among miniature ultrasound probe ADCs, enabling a subarray size of only 1x3 elements and thereby pushing the maximum frame rate to the targeted 1000 volumes/s. Moreover, it allows for the integration of per-element 65 V transmitters [35] and front-ends, analog subarray beamformers, and digitization in a pitch-matched fashion. The system has a 12-fold data channel count reduction, resulting in 96 data channels for the envisioned full system [17]. In a trade-off between the available circuit area and the achievable image quality, the transducer pitch was chosen just above the half-wavelength margin. The resulting grating lobe artifacts stay below an acceptable level [17] and can be further reduced through coherent compounding of subvolume acquisitions [36] and potentially further mitigated through recently shown machine-learning-based image processing techniques [37, 38].

3.2. SYSTEM DESIGN

3.2.1. OVERVIEW

An overview of the conceptual system, showing common techniques in ultrasound imaging applied in this design, is given in Fig. 3.1(c). Each transducer element is used for the transmission (TX) of pressure waves and the subsequent reception (RX) of echoes, generated by reflectors in the imaged medium, in a pulse-echo (PE) cycle. The shared element usage between TX and RX maximizes the achievable aperture in size-constrained probes, as displayed in Fig. 3.1(b).

During the TX phase, HV pulsers are driving the transducer elements based on the inputs from a TX controller. The controller applies delays to achieve TX beam steering, forming diverging waves to scan the whole volume with a small number of transmissions. To protect the low-voltage (LV) RX circuits from HV operation of the transmitter, a transmit/receive (T/R) switch is placed between the two sections of the design.

Once the transmission is completed, the switch closes and a readout circuit can access the transducer. A common issue in ultrasound imaging systems is the large dynamic range (DR) accumulated by propagation in an exponentially attenuating medium. The attenuation A , in dB, is proportional to the distance z , the attenuation coefficient α , and, for heart tissue, approximately the frequency f [39]

$$A = 2 \cdot z \cdot f \cdot \alpha \quad (3.1)$$

The imaging frequency has to be determined based on a trade-off between the axial resolution and the imaging depth and is in this design set to 6 MHz with a depth of 10 cm [17]. Combined with an attenuation coefficient of about 0.5 dB/MHz/cm for heart tissue [39], the attenuation could reach 60 dB. Considering an instantaneous DR of 40 dB, the total DR can therefore reach 100 dB. As not all that range is of interest throughout an RX period and the attenuation is time-dependent, the DR to be handled by the RX circuits can, however, be reduced by a procedure called time gain compensation (TGC). This is achieved by giving the analog front-end a variable gain that can be adjusted during

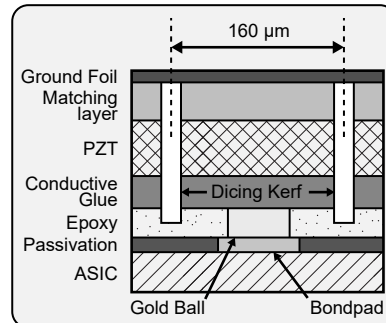


Figure 3.2: Conceptual sketch of the transducer stack.

one PE cycle, giving equally strong reflectors at different distances from the transmitter a similar output and easing the design requirements for the following circuitry [40].

The received signals from each channel in the device are combined in a beamforming operation to reconstruct the information of each voxel in the imaged volume. An SNR gain of \sqrt{N} for N elements in the beamformer is possible if the system SNR is limited by uncorrelated noise and can aid in the design for a large DR. To reduce the number of connections from the probe to a beamforming system, part of the reconstruction can already be performed in the probe per subarray. This subarray beamforming, also referred to as micro-beamforming (μ BF), applies delay-and-sum operations to individual signals of a subarray, effectively steering the RX beam to target the previously insonified area [16]. The combined signals can then be digitized for further local processing and sent to an imaging system.

An overview of the cointegration of the ASIC and a bulk piezoelectric PZT transducer matrix array is given in Fig. 3.1(b). The $160 \mu\text{m}$ pitch stack is an optimized version of what has been presented in [41] and gets manufactured directly on the surface of ASIC. It connects to exposed top metal pads on one side and a shared aluminum ground foil on the other side, as shown in Fig. 3.2. The 8x9 -element assembly serves as a prototype with an architecture and layout design suitable for scaling to a full array of 64x18 elements [17]. While the prototype has a reduced aperture, it is already tailored toward the intended imaging scheme of acquiring a $70^\circ \times 70^\circ \times 10 \text{ cm}$ volume in front of the transducer matrix at a frame rate of 1000 volumes/s. Given an imaging depth z of 10 cm and the speed of sound c of 1540 m/s in tissue, a maximum pulse repetition frequency (PRF) = $c/(2z)$ of 7.7 kHz can be reached. This provides seven PE cycles for the formation of each volumetric image at a rate of 1000 volumes/s. To optimize their usage toward the best image quality, the beam profile and subarray receive beamformer size are determined in a trade-off with the required channel count reduction and necessary circuit area. This work applies seven transmit beams of 70° divergence in the azimuth direction and 10.7° divergence in the elevation direction in a sweep of the elevation steering angle to cover the full $70^\circ \times 70^\circ \times 10 \text{ cm}$ volume. In receive, subarrays of three elements along the elevation direction are applied which presteer the received signal in the same direction as the transmit beams [17].

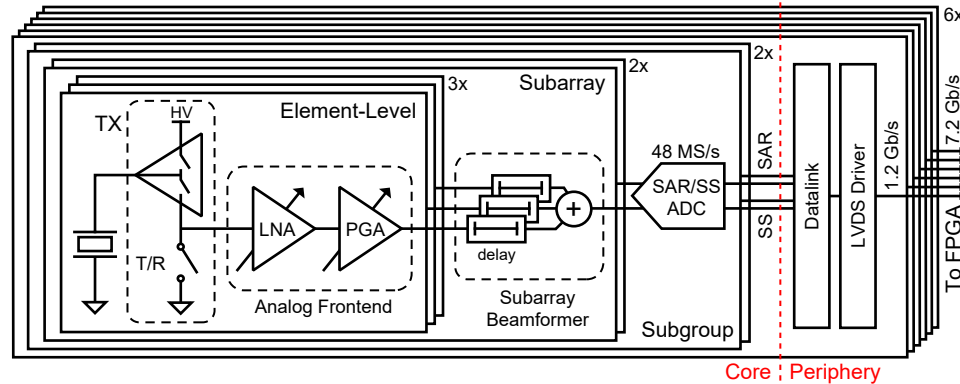


Figure 3.3: System architecture including element-level pulsers and analog front-ends, subarray beamformers, and a shared hybrid ADC structure per subgroup. On the periphery, each channel is connected to an FPGA via a datalink and an LVDS driver.

3.2.2. ARCHITECTURE

The implemented system architecture of the prototype is shown in Fig. 3.3. Each transducer element's bottom plate is connected to an individual pulser and a variable-gain analog front-end (AFE), implementing TGC. The TX part is realized as a unipolar, 65-V design with a pull-up and a pull-down path provided by DMOS transistors. To facilitate test modes and reduce the complexity, the TX control signals are provided externally per row, with an area reserved for an integrated TX controller in a future version. A single LV transistor, protected against voltage breakdown by the HV NMOS of the pulser, enables T/R switching to the input of a low-noise amplifier (LNA) [42] in the receive phase [35]. LNA is configurable to a voltage gain between -12 and 24 dB at a step size of 18 dB and, together with the second-stage programmable gain amplifier (PGA) that provides 6-24 dB at a step size of 6 dB, achieves a total variable gain between -6 and 48 dB at a step size of 6 dB [15]. In each PE cycle, the gain is gradually switched from the lowest to the highest gain setting to first grant sufficient linearity for the initially received strong echoes and later enough gain to detect strongly attenuated echoes out of the noise floor. The PGA is a voltage amplifier with a compact T-type capacitive feedback network [43], configured for quick settling after switching the gain during active operation. To provide rejection of common interference in the following signal chain, it converts the single-ended signal into a differential output.

The outputs of three element-level circuits are merged in a 1x3 -element subarray beamformer, of which two are combined in a 2x3 -element subgroup. Each subgroup shares a hybrid SAR/SS ADC structure that separately digitizes the two channels at 24 MS/s with a resolution of 10 bits each. The outputs of two subgroups are received by a periphery-level block, providing a datalink to process the received data and applying TDM onto an LV differential signal (LVDS) driver to transfer the data to an OFF-chip field-programmable gate array (FPGA). Each periphery block serves a 4x3 matrix of elements, and six of these are arranged to form the prototype of 8x9 elements. A total channel count reduction of 12 is implemented by the subarray beamformer size of 3 and TDM of

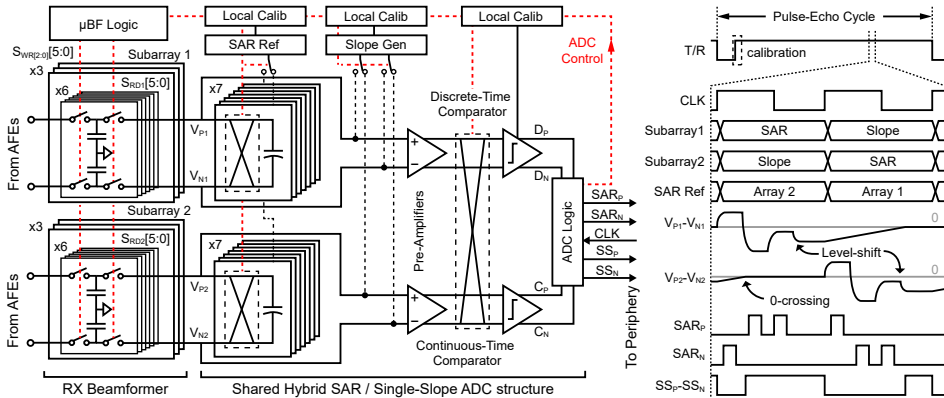


Figure 3.4: Architecture of the proposed hybrid ADC formed between am SAR first stage and an SS second stage with a conceptual timing diagram showing essential nodes and how two subarray outputs are digitized by the shared structure.

the digital outputs of four subarrays onto one channel.

3.2.3. HYBRID ADC

To cover the discussed DR of up to 100 dB, a 10-bit resolution is chosen to complement the 54-dB TGC and \sqrt{N} beamforming gain. The sampling frequency should be at least four times higher than the frequency of the transducer to maintain an acceptable sidelobe level [44], leading to a 24-MHz sampling rate for the 6-MHz device. For similar specifications, SAR ADCs have been shown to be an effective solution due to their high efficiency and Nyquist rate sampling [45]. Similar to [15], SAR conversion is performed in the charge domain to benefit from direct integration with a subarray beamformer into a beamforming ADC. However, this design uses a capacitive digital-to-analog converter (CDAC) with metal-oxide-semiconductor capacitors (MOSCAPs). While their voltage-dependent capacitance excludes them from use in charge redistribution ADCs, in charge-sharing topologies MOSCAPs reduce area through high integration density and improve comparator offset as well as noise tolerance [46].

One drawback of SAR ADCs in general is the exponential increase in CDAC size per added bit of resolution in the binary search algorithm. This can be alleviated by means of combination with a slope ADC that digitizes the residual of an SAR first stage in a hybrid converter [33, 47]. A slope ADC can be compact but suffers in efficiency when converting with a high resolution and sampling rate. In the following, the architecture of a hybrid SAR/SS beamforming ADC operating in the charge domain is presented. An optimal split between the two stages is found in a 6-bit SAR and a 5-bit SS conversion with one bit of redundancy between them. This considers the required size reduction in SAR stage and added complexity to the slope stage of the design. To benefit from the reduction in CDAC size, the gained area must outweigh that of the added SS blocks. As the unit capacitor of CDAC is still sized for 10-bit linearity, this is mainly achieved by enabling a CDAC size that is actually linearity-limited, good MOSCAP matching, and the overhead reduction due to a reduced number of unit capacitors.

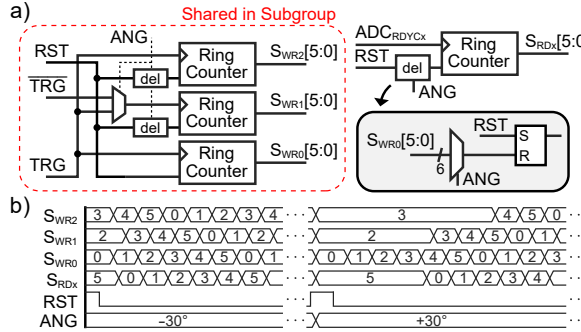


Figure 3.5: (a) Schematic overview of the subarray beamformer. (b) Conceptual S/H-cell timing diagram with maximum positive and negative angles.

3

The ADC is interfacing with the subarray beamformer as shown in Fig. 3.4, avoiding the need for an additional high-bandwidth buffer compared with converters with conventional sampling [33, 47]. The delaying of the received signals is implemented by means of capacitive sample-and-hold (S/H) cells, similar to [48]. The summation of the delayed signals can then be achieved passively by switching the right cells together at the input of the ADC, as in [15]. In contrast to [15], the control logic of the subarray beamformer, as shown in Fig. 3.5(a), can also provide delay quantization independent of the sampling frequency. This is enabled by separate read and write pointers, SRDx and SWRx. The former is advancing based on completed ADC conversion cycles, ADCRDY_C, while the latter advances based on an adjustable input trigger, in this case a locally generated 24-MHz signal and its 180°-phase-shifted version, TRG and \overline{TRG} . While each ADC requires its own read pointer, the write pointers can be shared between multiple channels. The pointers are realized as ring counters, and different steering angles, determined by ANG, can be realized by delaying the reset signal between the pointers. An area-efficient implementation of this delay is achieved by reusing the pointer of one AFE, AFE0, as the reference counter for the delay. Based on ANG, this can be used to implement the delay with a simple multiplexer and a compact set-reset (SR) latch. The resulting S/H-cell switching patterns are shown for a maximum positive and negative steering angle in Fig. 3.5(b). A delay resolution of 20.8 ns is achieved with a range up to 125.0 ns, offering steering capability of the beam in a $\pm 30^\circ$ window.

Following the subarray beamformer, the combined charge can be quantized through the positive or negative connection of binary-scaled units of a precharged CDAC and detection of the polarity with a discrete-time comparator (DTC). After this SAR conversion, the possible residual charge range between nodes VP_x and VN_x has been reduced to least significant bits (LSBs) and can thereafter be digitized by applying a differential slope with compact current sources on the same nodes. To have the redundant range between the two stages work for positive and negative decision errors in SAR conversion, part of CDAC is switched after the first phase to implement a level shift, placing the SAR residual in the middle of the SS conversion range. As long as the residual is not contaminated and they are within the redundant range, all the SAR decision errors, such as DTC noise, CDAC settling errors, and mismatch between the SAR and SS comparator offset,

can be covered.

High area efficiency is achieved by hardware-sharing between two neighboring subarrays, forming one shared ADC structure. The two phases of the conversion are executed in two periods of a 48-MHz clock, twice as high as the ADC sample rate, and while the first subarray performs SAR conversion, the second applies the slope and vice versa. In this fashion, the SAR reference precharger and the slope generator can be shared, and a drawback that is typically introduced in the hybrid architecture can be mitigated: Usually, the combination of an SAR and an SS stage requires the introduction of an asynchronous DTC for an efficient SAR part and a continuous-time comparator (CTC) to avoid a high-frequency comparator clock for SS [33, 47]. While this is still the case, they can be shared between the two subarrays with the addition of a small preamplifier that provides isolation and serves as part of both comparisons. Another benefit of hardware-sharing is that SAR CDAC can be switched out and slowly precharged during slope conversion. Compared to designs with conventional references [33, 47], this allows for the use of a low-bandwidth reference with a constant current drawn from the supply. Moreover, it does not require an additional CDAC used for ping-pong operation as in [15]. To further facilitate application in large imager arrays, critical nodes in the circuit, including SAR reference, slope generator, and DTC offset, are calibrated against mismatch.

As in ultrasound probes, the area underneath the transducer matrix is typically very limited to achieve a scalable, pitch-matched design but there is more space available at the periphery [32, 40, 48], and the received signals are brought out of the core as soon as they are quantized. This applies to return-to-zero (RZ), asynchronous SAR outputs, SARP and SARN, which are gated versions of the DTC outputs, DP and DN, and the SS outputs, SSP and SSN. The SAR and SS outputs of both the converted channels are each carried on one connection to the periphery and correctly merged there to minimize the interconnect space. As the key enabling block of the system, the implementation of the shared hybrid ADC structure is further detailed in [49].

3.2.4. DATALINK

An overview of the datalink is shown following Fig. 3.6. The SAR and SS outputs of two shared ADC structures, serving 12 elements in total, are captured on the periphery by separate receivers. The SAR receiver recovers the SAR output data, as well as a clock that can be used to sample the data in the following stage, directly from the asynchronous RZ SAR output [15]. The SS receiver, on the other hand, converts the differential time-domain output of the SS into a short pulse. This pulse is used to latch the output of a delay locked loop (DLL) that divides the 48-MHz clock period into 32 segments, corresponding to a 5-bit word. As the SS comparison in the core is based on the same time reference, this word is an accurate representation of the second-stage ADC output. The resulting 32-bit word is then converted from a thermal into a binary code to simplify further processing and can be sampled with the same pulse as the latch array. The asynchronous SAR and SS data can subsequently be synchronized to the periphery clock by dual-clock first-in, first-out (FIFO) memories. To reduce the final data bandwidth to the imaging system, the recombination block merges the 6-bit SAR and 5-bit SS codes into the actual 10-bit output code of the ADC. This is done by summing both the parts and removing the redundancy introduced between the two stages in the following manner

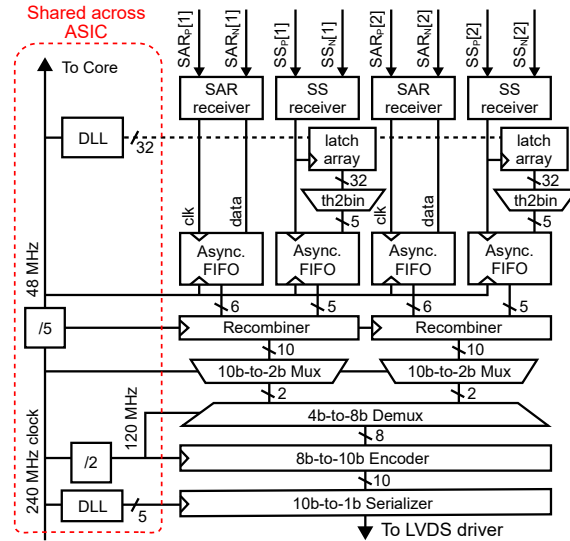


Figure 3.6: Datalink block diagram showing processing of the outputs of four ADCs and the clocking scheme shared across ASIC.

[47]:

$$\begin{array}{r}
 \text{SAR} \quad \begin{array}{ccccccc} 1 & 0 & 0 & 1 & 0 & 1 & -1 \end{array} \\
 \text{SS} \quad \begin{array}{c} + \\ \hline \end{array} \quad \begin{array}{ccccccc} & & & 1 & 0 & 1 & 0 \end{array} \\
 \text{Combined} \quad \begin{array}{c} \hline \\ 1 & 0 & 0 & 1 & 0 & 1 & 1 \end{array}
 \end{array}$$

The subtraction of the redundancy is implemented with the two's complement. The outputs of two recombiners are subsequently merged through TDM, realized by arranging two 10-bit words at 48 MHz to 8-bit words at 120 MHz. The following structures are based on [15] and first apply 8b10b-encoding to enable a standard transmission protocol [50]. The 10-bit output words are then serialized to a 1.2-Gbps output stream to the conventional LVDS drivers with timing provided by a DLL. Both the DLLs are based on [51], shared among the whole ASIC and operate on a single 240-MHz system clock provided from an FPGA. A 120-MHz clock is generated locally at the periphery for the encoder and TDM, while a 48-MHz clock provides the timing for all core circuitry and data reconstruction on the periphery. While a balanced clock distribution in the core is required as a time reference for the generation of the intended RX and TX beams, the 48-MHz clock phase of the core does not need to be precisely matched to that of the periphery as only the clock period is relevant for clock data recovery (CDR).

3.3. EXPERIMENTAL RESULTS

The reported design has been fabricated in a 0.18- μm HV BCD process with an active area of about 1.8 mm² for the 8x9 -element core and about 0.8 mm² for the periphery

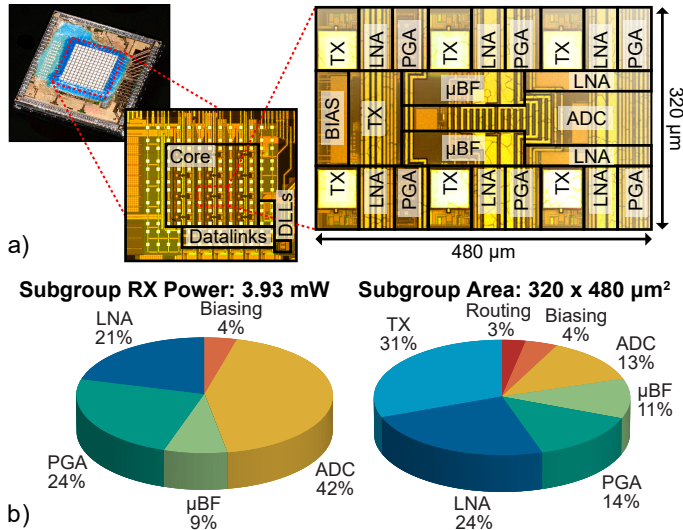


Figure 3.7: (a) Micrograph of the chip including transducer matrix array with magnifications of the core and subgroup areas. (b) Distribution of receive power and area per subgroup 3x2 elements.

circuitry. A chip with a prototype transducer array manufactured on its surface is shown in Fig. 3.7(a).

It measures 5x5 mm² to ease the prototype transducer manufacturing and includes two rings of dummy transducers to reduce edge effects of the small array. The array is designed to have a center frequency of 6 MHz and a fractional bandwidth in the order of 50%. A magnification shows the pitch-matched floor plan of a 3x2 -element subgroup consisting of element-level pulsers, two 3x1 -element subarray beamformers, and two hardware-sharing ADCs. The transmit circuits operate from a 65-V HV supply, a 5-V supply to drive the pulser transistors, and a 1.8-V supply for logic-level control. All receive circuitry is powered from a 1.8-V supply with the addition of a 1.2-V supply for DLL delay cells and a 2.3-V supply for SAR reference. An overview of the area and receive power distribution per subgroup is given in Fig. 3.7(b). Due to area-intense HV isolation, the pulser circuits (TX) occupy the largest part of the subgroup area with 31%, while the hybrid ADCs cover only 13% of the space and consume about as much power as the analog front-end. As the TX operation has a very small duty cycle, the total power consumption is dominated by the receiver, with 0.65 mW/element in the core and 1.23 mW/element including the datalink and LVDS drivers.

Electrical and acoustic experiments have been conducted. The chips are wire-bonded to separate daughter boards, and samples for electrical characterization have additional wire bonds to connect transducer pads to PCB while acoustic samples have a co-integrated transducer array. All the daughter boards are mounted on a common, custom mother board that is connected to a commercial FPGA [52]. The measurements are conducted by observing the ADC outputs as provided through the datalink, received by the FPGA and forwarded to a PC. Characterization of the TX part has previously been shown in [35] and is not covered in this section.

3.3.1. ELECTRICAL MEASUREMENTS

The characterization of the receive transfer function shown in Fig. 3.8 is obtained by providing sinusoidal inputs of varying frequencies to the transducer pads from a waveform generator and referring the ADC output to the output of AFE. The circuit shows the expected mid-band gain range of 54 dB in ten steps from -6 to 48 dB with an 8.1-MHz cut-off frequency in the highest gain setting. The difference among the gain steps in low-frequency roll-off is caused by the feedback configuration and does not affect the imaging as the output is filtered around the center frequency of the transducer.

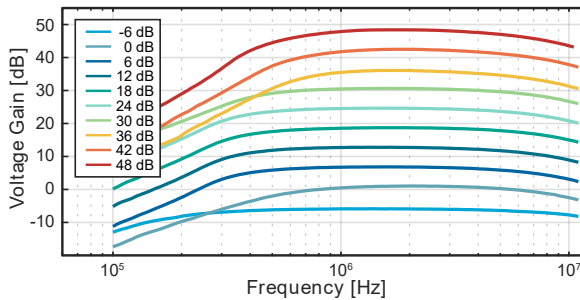


Figure 3.8: Receive transfer function measured across frequency for all the gain settings of the analog front-end.

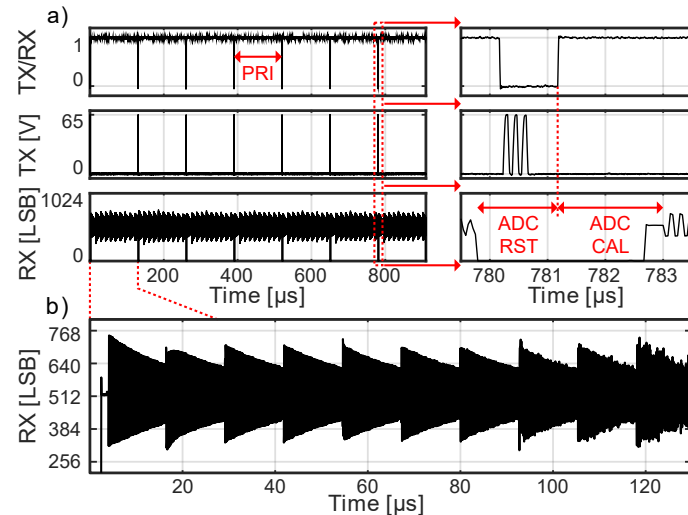


Figure 3.9: (a) TX/RX control, TX voltage, and RX output code recorded with the intended PRI, with zoom-in of the switching period. (b) Recording of one RX output with an exponentially decaying sinusoidal signal at the analog front-end input and active time gain compensation.

Fig. 3.9(b) shows the time-domain recording of an ADC output code with an exponentially decaying 6-MHz sinusoidal signal provided at the input of the analog front-end. By switching through the ten gain settings of the analog front-end, the output amplitude

can be kept within the observable range, verifying functional time-gain compensation within one receive period, with a small settling time after gain switching. Combined with the ability to operate at the intended PRF of 7.7 kHz, corresponding to a pulse repetition interval (PRI) of $130\mu\text{s}$, as demonstrated in Fig. 3.9(a), this verifies that the chip enables recording of the full imaging depth at the targeted frame rate.

The peak ADC output power spectral density is shown in Fig. 3.10, measured with a 5.95 MHz sinusoidal signal from a waveform generator. As the waveform is provided at the analog front-end input, the whole receive path is characterized to a peak SNR of 52.3 dB, with a folded -35 dB third harmonic and -62 dB fifth harmonic from the PGA output stage in an 80% bandwidth around the transducer center frequency.

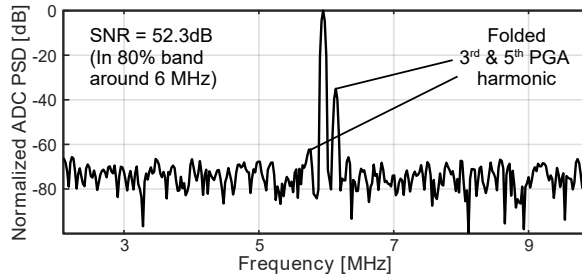


Figure 3.10: Power spectral density plot showing the peak SNR of the entire receive signal path with a 5.95-MHz sinusoidal input to the analog front-end.

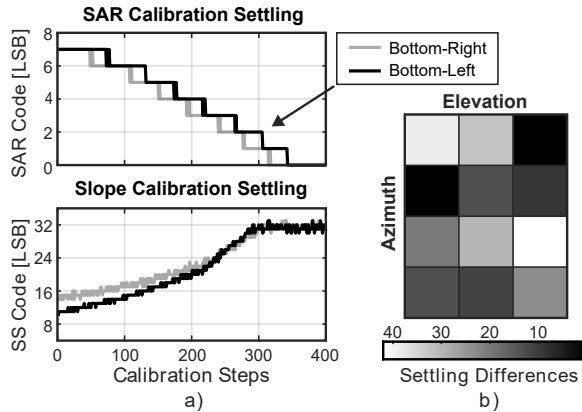


Figure 3.11: (a) Example of the SAR and SS calibration procedures of two different ADCs. (b) Heatmap showing the relative difference in the total calibration settling time from a common starting point across ASIC.

A test mode in which the ADC output of one channel can be read without recombination of the SAR and slope output data is used to follow the ADC calibration procedures. The global starting potentials for SAR and slope reference can be individually set in a reset state and are prior to this test placed away from the final settling points. Fig. 3.11(a) shows how the SAR and slope local calibration nodes converge to the final values at the example of the bottom-right and bottom-left output codes of the SAR and slope stage

(see [35] for detailed explanation of the calibration). The SAR algorithm tries to fully reduce a full-scale input, leading to a settled value at an output code of zero. The slope algorithm, on the other hand, adjusts the slope current to detect the zero-crossing of a full-scale slope stage input just at the end of the associated time interval and therefore settles around the maximum slope output code. An overview of the combined SAR and slope calibration time until a settled state is reached from the same starting point is shown per shared ADC structure in Fig. 3.11(b), giving an indication of the channel-to-channel mismatch.

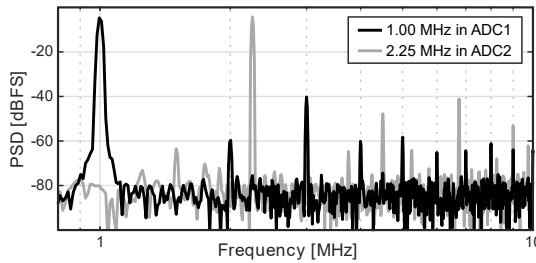


Figure 3.12: Interference test showing the power spectral densities of both the outputs of one shared ADC structure with concurrent 1-MHz and 2.25-MHz inputs.

To investigate how the high integration density and hardware-sharing within each subgroup and at the periphery affect the crosstalk between channels, an electrical measurement, studying the outputs of the two cointegrated subgroup ADCs, is performed. Their inputs can be accessed separately and are concurrently driven by two outputs of a waveform generator, in this example at 1.00 and 2.25 MHz. The corresponding output spectra of the two ADCs are both plotted in Fig. 3.12 and show no significant tones at the fundamental or harmonic frequencies of the other channel. This implies that a circuit crosstalk better than -75 dBc is achieved and that other sources such as mechanical crosstalk in the transducer array should be dominant.

Table 3.1: Prior Art Comparison in Miniature Ultrasound Probe ADCs

	This work	JSSC'21 [32]	VLSI'19 [33]	JSSC'18 [15]
Architecture	SAR & SS	SAR	SAR & SS	SAR
Resolution	10 bit	10 bit	10 bit	10 bit
Sample Rate	24 MHz	20 MHz	30 MHz	30 MHz
Low BW Driver	✓	✗	✗	✓
Reference Included	✓	✗	✗	✓
Area *	0.010 mm²	0.026 mm ²	0.013 mm ²	0.046 mm ²
Power *	0.82 mW	1.23 mW	1.14 mW	1.42 mW

* Per subarray

Table 3.1 summarizes the performance of the hybrid ADC and gives a comparison to the state-of-the-art. In contrast to general-purpose converters, this design implements several application-oriented features such as direct integration with a subarray beam-

former, allowing for a low-bandwidth ADC driver and including a low-bandwidth SAR reference. Therefore, Table 3.1 shows comparison of the design with prior ADC designs targeting miniature ultrasound probes. Set against the most comparable design [15], the ADC occupies more than 4x less area and consumes more than 1.5x less power. Even in comparison to the more general designs [32, 33], the efficient architecture enables the lowest reported area and power consumption.

3.3.2. ACOUSTIC MEASUREMENTS

3

An overview of the acoustic measurement setup is given in Fig. 3.13(a). All the acoustic measurements are obtained with the daughter board and ASIC with the transducer array directly interfacing with a watertank. Fig. 3.14 shows the input-referred voltage noise spectral density in the highest gain setting with the transducer elements loaded by water. Two tones appear in the spectrum at $f_s / 6$ and its second harmonic, f_s , being the sampling frequency of the ADC. These are generated by mismatch of the subarray beamforming cells and can be removed by recording and subtracting the static pattern as shown. The input-referred voltage noise density is $12.7 \text{ nV}/\sqrt{\text{Hz}}$ at 6 MHz, around 5 $\text{nV}/\sqrt{\text{Hz}}$ higher than what the electronics are designed for, with the difference being attributed to the thermal noise of the transducer.

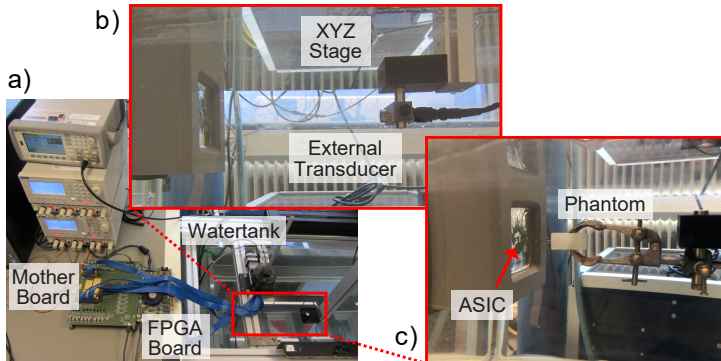


Figure 3.13: (a) Overview of the acoustic measurement setup. (b) Inset showing watertank with external transducer. (c) Imaging experiment details.

Fig. 3.15 displays a sweep of the transducer surface peak pressure with measured ADC output for all gain settings, used to characterize the DR of the receive path. The pressure waves are generated from an external commercial transducer [53] connected to a waveform generator that transmits sinusoidal waves at 5.5 MHz as shown in Fig. 3.13(b). The displayed surface pressure is calibrated with a commercial hydrophone [54] with known sensitivity in the place of ASIC before the measurement. A total DR of 91 dB is recorded between the 0-dB SNR point of the highest and the 1-dB compression point of the lowest gain setting.

An overview of the measurement setup used for imaging experiments is given in Fig. 3.13(c). A phantom of three needles with a total spacing of 7 mm is immersed in a watertank about 13 mm from an acoustic window used to interface with a daughter board carrying a chip with cointegrated transducers. Cables with a length of 1 m connect the

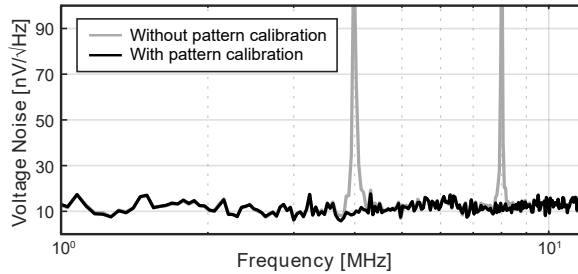


Figure 3.14: Input-referred spectral voltage noise density with and without calibration of the static mismatch pattern of the subarray beamformer.

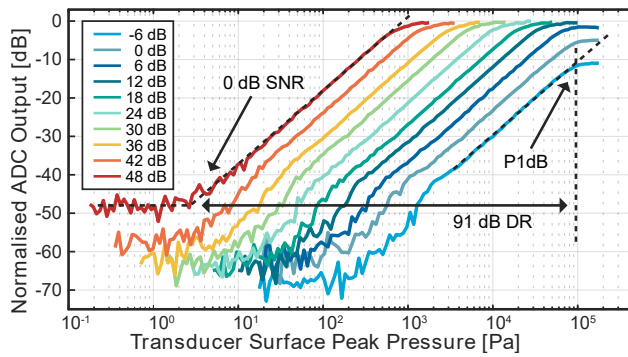


Figure 3.15: ADC output measured during sweep of the transducer surface pressure in all gain settings, showing a 91-dB DR.

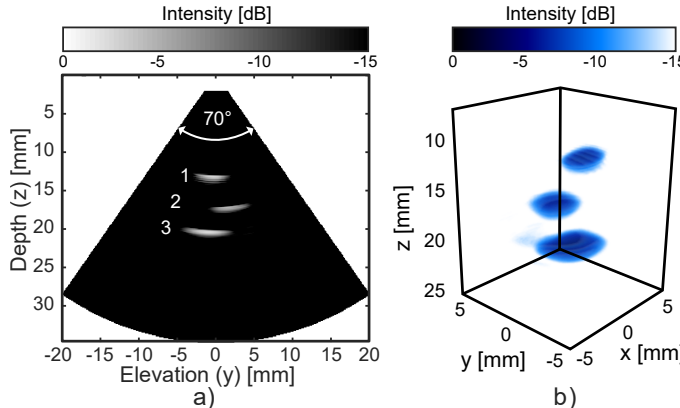


Figure 3.16: (a) Elevation plane image of the three-needle phantom recorded at 1000 volumes/s with the prototype. (b) Rendered 3-D image of the same recording.

Table 3.2: Comparison with the prior art in catheter-based ultrasound imagers

	This work	JSSC'21 [32]	JSSC'20 [40]	VLSI'19 [33]	JSSC'18 [15]	TUFFC'16 [6]
Technology	180nm BCD	180nm	180nm BCD	180nm	180nm	N/A
Transducer	2D PZT	2D PMUT	1D CMUT	2D PZT	2D PZT	2D PZT
Array Size	8 x 9	6 x 6	64	4 x 4	6 x 24	60 x 14
Integrated Trans- ducer	✓	X*	✓	✓	✓	✓
Center Frequency	6 MHz	5 MHz	7 MHz	5 MHz	5 MHz	5.6 MHz
Pitch- matched	✓	7‡	✓	✓	✓	✓
Element Pitch	160 µm x 160 µm	250 µm x 250 µm	205 µm x 1800 µm	150 µm x 150 µm	150 µm x 150 µm	110 µm x 180 µm
Integrated TX	✓	✓	X	✓	✓	X
Receiver Architec- ture	AFE + µBF + ADC + Datalink	AFE + ADC	AFE	AFE + ADC	AFE + µBF + ADC + Datalink	AFE + µBF
Channel Reduction	12-fold	N/A	N/A	N/A	36-fold	15 to 20- fold
Supported Frame Rate	1000 vol/s	N/A	N/A	N/A	200 vol/s	50 vol/s
Active Area / Element	0.032 mm² §	0.063 mm ²	0.464 mm ²	0.023 mm ²	0.026 mm ² §	N/A
RX power / Element	1.23 mW§	1.14 mW	5.2 mW	1.54 mW	0.91 mW§	< 0.12 mW
Input DR	91 dB	N/A	82 dB	N/A	85 dB	N/A
Peak SNR	52.3 dB	57.8 dB ‡	N/A	49.8 dB	52.8 dB	N/A

* Transducers on separate board connected with wires.

† Scalability limited by transducer connection outside of pitch.

§ Including the Datalink and LVDS drivers.

‡ ADC only, excluding AFE.

PCB assembly to an FPGA board that receives the high-bandwidth LVDS data via a motherboard and forward it to a measurement PC that performs the image reconstruction based on conventional delay-and-sum operations. In seven transmit/receive cycles, the ASIC first excites 6-MHz pressure waves with 65-V pulses and then records generated echoes from the phantom with the seven subarray beamformer settings. Fig. 3.16 shows the resulting image once in an elevation plane in a) and once as a rendered 3-D image in b). While the aperture is too small to provide the resolution of a full array, the needle heads can clearly be distinguished in 3-D space, demonstrating the functionality of the prototype.

A summary of the system characteristics and comparison to the prior art in catheter-based ultrasound systems [6, 15, 32, 33, 40] is provided in Table 3.2. This work describes the first design to integrate element-level HV transmitters and analog front-ends, subarray beamforming, and in-probe digitization in a scalable fashion for 3-D imaging. A dedicated architecture enables the highest reported frame rate with a channel count reduction sufficient to enable an array with less than 100 data channels in the catheter when scaled to full size.

3.4. CONCLUSION

A transceiver ASIC combining HV transmission with subarray beamforming and in-probe digitization for catheter-based 3-D ultrasound probes has been presented. A pitch-matched design is facilitated by an area- and power-efficient hybrid beamforming ADC tailored to the application in large imaging arrays. The novel architecture enables a high frame rate of 1000 volumes/s while also providing sufficient data channel reduction through subarray beamforming and time-division multiplexing. A prototype with a cointegrated transducer matrix has been manufactured and successfully applied in a 3-D imaging experiment. Together with competitive power consumption and large DR, the system is a promising solution for future miniature ultrasound probes.

REFERENCES

- [1] Z. M. Hijazi, K. Shivkumar, and D. J. Sahn, "Intracardiac echocardiography during interventional and electrophysiological cardiac catheterization", *Circulation*, vol. 119, no. 4, pp. 587–596, 2009. DOI: [10.1161/CIRCULATIONAHA.107.753046](https://doi.org/10.1161/CIRCULATIONAHA.107.753046).
- [2] G. Perk, R. M. Lang, M. A. Garcia-Fernandez, J. Lodato, L. Sugeng, J. Lopez, B. P. Knight, D. Messika-Zeitoun, S. Shah, *et al.*, "Use of real time three-dimensional transesophageal echocardiography in intracardiac catheter based interventions", *Journal of the American Society of Echocardiography*, vol. 22, no. 8, pp. 865–882, 2009. DOI: doi.org/10.1016/j.echo.2009.04.031.
- [3] B. Luani, T. Rauwolf, C. Genz, A. Schmeißer, M. Wiemer, and R. C. Braun-Dullaeus, "Intracardiac echocardiography versus fluoroscopy for endovascular and endocardial catheter navigation during cryo-ablation of the slow pathway in AVNRT patient", *Cardiovascular Ultrasound*, vol. 17, no. 1, pp. 1–8, 2019. DOI: doi.org/10.1186/s12947-019-0162-2.
- [4] S. S. Kim, Z. M. Hijazi, R. M. Lang, and B. P. Knight, "The use of intracardiac echocardiography and other intracardiac imaging tools to guide noncoronary cardiac interventions", *Journal of the American College of Cardiology*, vol. 53, no. 23, pp. 2117–2128, 2009. DOI: [10.1016/j.jacc.2009.01.071](https://doi.org/10.1016/j.jacc.2009.01.071).
- [5] A. Enriquez, L. C. Saenz, R. Rosso, F. E. Silvestry, D. Callans, F. E. Marchlinski, and F. Garcia, "Use of intracardiac echocardiography in interventional cardiology: working with the anatomy rather than fighting it", *Circulation*, vol. 137, no. 21, pp. 2278–2294, 2018. DOI: doi.org/10.1161/CIRCULATIONAHA.117.031343.

- [6] D. Wildes, W. Lee, B. Haider, S. Cogan, K. Sundaresan, D. M. Mills, C. Yetter, P. H. Hart, C. R. Haun, *et al.*, “4-D ICE: A 2-D Array Transducer with Integrated ASIC in a 10-Fr Catheter for Real-Time 3-D Intracardiac Echocardiography”, *IEEE Transactions on Ultrasonics, Ferroelectrics, and Frequency Control*, vol. 63, no. 12, pp. 2159–2173, 2016. DOI: [10.1109/TUFFC.2016.2615602](https://doi.org/10.1109/TUFFC.2016.2615602).
- [7] C. Knackstedt, A. Franke, K. Mischke, M. Zarse, F. Gramley, T. Schimpf, J. Plisiene, G. Muehlenbruch, E. Spuentrup, *et al.*, “Semi-automated 3-dimensional intracardiac echocardiography: development and initial clinical experience of a new system to guide ablation procedures”, *Heart Rhythm*, vol. 3, no. 12, pp. 1453–1459, 2006. DOI: [10.1016/j.hrthm.2006.05.026](https://doi.org/10.1016/j.hrthm.2006.05.026).
- [8] W. Lee, W. Griffin, D. Wildes, D. Buckley, T. Topka, T. Chodakauskas, M. Langer, S. Calisti, S. Bergstol, *et al.*, “A 10-Fr ultrasound catheter with integrated micromotor for 4-D intracardiac echocardiography”, *IEEE transactions on ultrasonics, ferroelectrics, and frequency control*, vol. 58, no. 7, pp. 1478–1491, 2011. DOI: [10.1109/TUFFC.2011.1967](https://doi.org/10.1109/TUFFC.2011.1967).
- [9] W. T. Wilser, S. R. Barnes, and L. Garbini, *Helical acoustic array for medical ultrasound*, US Patent 8,449,467, May 2013.
- [10] G. Gurun, C. Tekes, J. Zahorian, T. Xu, S. Satir, M. Karaman, J. Hasler, and F. L. Degertekin, “Single-chip CMUT-on-CMOS front-end system for real-time volumetric IVUS and ICE imaging”, *IEEE transactions on ultrasonics, ferroelectrics, and frequency control*, vol. 61, no. 2, pp. 239–250, 2014. DOI: [10.1109/TUFFC.2014.6722610](https://doi.org/10.1109/TUFFC.2014.6722610).
- [11] J. W. Choe, O. Oralkan, A. Nikoozadeh, M. Gencel, D. N. Stephens, M. O'Donnell, D. J. Sahn, and B. T. Khuri-Yakub, “Volumetric real-time imaging using a CMUT ring array”, *IEEE transactions on ultrasonics, ferroelectrics, and frequency control*, vol. 59, no. 6, pp. 1201–1211, 2012. DOI: [10.1109/TUFFC.2012.2310](https://doi.org/10.1109/TUFFC.2012.2310).
- [12] E. D. Light, S. F. Idriss, P. D. Wolf, and S. W. Smith, “Real-time three-dimensional intracardiac echocardiography”, *Ultrasound in medicine & biology*, vol. 27, no. 9, pp. 1177–1183, 2001. DOI: [doi.org/10.1016/S0301-5629\(01\)00421-5](https://doi.org/10.1016/S0301-5629(01)00421-5).
- [13] W. Lee, S. F. Idriss, P. D. Wolf, and S. W. Smith, “A miniaturized catheter 2-D array for real-time, 3-D intracardiac echocardiography”, *IEEE transactions on ultrasonics, ferroelectrics, and frequency control*, vol. 51, no. 10, pp. 1334–1346, 2004. DOI: [10.1109/TUFFC.2004.1350962](https://doi.org/10.1109/TUFFC.2004.1350962).
- [14] D. E. Dausch, K. H. Gilchrist, J. B. Carlson, S. D. Hall, J. B. Castellucci, and O. T. von Ramm, “In vivo real-time 3-D intracardiac echo using PMUT arrays”, *IEEE transactions on ultrasonics, ferroelectrics, and frequency control*, vol. 61, no. 10, pp. 1754–1764, 2014. DOI: [10.1109/TUFFC.2014.006452](https://doi.org/10.1109/TUFFC.2014.006452).
- [15] C. Chen, Z. Chen, D. Bera, E. Noothout, Z. Y. Chang, M. Tan, H. J. Vos, J. G. Bosch, M. D. Verweij, *et al.*, “A pitch-matched front-end ASIC with integrated subarray beamforming ADC for miniature 3-D ultrasound probes”, *IEEE Journal of Solid-State Circuits*, vol. 53, no. 11, pp. 3050–3064, 2018. DOI: [10.1109/JSSC.2018.2864295](https://doi.org/10.1109/JSSC.2018.2864295).
- [16] B. Savord and R. Solomon, “Fully sampled matrix transducer for real time 3D ultrasonic imaging”, in *IEEE Symposium on Ultrasonics*, vol. 1, IEEE, 2003, pp. 945–953. DOI: [10.1109/ULTSYM.2003.1293556](https://doi.org/10.1109/ULTSYM.2003.1293556).
- [17] M. Soozande, B. W. Ossenkoppele, Y. Hopf, M. A. P. Pertijs, M. D. Verweij, N. De Jong, H. J. Vos, and J. G. Bosch, “Imaging Scheme for 3-D High-Frame-Rate Intracardiac Echography: A Simulation Study”, *IEEE Transactions on Ultrasonics, Ferroelectrics, and Frequency Control*, vol. 69, no. 10, pp. 2862–2874, 2022. DOI: [10.1109/TUFFC.2022.3186487](https://doi.org/10.1109/TUFFC.2022.3186487).
- [18] P. Santos, G. U. Haugen, L. Lovstakken, E. Samset, and J. D'Hooge, “Diverging Wave Volumetric Imaging Using Subaperture Beamforming”, *IEEE Transactions on Ultrasonics, Ferroelectrics, and Frequency Control*, vol. 63, no. 12, pp. 2114–2124, 2016. DOI: [10.1109/TUFFC.2016.2616172](https://doi.org/10.1109/TUFFC.2016.2616172).
- [19] O. Villemain, J. Baranger, M. K. Friedberg, C. Papadacci, A. Dizeux, E. Messas, M. Tanter, M. Pernot, and L. Mertens, “Ultrafast ultrasound imaging in pediatric and adult cardiology: techniques, applications, and perspectives”, *JACC: Cardiovascular Imaging*, vol. 13, no. 8, pp. 1771–1791, 2020. DOI: doi.org/10.1016/j.jcmg.2019.09.019.
- [20] P. Wagner, C. Daft, S. Panda, and I. Ladabaum, “5G-1 Two Approaches to Electronically Scanned 3D Imaging Using cMUTs”.
- [21] T. M. Carpenter, M. W. Rashid, M. Ghovanloo, D. M. Cowell, S. Freear, and F. L. Degertekin, “Direct digital demultiplexing of analog TDM signals for cable reduction in ultrasound imaging catheters”, *IEEE transactions on ultrasonics, ferroelectrics, and frequency control*, vol. 63, no. 8, pp. 1078–1085, 2016. DOI: [10.1109/TUFFC.2016.2557622](https://doi.org/10.1109/TUFFC.2016.2557622).
- [22] M. W. Rashid, C. Tekes, M. Ghovanloo, and F. L. Degertekin, “Design of frequency-division multiplexing front-end receiver electronics for CMUT-on-CMOS based intracardiac echocardiography”, in *2014*

IEEE International Ultrasonics Symposium, IEEE, 2014, pp. 1540–1543. DOI: [10.1109/ULTSYM.2014.0381](https://doi.org/10.1109/ULTSYM.2014.0381).

[23] Q. Liu, C. Chen, Z. Chang, C. Prins, and M. A. P. Pertijs, “A mixed-signal multiplexing system for cable-count reduction in ultrasound probes”, in *2015 IEEE International Ultrasonics Symposium (IUS)*, IEEE, 2015, pp. 1–4. DOI: [10.1109/ULTSYM.2015.0141](https://doi.org/10.1109/ULTSYM.2015.0141).

[24] G. Pilikos, L. Horchens, K. J. Batenburg, T. van Leeuwen, and F. Lucka, “Deep data compression for approximate ultrasonic image formation”, in *2020 IEEE International Ultrasonics Symposium (IUS)*, IEEE, 2020, pp. 1–4. DOI: [10.1109/IUS46767.2020.9251753](https://doi.org/10.1109/IUS46767.2020.9251753).

[25] N. Shlezinger, A. Amar, B. Luijten, R. J. van Sloun, and Y. C. Eldar, “Deep Task-Based Analog-to-Digital Conversion”, *ArXiv preprint arXiv:2201.12634*, 2022. DOI: [10.1109/TSP.2022.3229947](https://doi.org/10.1109/TSP.2022.3229947).

[26] B. Lam, M. Price, and A. P. Chandrakasan, “An ASIC for energy-scalable, low-power digital ultrasound beamforming”, in *2016 IEEE International Workshop on Signal Processing Systems (SiPS)*, IEEE, 2016, pp. 57–62. DOI: [10.1109/SiPS.2016.18](https://doi.org/10.1109/SiPS.2016.18).

[27] M. Chen, A. P. Perez, S.-R. Kothapalli, P. Cathelin, A. Cathelin, S. S. Gambhir, and B. Murmann, “A pixel pitch-matched ultrasound receiver for 3-D photoacoustic imaging with integrated delta-sigma beamformer in 28-nm UTBB FD-SOI”, *IEEE journal of solid-state circuits*, vol. 52, no. 11, pp. 2843–2856, 2017. DOI: [10.1109/JSSC.2017.2749425](https://doi.org/10.1109/JSSC.2017.2749425).

[28] Y. Kim, S.-E. Cho, J. Um, M.-K. Chae, J. Bang, J. Song, T. Jeon, B. Kim, J.-Y. Sim, *et al.*, “A single-chip 64-channel ultrasound RX-beamformer including analog front-end and an LUT for non-uniform ADC-sample-clock generation”, *IEEE Transactions on Biomedical Circuits and Systems*, vol. 11, no. 1, pp. 87–97, 2016. DOI: [10.1109/TBCAS.2016.2571739](https://doi.org/10.1109/TBCAS.2016.2571739).

[29] M. D’Urbino, C. Chen, Z. Chen, Z. Chang, J. Ponte, B. Lippe, and M. Pertijs, “An Element-Matched Electromechanical $\Delta\Sigma$ ADC for Ultrasound Imaging”, *IEEE Journal of Solid-State Circuits*, vol. 53, no. 10, pp. 2795–2805, 2018. DOI: [10.1109/JSSC.2018.2859961](https://doi.org/10.1109/JSSC.2018.2859961).

[30] J.-Y. Um, Y.-J. Kim, S.-E. Cho, M.-K. Chae, J. Song, B. Kim, S. Lee, J. Bang, Y. Kim, *et al.*, “An analog-digital hybrid RX beamformer chip with non-uniform sampling for ultrasound medical imaging with 2D CMUT array”, *IEEE transactions on biomedical circuits and systems*, vol. 8, no. 6, pp. 799–809, 2014. DOI: [10.1109/TBCAS.2014.2375958](https://doi.org/10.1109/TBCAS.2014.2375958).

[31] T. Kim, S. Shin, and S. Kim, “An 80.2 dB DR 23.25 mW/channel 8-channel ultrasound receiver with a beamforming embedded SAR ADC”, *IEEE Transactions on Circuits and Systems II: Express Briefs*, vol. 66, no. 9, pp. 1487–1491, 2018. DOI: [10.1109/TCSII.2018.2889810](https://doi.org/10.1109/TCSII.2018.2889810).

[32] J. Lee, K.-R. Lee, B. E. Eovino, J. H. Park, L. Y. Liang, L. Lin, H.-J. Yoo, and J. Yoo, “A 36-channel auto-calibrated front-end ASIC for a pMUT-based miniaturized 3-D ultrasound system”, *IEEE Journal of Solid-State Circuits*, vol. 56, no. 6, pp. 1910–1923, 2021. DOI: [10.1109/JSSC.2021.3049560](https://doi.org/10.1109/JSSC.2021.3049560).

[33] J. Li, Z. Chen, M. Tan, D. Van Willigen, C. Chen, Z.-y. Chang, E. Noothout, N. de Jong, M. Verweij, *et al.*, “A 1.54 mW/element 150 μ m-pitch-matched receiver ASIC with element-level SAR/shared-single-slope hybrid ADCs for miniature 3D ultrasound probes”, in *2019 Symposium on VLSI Circuits*, IEEE, 2019, pp. C220–C221. DOI: [10.23919/VLSIC.2019.8778200](https://doi.org/10.23919/VLSIC.2019.8778200).

[34] Y. Hopf, B. Ossenkoppele, M. Soozande, E. Noothout, Z.-Y. Chang, C. Chen, H. Vos, H. Bosch, M. Verweij, *et al.*, “A Pitch-Matched ASIC with Integrated 65V TX and Shared Hybrid Beamforming ADC for Catheter-Based High-Frame-Rate 3D Ultrasound Probes”, in *2022 IEEE International Solid-State Circuits Conference (ISSCC)*, vol. 65, 2022, pp. 494–496. DOI: [10.1109/ISSCC42614.2022.9731597](https://doi.org/10.1109/ISSCC42614.2022.9731597).

[35] Y. M. Hopf, B. Ossenkoppele, M. Soozande, E. Noothout, Z. Y. Chang, H. J. Vos, J. G. Bosch, M. D. Verweij, N. de Jong, *et al.*, “A Compact Integrated High-Voltage Pulser Insensitive to Supply Transients for 3D Miniature Ultrasound Probes”, *IEEE Solid-State Circuits Letters*, vol. 5, pp. 166–169, 2022. DOI: [10.1109/LSSC.2022.3180071](https://doi.org/10.1109/LSSC.2022.3180071).

[36] “Methods for grating lobe suppression in ultrasound plane wave imaging, author=Bae, Sua and Song, Tai-Kyong”, *Applied Sciences*, vol. 8, no. 10, p. 1881, 2018. DOI: doi.org/10.3390/app8101881.

[37] V. Kumar, P.-Y. Lee, B.-H. Kim, M. Fatemi, and A. Alizad, “Gap-filling method for suppressing grating lobes in ultrasound imaging: Experimental study with deep-learning approach”, *IEEE Access*, vol. 8, pp. 76 276–76 286, 2020. DOI: [10.1109/ACCESS.2020.2989337](https://doi.org/10.1109/ACCESS.2020.2989337).

[38] D. Perdios, M. Vonlanthen, F. Martinez, M. Ardit, and J.-P. Thiran, “CNN-based image reconstruction method for ultrafast ultrasound imaging”, *IEEE Transactions on Ultrasonics, Ferroelectrics, and Frequency Control*, vol. 69, no. 4, pp. 1154–1168, 2021. DOI: [10.1109/TUFFC.2021.3131383](https://doi.org/10.1109/TUFFC.2021.3131383).

[39] T. L. Szabo, *Diagnostic ultrasound imaging: inside out*. Academic press, 2004.

[40] E. Kang, M. Tan, J.-S. An, Z. Chang, P. Vince, N. Sénégond, T. Mateo, C. Meynier, and M. A. P. Pertijis, "A variable-gain low-noise transimpedance amplifier for miniature ultrasound probes", *IEEE Journal of Solid-State Circuits*, vol. 55, no. 12, pp. 3157–3168, 2020. DOI: [10.1109/JSSC.2020.3023618](https://doi.org/10.1109/JSSC.2020.3023618).

[41] C. Chen, S. B. Raghunathan, Z. Yu, M. Shabanimotagh, Z. Chen, Z. Chang, S. Blaak, C. Prins, J. Ponte, *et al.*, "A prototype PZT matrix transducer with low-power integrated receive ASIC for 3-D transesophageal echocardiography", *IEEE transactions on ultrasonics, ferroelectrics, and frequency control*, vol. 63, no. 1, pp. 47–59, 2016. DOI: [10.1109/TUFFC.2015.2496580](https://doi.org/10.1109/TUFFC.2015.2496580).

[42] C. Chen, Z. Chen, Z. Chang, and M. A. P. Pertijis, "A compact 0.135-mW/channel LNA array for piezoelectric ultrasound transducers", in *ESSCIRC Conference 2015-41st European Solid-State Circuits Conference (ESSCIRC)*, IEEE, 2015, pp. 404–407. DOI: [10.1109/ESSCIRC.2015.7313913](https://doi.org/10.1109/ESSCIRC.2015.7313913).

[43] K. A. Ng and Y. P. Xu, "A compact, low input capacitance neural recording amplifier", *IEEE Transactions on biomedical circuits and systems*, vol. 7, no. 5, pp. 610–620, 2013. DOI: [10.1109/TBCAS.2013.2280066](https://doi.org/10.1109/TBCAS.2013.2280066).

[44] B. D. Steinberg, "Digital beamforming in ultrasound", *IEEE Transactions on ultrasonics, ferroelectrics, and frequency control*, vol. 39, no. 6, pp. 716–721, 1992. DOI: [10.1109/58.165556](https://doi.org/10.1109/58.165556).

[45] B. Murmann, *ADC performance survey 1997-2021 (isscc & vlsi symposium)*, 2015.

[46] T. Rabuske and J. Fernandes, "A sar ade with a moscap-dac", *IEEE Journal of Solid-State Circuits*, vol. 51, no. 6, pp. 1410–1422, 2016. DOI: [10.1109/JSSC.2016.2548486](https://doi.org/10.1109/JSSC.2016.2548486).

[47] C.-C. Liu, M.-C. Huang, and Y.-H. Tu, "A 12 bit 100 MS/s SAR-assisted digital-slope ADC", *IEEE Journal of Solid-State Circuits*, vol. 51, no. 12, pp. 2941–2950, 2016. DOI: [10.1109/JSSC.2016.2591822](https://doi.org/10.1109/JSSC.2016.2591822).

[48] C. Chen, Z. Chen, D. Bera, S. B. Raghunathan, M. Shabanimotagh, E. Noothout, Z.-Y. Chang, J. Ponte, C. Prins, *et al.*, "A Front-End ASIC With Receive Sub-array Beamforming Integrated With a 32 x 32 PZT Matrix Transducer for 3-D Transesophageal Echocardiography", *IEEE Journal of Solid-State Circuits*, vol. 52, no. 4, pp. 994–1006, 2017. DOI: [10.1109/JSSC.2016.2638433](https://doi.org/10.1109/JSSC.2016.2638433).

[49] Y. M. Hopf, B. W. Ossenkoppele, M. Soozande, E. Noothout, Z.-Y. Chang, C. Chen, H. J. Vos, J. G. Bosch, M. D. Verweij, *et al.*, "A Pitch-Matched Transceiver ASIC With Shared Hybrid Beamforming ADC for High-Frame-Rate 3-D Intracardiac Echocardiography", *IEEE Journal of Solid-State Circuits*, vol. 57, no. 11, pp. 3228–3242, 2022. DOI: [10.1109/JSSC.2022.3201758](https://doi.org/10.1109/JSSC.2022.3201758).

[50] A. X. Widmer and P. A. Franaszek, "A DC-balanced, partitioned-block, 8B/10B transmission code", *IBM Journal of research and development*, vol. 27, no. 5, pp. 440–451, 1983. DOI: [10.1147/rd.275.0440](https://doi.org/10.1147/rd.275.0440).

[51] H.-H. Chang, J.-W. Lin, C.-Y. Yang, and S.-I. Liu, "A wide-range delay-locked loop with a fixed latency of one clock cycle", *IEEE journal of solid-state circuits*, vol. 37, no. 8, pp. 1021–1027, 2002. DOI: [10.1109/JSSC.2002.800922](https://doi.org/10.1109/JSSC.2002.800922).

[52] *Cyclone V Device Datasheet*, Intel, Santa Clara, CA, USA, 2019.

[53] *V309 Datasheet*, Olympus Corp, Tokyo, Japan, 2014.

[54] *SN2082 Datasheet*, Precis. Acoust, Dorchester, U.K, 2013.

4

AN ULTRASOUND MATRIX TRANSDUCER FOR HIGH-FRAME-RATE 3D INTRACARDIAC ECHOCARDIOGRAPHY

This chapter is in preparation for submission:

B. W. Ossenkoppеле*, D.S. Dos Santos*, Y.M. Hopf, M. Soozande, E. Noothout, H.J. Vos, J.G. Bosch, M.A.P. Pertijs, M.D. Verweij, N. de Jong, An ultrasound matrix transducer for high-frame-rate 3D intracardiac echocardiography. (*to be submitted in: Ultrasound in Medicine & Biology*)

* The first and second author contributed equally to this work.

4

This chapter presents the development of an ultrasound matrix transducer prototype for high-frame-rate three-dimensional (3D) intracardiac echocardiography (ICE). The matrix array consists of 16×18 lead zirconate titanate (PZT) elements with a pitch of $160 \mu\text{m} \times 160 \mu\text{m}$ built on top of an application-specific integrated circuit (ASIC) that generates transmission signals and digitizes the received signals. To reduce the number of cables in the catheter to a feasible number, we implement subarray beamforming and digitization in receive and use a combination of time-division multiplexing and pulse amplitude modulation data transmission, achieving an 18-fold reduction. The proposed imaging scheme employs seven fan-shaped diverging transmit beams operating at a pulse repetition frequency of 7.7 kHz to obtain a high frame rate. The performance of the prototype is characterized and its functionality is fully verified. The transducer exhibits a transmit efficiency of 28 Pa/V at 5 cm per element and a bandwidth of 60% in transmission. In receive, a dynamic range of 80 dB is measured with a minimum detectable pressure of 10 Pa per element. The element yield of the prototype is 98%, indicating the efficacy of the manufacturing process. The transducer is capable of imaging at a frame rate of up to 1000 volumes/s and is intended to cover a volume of $70^\circ \times 70^\circ \times 10 \text{ cm}$. These advanced imaging capabilities have the potential to support complex interventional procedures and enable full-volumetric flow, tissue, and electro-mechanical wave tracking in the heart.

4.1. INTRODUCTION

Arrhythmia is an abnormal rhythm of the heart that results from disruptions or irregularities in the electrical signals that regulate the heart's beating. These disruptions can cause the heart to beat too fast, too slow, or in an irregular pattern, which can affect the heart's ability to pump blood effectively. The most frequently occurring arrhythmia is atrial fibrillation, which is the major cardiac cause of stroke [1]. According to estimates, more than 5.6 million people will experience this condition in the United States by 2050 [2], while in the European Union, the number is expected to reach 17.9 million by 2060 [3]. Atrial fibrillation can initially be treated with drugs, but in some cases, catheter ablation may be necessary [4]. Ablation is a procedure that heat, cold, or radiofrequency waves to create small scars on the heart tissue, disrupting the abnormal electrical signals responsible for an irregular heartbeat, and restoring the normal rhythm and activation patterns of the heart [5].

Since the inception of ablation procedures, X-ray fluoroscopy has been employed to provide guidance due to its large field of view and ability to clearly visualize catheters and other devices. However, fluoroscopy also has significant disadvantages. First, the ionizing radiation exposure gives potentially harmful effects on the practitioner and the patient, hence imaging time is severely limited. Second, fluoroscopy provides limited visualization of atrial tissues, which can make it difficult to identify and target specific areas of interest. To overcome this limitation, the practitioner must rely on the combination of visual landmarks and subtle catheter sensations [6]. However, this approach can increase the risk of incomplete ablation or damage to surrounding tissues, leading to complications or the need for additional procedures [7].

As an alternative to relying solely on fluoroscopy, intracardiac ultrasound imaging can be used in combination with fluoroscopy to provide complementary imaging guidance, leading to improved accuracy and safety during interventional procedures [6]. In intracardiac echocardiography (ICE), a catheter containing a miniature ultrasound transducer is inserted into the cardiac cavities during the ablation procedure. This enables the practitioner to navigate the ablation catheter and visualize cardiac structures from an intracardiac perspective [8, 9]. Integrating ICE into ablation procedures for atrial fibrillation reduces both fluoroscopy time and the occurrence of major complications significantly [7, 10]. In addition to serving as a visualization tool of the cardiac structure, ultrasound can be used for electromechanical wave imaging (EWI), which is a novel ultrasound-based modality for mapping the electromechanical wave (EW), i.e. the transient tissue deformations occurring in immediate response to the electrical activation [11–13]. Several studies have reported a high correlation between cardiac electrical activity and the consequent EW for healthy and arrhythmic cases in both simulation [14] and in vivo data [11–13, 15, 16]. Therefore, by using EW mapping, the origin of the arrhythmia can be detected, and subsequently, ablation can be carried out on the source to terminate the arrhythmia effectively [16].

At present, EWI is primarily performed using a transthoracic transducer, which is placed on the surface of the chest. One limitation of that approach is that it is more prone to generate reflections on high-impedance materials, such as the rib cage or the pacemaker leads, leading to a poor acoustic window [13, 16]. In addition, the transthoracic transducer is limited in its ability to provide high-quality imaging of certain regions

of the heart that are difficult to access from the surface of the chest. To overcome these limitations and obtain a more comprehensive and accurate EW mapping, ICE imaging may be essential. An ICE device can provide both imaging guidance during interventional procedures and a map of the cardiac electromechanical activation. Furthermore, due to its proximity to the heart, ICE imaging enables the use of higher central frequencies, resulting in better axial resolution compared to transthoracic imaging [8].

Since EWs move with velocities ranging from 0.5 to 2 m/s, a high frame rate is necessary to capture their rapid movement [8]. Additionally, volumetric imaging is necessary for fully visualizing the complex patterns of EW propagation. This is because the waves propagate throughout the entire heart in three dimensions (3D), and their precise patterns of activation and conduction can be difficult to interpret from two-dimensional (2D) images alone [16]. Furthermore, since the activation patterns in atrial fibrillation are irregular in time and space [17, 18], the EW propagation needs to be visualized within a heartbeat rather than through the combination of acquisitions across subsequent heartbeats [16, 19]. Therefore, an ICE device that offers high-frame-rate 3D imaging capability is critical for effective visualization of EW propagation [8].

ICE technology currently faces challenges in meeting the demands of high-frame-rate 3D imaging. Designing ICE catheters that can handle these requirements is difficult because it requires using a 2D matrix array with a sufficiently large aperture and a large number of elements. However, the diameter of the catheter limits the size of the aperture and the number of cables that can fit inside the shaft. To address the latter limitation, application-specific integrated circuits (ASICs) can be used in ICE probes and the cable reduction can be achieved in various ways, including subarray beamforming, in-probe digitization, or time-division multiplexing [20–22]. In addition to reducing the number of channels, an ASIC can also amplify received signals to prevent attenuation caused by cable loading between the acoustic elements and the imaging system [23, 24]. However, recent 3D ICE designs are limited in functionality by the integration challenge. This expresses itself in lacking integration of a transmit beamformer [25], inadequate signal-to-noise ratio (SNR) due to low-voltage transmit [26], receive-only architectures [6, 21, 27] or low frame rate [6].

We have recently conducted a simulation study in which we proposed a novel imaging scheme for high-frame-rate 3D ICE imaging using a side-looking matrix comprised of 64×18 square elements [8]. The element pitch was 160 μm and the center frequency was in the range of 5–6 MHz. For channel count reduction, we implemented one-dimensional (1D) micro-beamforming in the elevation direction. Additionally, to achieve a high frame rate while covering a volume of $70^\circ \times 70^\circ \times 10$ cm, we employed a technique of transmitting fan-shaped diverging beams steered across 7 elevation angles, with a 20° divergence in elevation and 70° in azimuth. In simulations, the proposed method outperformed the current state of the art on 3D ICE in terms of frame rate.

This chapter presents the development of a side-looking ICE prototype transducer that utilizes an array of piezoelectric elements with a pitch of $160 \mu\text{m} \times 160 \mu\text{m}$ integrated with a pitch-matched ASIC. Details on the circuit implementation of the building blocks of this ASIC have been reported in [25]. The primary objective of this work is to demonstrate the feasibility of this prototype for high-frame-rate 3D ICE imaging. We provide a comprehensive analysis of the design, technical details, characterization, and

performance of the prototype. To our knowledge, this is the first study to report an ICE probe that is capable of generating high-frame-rate 3D images with a wide field of view and having digital output.

4.2. MATERIALS AND METHOD

4.2.1. DESIGN CHOICES

The process of designing ICE transducers is very challenging and complex, as the size of the catheter poses significant physical limitations on both the transducer aperture and channel count. The prototype transducer herein presented is designed to fit within a 10-French catheter, which has an outer diameter of 3.3 mm. This limits the transducer aperture to approximately 3 mm in the elevation direction, while the number of cables that can be accommodated within the catheter shaft is limited to 100 [6, 9]. In our simulations [8], we have opted to use a rectangular aperture of about 10 mm \times 3 mm (azimuth \times elevation). The matrix array consisted of square elements with a pitch of 160 μ m in both directions, resulting in a total of 64 \times 18 elements. To achieve a penetration depth of up to 10 cm, we have selected a center frequency of 6 MHz. A schematic representation of the proposed side-looking ICE transducer is shown in Fig. 4.1(a).

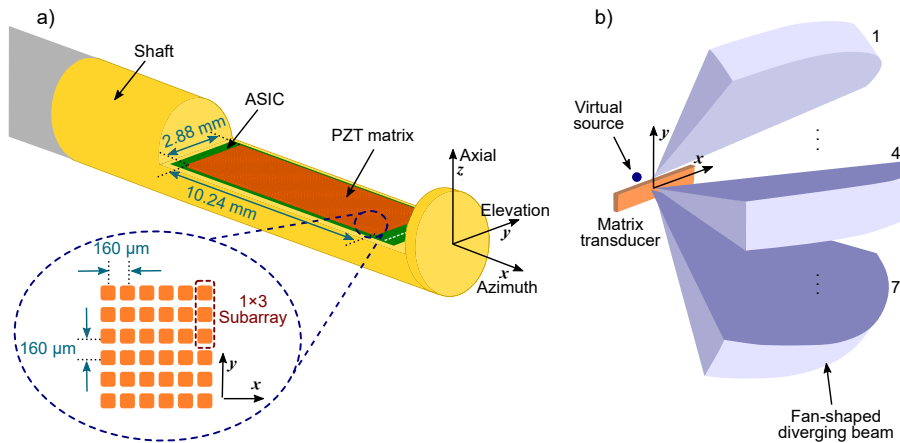


Figure 4.1: a) Schematic representation of the proposed ICE transducer. b) Transmit scheme using fan-shaped beams.

To achieve optimal 3D imaging, precise control of transmit and receive time delays as well as apodization for every element is crucial. This requires addressing each element of the array individually [28]. Since maintaining an element pitch that is below or close to half the wavelength is desirable to avoid grating lobes [29], the resulting matrix array consists of more than a thousand elements, exceeding by far the cable limit imposed by the catheter shaft. Therefore, it is necessary to reduce the number of channels of the probe significantly.

Several techniques have been proposed to reduce the complexity of fully populated matrix arrays, including sparse matrix arrays [30, 31] and row-column addressed ma-

trix arrays [32, 33]. However, these techniques have inherent limitations. Sparse matrix arrays suffer from lower signal-to-noise ratio (SNR) and higher clutter levels [34], while row-column addressed matrix arrays have more complex read-out sequences and a reduced flexibility in transmit beamforming, severely complicating the implementation of a diverging wave transmission scheme as is required to insonify the full imaging volume with a small number of transmissions for high-frame rate imaging [35]. One of the most effective ways to achieve channel reduction is by using the “micro-beamforming” technique, also known as “subarray/sub-aperture beamforming”, or “pre-steering”. This technique performs the first step of beamforming at the probe tip by applying micro-delays to the signal of small groups of adjacent elements and summing them all using an ASIC into one single channel. This partial beamforming reduces the number of signals that need to be transmitted through the cables and processed in the ultrasound system. The remaining beamforming and image reconstruction are performed in the ultrasound system [21, 28]. In our design, we have opted to use micro-beamforming for channel reduction. Our approach involves dividing the array into subarrays consisting of 1×3 elements, as this size offered a good balance between channel reduction and image quality according to earlier simulations [8]. With this, the number of cables was reduced by a factor of 3. Yet, a further on-chip reduction is still required to reduce the cable count sufficiently.

4.2.2. IMAGING SCHEME

In our earlier work [8], we introduced a novel imaging scheme that enables volumetric imaging with a sufficiently high frame rate and image quality for EWI, while also reducing the data rate to a practical level. Our objective was to achieve a frame rate of 1000 volumes/s, with a penetration depth of up to 10 cm and an opening angle of $70^\circ \times 70^\circ$. For a depth of 10 cm, the round-trip travel time of ultrasound waves requires approximately 130 μ s, assuming the speed of sound of 1540 m/s. As a result, the pulse repetition frequency (PRF) is limited to 7.7 kHz to allow enough time for the echoes to return before sending out another pulse. For this PRF and depth, a maximum of seven ultrasound pulses can be transmitted per frame to cover the entire region of interest, leading to a frame rate of 1000 volumes/s. Because we are limited to only seven transmissions to cover the entire volume, a diverging wave transmission scheme is necessary.

The proposed transmit scheme involves the use of seven fan-shaped diverging beams. These beams are steered in different directions in elevation, as illustrated in Fig. 4.1(b), and employ a 20° divergence in elevation and 70° in azimuth. We utilize a single virtual source to generate the desired fan-shaped diverging beam. In receive, the subarray beamformers are capable of covering a pre-steering range of $\pm 30^\circ$ in the elevation direction. To reduce grating lobes and improve image quality, we use angular weighted coherent compounding. This technique accounts for transmit beam contours, such that the noise and grating lobes from non-insonified regions are suppressed, while overlapping areas from neighboring transmissions are weighted and coherently compounded, resulting in a more accurate image [36].

4.2.3. ASIC IMPLEMENTATION

In Fig. 4.2, the architecture overview of the designed ASIC is illustrated. It includes high-voltage transmitters, analog frontends, hybrid beamforming analog-to-digital converters (ADCs), and data transmission to the imaging system [25]. The element-level circuitry is $160 \mu\text{m} \times 160 \mu\text{m}$ in size and is pitch-matched with the matrix array. The transmit (TX) part incorporates an on-chip unipolar pulser [37] (that can generate pulses up to 30 V. In addition to diverging waves, the implemented TX beamformer can produce other commonly used delay patterns, such as angled plane waves or focused waves.

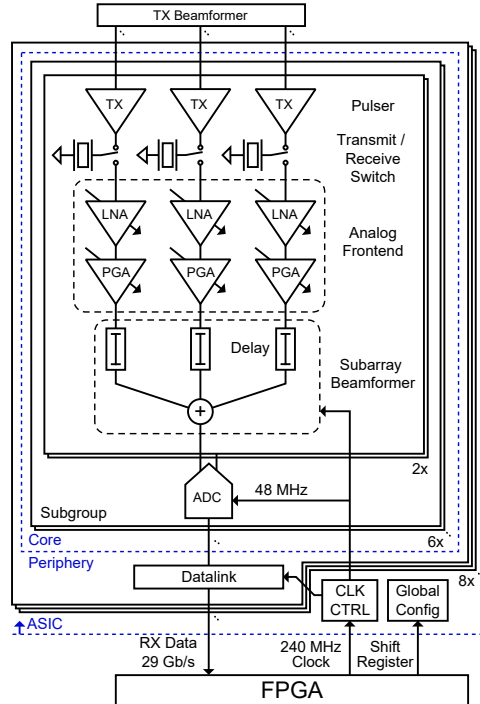


Figure 4.2: Block diagram of the ASIC architecture.

In receive (RX), the signal from each element is connected to a low-noise amplifier (LNA), followed by a second-stage programmable gain amplifier (PGA) [25]. The LNA can be switched in discrete steps of 18 dB ranging from -12 dB to 24 dB, while the second stage can be configured in 6 dB steps ranging from 6 dB to 24 dB. Together, this enables the implementation of time gain compensation (TGC) with a range of 54 dB. This is achieved through the use of 10 discrete steps of 6 dB, spanning from -6 dB to 48 dB. The outputs of three individual element-level circuits are merged using a 1×3 -element subarray beamformer. Two of these subarrays are then combined to form a 2×3 -element subgroup. Following this, the merged signals are digitized by an ADC at a rate of 24 MS/s with a resolution of 10 bits. The outputs are received by a periphery-level block, which provides a datalink to process the received data. In order to further reduce cable count in receive, a channel that combines time-division multiplexing (TDM) and 4-level pulse

amplitude modulation (PAM) data transmission has been implemented. [38]. This approach, together with the subarray beamforming, results in an 18-fold reduction in cable count.

4.2.4. TRANSDUCER FABRICATION

In order to simplify the fabrication process of the prototype transducer, we made two key decisions. Firstly, we chose to mount the transducer onto a custom daughterboard printed circuit board (PCB) rather than assembling it into a catheter at this stage. Secondly, instead of building the full size of the proposed ICE transducer (a 64×18 matrix array), we opted to build one-quarter of the aperture in the azimuth direction, resulting in a 16×18 matrix array. Building a smaller aperture at this stage of prototype development reduces cost and complexity while all of the functionality can still be tested.

4

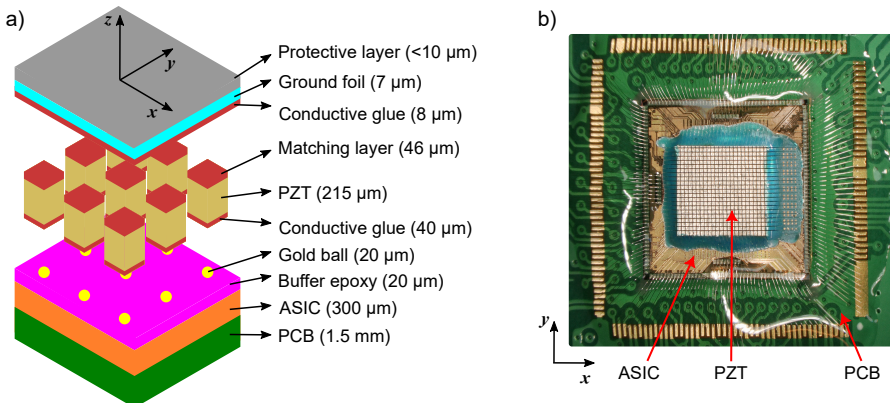


Figure 4.3: a) Acoustic stack with the indication of the thickness of each layer (not drawn to scale). b) Microscopic photo of the manufactured prototype.

Fig. 4.3(a) illustrates the proposed acoustic stack, which includes a matrix array made of lead zirconate titanate (PZT) piezoelectric material, the ASIC, a buffer layer, a matching layer, an aluminum ground foil, and a protective top layer. This stack design is similar to the ones we have presented in our previous works [23, 28, 39]. To fabricate the acoustic stack, gold balls are first deposited onto the transducer bond pads of the ASIC. The gaps between the balls are filled with an electrically isolating epoxy material, which is then ground down until the gold balls are exposed again. A conductive glue matching layer is applied on top of the piezoelectric material (3203HD, CTS Corporation, Lisle, IL, EUA), followed by gluing the PZT and matching layer stack onto the gold balls. The acoustical stack is then diced using a 20 μm dicing saw. To create a common ground electrode, a 7 μm thick aluminum foil is glued on top of the entire matrix array. Finally, to prevent moisture and damage, a thin layer of encapsulation material (AptFlex F7, Precision Acoustics Ltd., Dorchester, UK) is placed on top of the stack. Fig. 4.3(b) displays a photograph of the acoustic stack mounted on top of the ASIC and PCB before the ground foil is deposited.

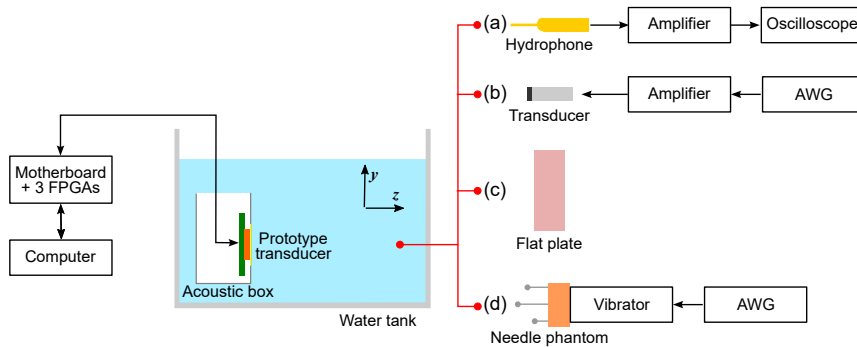


Figure 4.4: Measurement setup. *a)* Transmit characterization. *b)* Receive characterization. *c)* Pulse-echo measurements. *d)* Imaging.

4.2.5. ACOUSTIC CHARACTERIZATION

For the acoustic characterization and tests, the prototype was placed in a watertight box with a 25 μm thick polyimide acoustic window and submerged in a water tank filled with deionized water. A custom motherboard was utilized to interface the prototype with a computer for data processing through commercial field programmable gate arrays (FPGAs), as shown in Fig. 4.4.

To assess the transmit performance (Fig. 4.4(a)), we evaluated the time and frequency responses of individual transducer elements. For this, we applied 30-V pulses to the element under test and measured the resulting acoustic pressure generated by it using a calibrated 1-mm needle hydrophone (PVDF, Precision Acoustics Ltd., Dorchester, UK) placed at a distance of 5 cm from the transducer. The hydrophone output was then amplified by a 60 dB amplifier (AU-1519, Miteq, Inc., Hauppauge, NY, USA) and digitized by an oscilloscope (DSO-X 4024A, Agilent Technologies, Santa Clara, CA, USA). Next, we characterized the directivity pattern of specific transducer elements using hydrophone scans with a calibrated 0.2-mm needle hydrophone (SN3800, Precision Acoustics Ltd.). We performed rotational scans ranging from -60° to 60° at a distance of 5 cm from the transducer. Using the same setup, we evaluated the directivity pattern of the entire transducer when transmitting diverging waves steered at seven different angles in elevation. To provide a comprehensive assessment, we compared the measured directivity patterns with simulations performed using the ultrasound simulator FOCUS [40].

To assess the receive performance (Fig. 4.4(b)), we used a pre-calibrated 1 mm circular single-element transducer (PA865, Precision Acoustics Ltd., Dorchester, UK) as a transmitter placed at 5 mm away from the prototype. We drove the single-element transducer with an 8-cycle sine wave generated by an arbitrary waveform generator (AWG; 33250A, Agilent Technologies, Santa Clara, CA, USA) and measured the response at each individual element of the prototype to evaluate the sensitivity variation and element yield. With the same setup, we evaluated the dynamic range of the prototype, which is defined as the difference between the highest and lowest detectable pressures. Hence, we varied the surface pressure applied to the prototype between 1 Pa and 100 kPa while

varying the gain setting of the ASIC from -6 to 48 dB. Lastly, we measured the directivity pattern of one subarray when pre-steering it at seven different angles in the elevation direction. For this, the prototype was rotated from -60° to 60° in increments of 1° . At each angle, the received data was transferred to the computer for processing. For pulse-echo measurements (Fig. 4.4(c)), we positioned a quartz flat plate 5 cm from the prototype. A plane wave was transmitted with all elements excited with 3 cycles of 30 V, and the resulting echoes were received by each individual element.

4.2.6. HIGH-FRAME-RATE 3D IMAGING

To assess the high-frame-rate 3D imaging capability, we utilized a custom phantom consisting of three needles. The phantom was positioned at a distance of about 4 cm from the prototype transducer (Fig. 4.4(d)). To introduce motion into the system, we attached the phantom to a mechanical shaker (Type 4810, Brüel & Kjær, Nærum, Denmark) and applied a low-frequency sine vibration of 20 Hz. To capture the dynamic movement of the needles in 3D, we acquired 280 pulse-echo cycles at a PRF of 7 kHz. Since seven pulse-echo cycles are required to generate each 3D volume image, a total of 40 volumetric images were obtained from the 280 pulse-echo cycles at 1 kHz volumetric frame rate. The 3D volume image reconstruction was performed offline. To provide a comparison to the high-frame-rate 3D imaging results, we used a commercial diagnostic ultrasound machine (Aplio Artida, Toshiba Medical Systems, Otawara, Japan) with a linear probe (PLT-704SBT, Toshiba Medical Systems, Otawara, Japan) to measure the displacement of the needles using M-mode imaging.

4.3. RESULTS

4.3.1. TRANSMIT CHARACTERIZATION

Fig. 4.5(a) shows the time and frequency responses of five transducer elements recorded with the hydrophone. At 5 cm, the average peak pressure for a single element is about 0.85 kPa. In the frequency domain, the center frequency is about 5.5 MHz and the average -6 dB bandwidth is about 60%. In Fig. 4.5(b), the directivity pattern of five elements together with the simulated curve along the elevation direction is shown. The experimental observations reveal a -6 dB beam width of approximately 55° , while the simulated result is about 112° . This deviation is due to the dips seen at approximately $\pm 40^\circ$ in the measured directivity. Similar results were observed along the azimuth direction since the element has a square geometry.

Fig. 4.6 depicts the locally-normalized directivity pattern of the entire matrix array transmitting diverging waves steered at seven different angles ranging from -30° to 30° in the elevation direction. The measured and simulated profiles are in good agreement, with a -6 dB beam width of approximately 20° observed in both cases. This confirms the effectiveness of the prototype in generating and steering diverging beams. In Fig. 4.7, the directivity pattern along the azimuth direction is displayed for the current and the full-size aperture. As seen, there is an excellent agreement between the measured and simulated profiles up to about -17 dB levels, with the -6 dB beam width of about 20° for the current aperture. For the full-size aperture, we observe a -6 dB beam width of about 70° , which is according to our design goal.

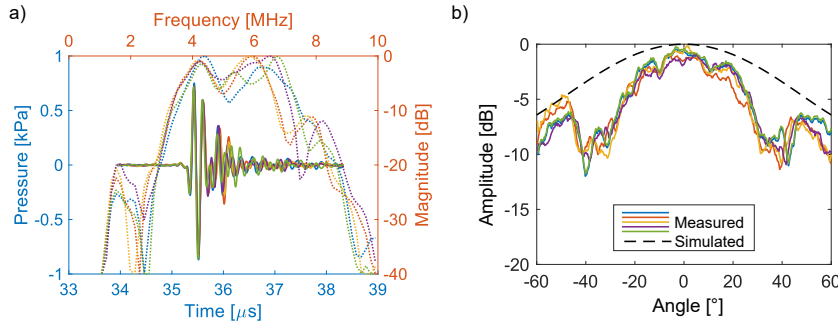


Figure 4.5: a) Time and frequency responses of individual elements. b) Measured and simulated directivity pattern of individual elements.

4

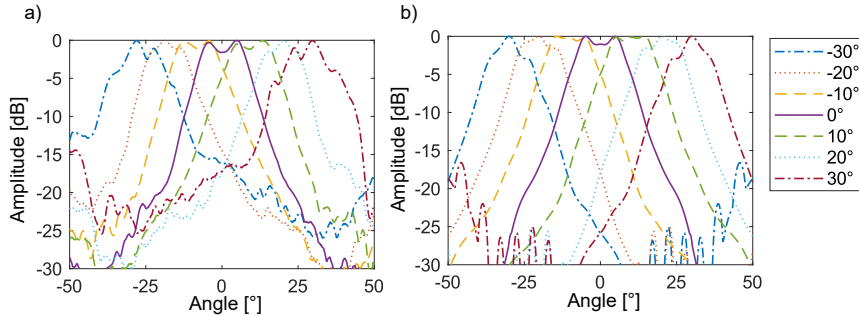


Figure 4.6: Directivity pattern of the transducer transmitting steered diverging waves in elevation. a) Measured. b) Simulated.

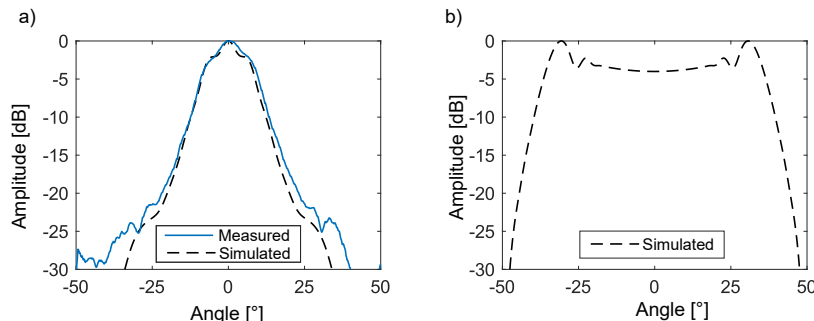


Figure 4.7: Directivity pattern of the transducer transmitting a diverging wave in azimuth a) Current aperture. b) Intended aperture.

4.3.2. RECEIVE CHARACTERIZATION

Fig. 4.8(a) displays the sensitivity variation in receive across all elements of the prototype transducer. The results demonstrate a high yield, with 282 out of 288 elements (i.e., 98%) falling within the 0 dB to -6 dB range. Only one element, indicated in dark blue, exhibits no signal and is considered defective in receive. Fig. 4.8(b) displays the relationship between the received pressure at the surface of the prototype and the corresponding normalized ADC output for all gain levels. To reduce measurement time, the measurements were conducted using one-third of the array, i.e. 96 elements. The plotted values represent the average across these 96 elements. The lowest detectable pressure is around 10 Pa, which was measured when the ASIC gain was set to 48 dB. The highest detectable pressure was about 100 kPa, which was measured for a gain of -6 dB. An overall dynamic range of about 80 dB is obtained between the 0-dB SNR point of the highest gain and the 1-dB compression point of the lowest gain setting.

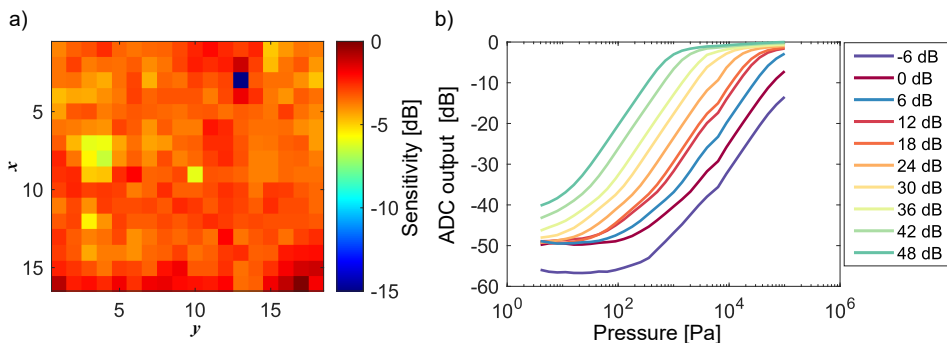


Figure 4.8: a) Sensitivity variation in receive. b) Relation between received pressure and ADC output for all ASIC gains.

Fig. 4.9 illustrates the measured and simulated directivity pattern of a 1x3 subarray pre-steering at seven different angles, ranging from -30° to 30° in the elevation direction. The measured and simulated profiles exhibit a good agreement, which demonstrates that the designed ASIC can efficiently generate the necessary delays to steer the subarrays toward the intended directions. The -6 dB beam width is approximately 40° for all steering angles, except for -30° steering, which has a beam width of about 50° . Note that as the steering angle increases, the side lobe levels tend to rise too.

4.3.3. PULSE-ECHO MEASUREMENTS

Fig. 4.10 displays the pulse-echo measurements obtained by transmitting 3 cycles with all elements (no steering) and receiving the echo with individual elements without applying micro-beamforming. The measurements were conducted using five arbitrarily selected elements as receivers. All measured elements exhibit a comparable amplitude response and a center frequency of about 6.1 MHz. Note that a dip around 6 MHz causes the -6 dB bandwidth to narrow to roughly 10%.

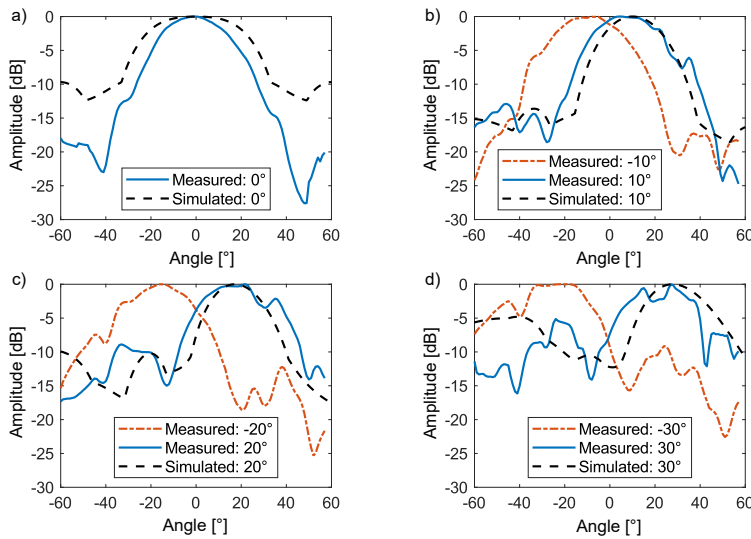


Figure 4.9: Measured and simulated directivity pattern of a 1×3 subarray pre-steered at *a)* 0° , *b)* $\pm 10^\circ$, *c)* $\pm 20^\circ$, and *d)* $\pm 30^\circ$ in the elevation direction.

4

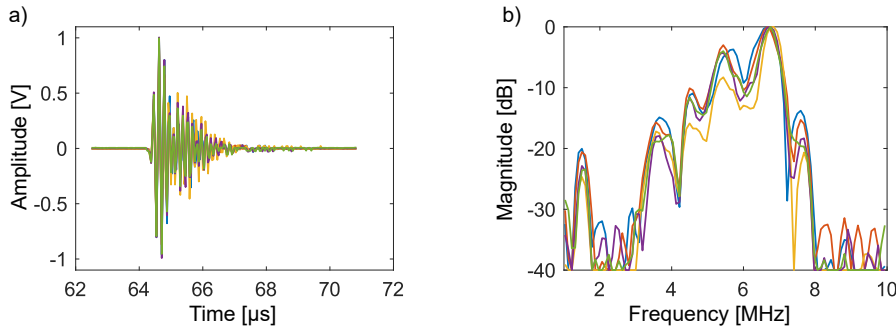


Figure 4.10: Pulse-echo responses obtained from 3-cycle transmissions using all elements and a single-element receiver. *a)* Time domain. *b)* Frequency domain.

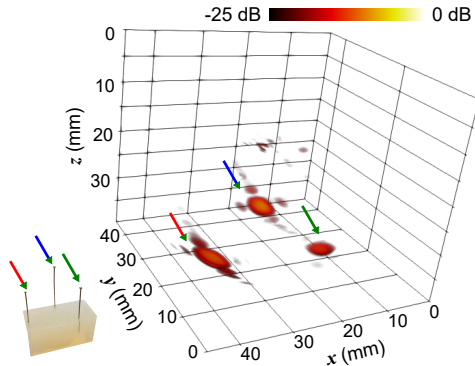


Figure 4.11: Needle phantom and its reconstructed 3D image acquired with the prototype at a frame rate of 1000 volumes/s.

4

4.3.4. IMAGING

Fig. 4.11 presents one of the 40 volumetric images of the needle phantom captured by our prototype transducer at a frame rate of 1000 volumes/s. After the acquisition, the data was transferred from the motherboard to a computer for offline image processing. The reconstructed image clearly distinguishes the needles in 3D space, and the positions of the point scatterers closely match the position of the needles in the photograph of the phantom. Note, however, that each imaged needle exhibits one main lobe accompanied by secondary lobes in both the azimuth and elevation directions.

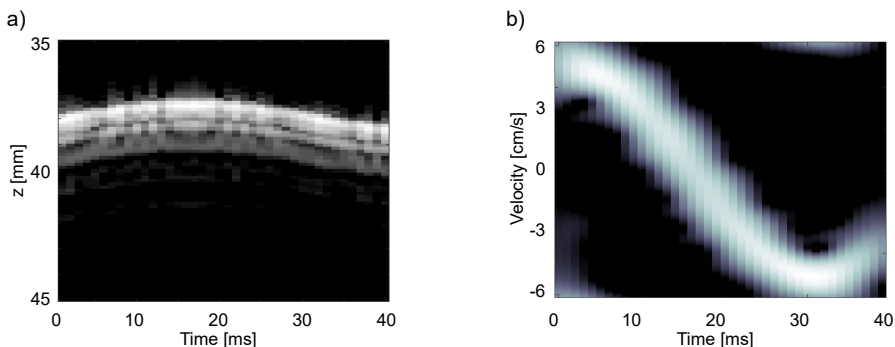


Figure 4.12: Motion of a single needle extracted from high-frame-rate 3D images acquired with the prototype transducer. a) Needle displacement. b) Needle velocity.

We utilized the dataset consisting of 40 images to track the axial motion of a single needle to show the high-frame-rate imaging capability of the ASIC. Fig. 4.12(a) shows the resulting displacement of one needle, while Fig. 4.12(b) shows its instantaneous velocity derived by pulsed-wave Doppler processing of the high-framerate images at the position of a needle. The 20 Hz vibration of the needle is clearly visible, and we were able to capture about 80% of its sinusoidal motion within the 40 ms acquisition time.

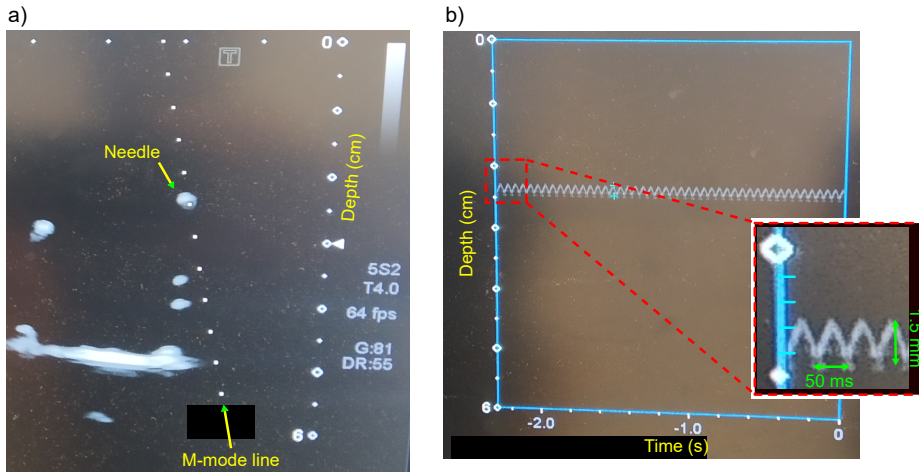


Figure 4.13: Images of the needle phantom acquired with the Toshiba system. *a)* B-mode image. *b)* M-mode image

We observed a peak-to-peak displacement of approximately 1.5 mm, with a maximum measured velocity of around 5 cm/s.

In Fig. 4.13(a), we present the B-mode image of the needle phantom acquired with the commercial imaging system, which was used for validation. To track the motion of one of the needles, we drew a line on it and performed M-mode imaging, as depicted in Fig. 4.13(b). The 20 Hz vibration of the needle is also evident and we measured the same peak-to-peak displacement of about 1.5 mm. This agreement highlights our capability to achieve high frame 3D imaging.

4.4. DISCUSSION

We presented the development of a high-frame-rate 3D imaging prototype ICE transducer. This involved constructing a PZT matrix array with 16×18 elements interfaced with a pitch-matched ASIC. To address the challenge of cable count reduction, we implemented subarray beamforming in receive, on-chip digitization, and utilized a combination of TDM and PAM data transmission. This allowed us to reduce the total cable count by 18-fold lower than the acoustic element number, resulting in a feasible number of cables for practical implementation. Due to complexity and cost constraints, we built a prototype that corresponds to a quarter of the full aperture design (64×18), with a single channel providing a platform to evaluate PAM data transmission, as well as conventional LVDS drivers. The transducer was mounted on a PCB for convenience. Despite these modifications, we were able to conduct comprehensive tests to examine the prototype's performance and verify its functionality.

As depicted in Fig. 4.5(a), the responses of the five individual elements exhibit similar behavior in transmit. At a distance of 5 cm, each element has a transmit efficiency of around 28 Pa/V, which is consistent with previous designs [28, 39]. On average, the center frequency of the elements is 5.5 MHz, and the -6 dB bandwidth is 60% in transmit. Note

that the frequency spectrum displays a dip at approximately the center frequency, which decreases the overall bandwidth. This dip is also observed in the pulse-echo response, shown in Fig. 4.10, and is likely the result of reflections and standing waves from the ASIC [39, 41]. To mitigate this effect, an interposer layer between the PZT and the ASIC could be utilized [6, 39, 42]. We may explore this option in future designs.

The directivity pattern of the single elements, as shown in Fig. 4.5(b), generally follows the trend of the simulated directivity. However, we observed dips at $\pm 40^\circ$, which is likely caused by acoustic crosstalk [43, 44], as we have previously reported [39, 41]. The directivity pattern of the entire transducer, as shown in Fig. 4.6 and Fig. 4.7, aligns very well with simulations and demonstrates that the prototype is capable of steering from -30° to 30° in the elevation direction. Considering that the azimuth aperture is extended as originally designed (i.e., with 64 elements), our prototype is expected to provide a coverage of $70^\circ \times 70^\circ$. In receive, the directivity pattern of the 1x3 subarrays (Fig. 4.9) also exhibits the expected behavior, albeit with an increase in degradation and artifacts at higher steering angles [45]. Overall, the directivity pattern measurements confirm that the ASIC is effective in generating the desired delay patterns, as specified in our design.

The sensitivity map depicted in Fig. 4.8(a) reveals that 282 out of 288 elements of the prototype are within the -6 dB range. This element yield of 98% demonstrates the efficacy of our fabrication process and encourages us to consider scaling up the aperture size to 64×18 elements in future developments. In Fig. 4.8(b), we observed that the lowest detectable pressure of 10 Pa is limited by the ASIC's noise floor for a gain setting of 48 dB, whereas the highest detectable pressure of 100 kPa is limited by the ASIC's saturation level for a gain of -6 dB. This results in a total dynamic range of 80 dB, which is suitable for ICE. Note that there seems to be an overlap in the gain step between 12 and 18 dB, which is not consistent with the expected 6 dB difference. This is likely due to a mismatch in the amplifier circuitry, which can be easily corrected for in a future re-adjustment of the design.

In the imaging experiment with the vibrating needle phantom, we successfully acquired 40 volumes within a 40 ms interval, achieving the intended frame rate of 1000 volumes/s. The reconstructed 3D image of the needles depicted in Fig. 11 confirms the prototype's 3D imaging capabilities, even though some side lobes are present in the image. Nonetheless, it's worth noting that for the full-size array, the side lobes will be reduced and the overall imaging quality will be improved. By analyzing the 40 acquired volumetric images, we were able to extract the motion pattern of the needle and accurately estimate its velocity with retrospective pulsed-wave Doppler analysis, as shown in Fig. 4.12. The clean Doppler spectrogram indicates proper internal timing and digitization of the signals. These results are very promising, as we were able to precisely validate them with a clinical ultrasound system as a reference (Fig. 4.3). Since the ICE prototype transducer is currently mounted on a large PCB for testing purposes, it is not yet ready for (pre)clinical use. In future work, we plan to assemble a complete prototype and integrate it into a catheter for EWI validation.

4.5. CONCLUSIONS

In this study, we have presented the design, fabrication, and characterization of a prototype transducer with an integrated ASIC for high-frame-rate 3D intracardiac echocar-

diography. By applying subarray beamforming alongside on-chip digitization, time-division multiplexing and pulse amplitude modulation data transmission, we were able to significantly reduce the cable count to a realistic number that can fit within a catheter shaft. The acoustic performance of the prototype met the design requirements, allowing us to achieve 3D imaging with a large field of view and a frame rate of 1000 volumes/s. This high frame rate outperforms current state-of-the-art ICE probes and paves the way towards implementation of electromechanical wave imaging on future ICE catheters. Future work should focus on realizing a full aperture transducer inside a catheter to enable *in vivo* testing.

REFERENCES

- [1] J. Jalife, O. Berenfeld, and M. Mansour, "Mother rotors and fibrillatory conduction: A mechanism of atrial fibrillation", *Cardiovascular Research*, vol. 54, no. 2, pp. 204–216, 2002. DOI: [10.1016/S0008-6363\(02\)00223-7](https://doi.org/10.1016/S0008-6363(02)00223-7).
- [2] A. S. Go, E. M. Hylek, K. A. Phillips, Y. Chang, L. E. Henault, J. V. Selby, and D. E. Singer, "Prevalence of Diagnosed Atrial Fibrillation in Adults National Implications for Rhythm Management and Stroke Prevention: the AnTicoagulation and Risk Factors In Atrial Fibrillation (ATRIA) Study", *JAMA*, vol. 285, no. 18, pp. 2370–2375, May 2001. DOI: [10.1001/jama.285.18.2370](https://doi.org/10.1001/jama.285.18.2370).
- [3] B. P. Krijthe, A. Kunst, E. J. Benjamin, G. Y. Lip, O. H. Franco, A. Hofman, J. C. Witteman, B. H. Stricker, and J. Heeringa, "Projections on the number of individuals with atrial fibrillation in the European Union, from 2000 to 2060", *European Heart Journal*, vol. 34, no. 35, pp. 2746–2751, Jul. 2013. DOI: [10.1093/eurheartj/eht280](https://doi.org/10.1093/eurheartj/eht280).
- [4] B. Kheiri, T. F. Simpson, R. Przybylowicz, M. Merrill, H. Alhamoud, M. Osman, K. Dalouk, E. Stecker, C. A. Henrikson, *et al.*, "Ablation versus antiarrhythmic drugs as first-line treatment of paroxysmal atrial fibrillation: a meta-analysis of randomized trials", *Circulation: Arrhythmia and Electrophysiology*, vol. 14, no. 8, Aug. 2021. DOI: [10.1161/circep.120.009692](https://doi.org/10.1161/circep.120.009692).
- [5] G. Katritsis, H. Calkins, and and, "Catheter ablation of atrial fibrillation – techniques and technology", *Arrhythmia and Electrophysiology Review*, vol. 1, p. 29, 2012. DOI: [10.15420/aer.2012.1.29](https://doi.org/10.15420/aer.2012.1.29).
- [6] D. Wildes, W. Lee, B. Haider, S. Cogan, K. Sundaresan, D. M. Mills, C. Yetter, P. H. Hart, C. R. Haun, *et al.*, "4-D ICE: A 2-D Array Transducer with Integrated ASIC in a 10-Fr Catheter for Real-Time 3-D Intracardiac Echocardiography", *IEEE Transactions on Ultrasonics, Ferroelectrics, and Frequency Control*, vol. 63, no. 12, pp. 2159–2173, 2016. DOI: [10.1109/TUFFC.2016.2615602](https://doi.org/10.1109/TUFFC.2016.2615602).
- [7] J. M. Cooper and L. M. Epstein, "Use of intracardiac echocardiography to guide ablation of atrial fibrillation", *Circulation*, vol. 104, no. 25, pp. 3010–3013, Dec. 2001. DOI: [10.1161/hc5001.101503](https://doi.org/10.1161/hc5001.101503).
- [8] M. Soozande, B. W. Ossenkoppele, Y. Hopf, M. A. P. Pertijis, M. D. Verweij, N. De Jong, H. J. Vos, and J. G. Bosch, "Imaging Scheme for 3-D High-Frame-Rate Intracardiac Echography: A Simulation Study", *IEEE Transactions on Ultrasonics, Ferroelectrics, and Frequency Control*, vol. 69, no. 10, pp. 2862–2874, 2022. DOI: [10.1109/TUFFC.2022.3186487](https://doi.org/10.1109/TUFFC.2022.3186487).
- [9] W. Lee, S. F. Idriss, P. D. Wolf, and S. W. Smith, "A miniaturized catheter 2-D array for real-time, 3-D intracardiac echocardiography", *IEEE transactions on ultrasonics, ferroelectrics, and frequency control*, vol. 51, no. 10, pp. 1334–1346, 2004. DOI: [10.1109/TUFFC.2004.1350962](https://doi.org/10.1109/TUFFC.2004.1350962).
- [10] C. La Greca, A. Cirasa, D. Di Modica, A. Sorgato, U. Simoncelli, and D. Pecora, "Advantages of the integration of ICE and 3D electroanatomical mapping and ultrasound-guided femoral venipuncture in catheter ablation of atrial fibrillation", *Journal of Interventional Cardiac Electrophysiology*, vol. 61, no. 3, pp. 559–566, 2021. DOI: [10.1007/s10840-020-00835-6](https://doi.org/10.1007/s10840-020-00835-6).
- [11] J. Provost, W.-N. Lee, K. Fujikura, and E. E. Konofagou, "Imaging the electromechanical activity of the heart *in vivo*", *Proceedings of the National Academy of Sciences*, vol. 108, no. 21, pp. 8565–8570, 2011. DOI: [10.1073/pnas.1011688108](https://doi.org/10.1073/pnas.1011688108).
- [12] E. E. Konofagou and J. Provost, "Electromechanical wave imaging for noninvasive mapping of the 3D electrical activation sequence in canines and humans *in vivo*", *Journal of Biomechanics*, vol. 45, no. 5, pp. 856–864, 2012. DOI: doi.org/10.1016/j.jbiomech.2011.11.027.

[13] J. Provost, V. T.-H. Nguyen, D. Legrand, S. Okrasinski, A. Costet, A. Gambhir, H. Garan, and E. E. Konofagou, "Electromechanical wave imaging for arrhythmias", *Physics in Medicine & Biology*, vol. 56, no. 22, p. L1, 2011. DOI: [10.1088/0031-9155/56/22/F01](https://doi.org/10.1088/0031-9155/56/22/F01).

[14] J. Provost, V. Gurev, N. Trayanova, and E. E. Konofagou, "Mapping of cardiac electrical activation with electromechanical wave imaging: an in silico-in vivo reciprocity study", *Heart Rhythm*, vol. 8, no. 5, pp. 752–759, 2011. DOI: [10.1016/j.hrthm.2010.12.034](https://doi.org/10.1016/j.hrthm.2010.12.034).

[15] J. Provost, A. Costet, E. Wan, A. Gambhir, W. Whang, H. Garan, and E. E. Konofagou, "Assessing the atrial electromechanical coupling during atrial focal tachycardia, flutter, and fibrillation using electromechanical wave imaging in humans", *Computers in biology and medicine*, vol. 65, pp. 161–167, 2015. DOI: [10.1016/j.combiomed.2015.08.005](https://doi.org/10.1016/j.combiomed.2015.08.005).

[16] A. Costet, E. Wan, E. Bunting, J. Grondin, H. Garan, and E. Konofagou, "Electromechanical wave imaging (EWI) validation in all four cardiac chambers with 3D electroanatomic mapping in canines in vivo", *Physics in Medicine & Biology*, vol. 61, no. 22, p. 8105, 2016. DOI: [10.1088/0031-9155/61/22/8105](https://doi.org/10.1088/0031-9155/61/22/8105).

[17] M. Allessie and N. de Groot, "CrossTalk opposing view: Rotors have not been demonstrated to be the drivers of atrial fibrillation", *The Journal of physiology*, vol. 592, no. Pt 15, p. 3167, 2014. DOI: [10.1113/jphysiol.2014.271809](https://doi.org/10.1113/jphysiol.2014.271809).

[18] M. T. Pope, P. Kuklik, A. B. e Gala, M. Leo, M. Mahmoudi, J. Paisey, and T. R. Betts, "Spatial and temporal variability of rotational, focal, and irregular activity: practical implications for mapping of atrial fibrillation", *Journal of Cardiovascular Electrophysiology*, vol. 32, no. 9, pp. 2393–2403, Jul. 2021. DOI: [10.1111/jce.15170](https://doi.org/10.1111/jce.15170).

[19] F. Bessiere, A. Zorgani, L. Daunizeau, E. Cao, F. Vaillant, E. Abell, B. Quesson, S. Catheline, P. Chevalier, *et al.*, "High frame rate ultrasounds for electromechanical wave imaging to characterize and differentiate endocardial from epicardial activation of ventricular arrhythmia: a proof of concept study", *Archives of Cardiovascular Diseases Supplements*, vol. 11, no. 2, p. 259, Apr. 2019. DOI: [10.1016/j.acvdsp.2019.02.164](https://doi.org/10.1016/j.acvdsp.2019.02.164).

[20] B. Savord and R. Solomon, "Fully sampled matrix transducer for real time 3D ultrasonic imaging", in *IEEE Symposium on Ultrasonics*, vol. 1, IEEE, 2003, pp. 945–953. DOI: [10.1109/ULTSYM.2003.1293556](https://doi.org/10.1109/ULTSYM.2003.1293556).

[21] C. Chen, Z. Chen, D. Bera, E. Noothout, Z. Y. Chang, M. Tan, H. J. Vos, J. G. Bosch, M. D. Verweij, *et al.*, "A pitch-matched front-end ASIC with integrated subarray beamforming ADC for miniature 3-D ultrasound probes", *IEEE Journal of Solid-State Circuits*, vol. 53, no. 11, pp. 3050–3064, 2018. DOI: [10.1109/JSSC.2018.2864295](https://doi.org/10.1109/JSSC.2018.2864295).

[22] T. M. Carpenter, M. W. Rashid, M. Ghovanloo, D. M. Cowell, S. Freear, and F. L. Degertekin, "Direct digital demultiplexing of analog TDM signals for cable reduction in ultrasound imaging catheters", *IEEE transactions on ultrasonics, ferroelectrics, and frequency control*, vol. 63, no. 8, pp. 1078–1085, 2016. DOI: [10.1109/TUFFC.2016.2557622](https://doi.org/10.1109/TUFFC.2016.2557622).

[23] E. Kang, Q. Ding, M. Shabanimotagh, P. Kruizinga, Z. Y. Chang, E. Noothout, H. J. Vos, J. G. Bosch, M. D. Verweij, *et al.*, "A Reconfigurable Ultrasound Transceiver ASIC With 24 x 40 Elements for 3-D Carotid Artery Imaging", *IEEE Journal of Solid-State Circuits*, vol. 53, no. 7, pp. 2065–2075, 2018. DOI: [10.1109/JSSC.2018.2820156](https://doi.org/10.1109/JSSC.2018.2820156).

[24] C. Chen, Z. Chen, D. Bera, S. B. Raghunathan, M. Shabanimotagh, E. Noothout, Z.-Y. Chang, J. Ponte, C. Prins, *et al.*, "A Front-End ASIC With Receive Sub-array Beamforming Integrated With a 32 x 32 PZT Matrix Transducer for 3-D Transesophageal Echocardiography", *IEEE Journal of Solid-State Circuits*, vol. 52, no. 4, pp. 994–1006, 2017. DOI: [10.1109/JSSC.2016.2638433](https://doi.org/10.1109/JSSC.2016.2638433).

[25] Y. M. Hopf, B. W. Ossenkoppele, M. Soozande, E. Noothout, Z.-Y. Chang, C. Chen, H. J. Vos, J. G. Bosch, M. D. Verweij, *et al.*, "A Pitch-Matched Transceiver ASIC With Shared Hybrid Beamforming ADC for High-Frame-Rate 3-D Intracardiac Echocardiography", *IEEE Journal of Solid-State Circuits*, vol. 57, no. 11, pp. 3228–3242, 2022. DOI: [10.1109/JSSC.2022.3201758](https://doi.org/10.1109/JSSC.2022.3201758).

[26] J. Lee, K.-R. Lee, B. E. Eovino, J. H. Park, L. Y. Liang, L. Lin, H.-J. Yoo, and J. Yoo, "A 36-channel auto-calibrated front-end ASIC for a pMUT-based miniaturized 3-D ultrasound system", *IEEE Journal of Solid-State Circuits*, vol. 56, no. 6, pp. 1910–1923, 2021. DOI: [10.1109/JSSC.2021.3049560](https://doi.org/10.1109/JSSC.2021.3049560).

[27] J. Li, Z. Chen, M. Tan, D. Van Willigen, C. Chen, Z.-y. Chang, E. Noothout, N. de Jong, M. Verweij, *et al.*, "A 1.54 mW/element 150 μ m-pitch-matched receiver ASIC with element-level SAR/shared-single-slope hybrid ADCs for miniature 3D ultrasound probes", in *2019 Symposium on VLSI Circuits*, IEEE, 2019, pp. C220–C221. DOI: [10.23919/VLSIC.2019.8778200](https://doi.org/10.23919/VLSIC.2019.8778200).

[28] V. Daeichin, D. Bera, S. Raghunathan, M. Shabani Motlagh, Z. Chen, C. Chen, E. Noothout, H. J. Vos, M. Pertij, *et al.*, "Acoustic characterization of a miniature matrix transducer for pediatric 3D trans-

esophageal echocardiography", *Ultrasound in Medicine and Biology*, vol. 44, no. 10, pp. 2143–2154, 2018. DOI: [10.1016/j.ultrasmedbio.2018.06.009](https://doi.org/10.1016/j.ultrasmedbio.2018.06.009).

[29] N. de Jong, N. Bom, J. Souquet, and G. Faber, "Vibration modes, matching layers and grating lobes", *Ultrasonics*, vol. 23, no. 4, pp. 176–182, 1985. DOI: [https://doi.org/10.1016/0041-624X\(85\)90027-7](https://doi.org/10.1016/0041-624X(85)90027-7).

[30] N. Ellens, A. Pulkkinen, J. Song, and K. Hynynen, "The utility of sparse 2d fully electronically steerable focused ultrasound phased arrays for thermal surgery: a simulation study", *Physics in Medicine and Biology*, vol. 56, no. 15, pp. 4913–4932, Jul. 2011. DOI: [10.1088/0031-9155/56/15/017](https://doi.org/10.1088/0031-9155/56/15/017).

[31] A. Ramalli, E. Boni, A. S. Savoia, and P. Tortoli, "Density-tapered spiral arrays for ultrasound 3-D imaging", *IEEE Transactions on Ultrasonics, Ferroelectrics, and Frequency Control*, vol. 62, pp. 1580–1588, 8 2015. DOI: [10.1109/TUFFC.2015.007035](https://doi.org/10.1109/TUFFC.2015.007035).

[32] K. Chen, H.-S. Lee, and C. G. Sodini, "A column-row-parallel asic architecture for 3-d portable medical ultrasonic imaging", *IEEE Journal of Solid-State Circuits*, vol. 51, no. 3, pp. 738–751, 2016. DOI: [10.1109/JSSC.2015.2505714](https://doi.org/10.1109/JSSC.2015.2505714).

[33] M. Flesch, M. Pernot, J. Provost, G. Ferin, A. Nguyen-Dinh, M. Tanter, and T. Deffieux, "4d in vivo ultrafast ultrasound imaging using a row-column addressed matrix and coherently-compounded orthogonal plane waves", *Physics in Medicine and Biology*, vol. 62, no. 11, pp. 4571–4588, May 2017. DOI: [10.1088/1361-6560/aa63d9](https://doi.org/10.1088/1361-6560/aa63d9).

[34] L. Wei, G. Wahyulaksana, B. Meijlink, A. Ramalli, E. Noothout, M. D. Verweij, E. Boni, K. Kooiman, A. E. Van Der Steen, *et al.*, "High Frame Rate Volumetric Imaging of Microbubbles Using a Sparse Array and Spatial Coherence Beamforming", *IEEE Transactions on Ultrasonics, Ferroelectrics, and Frequency Control*, vol. 68, no. 10, pp. 3069–3081, 2021. DOI: [10.1109/TUFFC.2021.3086597](https://doi.org/10.1109/TUFFC.2021.3086597).

[35] H. Bouzari, M. Engholm, C. Beers, M. B. Stuart, S. I. Nikolov, E. V. Thomsen, and J. A. Jensen, "Curvilinear 3-D Imaging Using Row-Column-Addressed 2-D Arrays With a Diverging Lens: Feasibility Study", *IEEE Transactions on Ultrasonics, Ferroelectrics, and Frequency Control*, vol. 64, no. 6, pp. 978–988, 2017. DOI: [10.1109/TUFFC.2017.2687521](https://doi.org/10.1109/TUFFC.2017.2687521).

[36] C. Papadacci, M. Pernot, M. Couade, M. Fink, and M. Tanter, "High-contrast ultrafast imaging of the heart", *IEEE Transactions on Ultrasonics, Ferroelectrics, and Frequency Control*, vol. 61, no. 2, pp. 288–301, 2014. DOI: [10.1109/TUFFC.2014.6722614](https://doi.org/10.1109/TUFFC.2014.6722614).

[37] Y. M. Hopf, B. Ossenkoppеле, M. Soozande, E. Noothout, Z. Y. Chang, H. J. Vos, J. G. Bosch, M. D. Verweij, N. de Jong, *et al.*, "A Compact Integrated High-Voltage Pulser Insensitive to Supply Transients for 3D Miniature Ultrasound Probes", *IEEE Solid-State Circuits Letters*, vol. 5, pp. 166–169, 2022. DOI: [10.1109/LSSC.2022.3180071](https://doi.org/10.1109/LSSC.2022.3180071).

[38] Y. Hopf, "Integrated circuits for 3d high-frame-rate intracardiac echocardiography probes", Ph.D. dissertation, 2023. DOI: [10.4233/UUID:7016E74D-C7DF-42A8-8257-11326940AD7F](https://doi.org/10.4233/UUID:7016E74D-C7DF-42A8-8257-11326940AD7F).

[39] D. S. Dos Santos, F. Fool, M. Mozaffarzadeh, M. Shabanimotlagh, E. Noothout, T. Kim, N. Rozsa, H. J. Vos, J. G. Bosch, *et al.*, "A Tiled Ultrasound Matrix Transducer for Volumetric Imaging of the Carotid Artery", *Sensors*, vol. 22, no. 24, p. 9799, 2022. DOI: [10.3390/s22249799](https://doi.org/10.3390/s22249799).

[40] R. J. McGough, "Rapid calculations of time-harmonic nearfield pressures produced by rectangular pistons", *The Journal of the Acoustical Society of America*, vol. 115, no. 5, pp. 1934–1941, May 2004. DOI: [10.1121/1.1694991](https://doi.org/10.1121/1.1694991).

[41] M. Shabanimotlagh, V. Daeichin, S. B. Raghunathan, P. Kruizinga, H. J. Vos, J. G. Bosch, M. Pertij, N. De Jong, and M. Verweij, "Optimizing the directivity of piezoelectric matrix transducer elements mounted on an ASIC", in *IEEE International Ultrasonics Symposium, IUS*, 2017, pp. 5–8. DOI: [10.1109/ULTSYM.2017.8091752](https://doi.org/10.1109/ULTSYM.2017.8091752).

[42] R. Wodnicki, D. N. Stephens, Q. Zhou, K. W. Ferrara, H. Kang, R. Chen, N. E. Cabrera-Munoz, H. Jung, L. Jiang, *et al.*, "Co-Integrated PIN-PMN-PT 2-D Array and Transceiver Electronics by Direct Assembly Using a 3-D Printed Interposer Grid Frame", *IEEE Transactions on Ultrasonics, Ferroelectrics, and Frequency Control*, vol. 67, no. 2, pp. 387–401, 2020. DOI: [10.1109/TUFFC.2019.2944668](https://doi.org/10.1109/TUFFC.2019.2944668).

[43] M. Celmer and K. Opielinski, "Research and modeling of mechanical crosstalk in linear arrays of ultrasonic transducers", *Archives of Acoustics*, vol. 41, no. 3, pp. 599–612, 2016.

[44] A. Bybi, D. Khoulli, C. Granger, M. Garouf, A. Mzerd, and A.-C. Hladky-Hennion, "Experimental characterization of a piezoelectric transducer array taking into account crosstalk phenomenon", *International Journal of Engineering and Technology Innovation*, vol. 10, no. 1, pp. 01–14, Jan. 2020. DOI: [10.46604/ijeti.2020.4348](https://doi.org/10.46604/ijeti.2020.4348).

[45] S.-C. Wooh and Y. Shi, "Optimum beam steering of linear phased arrays", *Wave Motion*, vol. 29, no. 3, pp. 245–265, Apr. 1999. DOI: [10.1016/s0165-2125\(98\)00039-0](https://doi.org/10.1016/s0165-2125(98)00039-0).

5

IMPROVING LATERAL RESOLUTION IN 3D IMAGING WITH MICRO-BEAMFORMING THROUGH ADAPTIVE BEAMFORMING BY DEEP LEARNING

This chapter has been published as:

Boudewine. W. Ossenkoppele, Ben W. Luijten, Deep Bera, Nico de Jong, Martin D. Verweij, and Ruud J.G. van Sloun, Improving Lateral Resolution in 3-D Imaging with Micro-beamforming through Adaptive Beamforming by Deep Learning, *Ultrasound in Medicine & Biology*, vol. 49, no. 1, pp. 237-255, 2023

*There is an increased desire for miniature ultrasound probes with small apertures to provide volumetric images at high frame rates for in-body applications. Satisfying these increased requirements makes simultaneously achieving a good lateral resolution a challenge. Since micro-beamforming is often employed to reduce data rate and cable count to acceptable levels, receive processing methods that try to improve spatial resolution will have to compensate the introduced reduction in focusing. Existing beamformers do not realize sufficient improvement and/or have a computational cost that prohibits their use. Here we propose to use Adaptive Beamforming by deep LEarning (ABLE) in combination with training targets generated by a large aperture array, which inherently has better lateral resolution. In addition, we modify ABLE to extend its receptive field across multiple voxels. We show that this method improves lateral resolution both quantitatively and qualitatively, such that image quality is improved compared to that achieved by existing Delay-and-Sum, Coherence Factor, Filtered-Delay-Multiplication-and-Sum and Eigen-Based Minimum Variance beamformers. We found that only *in silico* data is required to train the network, making the method easily implementable in practice.*

5.1. INTRODUCTION

Fast volumetric ultrasound imaging has become possible through the application of 2D ultrasound arrays. Having ultrasound elements in two dimensions enables receive focusing in the azimuth and elevational direction as well as applying wide unfocused transmit fields, such that few transmissions are needed to insonify a large field of view [1, 2]. However, the use of unfocused transmit beams comes at the expense of image contrast and reduces spatial resolution. This can be mitigated by coherent compounding of multiple angled unfocused transmissions or by using multiple narrower diverging waves. However, both come at the expense of the desired high frame rate.

Another concern in fast volumetric ultrasound imaging is that access to all transducer elements is usually not possible in matrix transducers, due to the very large numbers of elements they need to consist of to allow full spatial sampling both in azimuth and elevation. Transporting the data from all these elements to the back-end system becomes infeasible due to limitations in the number and bandwidth of cable connections. Sparse arrays, where only a limited number of elements in a 2D array are connected, have been proposed as a solution. However, reducing the number of active elements reduces image resolution, contrast and SNR with respect to fully populated matrix arrays. The cable connection and data rate problem of matrix transducers can be solved by employing micro-beamforming on in-probe ASICs at the cost of image quality [3–6]. This method reduces the number of channels by applying a set of pre-determined analogue delays to a sub-array of neighboring elements and subsequently summing the steered sub-array data into a single output. Data rate and channel reduction become an especially important concern for small aperture devices that can be used from within the body.

In-body ultrasound transducers allow visualizing parts of the body where ultrasound imaging would otherwise be hampered by attenuation, aberration and possible shadowing of the overlying tissues. For instance, transesophageal echocardiography (TEE) probes are mounted at the tip of a gastric tube such that images can be made from the esophagus where the probe is located within millimeters of the heart [7]. For patient safety and comfort, smaller TEE probes are desired [8, 9], which constrains the size of the ultrasound array. For intracardiac echography (ICE) [10, 11], where a catheter-based device is positioned inside the heart during interventional cardiology, the need for compact ultrasound arrays is especially apparent. Reducing the size of the imaging aperture, however worsens the lateral resolution and consequently image quality.

Satisfying the requirement of a small aperture, large field of view, volumetric image and high frame rate simultaneously, results in trade-offs in the imaging transmit-receive scheme that sacrifice spatial resolution. As a result the burden to achieve sufficient spatial resolution for in-body high frame rate 3D ultrasound devices, falls on the receive processing branch of the imaging chain.

The core step of the ultrasound image formation is beamforming, which transforms the received time-domain signals into an estimation of the acoustic reflectivity in the spatial domain. To improve image quality beyond the traditional low-complexity Delay-And-Sum (DAS) beamformer, various adaptive beamformers have been developed. The Coherence Factor (CF) based beamformer [12] reduces image clutter by reducing clutter from phase aberrations and has low computational complexity. Unfortunately it suf-

fers from artifacts in low SNR imaging scenarios [13], and a degraded speckle pattern. The Filtered-Delay-Multiply-And-Sum (F-DMAS) beamformer [14] involves a combinatorial coupling and multiplying of the received signals before summation. Prieur *et al.* [15] showed that the increased sensitivity to coherence of the F-DMAS beamformer contributes to improvements in contrast ratio and the depiction of coherent structures, but also comes with the drawbacks of grainier appearance and dark regions that can appear around coherent structures.

The minimum variance (MV) beamformer improves resolution by using a data-adaptive apodization of the aperture that minimizes the output energy of the signal while constraining the response to have unit gain at the focal point of the receive beam [16]. Further improving contrast without compromising the achieved resolution is possible with the Eigen-Based Minimum Variance beamformer (EBMV) [17]. However, there are a number of drawbacks to the application of MV beamforming. Firstly, the high computational burden resulting from the need to perform matrix inversion, and in the case of the EBMV beamformer also eigendecomposition, for every image pixel. This computational burden already limits practical application of EBMV-based methods for fast 2D imaging. For fast 3D imaging, where many more pixels need to be reconstructed to form a single frame, this becomes an even larger burden. Secondly, empirical tuning of parameters, such as diagonal loading and sub-aperture averaging is needed to achieve a good result across different imaging scenarios [18]. Thirdly, images reconstructed with EBMV can suffer from dark region artifacts next to hyperechoic structures [19]. Finally, the performance of (EB)MV beamforming has not been examined yet in combination with micro-beamforming.

Recently, deep learning techniques have also been employed to improve ultrasound image quality [20, 21]. Some have applied a neural network to transform an already beamformed gray-scale ultrasound image of low-quality to a high-quality image [22–27]. The downside of using images as input data to the neural network is that a lot of the acquired information present in the RF data has been discarded in the image formation process. As a result it is not available to the neural network. Therefore, others have avoided this by implementing deep neural networks not after image formation, but to replace the beamformer partially [28–32] or as a whole [33]. Replacing the complete beamforming process with a neural network [33, 34] means that the network also has to learn the geometric time-of-flight (TOF) correction. Therefore, many have instead implemented a neural network that replaces part of the beamforming process after the time-to-space migration [28–32, 35–37].

In 2D imaging deep learning solutions that replace part of the beamforming process after TOF correction achieved an improved resolution, while being data efficient in training and computationally efficient in reconstructing unseen ultrasound data [29, 32, 38]. The adaptive beamforming by deep learning (ABLE) method [32] and the Delay-And-Neural-Network (DANN) method [29] both employ a neural network on the channel data after time-of-flight correction, but replace slightly different parts of the beamforming process. The ABLE method explicitly calculates pixel-wise data-adaptive apodization weights from the channel data of that pixel. The DANN method instead uses convolutional layers to directly transforms the time-of-flight corrected RF-data into an axial line of pixel values, thereby replacing the beamsumming step. The method developed by

Luchies and Byram [30] also replaces the beamsumming step, but operates on the frequency domain instead. A frequency specific deep neural network is trained for each discrete Fourier transform bin. Subsequently, data is transformed back to the time domain and the filtered signals are summed along the aperture channels to form a beamformed image. Zhou *et al.* [38] sought to maintain the advantage of image-based methods that are able to capture global features, as well as the advantages of access to full RF-data. They combined a neural network that learns apodization weights with a neural network that works on an image-to-image basis in a hybrid approach. Their method is computationally efficient through reducing the needed pre- and post-processing steps such as envelope detection, but it loses some of the interpretability of ABLE were a generated pixel value can be directly linked to the the angular response (beampattern) formed by the generated apodization weights.

Other approaches have implemented a neural network after combination of the channel data, but before the final image formation steps of envelope detection and log compression. This includes methods that combine data from multiple transmissions, thereby replacing the compounding process [22, 39]. Applying deep learning in the beamforming process inherently requires access to the RF data, but gives the neural network access to a rich set of information that is not available when working on beamformed images. Methods that replace only part of beamforming process, after time-to-space migration, require smaller amounts of training data and less trainable parameters.

Training a deep-learning-based beamformer in a supervised fashion, requires target data. In some scenarios *in vivo* data can be used as part of the training set. For example, when deep learning is used to get the same high image quality as an existing beamformer at improved inference speeds or when the goal is to achieve the image quality of a full acquisition with an acquisition set-up that is compressed or under-sampled in some way. EBMV beamforming has been used as a method to obtain high-quality target images in 2D imaging [32, 38]. In other scenarios the training data consisted purely of simulations. One example includes training data where the target is directly based on the properties of the simulated medium [34, 40]. Other examples include a training target created by an ultrasound transducer with more desirable properties, such as a larger aperture [29], or higher frequency without increased attenuation [39]. A more complete overview of deep learning methods for ultrasound image reconstruction than described here can be found in Sloun *et al.* [21].

The ability of deep-learning-based beamformers to improve resolution has not been shown for 3D ultrasound imaging with matrix transducers in general or in combination with micro-beamforming in particular. This is not a trivial extension, since micro-beamforming prevents direct access to signals from all transducer elements by the back-end system. As a result the beamformer must work with the lower spatial sampling and focusing errors contained in the micro-beamformed signals. Inspired by the improved image quality in 2D imaging we hypothesize in this paper that the lateral resolution of volumetric ultrasound images, acquired by on-chip micro-beamforming, can be improved by using a deep-learning-based beamformer trained on target images formed by a larger aperture. Since little research has applied (EB)MV beamforming in 3D imaging with matrix transducers in general [41] and for micro-beamformed data in particular, we choose to use training targets generated by a larger aperture and thereby avoid

the limitations of existing adaptive beamformers. The ABLE beamformer is used as a starting point since it offers an data-efficient deep-learning-based solution to beamforming. ABLE operates on a per-pixel basis. However, we hypothesize that the pixel-based approach might be sub-optimal for handling the focusing errors present in micro-beamformed data and evaluate the effect of increasing the receptive field of the neural network to include the channel data of neighboring voxels. We moreover show the results achieved by using only simulation data to train the neural network and compare this with the results achieved when the training set also includes *in vitro* and *in vivo* data.

5.2. MATERIALS AND METHODS

5.2.1. NETWORK ARCHITECTURE

The deep-learning-based adaptive beamformer (ABLE) developed by Luijten *et al.* [32] is used as a basis for the neural network architecture used in this work. Thus, a neural network f_θ with a small number of layers is used to calculate apodization weights for each voxel from the time-of-flight corrected channel data. We maintain the per-pixel operation, where a beamformed pixel value $V_{\text{ABLE},k,l,m}$ is obtained by per-pixel multiplication of the apodization weights with the input data. However, we extend the receptive field of the network spatially, from the time-of-flight corrected RF data of a single voxel ($Y \in \mathbb{R}^{1 \times C}$) to a tensor that contains the RF data of a small group of voxels ($Y \in \mathbb{R}^{Az \times El \times Ax \times C}$):

$$\begin{aligned} V_{\text{ABLE},k,l,m} &= \sum_{c=1}^C [f_\theta(Y_{k:k+Az-1, l:l+El-1, m:m+Ax-1}) Y_{k,l,m,c}] \\ V_{\text{ABLE},k,l,m} &= \sum_{c=1}^C [f_\theta(Y)_{k,l,m,c} Y_{k,l,m,c}]. \end{aligned} \quad (5.1)$$

Here Az , El and Ax are the receptive field of the neural network in azimuth, elevational and axial direction respectively, denoting the size of the group of neighboring voxels whose TOF corrected RF data influences the computed apodization weights for a single voxel. We increase the receptive field, since micro-beamformed data is sub-optimally focused. Even when the micro- and postbeamforming delays are applied perfectly, errors occur in TOF correction, since focusing has a range dependent component, which can no longer be implemented accurately for each individual element after applying the static micro-beamforming delays and the summing operation. For some transducer elements a slightly later or earlier sampling of the raw RF data is more accurate. The TOF corrected data of neighboring pixels consists of raw RF data that has been sampled with slightly larger or smaller delays due to the slightly different distances between these voxels and the transducer elements. Therefore, we consider that the network might make use of the increased information that is available from the TOF data of a broader region of voxels to generate a better estimation of apodization weights.

The receptive field is extended by using convolutional layers. Each layer contains a number of 3-D convolutional kernels, as shown in Figure 5.1, which work along the spatial dimensions. The network remains fully connected along the channel dimension,

across which the encoder-decoder structure is preserved. Zero-padding is used to avoid compression in the spatial dimensions.

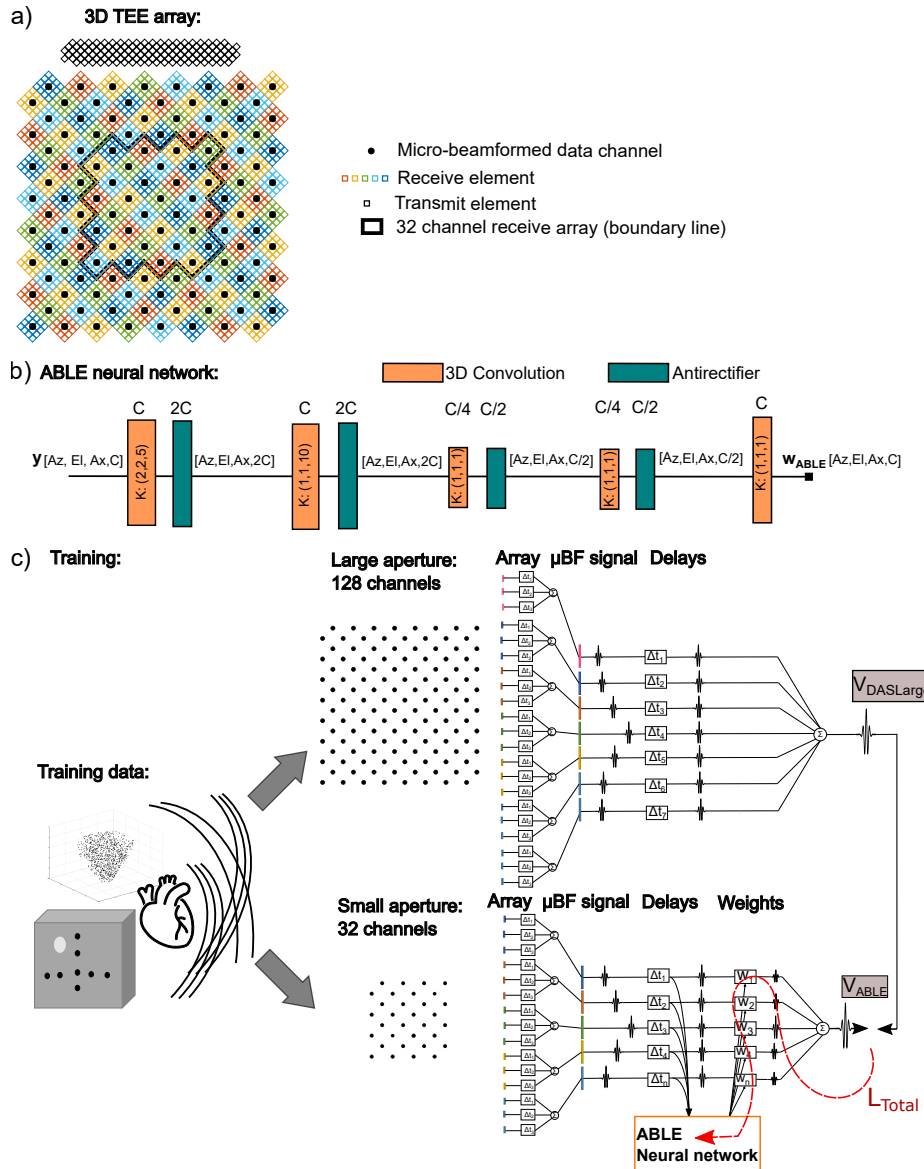


Figure 5.1: *a*) The layout of the 3D TEE probe with split transmit receive design. The large receive aperture of 2048 elements is combined into 128 data channels through micro-beamforming with 4x4 sub-arrays. *b*) The modified ABLE network consists of 3D convolutional layers and antirectifier activation functions. The number of channels $C = 32$. The kernel size K is indicated in the convolutional layers. *c*) RF data of *in silico*, *in vitro* and/or *in vivo* data is acquired. All 128 channels are used to DAS beamform target images. Time-of-flight corrected RF data from the 32 centre channels is used as input to the ABLE neural network. The network is trained by backpropagation based on the loss value between V_{ABLE} and the target V_{DASLarge} .

We evaluated the effect of receptive field size using four networks with different receptive field size, but the same number of layers. ABLE1 has a single voxel receptive field, similar to the original ABLE network. For the other three networks we chose an axial receptive field size that extends 14 voxels (about 1.75 wavelengths). To see the impact of increasing the receptive field in lateral direction we set the azimuthal and elevational receptive field of ABLE2, ABLE3 and ABLE4 to 2, 3 and 6 voxels respectively (where one voxel has a width of 0.5°). The architecture of ABLE2 is shown in Figure 5.1 and all architectures are shown in the Appendix.

Identical to the original ABLE [32], the antirectifier is chosen as the activation function:

$$g(\mathbf{z}) = \begin{cases} \max\left(0, \frac{\mathbf{z} - \mu_z}{\|\mathbf{z} - \mu_z\|_2}\right) \\ \max\left(0, -\frac{\mathbf{z} - \mu_z}{\|\mathbf{z} - \mu_z\|_2}\right) \end{cases}, \quad (5.2)$$

since it avoids losing the negative signal components, by concatenating the positive and negative components of the signal after l_2 -normalization and then returning their absolute value. At the same time it maintains the favorable properties of computational efficiency and resistance against vanishing gradients that ReLus have and since the activation function is not bounded it helps preserve the dynamic range of the input. Inspired by the lack of summation terms in the calculation of apodization weights by the minimum variance beamformer we have not used bias terms in our network.

5

5.2.2. TRAINING SET-UP

We used supervised learning, with high-resolution training targets that were generated by DAS beamforming with a larger aperture array V_{DASLarge} . The loss function $\mathcal{L}_{\text{total}}$ consists of a weighted combination of an image loss $\mathcal{L}_{\text{SMSLE}}$ based on the pixel values and a loss based on the apodization weights $\mathcal{L}_{\text{unity}}$:

$$\mathcal{L}_{\text{total}} = \frac{1}{I} \sum_{i=1}^I \lambda \mathcal{L}_{\text{SMSLE}}(V_{\text{ABLE}}^{(i)}, V_{\text{DASLarge}}^{(i)}) + (1 - \lambda) \mathcal{L}_{\text{unity}}(V_{\text{ABLE}}^{(i)}, V_{\text{DASLarge}}^{(i)}) \quad (5.3)$$

Here $V_{\text{ABLE}}^{(i)}$ and $V_{\text{DASLarge}}^{(i)}$ refer to respectively the network outputs and targets for a voxel i . To take into account the large dynamic range and both positive and negative components of the ultrasound signal, the image loss is computed as the signed-mean-squared-logarithmic error (SMSLE) between a target voxel (V_{DASLarge}) and the voxel calculated by ABLE (V_{ABLE}):

$$\begin{aligned} \mathcal{L}_{\text{SMSLE}}^{(i)} = & \frac{1}{2} \|\log_{10}(V_{\text{ABLE}}^{(i)})^+ - \log_{10}(V_{\text{DASLarge}}^{(i)})^+\|_2^2 + \\ & \frac{1}{2} \|\log_{10}(V_{\text{ABLE}}^{(i)})^- - \log_{10}(V_{\text{DASLarge}}^{(i)})^-\|_2^2, \end{aligned} \quad (5.4)$$

where $(\cdot)^+$ and $(\cdot)^-$ denote the magnitude of a positive and negative value respectively. At the same time we promote a distortionless response with the $\mathcal{L}_{\text{unity}}$ loss term:

$$\mathcal{L}_{\text{unity}}^{(i)} = |\mathbf{I}^T \mathbf{w}_{\text{ABLE}}^{(i)} - 1|^2 \quad (5.5)$$

Stochastic optimization of (5.3) was done using the Adam optimizer with a learning rate of $\alpha = 10^{-3}$. The exponential decay rate for the first and second moment, $\beta_1 = 0.9$ and $\beta_2 = 0.999$, were set according to the values suggested by [42] and the constant for numerical stability was $\hat{\epsilon} = 10^{-7}$. All networks were trained for 400 epochs and evaluated based on the snapshot ensemble of the last 5 epochs. The network was implemented using Keras API with a Tensorflow (Google, CA, USA) backend.

5.2.3. TRAINING DATA ACQUISITION

Data was acquired with a miniature TEE prototype transducer, described in detail in Bera *et al.* [43]. The full array consists of 2176 PZT elements, with a pitch of 181 μm and a 30 μm kerf, which was cut at a 45° angle with respect to the probes center line. The aperture is split in a narrow transmit array of 128 elements, which are directly wired out to the external ultrasound system and a larger receive array of 2048 elements (see Figure 5.1). The signals of the receive array are micro-beamformed by the front-end ASIC in sub-arrays of 4 x 4 elements. The full receive aperture, consisting of 128 micro-beamformed data channels, was used to acquire the large aperture target data, while the center 32-micro-beamformed data channels (see Figure 5.1), were used to acquire the small aperture input data from the same transmit firing made by the narrow transmit array.

Each 60° x 60° volume was acquired with 85 steered transmit-receive events. A wide transmit beam, produced from a virtual source located at 100 mm behind the transducer, was steered to a combination of one of the 17 equally spaced azimuth angles between -24° and 24° degrees and one of the 5 equally spaced elevation directions between -20° and 20°. Micro-beamformed datasets were acquired by pre-steering the sub-arrays of the receive aperture to the transmission direction.

In vivo AND in vitro

Micro-beamformed datasets were acquired with the TEE probe and a Verasonics ultrasound acquisition system, which sampled the data at 20 MHz. A commercial tissue phantom (multi-purpose multi-tissue ultrasound phantom 040-GSE, CIRS, Norfolk, VA, USA) was used to acquire images of wire targets, hyper- and hypoechoic cysts. *In vivo* images of the heart of an anesthetized adult pig were acquired through a hole in the chest wall and the diaphragm by an experienced cardiologist, as described in more detail in [43] (This experiment was approved by the Erasmus MC Animal Experiments Committee Protocol 109-14-12).

In silico

Simulated RF-data was acquired by implementing the transducer geometry and imaging scheme in Field II [44, 45]. Two types of simulation phantoms were used. In the first, point scatterers were randomly distributed, with either 500 or 1000 scatterers in a volume. In the second type, cubes and spheres with fully developed speckle (10 scatterers per resolution cell) and a varying average amplitude (0-60 dB) and size (2-6 mm) were distributed against an hypoechoic background.

5.2.4. TRAINING DATA PREPARATION

All *in silico*, *in vitro* and *in vivo* data was split into training, validation and test data. Of the recorded porcine heart data, volumes acquired at different stages of the cardiac cycle were used in the training, validation and test data. Of the *in vitro* data the volumes used in the training, validation and test data were acquired at different non-overlapping positions on the CIRS phantom. Of the *in silico* data, the validation volumes contained different random scatterer locations compared to the training volumes. The volume used in the test set was constructed to have a more structured pattern of scatterers than that in the training and validation data, to facilitate the evaluation of ultrasound imaging related metrics. A single acquired volume of (TOF corrected) RF data provides a large amount of training data for the network, since the loss is calculated per individual pixel and the receptive field of the used neural networks are small. As a result, only a small number of volumetric acquisitions was needed to realize a sufficient amount of training data for the network. The training set consisted of five training volumes with a 60° x 60° opening angle and a depth varying between 4.6 and 8.0 cm. Three *in silico* training volumes were used in the first training set. In a second training set an *in vitro* volume was added and in a third training set an *in vivo* volume was added as well. When training on a combination of *in silico*, *in vitro* and/or *in vivo* data it was made sure that there was an equal probability of sampling training data patches from each of these data types. For each training set validation data was of the same types (*in silico*, *in vitro*, *in vivo*) as the training data. Each batch consisted of 16 randomly selected patches of training data. A patch consisted of an imaging region of 10x10x600 target pixels created by DAS beamforming with the large array and the corresponding input TOF corrected RF data recorded with the small array (input size single patch: 10x10x600x32). All values were pre-normalized with respect to the maximum of the volumetric image that they are part of, such that all values are between -1 and +1.

5.2.5. COMPARISON TO OTHER BEAMFORMERS

We compared the ABLE beamformers to the DAS beamformer as well as three adaptive beamformers: EBMV, CF and F-DMAS. For all methods the same pre- and post-processing steps were used. Before beamforming, a bandpass filter with a 5 MHz center frequency and 100% bandwidth was applied to the acquired signals. After beamforming and envelope detection of the data from the 85 transmit-receive events, the final volume was obtained as an angle-weighted combination of overlapping sub-volumes [43]. Finally the data was log-compressed to gray scale images with a dynamic range of 60 dB.

The first step of the beamforming process, the TOF correction was also the same for all beamformers. Based on the geometric relation between the voxel location and transducer channel locations, the delay needed to focus the signal received by a channel c , to an image point r , is given by:

$$\tau[x, y, z] = \frac{\| \mathbf{r}_{TX} - \mathbf{r} \|_2 + \| \mathbf{r}_c - \mathbf{r} \|_2}{v}. \quad (5.6)$$

Here v is the estimated speed of sound in the medium, \mathbf{r}_c is the location of the receive channel and \mathbf{r} is the voxel location. \mathbf{r}_{TX} is the location of the transmit firing, which for our diverging wave transmissions is specified by the coordinates of the virtual source

that it emanates from. For any focus point $[x, y, z]$ and channel c , the delayed response, y_c , is then given by

$$y_c[x, y, z] = x_c(\tau[x, y, z]), \quad (5.7)$$

where x_c is the received channel data.

DELAY-AND-SUM

Image voxels $V_{\text{DAS}}(x, y, z)$ are generated by summing across the channel dimension according to

$$V_{\text{DAS}}[x, y, z] = \mathbf{w}_{\text{DAS}}^T[x, y, z] \mathbf{y}[x, y, z], \quad (5.8)$$

where \mathbf{y} is the delayed response for all channels. Here the weight vector \mathbf{w}_{DAS} consists of predetermined data-independent weights, which can vary spatially. Here we used a boxcar window to emphasize resolution.

MINIMUM VARIANCE BASED ADAPTIVE BEAMFORMING

The minimum variance distortionless response beamformer applies time-of-flight correction in the same way as the DAS beamformer, but aims to improve image resolution and contrast by replacing the static apodization weights, used in DAS, with a set of data-adaptive apodization weights. These apodizations weights \mathbf{w}_{MV} are chosen to minimize the variance of the beamformed signal, such that interfering signals and noises are rejected, while maintaining a unity gain with respect to the signal from the beamformers focusing point. The optimal apodization weights are found by minimizing

$$\min_{\mathbf{w}_{\text{MV}}} \mathbf{w}_{\text{MV}}^H \mathbf{R} \mathbf{w}_{\text{MV}} \quad \text{s.t.} \quad \mathbf{w}_{\text{MV}}^H \mathbf{d} = 1, \quad (5.9)$$

which has an analytical solution [46] given by:

$$\mathbf{w}_{\text{MV}} = \frac{\mathbf{R}^{-1} \mathbf{d}}{\mathbf{d}^H \mathbf{R}^{-1} \mathbf{d}}. \quad (5.10)$$

Here \mathbf{d} is the so-called steering vector, which defines the signal that should be passed distortionless. For narrow-band applications this steering vector can be expressed as a complex exponential applying the required phase shifts, however for broadband applications this is not possible and we work with signals that are already time-of-flight corrected, as such the steering vector simply becomes $\mathbf{d} = \mathbf{1}^C$ [16]. \mathbf{R} is the spatial covariance matrix:

$$\mathbf{R} = \mathbb{E}[\mathbf{y}^H \mathbf{y}] \quad (5.11)$$

In practice the spatial covariance matrix $\mathbf{R}[x, y, z]$ must be estimated from a single or a small number of temporal samples, since the received signals change rapidly in time. To increase the robustness of the estimation of the sample covariance matrix, we applied spatial smoothing [47] and diagonal loading as described in Synnevåg *et al.* [48]. We used a diagonal loading of 0.001 and sub-array length of 16.

Eigen-Based Minimum Variance beamformer (EBMV) applies an additional update step on the apodization weights to further improve contrast and resolution [17]. The

weights of the EBMV beamformer are calculated by taking the eigendecomposition of \mathbf{R} and projecting the signal subspace $\mathbf{E}_{\text{signal}}$ on the weights determined by (5.10):

$$\mathbf{w}_{\text{EBMV}}[x, y, z] = \mathbf{E}_{\text{signal}}[x, y, z] \mathbf{E}_{\text{signal}}^H[x, y, z] \mathbf{w}_{\text{MV}}[x, y, z]. \quad (5.12)$$

COHERENCE FACTOR

The Coherence Factor weighting method also applies data-adaptive weights per-pixel. However, in contrast to the EBMV the calculated pixel-based weights are identical across channels. As such CF can also be viewed as a post-filter that is applied after a DAS (or another) beamformer. The CF weights are determined as the ratio between the coherent and incoherent energy received by the array [12]:

$$w_{\text{CF}}[x, y, z] = \frac{|\sum_{c=1}^{c=C} y[x, y, z, c]|^2}{\sum_{c=1}^{c=C} |y[x, y, z, c]|^2}. \quad (5.13)$$

Here C is the total number of channels in the aperture. The final voxel value is given by

5

$$V_{\text{CF}}[x, y, z] = w_{\text{CF}}[x, y, z] V_{\text{DAS}}[x, y, z]. \quad (5.14)$$

F-DMAS

The F-DMAS beamformer applies a pairwise multiplication of the signals. The signed square root is first applied to the signal pairs to ensure a correct scaling of the final pixel value $V_{\text{F-DMAS}}$:

$$V_{\text{F-DMAS}} = \sum_{i=1}^{C-1} \sum_{j=i+1}^C \text{sign}(y_i y_j) \sqrt{|y_i y_j|} \quad (5.15)$$

The resulting signal now has additional frequency components at zero and twice the center frequency, therefore the signal is bandpass filtered around the second harmonic to remove the DC component [14].

5.2.6. ALGORITHMIC COMPLEXITY

We exclude in the computational complexity calculation the part that is similar to all adaptive beamformers that were used: time-of-flight-correction, multiplication of the apodization weights and subsequent summation along the channels, envelope detection and log compression. We calculate the number of floating point operations (FLOPs) required for a single voxel, for the ABLE and EBMV beamformer. The version of the ABLE network that we used consisted of convolutional layers and antirectifiers. The amount of FLOPs required for an antirectifier layer is 4 times the number of nodes in that layer. The computational complexity (F) of a convolutional layer depends on the number of nodes N in the layer and the number of elements in the convolutional kernel K . The total computational cost of the convolutional version of the ABLE network with L layers becomes:

$$F_{\text{ABLEconv}} = \sum_{l=1}^{L-1} [2N_{\text{in}_l} N_{\text{out}_l} K_l + 4N_{\text{out}_l}] + 2N_{\text{in}_L} N_{\text{out}_L} K_L \quad (5.16)$$

The number of nodes is linearly related to the number of channels C . Thus, the computational complexity is order $\mathcal{O}(C^2)$.

The DAS and CF beamformer have a computational complexity of order $\mathcal{O}(C)$. Although the computational complexity of the F-DMAS beamformer as stated in Equation 14 is of order $\mathcal{O}(C^2)$ it can be reformulated such that it also reduces to order $\mathcal{O}(C)$ [49]. The components dominating the computational complexity of the EBMV beamformer are the inversion and eigendecomposition of the covariance matrix \mathbf{R} , which both use approximately C^3 FLOPS [18], making the computational complexity order $\mathcal{O}(C^3)$. The computational complexity of the EBMV beamformer is calculated as described in Luijten *et al.* [32].

5.2.7. EVALUATION CRITERIA

The Full-Width-at-Half Maximum (FWHM) of simulated point scatterers and *in vitro* wire targets (locations are shown in Figure 5.2) is used to evaluate resolution in elevation and azimuth. Contrast is evaluated with the Contrast-Ratio (CR) and Contrast-to-Noise Ratio (CNR) as well as the generalized Contrast-to-Noise ratio (GCNR). A high- and low-intensity region (see Figure 5.2) are selected in the *in silico* and *in vitro* images for evaluation. The CR and CNR are calculated by

$$CR = \frac{|\mu_L - \mu_H|}{(\mu_L + \mu_H)/2} \quad (5.17)$$

$$CNR = \frac{|\mu_L - \mu_H|}{\sqrt{\sigma_L^2 + \sigma_H^2}}, \quad (5.18)$$

where μ_L and μ_H are the mean voxel value of the low and high intensity region (V_L, V_H) respectively and σ_L and σ_H are the variances of the regions.

It is possible to change CR and CNR values with trivial dynamic range alterations, without image quality improvements that improve clinical value [50]. As such, we also include the GCNR metric which is shown to be resistant to such effects [51]. The GCNR determines the success rate that can be expected from an ideal observer at the task of separating the pixels from two different regions and values are always between 0 and 1. The GCNR is calculated according to

$$GCNR = 1 - \sum_{n=1}^N \min [h_n(V_L), h_n(V_H)], \quad (5.19)$$

where h_L and h_H represent the histogram of the voxel values of the low and high intensity region respectively and N is the number of bins in the histogram. Hyun *et al.* [52] showed that it is important to choose a bin size that is not too fine or too coarse to get a valid estimate of the GCNR. We have chosen the number of bins as the square root of the number of pixels in the low (or high) intensity region and examined the histograms to check that the sampling was appropriate.

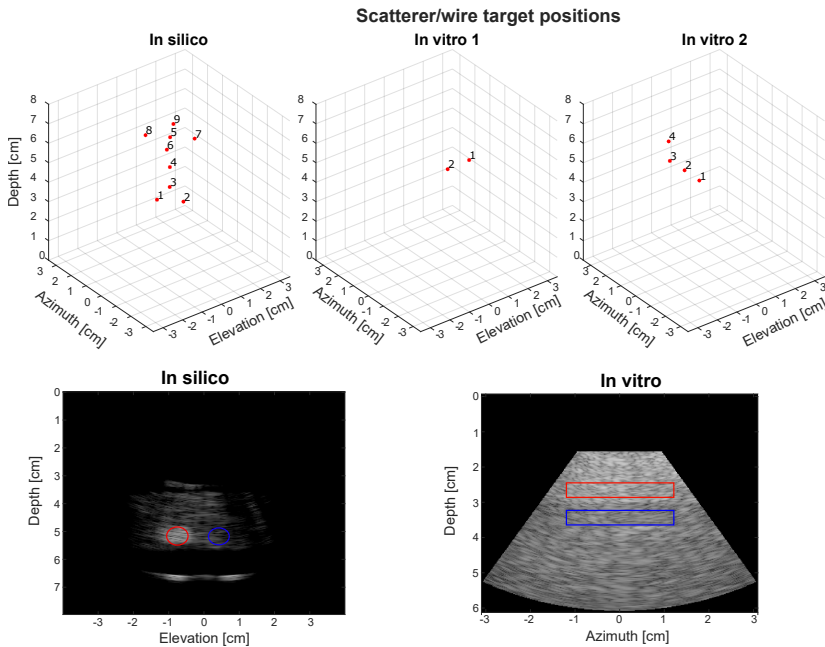
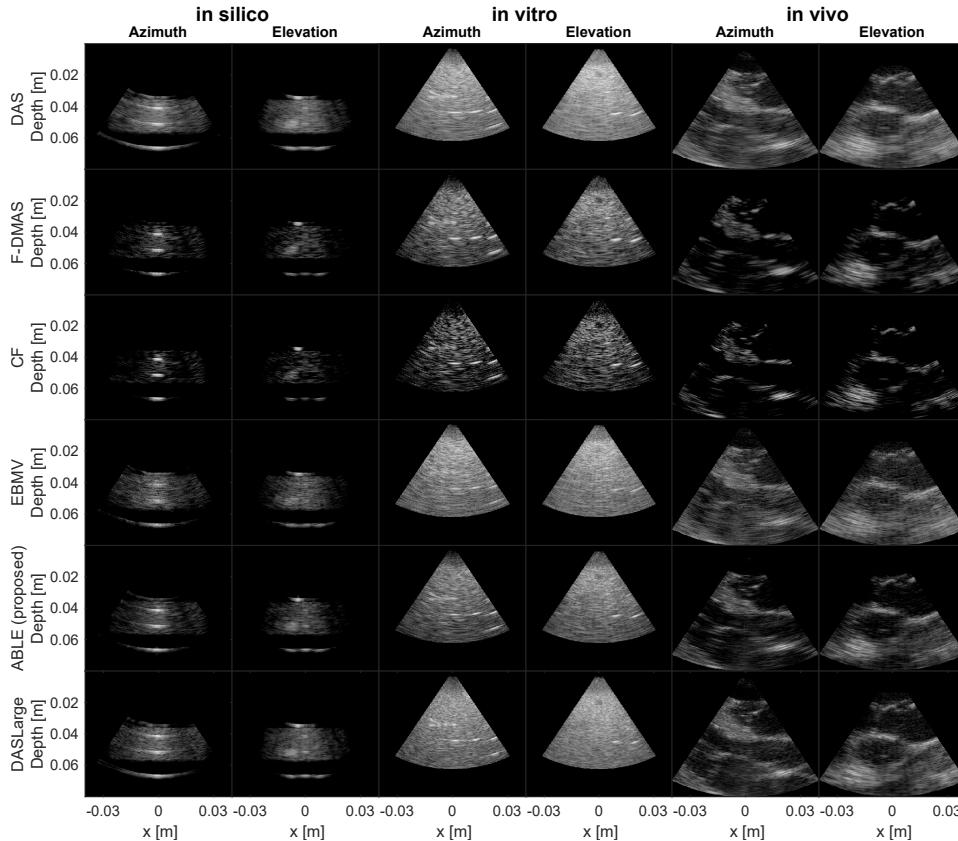


Figure 5.2: a) The nine scatterer locations used to evaluate the *in silico* resolution. b) The six scatterer locations used to evaluate *in vivo* resolution. c) The high and low intensity regions used to evaluate contrast metrics.

5.3. RESULTS

Elevation and azimuth slices of the 3D images that were obtained for the small array by beamforming with DAS, F-DMAS, CF, EBMV and the ABLE method trained on *in silico* data are shown in Figure 5.3, next to DAS beamformed images of the larger array (DASLarge). Additional image views from a single *in vivo* volume can be seen in Figure 5.4. The average FWHM of the scatterers in the *in silico* and *in vitro* data are summarized in Table 5.1. When averaging the FWHM across *in silico* and *in vitro* data and across both lateral directions, we see that the average FWHM of ABLE is only 62% of the average FWHM of DAS, 79% of that of F-DMAS and 81% of that of CF. The resolution improvement of ABLE is also clear from Figure 5.5, which shows C-planes of wire targets and simulated scatterers. The average FWHM of EBMV for the pointscatterers considered is 3.7° , which is smaller than the 6.3° achieved by ABLE when trained on *in silico* data and the 6.6° of DASLarge. However, if we look closer at Figure 5.3 then we see that the points lose consistency in their shape. Furthermore, the normalized beamprofiles along *in vitro* and *in silico* scatterers (see Figure 5.6), show that the use of the EBMV beamformer results in an erratic beamprofile. On the other hand the beamprofile reconstructed by ABLE shows smooth behavior, similar to the DAS beamformers. While ABLE also qualitatively improves resolution in the *in vivo* image (see Figure 5.3 and 5.4), this is not the case for the EBMV beamformed image. Table 5.1 shows that *in vitro* the GCNR of ABLE when trained on *in silico* data is 0.56, which is marginally lower than the GCNR of 0.59 for DAS, while *in silico* the GCNR of ABLE is 0.87, which is marginally higher than

the 0.85 of DAS. The GCNR of F-DMAS and CF is close to that of DAS and ABLE *in silico*. However on *in vitro* data, even though the CR is improved for F-DMAS and CF compared to DAS and ABLE, the CNR and GCNR are not. Specifically, the GCNR of F-DMAS is only 0.45 and that of CF is only 0.34 which is lower than the GCNR of ABLE which is 0.56.



5

Figure 5.3: Azimuth and elevation slices of an *in silico* and *in vitro* phantom as well as *in vivo* porcine heart data are shown for the DAS, CF, F-DMAS, EBMV and the proposed beamformer. In the *in silico* volume simulated point scatterers are visible both in an anechoic region and surround by other scatterers forming an hyperechoic region. The target DAS image formed by the larger array is shown on the last line. The images are shown for a dynamic range from -60 to 0 dB.

If we look closer at the speckle statistics in Figure 5.7, then we can see that after subtraction of the mean, the probability density function of the log-compressed pixel values, is very similar for DAS and DASLarge. The speckle distribution of CF is clearly skewed with a heavy tail, while that of F-DMAS is broader than that of DAS. Both the EBMV and ABLE image only have a slightly skewed distribution with respect to DAS. Figure 5.8 shows the apodization pattern calculated by ABLE for an image line where only background scattering is present and for an image line where a highly scattering wire target is present. For the voxels aligned with the wire target ABLE clearly selects different apodization weights than for the voxels aligned with background scattering. This

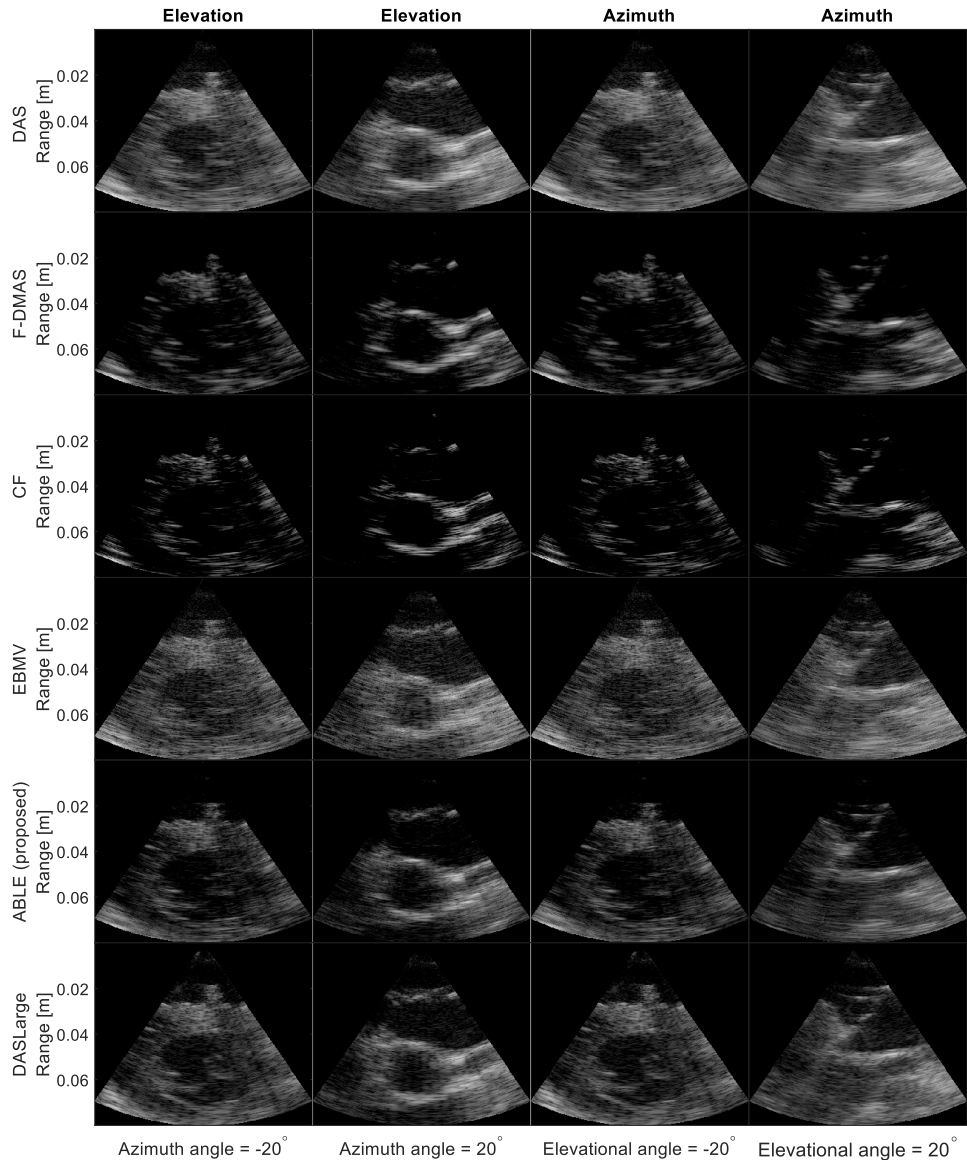


Figure 5.4: Azimuth and elevation slices of an *in vivo* procine heart are shown for the DAS, CF, F-DMAS, EBMV and the proposed beamformer. The images are shown for a dynamic range from -60 to 0 dB.

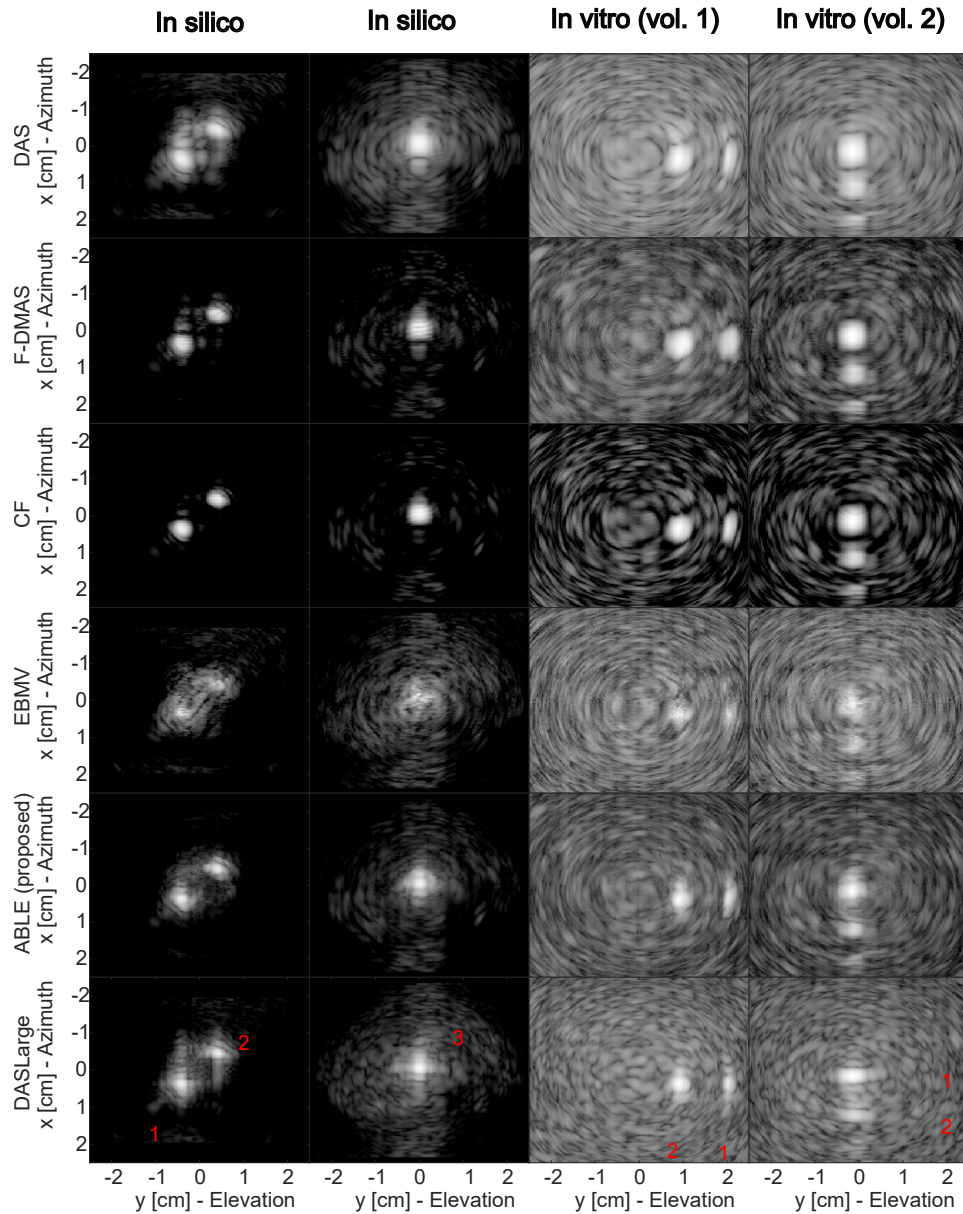


Figure 5.5: C-planes of an *in silico* and *in vitro* phantom. The images are shown for a dynamic range from -60 to 0 dB.

Table 5.1: Image quality metrics.

	DAS	F-DMAS	CF	EBMV	DASLarge	ABLE (<i>in silico</i>)	ABLE (<i>in silico</i> + <i>vitro</i>)	ABLE (<i>in silico</i> + <i>vitro</i> + <i>vivo</i>)
FWHM El [$^{\circ}$] <i>in silico</i>	8.1 +/- 0.6	7.7 +/- 0.8	6.7 +/- 0.4	4.7 +/- 1.8	5.6 +/- 0.2	5.1 +/- 0.3	5 +/- 0.4	5.7 +/- 0.6
FWHM Az [$^{\circ}$] <i>in silico</i>	10.4 +/- 0.7	4 +/- 2.3	7.7 +/- 0.6	2.3 +/- 1	6.4 +/- 0.5	6.6 +/- 0.4	5.8 +/- 0.8	6.7 +/- 0.5
GCNR [-] <i>in silico</i>	0.85	0.89	0.83	0.69	0.92	0.87	0.9	0.87
CNR [-] <i>in silico</i>	1.67	1.38	1.27	1.04	1.5	1.58	1.64	1.62
CR [-] <i>in silico</i>	1.44	1.69	1.8	1.25	1.51	1.55	1.52	1.47
FWHM El [$^{\circ}$] <i>in vitro</i>	9.7 +/- 1.3	9 +/- 1.3	7.8 +/- 0.8	4.3 +/- 1.7	7.6 +/- 1.2	6.1 +/- 0.7	6.6 +/- 0.5	7.4 +/- 0.7
FWHM Az [$^{\circ}$] <i>in vitro</i>	12.4 +/- 1.1	11.1 +/- 0.8	9 +/- 0.3	3.3 +/- 1.5	6.9 +/- 0.5	7.3 +/- 0.5	8.1 +/- 0.5	8.4 +/- 0.4
GCNR [-] <i>in vitro</i>	0.59	0.45	0.34	0.38	0.61	0.56	0.54	0.53
CNR [-] <i>in vitro</i>	1.11	0.75	0.57	0.68	1.1	0.96	1	0.95
CR [-] <i>in vitro</i>	0.75	0.83	0.91	0.56	0.79	0.81	0.77	0.74

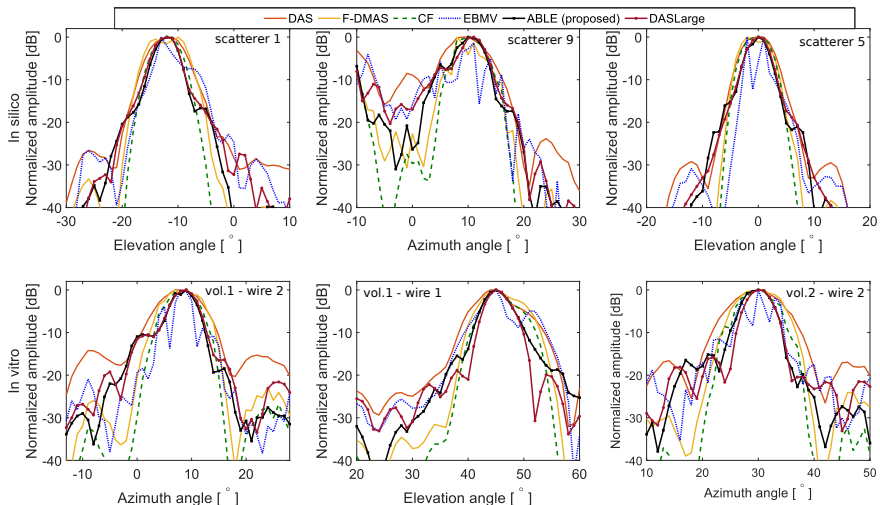


Figure 5.6: Beamprofiles around *in vitro* wire targets and *in silico* scatterers when beamformed with DAS, CF, F-DMAS, EBMV, the proposed ABLE method for the small array as well as the large array DAS target. (The probe was not rotated to produce the different imaging planes).

confirms that ABLE after training on large aperture targets, does not simply apply an advantageous manipulation of the dynamic range, but modifies the apodization weights

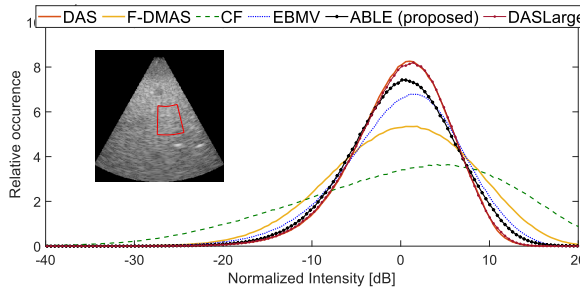


Figure 5.7: The probability density function of the log-compressed pixel values after subtraction of the mean for the DAS, CF, F-DMAS EBMV, proposed ABLE and larger array DAS target beamformers.

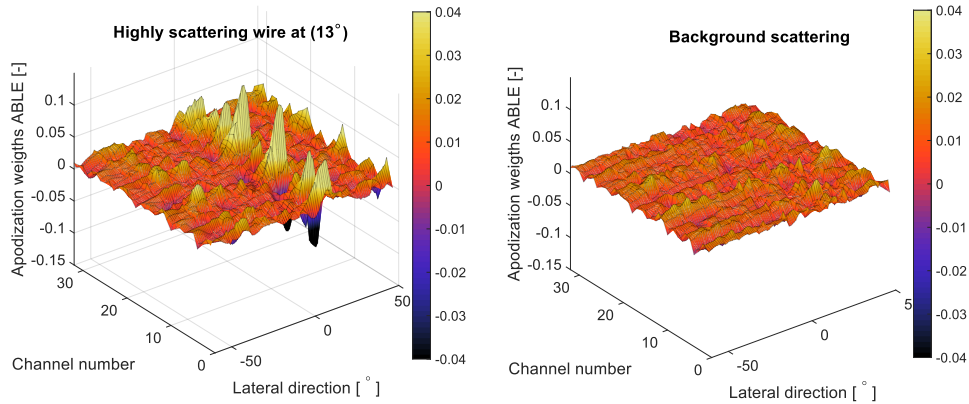


Figure 5.8: Apodization weights that ABLE assigns to the data channels for different image locations of the CIRS phantom, containing either a wire target or background scattering.

and thereby the beampattern based on the received data.

5.3.1. PERFORMANCE COMPARISON MODIFIED ABLE - TRAINING DATA

Figure 5.9 and the last three columns of Table 5.1 show the performance of ABLE when the neural network is trained only on *in silico* data and when *in vitro* and *in vivo* data are added to the training set. The average FWHM of ABLE is 6.3° when only *in silico* training data is used, which is marginally better than the 6.4° that is achieved when *in vitro* data is added to the training set, while further adding *in vivo* data to the training set worsens the average FWHM more significantly to 7.1° . When ABLE is trained on *in silico* data the average FWHM is 95% of the FWHM of the DASLarge target and the FWHM of ABLE remains marginally better than the target at 96% of the FWHM of DASLarge when *in vitro* data is added to the training set of ABLE. A very slight improvement of *in silico* GCNR from 0.87 to 0.9 is visible when adding *in vitro* data to the training set, but adding *in vivo* data as well decreases the GCNR again to 0.87. Meanwhile a very slight decrease of *in vitro* GCNR from 0.56 to 0.54 is visible when adding *in vitro* data to the training set and adding *in vivo* data decreases it slightly further to 0.53.

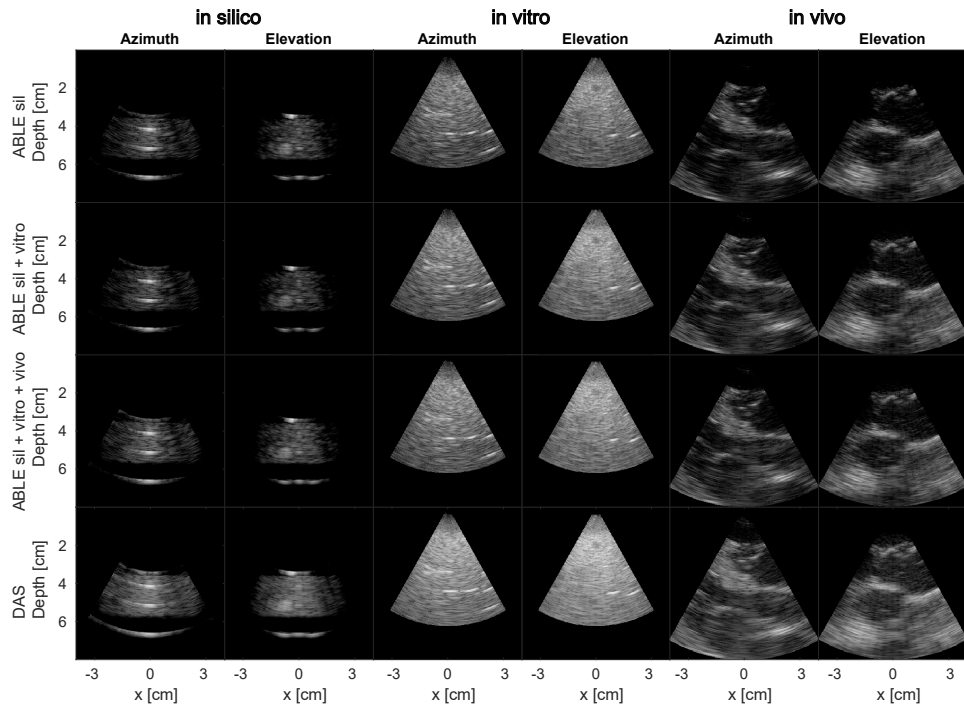


Figure 5.9: Azimuth and Elevation slices of an *in silico* and *in vitro* phantom as well as *in vivo* porcine heart data are shown for the ABLE beamformer when trained on either *in silico* data, *in silico* + *in vitro* data, or *in silico* + *in vitro* + *in vivo* data. In the bottom row the DAS beamformer is shown for comparison. The images are shown for a dynamic range from -60 to 0 dB.

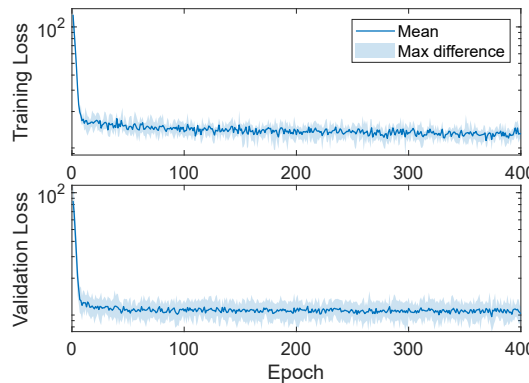


Figure 5.10: Mean and max difference in training and validation loss when training ABLE2 five times on different training data sets.

5.3.2. PERFORMANCE COMPARISON ABLE - RECEPTIVE FIELD SIZE

Figure 5.10 shows the variability in the training and validation loss of ABLE2 trained on *in silico* for five training runs with a different set of training and validation data. The

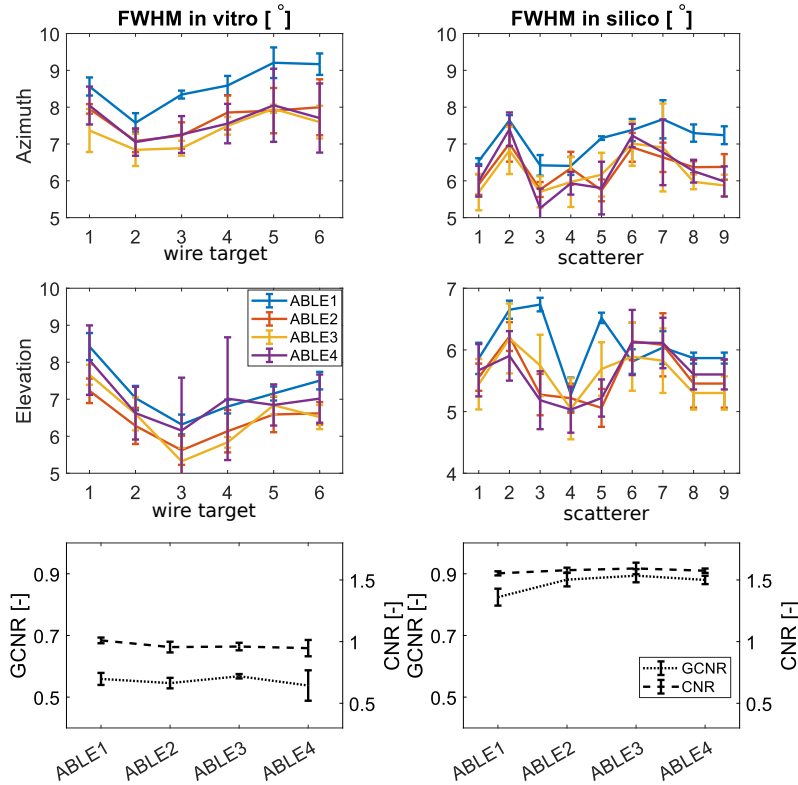


Figure 5.11: The achieved *in vitro* FWHM per scatterer and GCNR and CNR as achieved by ABLE beamformers with different receptive field sizes. (Full network architectures are given in Figure 5.13. Error bars indicate the standard deviation for five networks trained on five sets of training data. The mean GCNR and CNR are determined over a single hypoechoic region.

effect of the variability of five different training runs on the estimated FWHM can be seen in Figure 5.11, where the FWHM, GCNR and CNR are shown for ABLE1-4. Figure 5.11 shows that increasing the receptive field of the neural network from a single voxel (ABLE1) to a larger field of view (ABLE2-4) improves performance in terms of *in vitro* and *in silico* lateral FWHM. The average FWHM *in vitro* is 6.7° for ABLE2 while it is 7.9° for ABLE1. Increasing the lateral receptive field from two to three or six voxels has no clear benefit on the achieved lateral resolution.

The effect of receptive field size on contrast is overall less clear (see Figure 5.11). CNR and GCNR decrease slightly on *in vitro* data when increasing the receptive field from a single voxel, while increasing slightly on *in silico* data. Figure 5.12 shows that the increased performance of ABLE2 w.r.t. ABLE1 comes at the cost of greater algorithmic complexity. For the case of a 128 channel probe the computational cost of ABLE2 would still be below that of EBMV. However for 32 channels the algorithmic cost of ABLE2 is

about equal to that of EBMV.

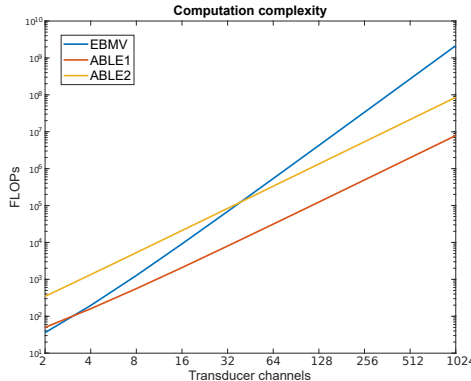


Figure 5.12: The number of FLOPS needed to calculate apodization weights for a single voxel with ABLE1, ABLE2 and EBMV.

5.4. DISCUSSION

In this study we used a modified ABLE beamformer and training data that consisted of RF signals as input and targets formed by a larger aperture matrix array. With the proposed method we were able to improve the lateral resolution of volumetric ultrasound images acquired by on-chip micro-beamforming, with respect to the traditional DAS beamformer. The average FWHM of ABLE reduced to 62% of the average FWHM of DAS. ABLE also improved lateral resolution, as measured by the FWHM with respect to the CF beamformer and F-DMAS beamformer whose average FWHM was respectively 124% and 127% of that of ABLE. The EBMV beamformer had on average a FWHM that was only 59% of that of ABLE, but unlike ABLE, this came at the cost of erratic behavior of the beamprofile around point scatterers and a severe reduction in contrast. We suspect that the undesirable performance of the EBMV beamformer is due to focusing inaccuracies resulting from the micro-beamforming step [53], needed to enable high-frame-rate read-out of the matrix array. Such inaccuracies may lead to incorrect estimation of signal statistics and as a result sub-optimal prediction of apodization weights. In contrast, ABLE is trained over a wide range of input signals, which allows for a more robust modeling of the underlying system parameters.

ABLE slightly decreased *in vitro* contrast compared to DAS as measured by the GCNR, from 0.59 to 0.56 and slightly improved *in silico* contrast with respect to DAS from 0.85 to 0.87. Thus, ABLE improves the achieved resolution without impacting contrast. Since, the resolution improvement of ABLE can be achieved by purely training with *in silico* data, this makes the method easily implementable in practice. To achieve good contrast and avoid increased amplitude variation in background speckle it was needed to add densely scattering regions (10 scatterers per resolution cell) to the *in silico* training data instead of using only volumes with sparse scattering. Furthermore, the fact that the *in silico* data does not need to be designed to closely match the organ that is im-

aged, but consists of basic geometric shapes and point scatterers gives some confidence that this approach is not just sufficient for this imaging scenario, but could generalize to other scenarios as well. Increasing the receptive field of the original ABLE method by replacing the fully connected layers of the neural network with convolutional layers led to an improvement in resolution, measured by a decrease in average FWHM from 71% of that of DAS to 63% of the average FWHM of DAS. We presume that this small amount of spatial context is beneficial especially for volumetric imaging with micro-beamforming, since time-of-flight corrected RF data of a single voxel will contain small receive focusing errors. Increasing the lateral receptive field size to a larger value than that of ABLE2 did not result in a clear performance improvement. The computational cost is increased by adding convolutional layers. The computational cost of ABLE1 with a single voxel receptive field is always below that of EBMV beamforming. For ABLE2 the computational cost is higher, but stays below that of EBMV beamforming for transducers with more than ~32 channels. We did not add dropout layers, since the ABLE network in combination with the large array training target, showed no signs of overfitting on the training data for all discussed network sizes.

The method surpassed the image quality of the DAS, F-DMAS, CF and EBMV beamformers quantitatively and qualitatively. *In silico* and *in vitro* resolution measures reach at least the same level as the target images. When training only on *in silico* data or on the combination of *in silico* and *in vitro* data, the FWHM was on average lower than that in the target images. A reason for this could be that the networks bottleneck forces a compact representation of the channel data such that certain elements that are present in the target data, such as noise cannot be accurately represented, thereby having a beneficial effect on the estimation of the apodization weights. However, further experiments would be needed to clarify this. The speckle size of ABLE is more similar to that achieved by the other beamformers, than to that achieved by a larger aperture DAS beamformer. Vignon *et al.* [29] already described that learning speckle signals from elements further away from the original aperture is highly challenging if not infeasible. Unlike the spatial covariance of specular reflectors, the spatial covariance of the incoherent signal arising from the sub-resolution tissue scatterers decreases with increasing distance between observation points. As a result, when distance between elements increases there is no relation between the speckle signals from the original array and that of a remote element in the target array, making the signal infeasible to estimate.

Previous work has shown that ABLE in combination with an EBMV based training target performs well across different 2D ultrasound imaging modalities [32]. Here we show not only that extension to 3D is possible, but we also demonstrate that the ABLE method is effective in a situation where a high quality target from existing beamformers is not available, by using a larger aperture target. A different approach to improving 3D ultrasound image quality with deep learning applied after beamforming is taken by Huh *et al.* [54]. They also used artificially generated targets to improve 3D ultrasound image quality, but instead used an unsupervised deep learning approach. A switchable CycleGan was used to learn a style-transfer from an unpaired training set of low-quality 3D ultrasound images and high-quality 2D reference images. Unlike the matrix array used here they used a 3D mechanical scanning probe. Image quality improvements were assessed through evaluation by a clinician, making the methods difficult to compare.

Here we specifically focused on 3D imaging with a matrix array that applies micro-beamforming, since this is a common strategy to solve the data rate and channel connection problem. However, we expect the ABLE method to also improve lateral resolution compared to DAS for fully populated arrays without micro-beamforming. For this case it would be interesting to evaluate whether a training target generated by a larger array or by EBMV beamforming as was used for 2D imaging [32] would be a more suitable choice. For such an array with a very large number of channels the advantages of computational cost when beamforming with ABLE1 or ABLE2 compared to EBMV would become especially apparent. Whether a receptive field larger than a single voxel would be beneficial here remains to be evaluated. The use of deep-learning-based beamforming with an artificial array target could also be investigated for row-column and fixed pattern sparse arrays. Furthermore jointly learning a sparse sub-sampling pattern and beamforming algorithm could be explored for fully populated matrix arrays, as shown for 1D arrays in [55]. Finally, in this work we used real apodization weights. Giving the network more freedom by letting it learn complex apodization weights and working with IQ data, can potentially further increase performance.

5

5.5. CONCLUSIONS

In this work we have shown that deep-learning-based adaptive beamforming can be used to improve lateral resolution of volumetric ultrasound images acquired by on-chip micro-beamforming. By using only *in silico* training data consisting of simulated RF data and a target created by a larger aperture, we trained a deep-learning-based adaptive beamformer. This beamformer improved lateral resolution, such that image quality is improved beyond that achieved by DAS, F-DMAS, CF and EBMV.

5.6. APPENDIX: NETWORK ARCHITECTURES

Full network architectures are given in Figure 5.13.

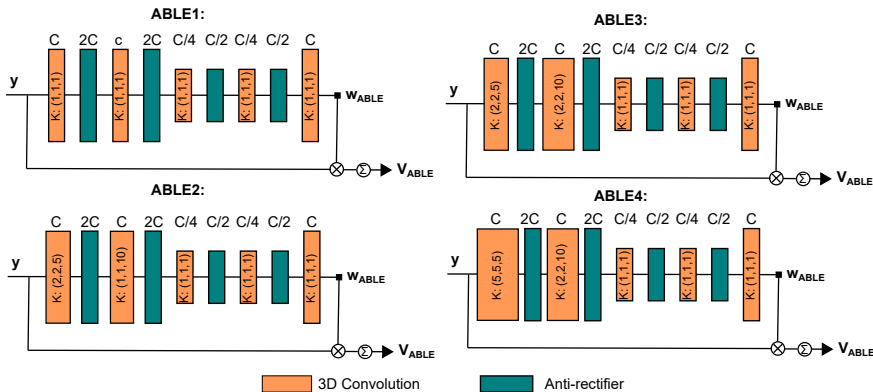


Figure 5.13: Modified ABLE networks, with different receptive field size. K indicates the kernel size in the 3 spatial directions (azimuth, elevation, axial). The number above each convolutional layer indicates the number of kernels in the layer. C is the number of receive channels of the transducer, which here was 32.

REFERENCES

- [1] D. Shattuck, M. D. Weinshenker, S. W. Smith, and O. T. von Ramm, "Explososcan: A parallel processing technique for high speed ultrasound imaging with linear phased arrays", *The Journal of the Acoustical Society of America*, vol. 75, no. 4, pp. 1273–1282, 1984. DOI: [10.1121/1.390734](https://doi.org/10.1121/1.390734).
- [2] J. Provost, C. Papadacci, J. E. Arango, M. Imbault, M. Fink, J. L. Gennisson, M. Tanter, and M. Pernot, "3D ultrafast ultrasound imaging in vivo", *Physics in Medicine and Biology*, vol. 59, no. 19, p. L1, 2014. DOI: [10.1088/0031-9155/59/19/L1](https://doi.org/10.1088/0031-9155/59/19/L1).
- [3] J. D. Larson III, *2-D phased array ultrasound imaging system with distributed phasing*, US Patent 5229933, Jul. 1993.
- [4] B. Savord and R. Solomon, "Fully sampled matrix transducer for real time 3D ultrasonic imaging", in *IEEE Symposium on Ultrasonics*, vol. 1, IEEE, 2003, pp. 945–953. DOI: [10.1109/ULTSYM.2003.1293556](https://doi.org/10.1109/ULTSYM.2003.1293556).
- [5] S. Blaak, Z. Yu, G. C. M. Meijer, C. Prins, C. T. Lancée, J. G. Bosch, and N. De Jong, "Design of a micro-beamformer for a 2D piezoelectric ultrasound transducer", in *2009 IEEE Ultrasonics Symposium*, 2009, pp. 1338–1341. DOI: [10.1109/ULTSYM.2009.5441534](https://doi.org/10.1109/ULTSYM.2009.5441534).
- [6] P. Santos, G. U. Haugen, L. Lovstakken, E. Samset, and J. D'Hooge, "Diverging Wave Volumetric Imaging Using Subaperture Beamforming", *IEEE Transactions on Ultrasonics, Ferroelectrics, and Frequency Control*, vol. 63, no. 12, pp. 2114–2124, 2016. DOI: [10.1109/TUFFC.2016.2616172](https://doi.org/10.1109/TUFFC.2016.2616172).
- [7] J. B. Seward, B. K. Khandheria, J. K. Oh, M. D. Abel, R. W. Hughes, W. D. Edwards, B. A. Nichols, W. K. Freeman, and A. J. Tajik, "Transesophageal Echocardiography: Technique, Anatomic Correlations, Implementation, and Clinical Applications", *Mayo Clinic proceedings*, vol. 63, no. 7, pp. 649–680, 1988. DOI: [10.1016/S0025-6196\(12\)65529-3](https://doi.org/10.1016/S0025-6196(12)65529-3).
- [8] K. T. Spencer, D. Krauss, J. Thurn, V. Mor-Avi, A. Poppas, P. Vignon, B. G. Connor, and R. M. Lang, "Transnasal transesophageal echocardiography", *Journal of the American Society of Echocardiography*, vol. 10, no. 7, pp. 728–737, 1997. DOI: [10.1016/S0894-7317\(97\)70116-0](https://doi.org/10.1016/S0894-7317(97)70116-0).
- [9] J. Hastie, O. P. Panzer, P. Weyker, and B. C. Flynn, "Miniatuerized Echocardiography in the Cardiac Intensive Care Unit", *Journal of Cardiothoracic and Vascular Anesthesia*, vol. 33, no. 6, pp. 1540–1547, 2019. DOI: [10.1053/j.jvca.2018.08.199](https://doi.org/10.1053/j.jvca.2018.08.199).
- [10] Z. M. Hijazi, K. Shivkumar, and D. J. Sahn, "Intracardiac echocardiography during interventional and electrophysiological cardiac catheterization", *Circulation*, vol. 119, no. 4, pp. 587–596, 2009. DOI: [10.1161/CIRCULATIONAHA.107.753046](https://doi.org/10.1161/CIRCULATIONAHA.107.753046).
- [11] D. Wildes, W. Lee, B. Haider, S. Cogan, K. Sundaresan, D. M. Mills, C. Yetter, P. H. Hart, C. R. Haun, *et al.*, "4-D ICE: A 2-D Array Transducer with Integrated ASIC in a 10-Fr Catheter for Real-Time 3-D Intracardiac Echocardiography", *IEEE Transactions on Ultrasonics, Ferroelectrics, and Frequency Control*, vol. 63, no. 12, pp. 2159–2173, 2016. DOI: [10.1109/TUFFC.2016.2615602](https://doi.org/10.1109/TUFFC.2016.2615602).
- [12] R. Mallart and M. Fink, "Adaptive focusing in scattering media through sound-speed inhomogeneities: The van Cittert Zernike approach and focusing criterion", *The Journal of the Acoustical Society of America*, vol. 96, no. 6, pp. 3721–3732, 1994. DOI: [10.1121/1.410562](https://doi.org/10.1121/1.410562).
- [13] C. I. Nilsen and S. Holm, "Wiener beamforming and the coherence factor in ultrasound imaging", *IEEE Transactions on Ultrasonics, Ferroelectrics, and Frequency Control*, vol. 57, no. 6, pp. 1329–1346, 2010. DOI: [10.1109/TUFFC.2010.1553](https://doi.org/10.1109/TUFFC.2010.1553).
- [14] G. Matrone, A. S. Savoia, G. Caliano, and G. Magenes, "The delay multiply and sum beamforming algorithm in ultrasound B-mode medical imaging", *IEEE Transactions on Medical Imaging*, vol. 34, no. 4, pp. 940–949, 2015. DOI: [10.1109/TMI.2014.2371235](https://doi.org/10.1109/TMI.2014.2371235).
- [15] F. Prieur, O. M. H. Rindal, and A. Austeng, "Signal coherence and image amplitude with the filtered delay multiply and sum beamformer", *IEEE Transactions on Ultrasonics, Ferroelectrics, and Frequency Control*, vol. 65, no. 7, pp. 1133–1140, 2018. DOI: [10.1109/TUFFC.2018.2831789](https://doi.org/10.1109/TUFFC.2018.2831789).
- [16] J. F Synnevåg, A. Austeng, and S. Holm, "Benefits of minimum-variance beamforming in medical ultrasound imaging", *IEEE Transactions on Ultrasonics, Ferroelectrics, and Frequency Control*, vol. 56, no. 9, pp. 1868–1879, 2009. DOI: [10.1109/TUFFC.2009.1263](https://doi.org/10.1109/TUFFC.2009.1263).
- [17] B. M. Asl and A. Mahloojifar, "Eigenspace-based minimum variance beamforming applied to medical ultrasound imaging", *IEEE Transactions on Ultrasonics, Ferroelectrics, and Frequency Control*, vol. 57, no. 11, pp. 2381–2390, 2010. DOI: [10.1109/TUFFC.2010.1706](https://doi.org/10.1109/TUFFC.2010.1706).
- [18] R. G. Lorenz and S. P. Boyd, "Robust minimum variance beamforming", *IEEE Transactions on Signal Processing*, vol. 53, no. 5, pp. 1684–1696, 2005. DOI: [10.1109/TSP.2005.845436](https://doi.org/10.1109/TSP.2005.845436).

[19] O. M. H. Rindal, A. Rodriguez-Molares, and A. Austeng, "The dark region artifact in adaptive ultrasound beamforming", *2017 IEEE International Ultrasonics Symposium (IUS)*, pp. 1–4, 2017. DOI: [10.1109/ULTSYM.2017.8091606](https://doi.org/10.1109/ULTSYM.2017.8091606).

[20] R. J. G. Van Sloun, R. Cohen, and Y. C. Eldar, "Deep learning in ultrasound imaging", *Proceedings of the IEEE*, vol. 108, no. 1, pp. 11–29, 2019. DOI: [10.1109/jproc.2019.2932116](https://doi.org/10.1109/jproc.2019.2932116).

[21] R. J. G. van Sloun, J. C. Ye, and Y. C. Eldar, "Deep Learning for Ultrasound Beamforming", *ArXiv preprint arXiv:2109.11431*, 2021.

[22] J. Lu, F. Millioz, D. Garcia, S. Salles, W. Liu, and D. Friboulet, "Reconstruction for Diverging-Wave Imaging Using Deep Convolutional Neural Networks", *IEEE Transactions on Ultrasonics, Ferroelectrics, and Frequency Control*, vol. 67, no. 12, pp. 2481–2492, 2020. DOI: [10.1109/TUFFC.2020.2986166](https://doi.org/10.1109/TUFFC.2020.2986166).

[23] Z. Zhou, Y. Wang, J. Yu, Y. Guo, W. Guo, and Y. Qi, "High Spatial - Temporal Resolution Reconstruction of Plane-Wave Ultrasound Images With a Neural Network", *IEEE Transactions on Ultrasonics, Ferroelectrics, and Frequency Control*, vol. 65, no. 11, pp. 1983–1996, 2018. DOI: [10.1109/TUFFC.2018.2865504](https://doi.org/10.1109/TUFFC.2018.2865504).

[24] Z. Zhou, Y. Wang, Y. Guo, X. Jiang, and Y. Qi, "Ultrafast Plane Wave Imaging with Line-Scan-Quality Using an Ultrasound-Transfer Generative Adversarial Network", *IEEE Journal of Biomedical and Health Informatics*, vol. 24, no. 4, pp. 943–956, 2020. DOI: [10.1109/JBHI.2019.2950334](https://doi.org/10.1109/JBHI.2019.2950334).

[25] F. Dietrichson, E. Smistad, A. Østvik, and L. Lovstakken, "Ultrasound Speckle Reduction Using Generative Adversarial Networks", *2018 IEEE International Ultrasonics Symposium (IUS)*, pp. 55–58, 2018. DOI: [10.1109/ULTSYM.2018.8579764](https://doi.org/10.1109/ULTSYM.2018.8579764).

[26] S. Goudarzi, A. Asif, and H. Rivaz, "Fast Multi-Focus Ultrasound Image Recovery Using Generative Adversarial Networks", *IEEE Transactions on Computational Imaging*, vol. 6, pp. 1272–1284, 2020. DOI: [10.1109/TCI.2020.3019137](https://doi.org/10.1109/TCI.2020.3019137).

[27] D. Hyun, L. L. Brickson, K. T. Looby, and J. J. Dahl, "Beamforming and speckle reduction using neural networks", *IEEE Transactions on Ultrasonics, Ferroelectrics, and Frequency Control*, vol. 66, no. 5, pp. 898–910, 2019. DOI: [10.1109/TUFFC.2019.2903795](https://doi.org/10.1109/TUFFC.2019.2903795).

[28] Y. H. Yoon and J. C. Ye, "Deep Learning for Accelerated Ultrasound Imaging", in *IEEE International Conference on Acoustics, Speech and Signal Processing Proceedings (ICASSP)*, IEEE, 2018, pp. 6673–6676. DOI: [10.1109/ICASSP.2018.8462304](https://doi.org/10.1109/ICASSP.2018.8462304).

[29] F. Vignon, J. S. Shin, F. C. Meral, I. Apostolakis, S. W. Huang, and J. L. Robert, "Resolution improvement with a fully convolutional neural network applied to aligned per-channel data", *2020 IEEE International Ultrasonics Symposium (IUS)*, pp. 1–4, 2020. DOI: [10.1109/IUS46767.2020.9251482](https://doi.org/10.1109/IUS46767.2020.9251482).

[30] A. C. Luchies and B. C. Byram, "Deep Neural Networks for Ultrasound Beamforming", *IEEE Transactions on Medical Imaging*, vol. 37, no. 9, pp. 2010–2021, 2018. DOI: [10.1109/TMI.2018.2809641](https://doi.org/10.1109/TMI.2018.2809641).

[31] ——, "Assessing the Robustness of Frequency-Domain Ultrasound Beamforming Using Deep Neural Networks", *IEEE Transactions on Ultrasonics, Ferroelectrics, and Frequency Control*, vol. 67, no. 11, pp. 2321–2335, 2020. DOI: [10.1109/TUFFC.2020.3002256](https://doi.org/10.1109/TUFFC.2020.3002256).

[32] B. Luijten, R. Cohen, F. J. De Bruijn, H. A. Schmeitz, M. Mischi, Y. C. Eldar, and R. J. Van Sloun, "Adaptive Ultrasound Beamforming Using Deep Learning", *IEEE Transactions on Medical Imaging*, vol. 39, no. 12, pp. 3967–3978, 2020. DOI: [10.1109/TMI.2020.3008537](https://doi.org/10.1109/TMI.2020.3008537).

[33] A. A. Nair, K. N. Washington, T. D. Tran, A. Reiter, and M. A. Lediju Bell, "Deep Learning to Obtain Simultaneous Image and Segmentation Outputs from a Single Input of Raw Ultrasound Channel Data", *IEEE Transactions on Ultrasonics, Ferroelectrics, and Frequency Control*, vol. 67, no. 12, pp. 2493–2509, 2020. DOI: [10.1109/TUFFC.2020.2993779](https://doi.org/10.1109/TUFFC.2020.2993779).

[34] A. A. Nair, T. D. Tran, A. Reiter, and M. A. Lediju Bell, "A Deep Learning Based Alternative to Beamforming Ultrasound Images", in *ICASSP, IEEE International Conference on Acoustics, Speech and Signal Processing - Proceedings*, IEEE, 2018, pp. 3359–3363. DOI: [10.1109/ICASSP.2018.8461575](https://doi.org/10.1109/ICASSP.2018.8461575).

[35] X. Huang, M. A. Lediju Bell, and K. Ding, "Deep Learning for Ultrasound Beamforming in Flexible Array Transducer", *IEEE Transactions on Medical Imaging*, vol. 40, no. 11, pp. 3178–3189, 2021. DOI: [10.1109/TMI.2021.3087450](https://doi.org/10.1109/TMI.2021.3087450).

[36] A. Mamistvalov, A. Amar, N. Kessler, and Y. C. Eldar, "Deep-learning based adaptive ultrasound imaging from sub-nyquist channel data", *IEEE Transactions on Ultrasonics, Ferroelectrics, and Frequency Control*, vol. 69, no. 5, pp. 1638–1648, 2022. DOI: [10.1109/TUFFC.2022.3160859](https://doi.org/10.1109/TUFFC.2022.3160859).

[37] A. C. Luchies and B. C. Byram, "Training improvements for ultrasound beamforming with deep neural networks", *Physics in Medicine and Biology*, vol. 64, no. 4, p. 045018, 2019. DOI: [10.1088/1361-6560/aaaf50](https://doi.org/10.1088/1361-6560/aaaf50).

[38] Z. Zhou, Y. Guo, and Y. Wang, "Ultrasound deep beamforming using a multiconstrained hybrid generative adversarial network", *Medical Image Analysis*, vol. 71, p. 102086, 2021. DOI: [10.1016/j.media.2021.102086](https://doi.org/10.1016/j.media.2021.102086).

[39] N. Chennakeshava, B. Luijten, O. Drori, M. Mischi, Y. C. Eldar, and R. J. Van Sloun, "High resolution plane wave compounding through deep proximal learning", in *2020 IEEE International Ultrasonics Symposium (IUS)*, 2020, pp. 1–4. DOI: [10.1109/IUS46767.2020.9251399](https://doi.org/10.1109/IUS46767.2020.9251399).

[40] J. Youn, M. L. Ommen, M. B. Stuart, E. V. Thomsen, N. B. Larsen, and J. A. Jensen, "Detection and localization of ultrasound scatterers using convolutional neural networks", *IEEE Transactions on Medical Imaging*, vol. 39, no. 12, pp. 3855–3867, 2020. DOI: [10.1109/TMI.2020.3006445](https://doi.org/10.1109/TMI.2020.3006445).

[41] S. A. I. Avanji, A. Mahloojifar, and B. M. Asl, "Adaptive 3D MV beamforming in medical ultrasound imaging", in *2013 20th Iranian Conference on Biomedical Engineering, ICBME 2013*, IEEE, 2013, pp. 81–86. DOI: [10.1109/ICBME.2013.6782197](https://doi.org/10.1109/ICBME.2013.6782197).

[42] D. P. Kingma and J. L. Ba, "Adam: A method for stochastic optimization", *3rd International Conference on Learning Representations, ICLR 2015 - Conference Track Proceedings*, pp. 1–15, 2015. DOI: [10.48550/arXiv.1412.6980](https://doi.org/10.48550/arXiv.1412.6980).

[43] D. Bera, F. van den Adel, N. Radeljic-Jakic, B. Lippe, M. Soozande, M. A. Pertij, M. D. Verweij, P. Kruizinga, V. Daeichin, *et al.*, "Fast Volumetric Imaging Using a Matrix Transesophageal Echocardiography Probe with Partitioned Transmit-Receive Array", *Ultrasound in Medicine and Biology*, vol. 44, no. 9, pp. 2025–2042, 2018. DOI: [10.1016/j.ultrasmobio.2018.05.017](https://doi.org/10.1016/j.ultrasmobio.2018.05.017).

[44] A. Jensen and B. Svendsen, "Calculation of Pressure Fields from Arbitrarily Shaped, Apodized, and Excited Ultrasound Transducers", *IEEE Transactions on Ultrasonics, Ferroelectrics, and Frequency Control*, vol. 39, no. 2, pp. 262–267, 1992. DOI: [10.1109/58.139123](https://doi.org/10.1109/58.139123).

[45] J. Jensen, "Field: A program for simulating ultrasound systems", in *10th Nordic-Baltic Conference on Biomedical Imaging*, vol. 34, Supple, 1996, pp. 351–353.

[46] J. Capon, "High-Resolution Frequency-Wavenumber Spectrum Analysis", *Proceedings of the IEEE*, vol. 57, no. 8, pp. 1408–1418, 1969. DOI: [10.1109/PROC.1969.7278](https://doi.org/10.1109/PROC.1969.7278).

[47] J. Evans, J. R. Johnson, and D. Sun, "High Resolution Angular Spectrum Estimation Techniques for Terrain Scattering Analysis and Angle of Arrival Estimation", in *Proc. of the First ASSP Workshop on Spectral Estimation*, 1981, pp. 134–139.

[48] J. F. Synnevåg, A. Austeng, and S. Holm, "Adaptive beamforming applied to medical ultrasound imaging", *IEEE Transactions on Ultrasonics, Ferroelectrics, and Frequency Control*, vol. 54, no. 8, pp. 1606–1613, 2007. DOI: [10.1109/TUFFC.2007.431](https://doi.org/10.1109/TUFFC.2007.431).

[49] A. Ramalli, A. Dallai, L. Bassi, M. Scaringella, E. Boni, G. E. Hine, G. Matrone, A. S. Savoia, and P. Tortoli, "High dynamic range ultrasound imaging with real-time Filtered-Delay Multiply and sum beamforming", *IEEE International Ultrasonics Symposium, IUS*, pp. 1–4, 2017. DOI: [10.1109/ULTSYM.2017.8091860](https://doi.org/10.1109/ULTSYM.2017.8091860).

[50] O. M. H. Rindal, A. Austeng, A. Fatemi, and A. Rodriguez-Molares, "The Effect of Dynamic Range Alterations in the Estimation of Contrast", *IEEE Transactions on Ultrasonics, Ferroelectrics, and Frequency Control*, vol. 66, no. 7, pp. 1198–1208, 2019. DOI: [10.1109/TUFFC.2019.2911267](https://doi.org/10.1109/TUFFC.2019.2911267).

[51] A. Rodriguez-Molares, O. M. H. Rindal, J. D'Hooge, S. E. Masoy, A. Austeng, M. A. Lediju Bell, and H. Torp, "The Generalized Contrast-to-Noise Ratio: A Formal Definition for Lesion Detectability", *IEEE Transactions on Ultrasonics, Ferroelectrics, and Frequency Control*, vol. 67, no. 4, pp. 745–759, 2020. DOI: [10.1109/TUFFC.2019.2956855](https://doi.org/10.1109/TUFFC.2019.2956855).

[52] D. Hyun, G. B. Kim, N. Bottenuus, and J. J. Dahl, "Ultrasound Lesion Detectability as a Distance Between Probability Measures", *IEEE Transactions on Ultrasonics, Ferroelectrics, and Frequency Control*, vol. 69, no. 2, pp. 732–743, 2022. DOI: [10.1109/TUFFC.2021.3138058](https://doi.org/10.1109/TUFFC.2021.3138058).

[53] U. W. Lok and P. C. Li, "Microbeamforming with error compensation", *IEEE Transactions on Ultrasonics, Ferroelectrics, and Frequency Control*, vol. 65, no. 7, pp. 1153–1165, 2018. DOI: [10.1109/TUFFC.2018.2834411](https://doi.org/10.1109/TUFFC.2018.2834411).

[54] J. Huh, S. Khan, S. Choi, D. Shin, J. E. Lee, E. S. Lee, and J. C. Ye, "Tunable image quality control of 3-d ultrasound using switchable cyclegan", *Medical Image Analysis*, vol. 83, p. 102651, 2023. DOI: <https://doi.org/10.1016/j.media.2022.102651>.

[55] I. A. M. Huijben, B. S. Veeling, K. Janse, M. Mischi, and R. J. G. van Sloun, "Learning sub-sampling and signal recovery with applications in ultrasound imaging", *IEEE Transactions on Medical Imaging*, vol. 39, no. 12, pp. 3955–3966, 2020. DOI: [10.1109/TMI.2020.3008501](https://doi.org/10.1109/TMI.2020.3008501).

6

NEURAL MAXIMUM-A-POSTERIORI AND DEEP LEARNING-BASED ADAPTIVE BEAMFORMING FOR 3-D CONTRAST ULTRASOUND WITH A SPARSE ARRAY

This chapter is an extended version of:

Boudewine W. Ossenkoppеле, Luxi Wei, Ben Luijten, Hendrik J. Vos, Nico de Jong, Ruud J.G. van Sloun, Martin D. Verweij, 3-D contrast-enhanced ultrasound imaging of an *in vivo* chicken embryo with a sparse array and deep learning-based adaptive beamforming, in 2022 IEEE International Ultrasonics Symposium (IUS), IEEE, 2022, pp. 1-4

3-D contrast-enhanced ultrasound enables better visualization of inherently 3-D vascular geometries compared to an intersecting plane. Additionally, it allows the application of motion correction techniques for all directions. Both contrast detection and motion correction work better on high-frame-rate data. However high-frame-rate 3-D ultrasound imaging with dense matrix arrays is challenging to realize. Sparse arrays alleviate some of the limitations in cable count and data rate that fully populated arrays encounter, however, their increased level of secondary lobes negatively impacts image contrast. Meanwhile, the use of unfocused transmit beams needed to achieve high frame rates negatively impacts resolution. Here we propose to use deep learning-based beamforming to improve the image quality of contrast-enhanced ultrasound images acquired with a sparse spiral array. Two types of deep learning-based beamforming are used: adaptive beamforming by deep learning (ABLE) and a novel deep learning-based beamformer called neural maximum-a-posteriori (neural MAP) beamforming. The neural MAP beamformer efficiently incorporates deep learning in the maximum-a-posteriori (MAP) beamforming framework, such that prior information about the distribution of the acoustic reflectivity can be incorporated into the beamforming process. The neural networks are trained on simulated data. Neural MAP and ABLE improve resolution compared to delay-and-sum (DAS) and spatial coherence (SC) beamforming on the simulated and *in vivo* data. The qualitative improvements persist after histogram matching, indicating that the image quality improvement was not purely due to dynamic range stretching. The impact of the different beamformers on ultrasound localization microscopy (ULM) was considered as well. Neural MAP showed the best performance on localizing *in silico* microbubbles followed by ABLE, SC and DAS. Finally, super-resolved images of an *in vivo* chicken embryo recording are shown.

6.1. INTRODUCTION

Contrast-enhanced ultrasound imaging (CEUS) has enabled the visualization of the microvasculature, which used to be difficult to distinguish from tissue due to the slow blood velocity and the weak scattering of red blood cells [1]. Microbubbles (MBs) are used in clinical practice to generate CEUS images of the vasculature, which serve as a diagnostic tool for various pathologies [2–6]. In CEUS imaging the maximum transducer center frequency is determined by the required imaging depth and the achievable spatial resolution is limited by the diffraction limit. When the microvessels are separated by distances smaller than half the wavelength a detailed map of the microvasculature cannot be distinguished. However, the achievable resolution at which maps of the (micro-) vasculature can be recorded has been significantly increased through the development of ultrasound localization microscopy (ULM) [7, 8]. ULM breaks the diffraction limit of ultrasound images by localizing the center of isolated microbubbles with subwavelength precision, in some cases reaching micrometer precision [9–14]. By tracking the trajectories of the contrastagents, super-resolution hemodynamic maps of the microvasculature can be realized. Many studies have contributed to improving localization precision, tracking accuracy and reducing acquisition time to further develop the emerging ULM technology, an overview of these can be found in two recent review papers [13, 14].

Three-dimensional images are highly desired for contrast-enhanced ultrasound and ULM, because they enable better visualization of the vasculature compared to 2-D images and allow for motion correction in all directions. High frame rates are not just desirable in scenarios with a high bloodflow velocity, but also allow more effective application of post-processing filters [15], better motion compensation and lower acquisition times. Sparse arrays are an attractive option to realize high-frame-rate volumetric imaging due to their relatively low cable count, data rate and cost. Although their transmit efficiency and receive sensitivity are lower compared to fully populated arrays, the high reflectivity of microbubbles makes this less of a concern in contrast-enhanced imaging than in imaging without contrast. Harput et al. [16] showed the suitability of a 2-D sparse array for high-frame-rate super-resolution imaging *in vitro*. Wei et al. [17] demonstrated contrast-enhanced vasculature mapping of a live chicken embryo chorioallantoic membrane with a sparse spiral array. However, the variation of magnitude and pulse shape within the emitted field of a sparse array is higher than with dense matrix arrays and the high-amplitude secondary lobes can cause artifacts when beamforming with Delay-and-Sum (DAS) and reduce contrast. Meanwhile, the unfocused transmit beams needed for high-frame-rate imaging negatively impact resolution. Spatial coherence (SC) beamforming has been used to improve image quality in contrast-enhanced ultrasound images acquired by a sparse array [17]. Through exploiting the coherence of signals, the level of microbubble clutter was reduced and a better separation of contrast w.r.t. the background was achieved.

The increased clutter level of sparse arrays and increased mainlobe width from high-frame-rate imaging with unfocused transmit beams also negatively impacts the application of ULM techniques on contrast-enhanced images. The larger PSF size results in more overlapping microbubbles and a greater variation in PSF shape can also hamper the application of ULM techniques. Although low concentrations of microbubbles have often been used to increase the localization precision of ULM by decreasing the num-

ber of overlapping microbubble PSFs, there has recently been increased attention on developing methods that increase the detection sensitivity and precision at higher microbubble concentrations. This is driven by the desire to use higher concentrations of contrast agents, which would be needed to reduce acquisition time, while still filling all desired arterioles. Reduced acquisition times are important to reduce the impact of motion artifacts and essential in applications that want to reveal physiological information from fast changes in blood flow [18–21]. The ULM algorithms focused on coping with overlapping PSFs have been based on deconvolution [22, 23], sparse recovery [24–27] and deep learning [28–33].

These methods all work on images that have been formed with DAS beamforming. Others have proposed to reduce the PSF overlap of nearby microbubbles by using minimum-variance beamforming (MV) [34] instead of DAS. However, minimum-variance beamforming is computationally expensive and not well-established for volumetric imaging with sparse arrays. Adaptive beamforming by deep learning (ABLE) [35] has a lower computational cost than minimum variance beamforming and has been applied to improve ultrasound image quality in non-contrast-enhanced images for arrays with regularly spaced elements and has been used jointly with deep learning-based localization [28] to improve the localization of microbubbles in contrast-enhanced ultrasound. Inspired by this, in [36] we trained an adapted version of the original ABLE network on *in silico* data and compared beamformed CEUS images of an *in vivo* chicken embryo to DAS and SC beamforming, showing an increased resolution.

Neither, DAS, SC, MV, ABLE or in general, the majority of ultrasound beamformers, exploits prior information about the distribution of the acoustic reflectivity in the image. Recently, we proposed a novel approach, neural maximum-a-posteriori (neural MAP) beamforming, which efficiently incorporates deep learning in the maximum-a-posteriori (MAP) beamforming framework [37]. For many prior distributions, MAP estimation has no closed-form solution and instead needs to be estimated through iterative methods such as proximal gradient descent. Neural MAP unfolds [38] the iterations of proximal gradient descent into a neural network consisting of a fixed number of iterations of data-consistency and prior steps. The neural MAP framework allows replacing both the data-consistency and prior steps with neural networks. However, for detecting sparsely distributed microbubbles the soft-thresholding operator has been shown to be an appropriate prior [39].

In this chapter, we hypothesize that both the ABLE and neural MAP beamformer with a sparse prior, increase the resolution of CEUS images acquired with a sparse spiral array compared to DAS and SC. Secondly, we hypothesize that ABLE and neural MAP to a larger degree, improve the sensitivity and precision of microbubble localization compared to DAS and SC beamformed images by increasing contrast and resolution through a reduced impact of secondary lobes and narrowing of the mainlobe.

We evaluate the contrast-enhanced ultrasound images made by each beamformer both on *in silico* data for which a ground truth is available and on *in vitro* and *in vivo* data. Using ULM techniques from the ultrasound super-resolution localization-and-tracking toolbox [40], we compare the localization performance on *in silico* data for each beamformer and show the super-resolved images of an *in vivo* chicken embryo recording.

6.2. METHODS

6.2.1. SPARSE SPIRAL ARRAY

We used a 5 MHz prototype sparse array with a 1.6 cm diameter aperture, consisting of 256 piezoelectric elements with an element size of $200 \mu\text{m} \times 200 \mu\text{m}$. The elements are arranged in a tapered spiral pattern, specifically designed to minimize sidelobe levels by decreasing the element density towards the edge of the array according to a Blackman window [41, 42], see Fig. 6.1.

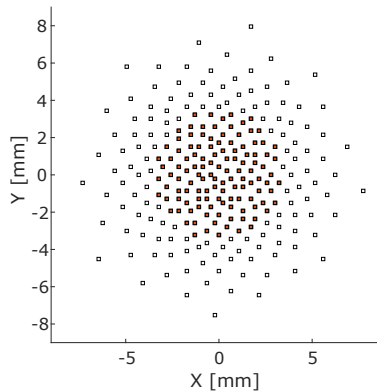


Figure 6.1: Layout of the 256 elements of the sparse spiral array. Only the center 120 elements indicated in red are used in transmit. All elements are used in receive.

6.2.2. IMAGING SCHEME

Diverging waves with a 30° opening angle were used to insonify a large region of interest. The final volumetric images were formed by angular compounding of five steered diverging waves (angles: $[0^\circ, 5^\circ]$, $[5^\circ, 0^\circ]$, $[0^\circ, -5^\circ]$, $[-5^\circ, 0^\circ]$, $[0^\circ, 0^\circ]$) to reach a volumetric frame rate of 1000 Hz. To increase the uniformity of the transmit field in both lateral and axial direction, only the center 120 elements were used in transmission (see Fig. 1). Further details on the probe and the design of the transmit and receive strategy can be found in [17].

6.2.3. SIMULATION DATA FOR TRAINING AND EVALUATION

Field II [43] was used to simulate the data acquisition of the sparse array during contrast-enhanced ultrasound imaging. Point scatterers with an amplitude between 0.5 and 1 were randomly distributed in a region spanning from -40° to 40° in azimuth and elevation direction. Hundred image volumes were simulated for training, of which 10% was used as validation data. The simulated concentration of microbubbles ranged from $50\text{-}600/\text{cm}^3$ with an average concentration of $200/\text{cm}^3$. The RF data was used as input to the neural networks, while the true location and amplitude of the point scatterers were used to form a target image. Test data to evaluate the performance of the ABLE, neural MAP, SC and DAS beamformers was generated for 15 concentrations between 4 and $208/\text{cm}^3$, with white Gaussian noise added to the RF data. Five different volumes with different

distributions of the simulated micro-bubbles were simulated for each concentration to allow averaging of performance metrics.

6.2.4. *In vitro* DATA ACQUISITION

A helical-shaped cellulose tube with a 200 μm outer diameter was used as an *in vitro* phantom for 3D flow in a microvessel. The tube had an inner diameter between 150 and 180 μm . It was embedded in tissue-mimicking PVA material. The custom-made microbubble solution (C4F10 gas core, phospholipid coating, F type, mean diameter 1.1 μm [44]) was pumped through the helical tube with a syringe pump at a flow rate of 25 $\mu\text{L}/\text{min}$ (mean velocity = 16.5 - 23.6 mm/s)[17].

6.2.5. *In vivo* DATA ACQUISITION

An *ex ovo* chicken embryo and chorioallantoic membrane (CAM) were used as the *in vivo* model to investigate the effect of the different beamformers on contrast-enhanced ultrasound imaging. The five-day-old chicken embryo and CAM were removed from the eggshell and further prepared according to the protocol of Meijlink et al. [45], after which four μL of custom-made F-type microbubble was injected into the vasculature of the chicken embryo. The chicken embryo was placed in a PBS solution and the ultrasound array was positioned on top of the chicken embryo at a 3 cm distance. More details of the procedure can be found in [17, 45]. The ultrasound recording lasted 3.9 s. Before off-line beamforming of the data, it was pre-processed with an SVD filter along the full frame length of 3900 frames to remove the quasi-stationary tissue and background signal. The RF data of each transmit angle was filtered separately and the twenty lowest ranks were removed.

6

6.2.6. BEAMFORMING WITH ADAPTIVE BEAMFORMING BY DEEP LEARNING

The ABLE method uses a neural network to calculate pixel-wise apodization weights that are adapted to the time-of-flight (TOF) corrected RF data received for that pixel. The voxel intensity of each pixel is obtained by per-pixel multiplication of the apodization weights with the TOF-corrected RF data [35]. By replacing only the apodization weight calculation rather than the full beamforming process including TOF correction, it is possible to use a compact network with a small number of layers. Here, convolutional layers with a small filter size are used to extend the receptive field of the network from just the TOF-corrected RF data for the pixel considered, to the TOF-corrected RF data of a few neighboring pixels, similar to [46]. The neural network architecture is shown in Fig. 6.2. Apodization weights were calculated for the RF data received from each of the five transmit angles in five separate branches, each with the same architecture. A branch consisted of four convolutional layers. Identical to the original ABLE implementation, each layer except for the last layer was followed with a dropout layer, which randomly disconnected nodes with a probability of 0.2, to prevent over-fitting and an anti-rectifier activation function. The anti-rectifier concatenates the positive and negative signal components before applying ReLU activations, thereby preventing loss of the negative signal components. At the same time, the anti-rectifier retains the properties of the ReLU activation function: being unbounded, preserving the dynamic range of the input, computational efficiency and a high resistance against vanishing gradients. After pixel-wise

multiplication of the apodization weights with the TOF correct RF data and subsequently summing across the channel dimension, the resulting voxel values from each of the five acquisition directions were compounded. Unlike the original ABLE beamformer, the voxels were then envelope detected to better match the output to the target and finally processed by a 1-D convolutional layer extending in the axial direction.

6.2.7. BEAMFORMING WITH NEURAL MAP

GENERAL FRAMEWORK

Most conventional beamforming methods such as DAS and MV beamforming don't utilize prior information about the tissue reflectivity of the imaged medium. Such beamforming methods can be derived from a general linear model of the measurement process

$$\mathbf{y} = \mathbf{ax} + \mathbf{n}, \quad (6.1)$$

where $\mathbf{y} \in \mathbb{R}^L$ is the observed signal for L transducer channels, \mathbf{x} is the signal of interest, the tissue reflectivity and \mathbf{n} is the noise vector. The steering vector \mathbf{a} simplifies to $\mathbf{a} = \mathbf{1}$ by applying TOF correction first to form \mathbf{y} . When no prior information about \mathbf{x} is taken into account, the most likely value of tissue reflectivity $\hat{\mathbf{x}}$ (for each individual pixel) given the measurements \mathbf{y} can then be found from the Maximum-likelihood (ML) estimate. The probability of $p(\mathbf{y}|\mathbf{x})$, can be maximized by minimizing the negative log-likelihood:

$$\hat{\mathbf{x}} = \underset{\mathbf{x}}{\operatorname{argmax}} \log p(\mathbf{x}|\mathbf{y}) = \underset{\mathbf{x}}{\operatorname{argmin}} \|\mathbf{y} - \mathbf{ax}\|_2^2 = \underset{\mathbf{x}}{\operatorname{argmin}} (\mathbf{y} - \mathbf{1}\mathbf{x})^T \mathbf{C}^{-1} (\mathbf{y} - \mathbf{1}\mathbf{x}), \quad (6.2)$$

6

here \mathbf{C} is the noise covariance matrix. When the noise distribution is assumed Gaussian, the closed-form solution gives the Delay-and-Sum beamformer and for colored noise the MV beamformer. When prior information $p(\mathbf{x})$ is available, the posterior probability $p(\mathbf{x}|\mathbf{y})$ can be found using

$$p(\mathbf{x}|\mathbf{y}) \sim p(\mathbf{y}|\mathbf{x})p(\mathbf{x}). \quad (6.3)$$

A solution for \mathbf{x} can be then be found using the maximum-a-posteriori (MAP) estimate by adding the prior knowledge of \mathbf{x} to (6.2) with a regularization term:

$$\hat{\mathbf{x}} = \underset{\mathbf{x}}{\operatorname{argmax}} \log p(\mathbf{x}|\mathbf{y}) = \underset{\mathbf{x}}{\operatorname{argmin}} \|\mathbf{y} - \mathbf{ax}\|_2^2 - \log p(\mathbf{x}) = (\mathbf{y} - \mathbf{1}\mathbf{x})^T \mathbf{C}^{-1} (\mathbf{y} - \mathbf{1}\mathbf{x}) - \log p(\mathbf{x}). \quad (6.4)$$

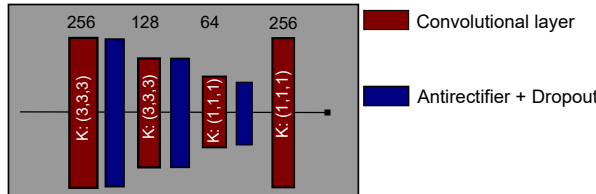
Since a closed-form solution to the MAP estimator does not exist for many prior distributions, iterative methods, such as proximal gradient descent are used to solve for $\hat{\mathbf{x}}$. One iteration of proximal gradient descent consists of taking a step towards satisfying the maximum likelihood equation, the data-consistency (DC) step and subsequently taking a step to satisfying the prior, the proximal step. For 6.4 this can be written as:

$$\tilde{\mathbf{x}}_{k+1} = \mathbf{x}_k + 2\mu \mathbf{1}^T \mathbf{C}^{-1} (\mathbf{y} - \mathbf{1}\mathbf{x}_k) \quad (6.5)$$

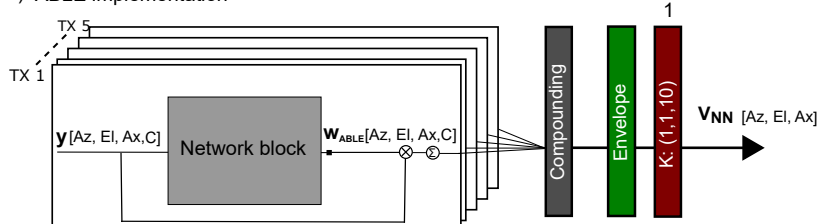
$$\hat{\mathbf{x}}_{k+1} = \operatorname{Prox}(\tilde{\mathbf{x}}_{k+1}) \quad (6.6)$$

where μ denotes the size of the gradient step and $\operatorname{Prox}(\cdot)$ denotes the proximal operator. This iterative procedure requires that the inverse covariance matrix is estimated for each

a) Network block



b) ABLE implementation



6

c) neural MAP implementation

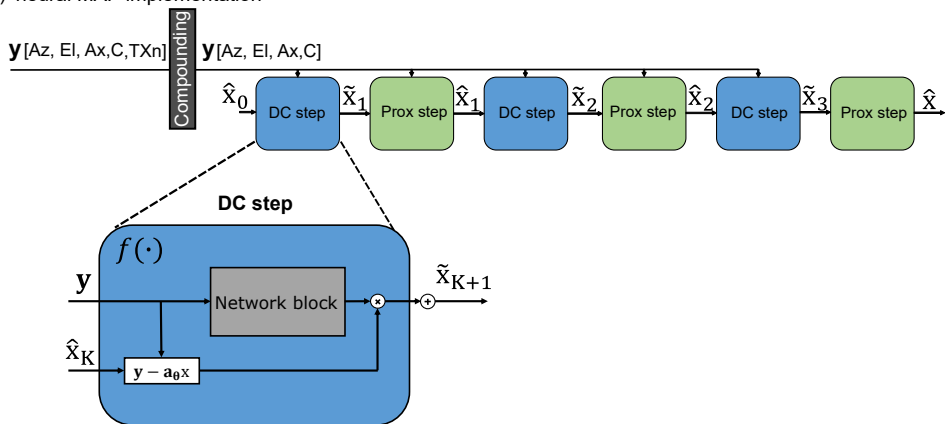


Figure 6.2: a) The main network block used for the ABLE and neural MAP implementation. The number of filters for each convolutional layer are indicated above the layer. The kernel size is indicated in the layer. b) The implementation of the ABLE beamformer. Five parallel branches are used to calculate apodization weights for the TOF corrected RF data of each transmit angle. c) The implementation of the neural MAP beamformer, 3 folds of dataconsistency and proximal steps are used.

image voxel, an often slow and unstable process. The neural MAP method [37] proposes to use neural networks to replace part of the DC step and part of the proximal step as well when it is desired to model more complex prior distributions. The iteration procedure is unfolded [38] into a forward neural network with a fixed number of iterations (also called folds) K . The general case can be written as:

$$\tilde{x}_{k+1} = x_k + f_{\theta,k}(x_k, \mathbf{y}) \quad (6.7)$$

$$\hat{x}_{k+1} = g_{\theta,k}(x_k, \mathbf{y}) \quad (6.8)$$

here θ are the trainable weights and k is the iteration number.

SPECIFIC IMPLEMENTATION

For ultrasound images acquired with a contrast agent, the acoustic reflectivity of the imaged region can be assumed to be sparse and thus modeled by a Laplace prior. The resulting proximal step has a closed-form solution, the soft-thresholding operator. It was shown that such a prior is appropriate for the detection of sparsely distributed microbubbles in ULM [30]. Here we choose a smoothed sigmoid-based soft-threshold as the proximal step in the unfolded beamformer, which is a smoothed version of the soft-threshold operator:

$$\mathcal{T}_\lambda(\tilde{x}_{k+1}) = \frac{x}{1 + e^{-\tau(|x| - \lambda)}}, \quad (6.9)$$

where τ is set equal to 1 and λ is a trainable parameter. Similar to [37] we used the ABLE model, to calculate content adaptive apodization weights based on \mathbf{y} . The calculated apodization weights are then multiplied by the residual, resulting in the following specific implementation of 1 fold of neural MAP:

$$\tilde{x}_{k+1} = \hat{x}_k + h_{\theta,k}(\mathbf{y})(\mathbf{y} - \mathbf{1}x_k), \quad (6.10)$$

$$\hat{x}_{k+1} = \mathcal{T}_\lambda(\tilde{x}_{k+1}, \mathbf{y}) \quad (6.11)$$

For $h_{\theta,k}$ the same block of four convolutional layers, dropout and antirectifier activation functions was used as for the ABLE beamformer, see Figure 6.2. Three folds were used, each containing independent weights. To keep the number of trainable parameters low, no separate branches were used for each transmit angle, instead the RF data was compounded beforehand and a single branch of the ABLE network block was used for the neural MAP implementation.

6.2.8. BEAMFORMERS FOR COMPARISON: DAS AND SC

Since the tapering of element density towards the edge of the aperture was specifically designed to reduce sidelobe levels, no further receive apodization was applied when beamforming with DAS. For SC beamforming the average spatial coherence value was calculated on the TOF corrected RF data of each voxel independently for each transmission angle and using all transducer channel pairs according to:

$$V_{SC} = \frac{\sum_{c=1}^{C-1} \sum_{l=1}^{C-c} y(c)y^*(c+l)}{\sum_{c=1}^N |y(c)|^2} \quad (6.12)$$

Here $y(c)$ is the TOF corrected signal of element c , C is the total number of elements in the array, l is the lag in number of elements and $*$ indicates the complex conjugate.

6.2.9. TRAINING PROCEDURE

During training, simulated image patches of $11 \times 11 \times 100$ voxels were randomly selected from a volume at 0.15 to 0.45 cm distance from the transducer extending -20° to 20° in azimuth and elevation. White Gaussian noise was added to the RF data during training before TOF correction to promote robustness under the influence of noise. Both the ABLE and neural MAP network were trained with the Adam[47] optimizer to minimize the mean-squared-logarithmic-error between the network output images and a Gaussian filtering of images containing the true point locations and amplitude:

$$\mathcal{L}_{\text{MSLE}}(y, x) = \frac{1}{I} \sum_{i=1}^I \left(\frac{1}{2} \left\| \log_{10}(V_{\text{NN}}^{(i)}) - \log_{10}(V_{\text{Target}}^{(i)}) \right\|_2^2 \right) \quad (6.13)$$

Here $V_{\text{NN}}^{(i)}$ refers to the network output for voxel i and $V_{\text{Target}}^{(i)}$ to the target voxel. The standard deviation of the gaussian filtering of the target voxels was annealed during training. The learning rate was $\alpha = 10^{-3}$, the exponential decay rate for the first and second moment were set according to the values suggested by [47] at $\beta_1 = 0.9$ and $\beta_2 = 0.999$. The constant for numerical stability was $\hat{\epsilon} = 10^{-7}$. The ABLE and neural MAP network were implemented using a Tensorflow (Google, CA, USA) backend.

6

6.2.10. CEUS AND ULM PROCESSING PIPELINE

Figure 6.3 summarizes the data processing pipeline. For CEUS imaging of the *in vitro* and *in vivo* data, the images were averaged in time after beamforming. For DAS imaging the averaging was performed on the envelope-detected frames, while no envelope detection was applied for the other beamforming methods. For the SC beamforming, after averaging the frames over time only the real part of the signal was kept and negative signal values were set to zero, since positive correlation values with zero phase are expected [17]. Finally, scan conversion and log compression are applied to display the CEUS images. Localization of the MBs in the simulated data and localization with tracking of the *in vivo* data was performed on the beamformed DAS, SC, ABLE and neural MAP images using the ultrasound super-resolution localization-and-tracking toolbox from Heiles et al. [40]. Small modifications were made to the framework to extend localization and tracking to three dimensions. The toolbox makes seven different algorithms available to perform the localization step. The weighted average (WA) algorithm was chosen for localization on all beamformed images since [40] showed that its overall performance together with radial symmetry-based algorithms was the highest. Although the maximum attainable resolution would be lower than RS and Gauss-fit-based algorithms it has a lower processing time.

The first step of the localization algorithm is finding the regional maxima in the image. Only the regional maxima with the highest amplitudes are kept. For the simulated data, the number of maxima that is kept N_{max} is set to the known true number of particles present in the image. For each of the remaining local maxima the WA localization kernel is applied to a cropped image centered on the local maxima. The size of this

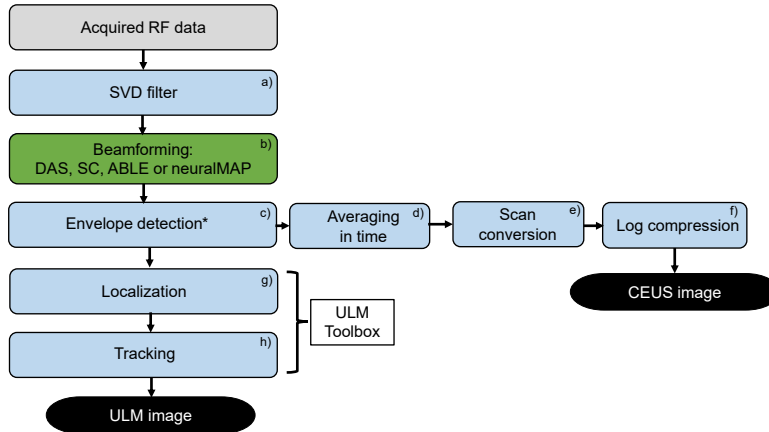


Figure 6.3: Diagram of the data processing pipeline for CEUS (steps a,b,c,d,e,f) and ULM (steps a,b,c,g,h). SVD filtering in step a) was only applied for the *in vivo* data. While envelope detection was only applied for the DAS beamformer and not for the other beamformers. The ultrasound super-resolution localization-and-tracking toolbox from Heiles et al. [40] was used for localization (g) of the simulated data and for localization and tracking (g,h) of the *in vivo* data.

cropped image S_{crop} was set based on the FWHM of the bubble after beamforming with the respective beamforming methods, see Table 6.1. It was confirmed that choosing the S_{crop} value of DAS equal to that of each of the other beamformers did not improve its localization results. Finally, local maxima were rejected if too many local maxima (N_{lmax}) were present in the cropped region around a local maximum, as well as when the final detected position was more than half the FWHM away in either direction from the initially found local maximum. All localization parameters are summarized in Table 6.1. For each beamformer, we present the results using the N_{lmax} parameter that gives the best localization results.

Table 6.1: Parameters for localization

Parameter	Value
N_{rmax} [-]	<i>in silico</i> : true # MBs, <i>in vitro</i> : 5, <i>in silico</i> : 40
S_{crop} [# pixels]	DAS: [9,9,7], SC/ABLE/neural MAP: [5,5,3].
N_{lmax} [-]	DAS: 9, SC/ABLE/neuralMAP: 3

Localization was performed on the beamformed image grid with spacing $[0.3^\circ, 0.3^\circ, \lambda/4]$. After localization, the positions were converted to Cartesian coordinates. For the *in vivo* data the toolbox[40] was then used to pair successive localizations together into tracks using Kuhn-Munkres assignment [48]. Tracks that consisted of a smaller number of localizations than the minimum track length L_{trackmin} were removed. The tracking parameters are summarized in Table 6.2.

The tracks were interpolated and then projected on a rendering grid with size R_{grid} where tracks were accumulated by incrementing the pixel intensity with 1 if a trajectory

Table 6.2: Parameters for tracking and display

Parameter	Value
$L_{trackmin}$ [# of localizations]	10
$L_{maxlink}$ [mm]	0.2
$L_{frameskip}$ [# frames]	2
$R_{grid}(x,y,z)$ [μm]	[10,10,10]
interpolation factor	10

$L_{maxlink}$ is the maximum distance between a MB in subsequent frames to reject pairing

$L_{frameskip}$ is the maximum allowed gap in microbubble pairings

passes through that pixel. Finally, a power compression factor of 1/3 was applied to the density for display of the image.

6.2.11. EVALUATION PROCESS AND METRICS

HISTOGRAM MATCHING

To make a fair visual and quantitative comparison between the performance of different beamformers the effect of dynamic range compression and displayed dynamic range must be separated from the information content in the image. Bottenus *et al.* [49] have proposed to separate the structural changes from the images' respective embeddings by placing the images all under the same embedding through histogram matching. The Matlab implementation made available by [49] was used to implement full histogram matching of both DAS and SC images towards the reference ABLE method. Full histogram matching was used since this resulted in a better match of overall appearance than partial histogram matching. The number of bins was set to 256.

SEPARATION OF NEIGHBORING SIMULATED MBs

The full-width at half-maximum (FWHM) is often used to describe the resolution of an imaging system. However, when using nonlinear beamformers the FWHM can easily be fooled, taking on a better value as it would through a simple dynamic range transformation, without having improved the information present in the image [50]. Sparrow's criterion [51], is a measure for resolution that uses the spacing between two points and is unaffected by dynamic range transformations. It expresses the resolution limit as the spacing between two points where the dip in intensity between them just disappears to form a flat plateau. Here, two pointscatterers have been simulated with Field II at increasing lateral distance to visualize when independent peaks start to appear.

LOCALIZATION OF SIMULATED MICROBUBBLES

For the simulated data the ground truth is available, therefore more quantitative criteria can be used to evaluate the result than for *in vivo* data. The following metrics are used to evaluate the performance of the localization algorithm on images generated by the

different beamformers: precision, recall, Jaccard index (JAC), detected density and localization error. The Precision is calculated as the fraction of correctly localized bubbles from the total amount of detected bubbles:

$$\text{Precision} = \frac{\text{TP}}{\text{TP} + \text{FP}}. \quad (6.14)$$

Here TP is the number of True Positive localizations and FP is the number of False Positive localizations. A localization is termed a correct localization when it is within a $\lambda/2$ distance w.r.t. the true position. Recall gives an indication of missed positive predictions and is calculated as the fraction of correctly localized bubbles from the total set of true micro-bubbles:

$$\text{Recall} = \frac{\text{TP}}{\text{TP} + \text{FN}}. \quad (6.15)$$

Here FN is the number of False Negative localizations. The Jaccard index is used as a measure of localization accuracy:

$$\text{JAC} = \frac{\text{TP}}{\text{TP} + \text{FN} + \text{FP}} \quad (6.16)$$

For the correct localizations (TPs), the localization error is calculated as the average root-mean-square-error between the localized bubble positions (x_i, y_i, z_i) and their ground truth locations $(x_i^{\text{GT}}, y_i^{\text{GT}}, z_i^{\text{GT}})$:

$$\text{RMSE}_{\text{loc}} = \frac{1}{\text{TP}} \sum_{i=1}^{\text{TP}} \sqrt{(x_i - x_i^{\text{GT}})^2 + (y_i - y_i^{\text{GT}})^2 + (z_i - z_i^{\text{GT}})^2}. \quad (6.17)$$

The detected microbubble density ρ_{detected} is calculated from the true microbubble density ρ_{GT} and the Recall:

$$\rho_{\text{detected}} = \rho_{\text{GT}} \text{Recall} \quad (6.18)$$

6.3. RESULTS

6.3.1. SIMULATION: SEPARATION OF MICROBUBBLES

Fig. 6.4 shows beamformed C-plane images of a single point scatterer and two simulated points scatterers at increasing distances w.r.t. each other. Complimentary to this Fig. 6.5 shows the lateral intensity profile. For the single scatterer, the DAS beamformed image has the largest PSF, while that of the SC beamformer is smaller and the PSF of ABLE and neural MAP is smaller than SC by an approximately equal amount. After histogram matching the DAS and SC beamformed images to those of the ABLE beamformer, the PSF of the DAS beamformed image is reduced to approximately that of the original SC image and the PSF of the SC image is smaller than the PSF in the ABLE and neural MAP image. When the scatterers are placed at a distance of 1.4 mm the top-view is elongated w.r.t that of a single scatterer. However, the lateral intensity profile in Fig. 6.5 doesn't show a separation of the two peaks for the DAS and SC beamformed images and neither do their histogram-matched counterparts. For the ABLE and neural MAP image, two separate peaks are present, although their height is unequal. At 1.6 mm distance, it is

possible to observe the separation of the two scatterers in the lateral beamprofile for the ABLE and neural MAP beamformer as well as for the SC beamformed image. However, the dip for the SC beamformed image is barely -1 dB while that of ABLE and neural MAP and the SC image after histogram matching is between -15 and -18 dB. At a distance of 3.2 mm, there is a clear separation of the scatterers, where all beamformers show a dip in the beamprofile between the two peaks that is below -6 dB.

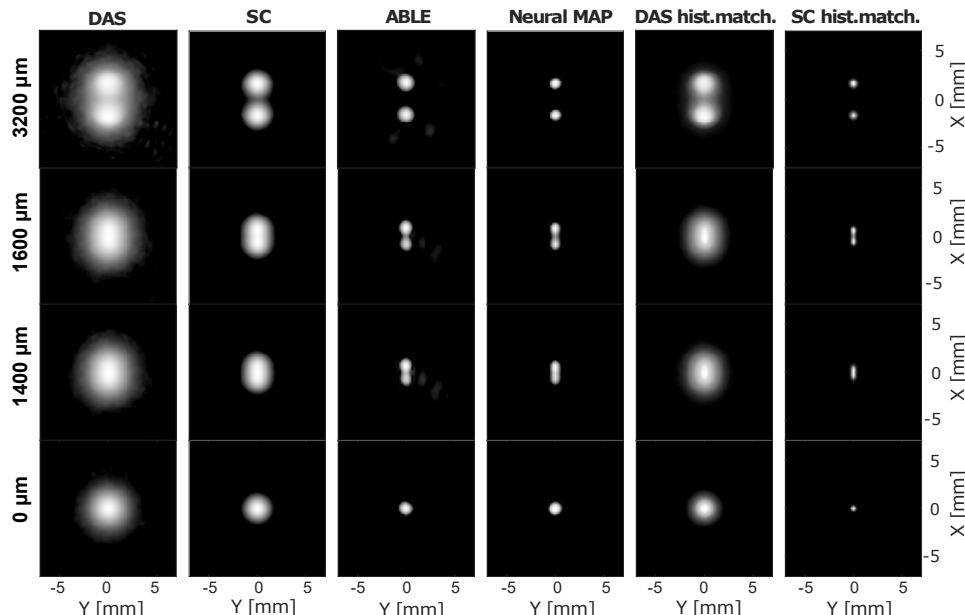


Figure 6.4: Simulated point scatterers at a number of distances, beamformed with DAS, SC, ABLE and neural MAP. The DAS and SC beamformer responses are also shown after histogram matching to ABLE. The images are shown for a dynamic range from -60 to 0 dB. From the top row to the bottom row the distance between point scatterers is decreased.

6.3.2. SIMULATION: IMAGE OF MICROBUBBLE CLOUDS

Figure 6.6 shows an example image from the test set. The concentration is 55 microbubbles / cm^3 . As reference the true locations are shown with a gaussian filtering. It is visible that both ABLE and neural MAP display two closeby scatterers more clearly as individual microbubbles than the DAS and SC image. After histogram matching the resolution of the DAS and SC images is improved, however some of the microbubbles with lower intensity are no longer visible in the DAS and SC images.

6.3.3. SIMULATION: LOCALIZATION

Fig. 6.7 shows the results of microbubble localization on volumetric images with a microbubble concentration between 4 and 181 microbubbles/ cm^3 for all four beamformers. The lowest recall and precision and thereby also the lowest JAC index is achieved by localization on the DAS images. The JAC index for localization on the SC beamformed

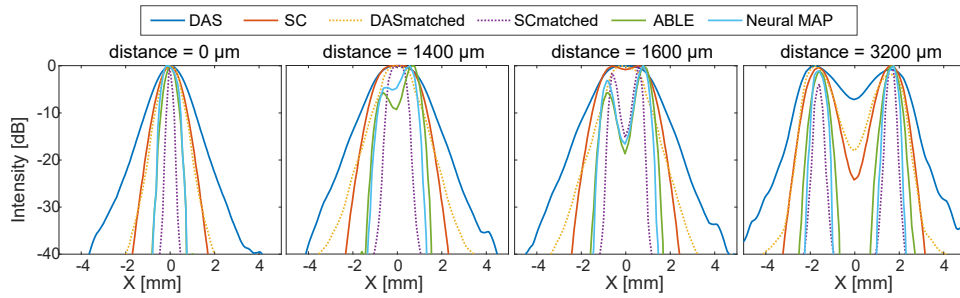


Figure 6.5: Intensity of beamformed response of simulated point scatterers for the DAS, SC, ABLE and neural MAP beamformer. The result of the DAS and SC beamformer are also shown after histogram matching to ABLE.

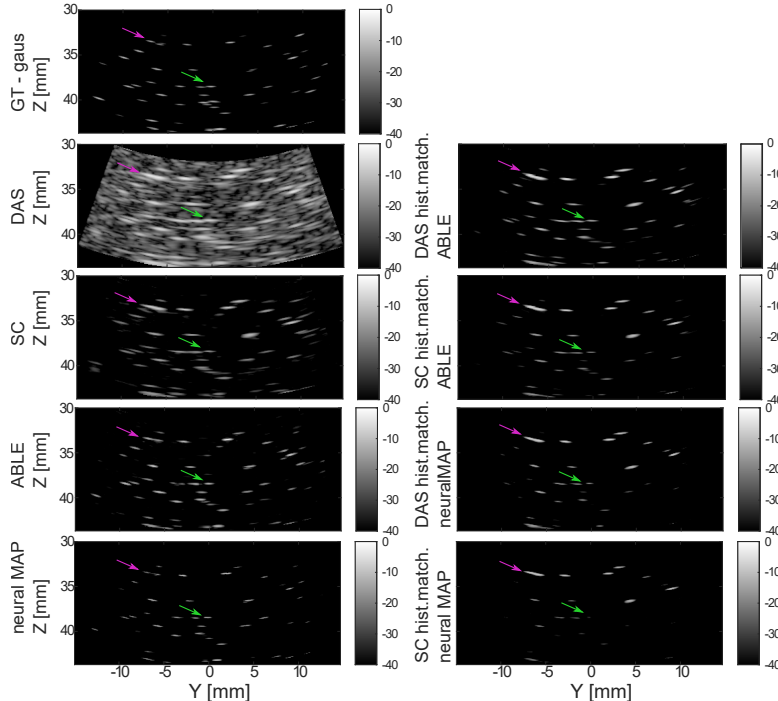


Figure 6.6: *Left Top*) The ground truth positions and amplitude of the simulated microbubbles are visualized in a lateral plane by a Gaussian filtering of the point scatterers. *Left row 2-5)* Beamformed images with DAS, SC, ABLE and neural MAP respectively. *Right row 2-3)* DAS and SC beamformed image after histogram matching to ABLE. *Right row 4-5)* DAS and SC beamformed image after histogram matching to neural MAP. The pink arrow shows two microbubbles that are more clearly separated by ABLE and neural MAP than DAS and SC, also after histogram matching. The green arrow shows two microbubbles that are more clearly separated by neural MAP than the other beamformers.

images is higher for every concentration. For all but the highest two concentrations, where their scores become equal, the ABLE beamformer has a higher JAC index than the SC beamformer. Neural MAP has a further improved JAC index for all concentrations. On average the JAC index of SC is 0.19 higher than that of DAS, that of ABLE is 0.26 higher than DAS and neural MAP is 0.31 higher than DAS. The localization error is highest for DAS, lowest for the SC beamformer and the neural MAP and ABLE beamformer have a localization error in between these two. The highest microbubble density is detected with the neural MAP beamformer for all concentrations.

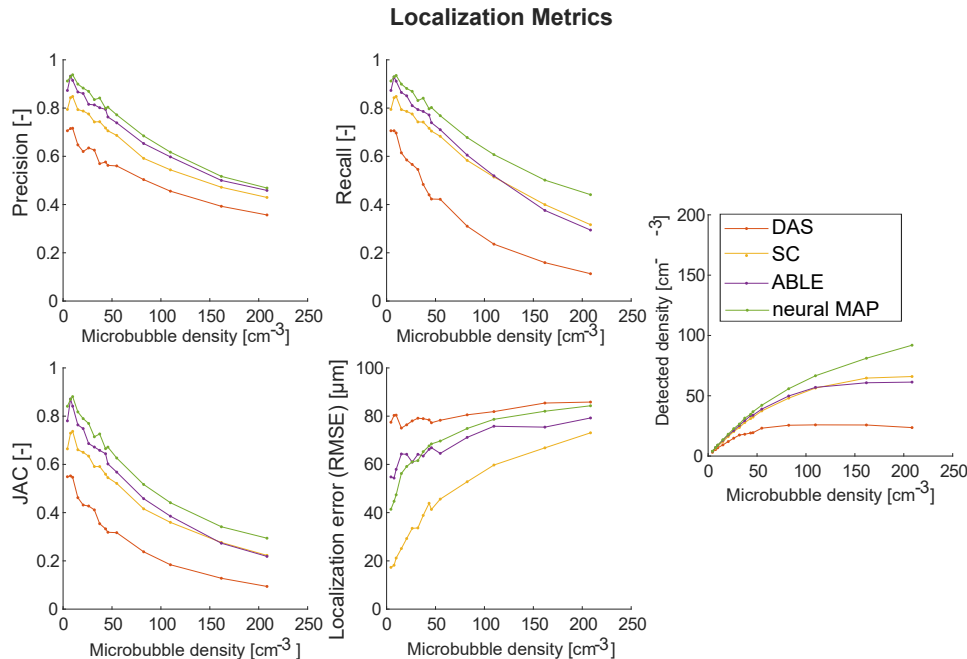


Figure 6.7: Comparison of localization metrics after localization on DAS, SC, ABLE and neural MAP images of clouds of randomly placed point scatterers with varying density.

6.3.4. IN *vitro* EXPERIMENT: HELICAL TUBE

Fig. 6.8 shows time-averaged images of the helical tube after beamforming with DAS, SC, ABLE and neural MAP. Using the same dynamic range to display all images would either not allow visualizing the tube with DAS due to the high amplitude of the background, or would remove a large part of the signal from the bubbles in the tube for the other beamformers. Therefore, images are displayed in a dynamic range where the background intensity falls just outside of the dynamic range displayed (up to the nearest 5 dB). The DAS and SC images are smoother, whereas in the ABLE and neural MAP images more individual bubbles are visible in the time-averaged image.

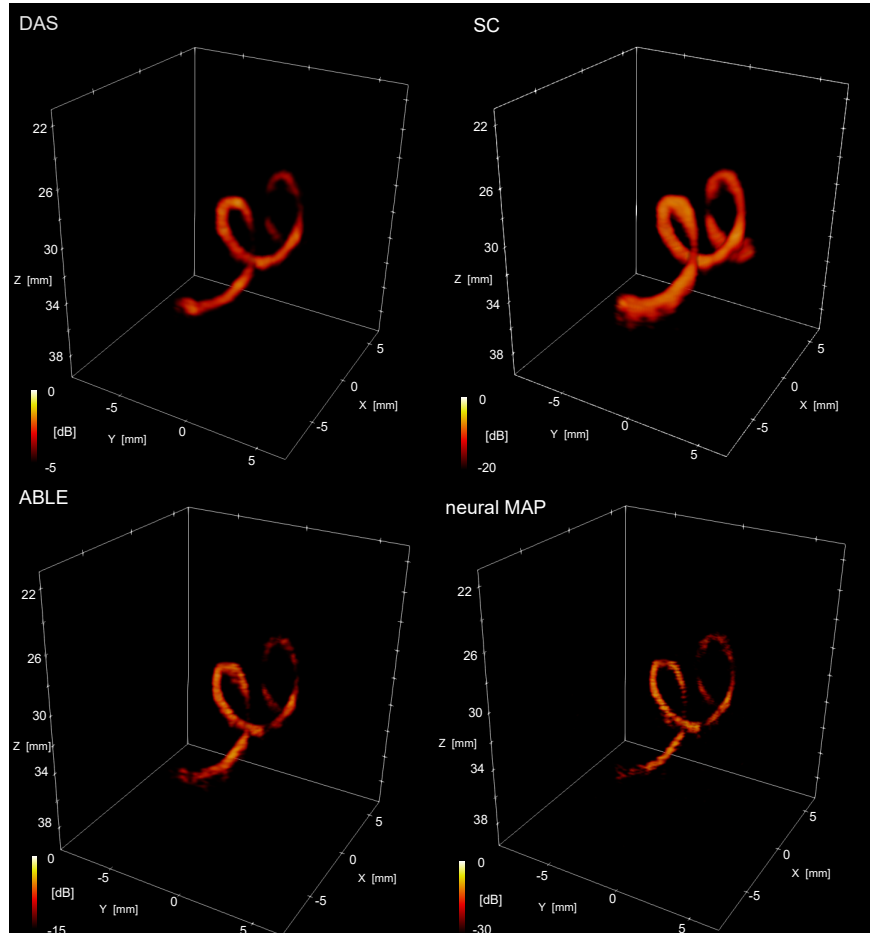


Figure 6.8: Volume render of microbubbles flowing through a helical tube. 390 frames at 100 Hz are beam-formed with either, DAS, SC, ABLE or neural MAP and then averaged. For each beamformer a dynamic range is used where the background signal falls just below the lower bound of the dynamic range.

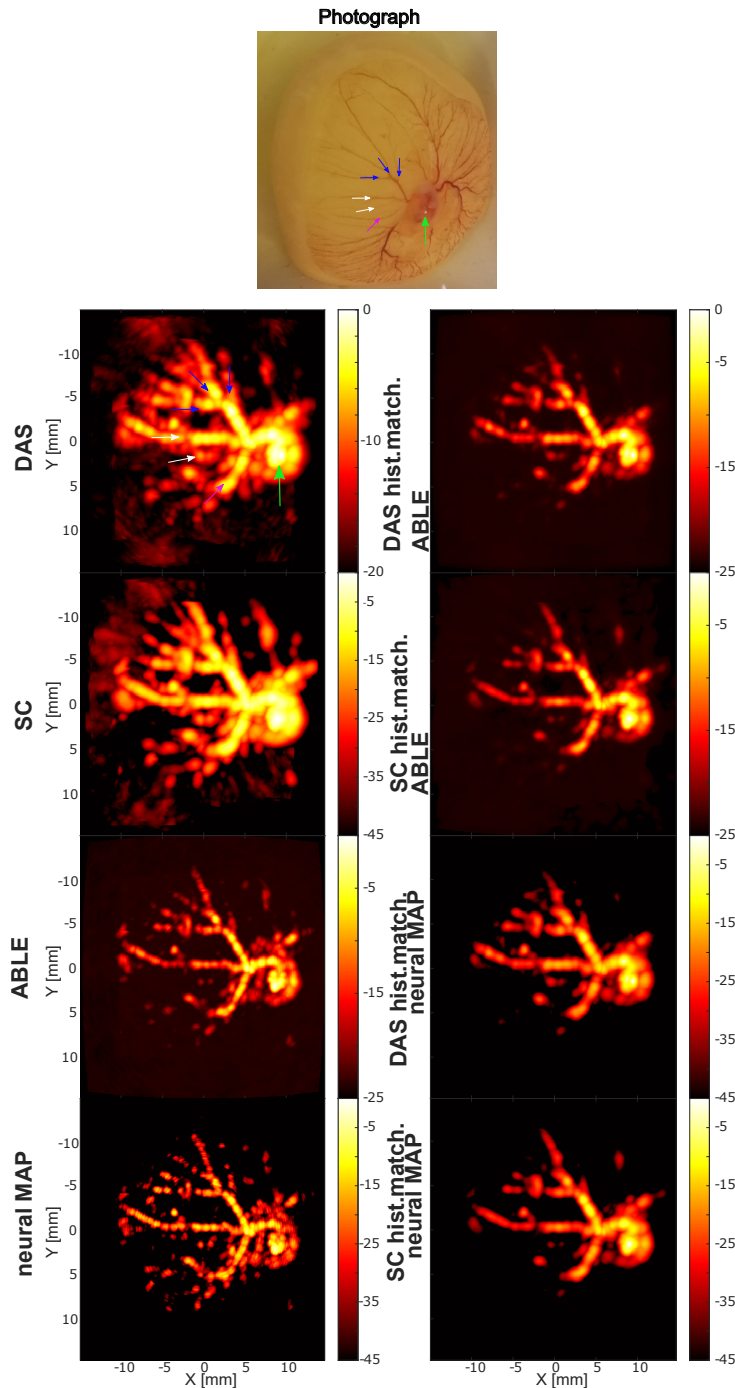


Figure 6.9: *Top row*) Photograph of the chicken embryo and CAM. The arrows indicate vessels (blue, white, purple) and the heart (green) that are also indicated in the ultrasound image below it. *Left row* 2-5 maximum intensity projection (MIP) image in the XY plane of 3900 time-averaged frames recorded at 1kHz, for DAS, SC, ABLE and neural MAP beamforming. *Right row* 2-3) MIP image beamformed by DAS an SC, displayed after histogram matching to ABLE. *Right row* 4-5) MIP image beamformed by DAS an SC, displayed after histogram matching to neural MAP.

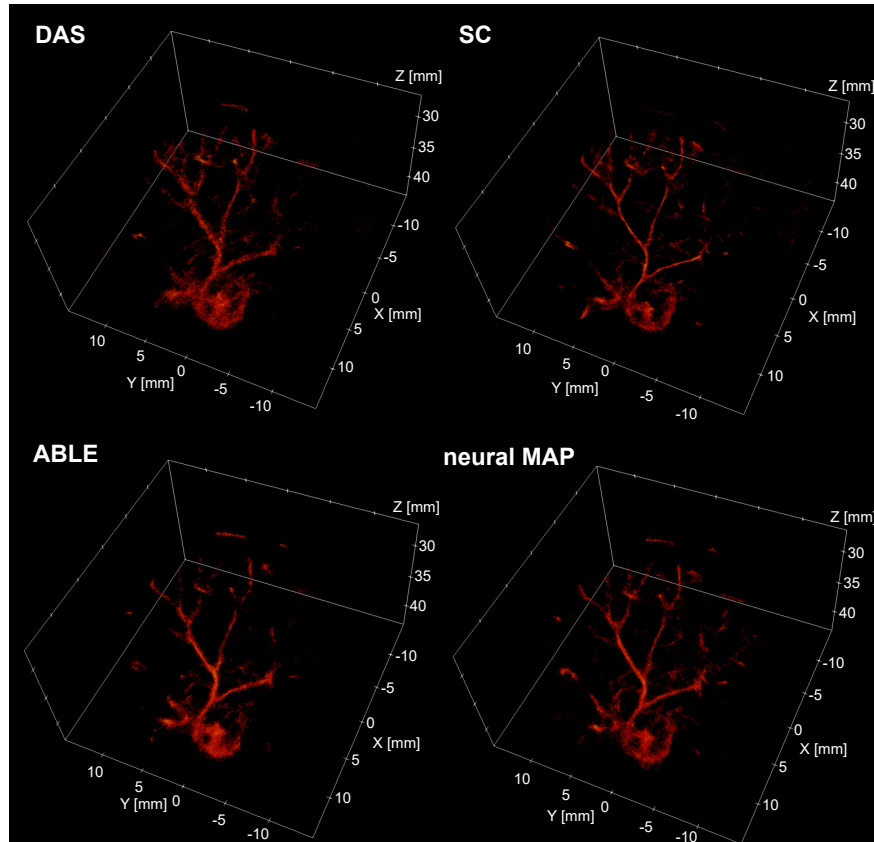


Figure 6.10: Microbubble density renderings after interpolation in tracking based on 3900 frames recorded at 1kHz. The renderings shown are based on localization and tracking of DAS, SC, ABLE and neural MAP beamformed images.

6.3.5. *In vivo* EXPERIMENT: CHICKEN EMBRYO

Fig. 6.9 shows the maximum intensity projection (MIP) of 3900 subsequent frames. After SVD filtering the RF data it was beamformed with DAS, SC, ABLE and neural MAP respectively and subsequently each set was averaged over time. After matching the histograms of the DAS and SC images to that of the ABLE or neural MAP image and displaying them in the same dynamic range, visually the contrast between the vessels and the background is similar. However, not all details that are present in the neural MAP or ABLE image are visible in the DAS and SC images. Furthermore, the resolution is higher in the ABLE and neural MAP images, such that there is an increased separation of the vessels and the heart is better separated from surrounding vessels. The neural MAP and ABLE images display approximately the same level of detail, however, the neural MAP beamformer simultaneously achieves an improved suppression of unwanted background signal.

Fig. 6.10 shows a super-resolved 3D render of the interpolated microbubble density of the chicken embryo and CAM. The super-resolved image based on the DAS beamformed images has the highest level of disorganization, showing the least clear tracks and least sharp delineation of the heart. SC, ABLE and neural MAP show a more narrow vessel diameter. Both SC and neural MAP depict some more distal parts of vessel branches more clearly than DAS and ABLE.

6

6.4. DISCUSSION AND CONCLUSION

High-frame-rate volumetric CEUS and ULM recordings of the vasculature are highly desired to enable a full visualization of the underlying 3D structure, out-of-plane motion correction, the effective application of post-processing filters as well as shorter acquisition times. With sparse arrays, high-frame-rate volumetric imaging can be realized at a reduced channel count and electronic complexity compared to fully populated arrays integrated with application-specific integrated circuits (ASICs). Unlike row-column arrays, sparse array retain the flexibility to transmit diverging waves thereby allowing a wide field of view to be realized from a small acoustic window. However, the high level of secondary lobes associated with sparse arrays compared to fully populated arrays can cause image artifacts, while the unfocused transmit beams needed to realize high-frame-rate imaging negatively impact resolution. The reduced image quality has a negative effect on the visualization of the microvasculature. Therefore improving the image quality with better beamforming methods is desirable. In this chapter, we have applied the deep learning-based ABLE and neural MAP beamformer to reconstruct volumetric contrast images acquired with a sparse spiral array. CEUS images of *in silico*, *in vitro* and *in vivo* data were compared for the DAS, SC, ABLE and neural MAP beamformers, while localization performance was quantitatively evaluated on *in silico* data and ULM performance was shown on *in vivo* data.

For a single *in silico* scatterer, the FWHM of ABLE and neural MAP are similar and reduced compared to that of DAS, even after histogram matching to separate effects from dynamic range stretching. However, after histogram matching, the FWHM of the SC beamformer has transformed from larger than that of ABLE and neural MAP to smaller. The DAS beamformer did not show a separation of two simulated microbubbles at 1.6 mm distance, even after histogram matching, while the separation was visible by a clear

dip (<-6 dB) in the lateral beamprofile for the ABLE and neural MAP beamformer. For the SC beamformer the separation was initially less than 1 dB, however, histogram matching transformed the dip in the beamprofile to a similar level of that of ABLE and neural MAP. This suggests that there is an increased ability of SC, ABLE and neural MAP compared to DAS to separate closeby microbubbles, although an evaluation of closeby scatterers at a greater variation of positions and possibly noise levels would be required for a more definitive evaluation of the *in silico* potential to separate closeby scatterers.

In the simulation of bubble clouds SC, ABLE and neural MAP showed better suppression of noise and clutter compared to DAS beamforming. ABLE and especially neural MAP showed a better separation of bubbles compared to DAS and SC beamforming. This translated to an increased precision and recall in the localization of microbubbles in the simulated bubble clouds when beamforming with SC compared to DAS, a further increased precision and recall by ABLE and the highest precision and recall was achieved by neural MAP beamforming. This meant that the average JAC index, which can be considered as a weighted combination of precision and recall, when averaged over the concentrations considered, increased from 0.36 for DAS to 0.54 for SC, 0.61 for ABLE and 0.66 for neural MAP. The time-averaged *in vivo* image of a chicken embryo and chorioallantoic membrane showed that after histogram matching to ABLE or neural MAP, a similar level of contrast between the vessels and background can be achieved for all beamformers. However, the increased *in vivo* resolution of the ABLE and especially the neural MAP beamformed images is visible from an increased separation between vessels that cannot be simply recreated with an adjustment of the dynamic range.

Although, a clear qualitative improvement in the *in silico* and *in vivo* images is visible for the ABLE and even more so neural MAP beamformer and this translates to a quantitative improvement in localization performance of the *in silico* data, the effect of the different beamformers on the *in vivo* ULM images is less clear. The ULM rendering based on DAS beamformed images has the least sharp vessels, while vessels look visually sharper for ABLE, neural MAP and SC. Where SC vessels have the thinnest diameter. Neural MAP seems to show slightly more filling of the vessels most distal from the heart. Although these results seem to indicate that using SC or neural MAP is beneficial for ULM imaging and that ABLE only has a moderately positive effect on ULM imaging compared to DAS, it is difficult to draw definitive conclusions based on these images for a number of reasons. First of all, a good filling of the vessels in the image is not achieved. This is probably the result of the relatively low number of frames in the recording for ULM. Unwanted removal of some slow-moving bubbles by the SVD filter could also play a role. The chicken embryo and CAM vessels are an interesting *in vivo* model to investigate different ultrasound methods for CEUS and ULM, because it is an easily accessible and relatively low-cost method, which allows comparison to optical images [45]. *In vivo* models with more extensive branching patterns are interesting to use, however, *in vivo* ULM images remain hard to evaluate in general and are often evaluated subjectively due to the lack of a ground truth or gold standard to evaluate the images by.

Even though, the ABLE and even more so the neural MAP beamformer, qualitatively improve the CEUS image, the improvement of the ULM image could be limited for a number of reasons. It is possible that a beamformer has a positive effect on *in vivo* localization, but that the overall impact is low, because the improvement is limited to

removing localizations that would have been removed by tracking anyway. It is also possible, that the improvement in *in silico* localization does not extend to an improvement in *in vivo* localization. This is difficult to evaluate due to a lack of ground truth availability in an *in vivo* situation. However, ways to improve *in vivo* localization of the deep learning-based beamformers include making the training data closer to the *in vivo* imaging scenario. For example, by including information on the element sensitivity of the transducer used in the acquisition, or by including more realistic background clutter from real recordings in the training RF data. Next, it should be considered that a training target consisting of the true point scatterer location smoothed by a small gaussian filtering is not necessarily the ideal input for optimal performance of the localization algorithm. To realize a beamformer that performs in a way that is specifically tailored to localization performance a method as described in [28], where a neural network for beamforming and a neural network for localization are trained jointly, should be considered. Furthermore, since the final ULM image is made after performing tracking, a method that also includes tracking in the deep learning pipeline as shown in [52], could be considered.

Finally, the improvement of the ABLE and neural MAP beamformer should be considered against the increased computational cost compared to DAS and SC beamforming. For 2D imaging an inference time of 30–35 ms per frame was achieved for neural MAP [37], which would be increased for volumetric imaging. However, since off-line processing of the *in vivo* RF data was still required to achieve sufficient performance of the SVD filter and 3D ULM is not yet implemented in real-time, the beamformer would not be the limiting factor, but one of the factors that still require off-line processing.

REFERENCES

- [1] D. Cosgrove and N. Lassau, “Imaging of perfusion using ultrasound”, *European Journal of Nuclear Medicine and Molecular Imaging*, vol. 37, no. SUPPL. 1, pp. 65–85, 2010. DOI: [10.1007/s00259-010-1537-7](https://doi.org/10.1007/s00259-010-1537-7).
- [2] P. Frinking, T. Segers, Y. Luan, and F. Tranquart, “Three decades of ultrasound contrast agents: a review of the past, present and future improvements”, *Ultrasound in medicine & biology*, vol. 46, no. 4, pp. 892–908, 2020. DOI: [10.1016/j.ultrasmedbio.2019.12.008](https://doi.org/10.1016/j.ultrasmedbio.2019.12.008).
- [3] P. G. Ranganath, M. L. Robbin, S. J. Back, E. G. Grant, and D. T. Fetzer, “Practical advantages of contrast-enhanced ultrasound in abdominopelvic radiology”, *Abdominal Radiology*, vol. 43, no. 4, pp. 998–1012, 2018. DOI: [10.1007/s00261-017-1442-7](https://doi.org/10.1007/s00261-017-1442-7).
- [4] P. S. Sidhu, V. Cantisani, C. F. Dietrich, O. H. Gilja, A. Saftoiu, E. Bartels, M. Bertolotto, F. Calliada, D. A. Clevert, *et al.*, “The EFSUMB guidelines and recommendations for the clinical practice of contrast-enhanced ultrasound (CEUS) in Non-Hepatic Applications: Update 2017 (Long Version)”, *Ultraschall in der Medizin*, vol. 39, no. 2, e2–e44, 2018. DOI: [10.1055/a-0586-1107](https://doi.org/10.1055/a-0586-1107).
- [5] C. Dietrich, M. Averkiou, M. Nielsen, R. Barr, P. Burns, F. Calliada, V. Cantisani, B. Choi, M. Chammas, *et al.*, “How to perform Contrast-Enhanced Ultrasound (CEUS)”, *Ultrasound International Open*, vol. 04, no. 01, E2–E15, Jan. 2018. DOI: [10.1055/s-0043-123931](https://doi.org/10.1055/s-0043-123931).
- [6] J. Wang, R. Zhao, and J. Cheng, “Diagnostic accuracy of contrast-enhanced ultrasound to differentiate benign and malignant breast lesions: A systematic review and meta-analysis”, *European Journal of Radiology*, vol. 149, no. January, p. 110219, 2022. DOI: [10.1016/j.ejrad.2022.110219](https://doi.org/10.1016/j.ejrad.2022.110219).
- [7] M. Siepmann, G. Schmitz, J. Bzyl, M. Palmowski, and F. Kiessling, “Imaging tumor vascularity by tracing single microbubbles”, in *2011 IEEE International Ultrasonics Symposium*, IEEE, 2011, pp. 1906–1909. DOI: [10.1109/ULTSYM.2011.0476](https://doi.org/10.1109/ULTSYM.2011.0476).
- [8] O. Couture, B. Besson, G. Montaldo, M. Fink, and M. Tanter, “Microbubble ultrasound super-localization imaging (MUSLI)”, in *2011 IEEE International Ultrasonics Symposium*, IEEE, 2011, pp. 1285–1287. DOI: [10.1109/ULTSYM.2011.6293576](https://doi.org/10.1109/ULTSYM.2011.6293576).

[9] M. A. O'Reilly and K. Hynynen, "A super-resolution ultrasound method for brain vascular mapping", *Medical physics*, vol. 40, no. 11, p. 110 701, 2013. DOI: [10.1118/1.4823762](https://doi.org/10.1118/1.4823762).

[10] C. Errico, J. Pierre, S. Pezet, Y. Desailly, Z. Lenkei, O. Couture, and M. Tanter, "Ultrafast ultrasound localization microscopy for deep super-resolution vascular imaging", *Nature*, vol. 527, no. 7579, pp. 499–502, 2015. DOI: [10.1038/nature16066](https://doi.org/10.1038/nature16066).

[11] Y. Desailly, O. Couture, M. Fink, and M. Tanter, "Sono-activated ultrasound localization microscopy", *Applied Physics Letters*, vol. 103, no. 17, p. 174 107, 2013. DOI: [10.1063/1.4826597](https://doi.org/10.1063/1.4826597).

[12] K. Christensen-Jeffries, R. J. Browning, M.-X. Tang, C. Dunsby, and R. J. Eckersley, "In vivo acoustic super-resolution and super-resolved velocity mapping using microbubbles", *IEEE transactions on medical imaging*, vol. 34, no. 2, pp. 433–440, 2014. DOI: [10.1109/TMI.2014.2359650](https://doi.org/10.1109/TMI.2014.2359650).

[13] O. Couture, V. Hingot, B. Heiles, P. Muleki-Seya, and M. Tanter, "Ultrasound localization microscopy and super-resolution: A state of the art", *IEEE transactions on ultrasonics, ferroelectrics, and frequency control*, vol. 65, no. 8, pp. 1304–1320, 2018. DOI: [10.1109/TUFFC.2018.2850811](https://doi.org/10.1109/TUFFC.2018.2850811).

[14] K. Christensen-Jeffries, O. Couture, P. A. Dayton, Y. C. Eldar, K. Hynynen, F. Kiessling, M. O. Reilly, G. E. Pinton, G. Schmitz, *et al.*, "Super-resolution Ultrasound Imaging", *Ultrasound in Medicine and Biology*, vol. 46, no. 4, pp. 865–891, Apr. 2020. DOI: [10.1016/j.ultrasmedbio.2019.11.013](https://doi.org/10.1016/j.ultrasmedbio.2019.11.013).

[15] C. Demené, T. Deffieux, M. Pernot, B.-F. Osmanski, V. Biran, J.-L. Gennisson, L.-A. Sieu, A. Bergel, S. Franqui, *et al.*, "Spatiotemporal clutter filtering of ultrafast ultrasound data highly increases Doppler and fUltrasound sensitivity", *IEEE transactions on medical imaging*, vol. 34, no. 11, pp. 2271–2285, 2015. DOI: [10.1109/TMI.2015.2428634](https://doi.org/10.1109/TMI.2015.2428634).

[16] S. Harput, P. Tortoli, R. J. Eckersley, C. Dunsby, M. X. Tang, K. Christensen-Jeffries, A. Ramalli, J. Brown, J. Zhu, *et al.*, "3-D Super-Resolution Ultrasound Imaging with a 2-D Sparse Array", *IEEE Transactions on Ultrasonics, Ferroelectrics, and Frequency Control*, vol. 67, pp. 269–277, 2 2020. DOI: [10.1109/TUFFC.2019.2943646](https://doi.org/10.1109/TUFFC.2019.2943646).

[17] L. Wei, G. Wahyulaksana, B. Meijlink, A. Ramalli, E. Noothout, M. D. Verweij, E. Boni, K. Kooiman, A. F. Van Der Steen, *et al.*, "High Frame Rate Volumetric Imaging of Microbubbles Using a Sparse Array and Spatial Coherence Beamforming", *IEEE Transactions on Ultrasonics, Ferroelectrics, and Frequency Control*, vol. 68, no. 10, pp. 3069–3081, 2021. DOI: [10.1109/TUFFC.2021.3086597](https://doi.org/10.1109/TUFFC.2021.3086597).

[18] A. Urban, C. Dussaux, G. Martel, C. Brunner, E. Mace, and G. Montaldo, "Real-time imaging of brain activity in freely moving rats using functional ultrasound", *Nature methods*, vol. 12, no. 9, pp. 873–878, 2015. DOI: [10.1038/nmeth.3482](https://doi.org/10.1038/nmeth.3482).

[19] H. Kimura, R. D. Braun, E. T. Ong, R. Hsu, T. W. Secomb, D. Papahadjopoulos, K. Hong, and M. W. Dewhirst, "Fluctuations in red cell flux in tumor microvessels can lead to transient hypoxia and reoxygenation in tumor parenchyma", *Cancer research*, vol. 56, no. 23, pp. 5522–5528, 1996.

[20] E. Macé, G. Montaldo, I. Cohen, M. Baulac, M. Fink, and M. Tanter, "Functional ultrasound imaging of the brain", *Nature methods*, vol. 8, no. 8, pp. 662–664, 2011. DOI: [10.1038/nmeth.1641](https://doi.org/10.1038/nmeth.1641).

[21] L. I. Cárdenas-Navia, D. Mace, R. A. Richardson, D. F. Wilson, S. Shan, and M. W. Dewhirst, "The pervasive presence of fluctuating oxygenation in tumors", *Cancer research*, vol. 68, no. 14, pp. 5812–5819, 2008. DOI: [10.1158/0008-5472.CAN-07-6387](https://doi.org/10.1158/0008-5472.CAN-07-6387).

[22] J. Yu, L. Lavery, and K. Kim, "Super-resolution ultrasound imaging method for microvasculature in vivo with a high temporal accuracy", *Scientific reports*, vol. 8, no. 1, pp. 1–11, 2018. DOI: [10.1038/s41598-018-32235-2](https://doi.org/10.1038/s41598-018-32235-2).

[23] F. Foroozan, M. A. O'Reilly, and K. Hynynen, "Microbubble localization for three-dimensional super-resolution ultrasound imaging using curve fitting and deconvolution methods", *IEEE Transactions on Biomedical Engineering*, vol. 65, no. 12, pp. 2692–2703, 2018. DOI: [10.1109/TBME.2018.2813759](https://doi.org/10.1109/TBME.2018.2813759).

[24] A. Bar-Zion, C. Tremblay-Darveau, O. Solomon, D. Adam, and Y. C. Eldar, "Fast vascular ultrasound imaging with enhanced spatial resolution and background rejection", *IEEE transactions on medical imaging*, vol. 36, no. 1, pp. 169–180, 2016. DOI: [10.1109/TMI.2016.2600372](https://doi.org/10.1109/TMI.2016.2600372).

[25] R. J. G. van Sloun, O. Solomon, Y. C. Eldar, H. Wijkstra, and M. Mischi, "Sparsity-driven super-resolution in clinical contrast-enhanced ultrasound", in *2017 IEEE International Ultrasonics Symposium (IUS)*, IEEE, 2017, pp. 1–4. DOI: [10.1109/ULTSYM.2017.8092945](https://doi.org/10.1109/ULTSYM.2017.8092945).

[26] A. Bar-Zion, O. Solomon, C. Tremblay-Darveau, D. Adam, and Y. C. Eldar, "SUSHI: Sparsity-based ultrasound super-resolution hemodynamic imaging", *IEEE transactions on ultrasonics, ferroelectrics, and frequency control*, vol. 65, no. 12, pp. 2365–2380, 2018. DOI: [10.1109/TUFFC.2018.2873380](https://doi.org/10.1109/TUFFC.2018.2873380).

[27] O. Solomon, R. J. G. van Sloun, H. Wijkstra, M. Mischi, and Y. C. Eldar, "Exploiting flow dynamics for superresolution in contrast-enhanced ultrasound", *IEEE transactions on ultrasonics, ferroelectrics, and frequency control*, vol. 66, no. 10, pp. 1573–1586, 2019. DOI: [10.1109/TUFFC.2019.2926062](https://doi.org/10.1109/TUFFC.2019.2926062).

[28] J. Youn, B. Luijten, M. Schou, M. B. Stuart, Y. C. Eldar, R. J. Van Sloun, and J. A. Jensen, "Model-based Deep Learning on Ultrasound Channel Data for Fast Ultrasound Localization Microscopy", *IEEE International Ultrasonics Symposium, IUS*, pp. 21–24, 2021. DOI: [10.1109/IUS52206.2021.9593435](https://doi.org/10.1109/IUS52206.2021.9593435).

[29] R. J. G. van Sloun, O. Solomon, M. Bruce, Z. Z. Khaing, H. Wijkstra, Y. C. Eldar, and M. Mischi, "Super-resolution ultrasound localization microscopy through deep learning", *IEEE transactions on medical imaging*, vol. 40, no. 3, pp. 829–839, 2020. DOI: [10.1109/TMI.2020.3037790](https://doi.org/10.1109/TMI.2020.3037790).

[30] R. J. G. Van Sloun, R. Cohen, and Y. C. Eldar, "Deep learning in ultrasound imaging", *Proceedings of the IEEE*, vol. 108, no. 1, pp. 11–29, 2019. DOI: [10.1109/jproc.2019.2932116](https://doi.org/10.1109/jproc.2019.2932116).

[31] J. Youn, M. L. Ommen, M. B. Stuart, E. V. Thomsen, N. B. Larsen, and J. A. Jensen, "Detection and localization of ultrasound scatterers using convolutional neural networks", *IEEE Transactions on Medical Imaging*, vol. 39, no. 12, pp. 3855–3867, 2020. DOI: [10.1109/TMI.2020.3006445](https://doi.org/10.1109/TMI.2020.3006445).

[32] J. Youn, B. Luijten, M. Bo Stuart, Y. C. Eldar, R. J. Van Sloun, and J. Arendt Jensen, "Deep learning models for fast ultrasound localization microscopy", *IEEE International Ultrasonics Symposium, IUS*, vol. 2020-Septe, pp. 17–20, 2020. DOI: [10.1109/IUS46767.2020.9251561](https://doi.org/10.1109/IUS46767.2020.9251561).

[33] X. Liu, T. Zhou, M. Lu, Y. Yang, Q. He, and J. Luo, "Deep learning for ultrasound localization microscopy", *IEEE transactions on medical imaging*, vol. 39, no. 10, pp. 3064–3078, 2020. DOI: [10.1109/TMI.2020.2986781](https://doi.org/10.1109/TMI.2020.2986781).

[34] K. Diamantis, T. Anderson, M. B. Butler, C. A. Villagomez-Hoyos, J. A. Jensen, and V. Sboros, "Resolving ultrasound contrast microbubbles using minimum variance beamforming", *IEEE Transactions on Medical Imaging*, vol. 38, no. 1, pp. 194–204, 2019. DOI: [10.1109/TMI.2018.2859262](https://doi.org/10.1109/TMI.2018.2859262).

[35] B. Luijten, R. Cohen, F. J. De Bruijn, H. A. Schmeitz, M. Mischi, Y. C. Eldar, and R. J. Van Sloun, "Adaptive Ultrasound Beamforming Using Deep Learning", *IEEE Transactions on Medical Imaging*, vol. 39, no. 12, pp. 3967–3978, 2020. DOI: [10.1109/TMI.2020.3008537](https://doi.org/10.1109/TMI.2020.3008537).

[36] B. W. Ossenkoppele, L. Wei, B. Luijten, H. J. Vos, N. De Jong, R. J. Van Sloun, and M. D. Verweij, "3-D contrast enhanced ultrasound imaging of an *in vivo* chicken embryo with a sparse array and deep learning based adaptive beamforming", in *2022 IEEE International Ultrasonics Symposium (IUS)*, IEEE, 2022, pp. 1–4. DOI: [10.1109/IUS54386.2022.9957383](https://doi.org/10.1109/IUS54386.2022.9957383).

[37] B. Luijten, B. W. Ossenkoppele, N. de Jong, M. D. Verweij, Y. C. Eldar, M. Mischi, and R. J. van Sloun, "Neural maximum-a-posteriori beamforming for ultrasound imaging", in *ICASSP 2023 - 2023 IEEE International Conference on Acoustics, Speech and Signal Processing (ICASSP)*, 2023, pp. 1–5. DOI: [10.1109/ICASSP49357.2023.10096073](https://doi.org/10.1109/ICASSP49357.2023.10096073).

[38] K. Gregor and Y. LeCun, "Learning fast approximations of sparse coding", in *Proceedings of the 27th international conference on international conference on machine learning*, 2010, pp. 399–406.

[39] R. J. G. Van Sloun, R. Cohen, and Y. C. Eldar, "Deep learning in ultrasound imaging", *Proceedings of the IEEE*, vol. 108, no. 1, pp. 11–29, 2019. DOI: [10.1109/JPROC.2019.2932116](https://doi.org/10.1109/JPROC.2019.2932116).

[40] B. Heiles, A. Chavignon, V. Hingot, P. Lopez, E. Teston, and O. Couture, "Performance benchmarking of microbubble-localization algorithms for ultrasound localization microscopy", *Nature Biomedical Engineering*, vol. 6, no. 5, pp. 605–616, 2022. DOI: [10.1038/s41551-021-00824-8](https://doi.org/10.1038/s41551-021-00824-8).

[41] A. Ramalli, E. Boni, A. S. Savoia, and P. Tortoli, "Density-tapered spiral arrays for ultrasound 3-D imaging", *IEEE Transactions on Ultrasonics, Ferroelectrics, and Frequency Control*, vol. 62, pp. 1580–1588, 8 2015. DOI: [10.1109/TUFFC.2015.007035](https://doi.org/10.1109/TUFFC.2015.007035).

[42] H. J. Vos, E. Boni, A. Ramalli, F. Piccardi, A. Traversi, D. Galeotti, E. C. Noothout, V. Daeichin, M. D. Verweij, *et al.*, "Sparse volumetric PZT array with density tapering", in *2018 IEEE International Ultrasonics Symposium (IUS)*, IEEE, 2018, pp. 1–4. DOI: [10.1109/ULTSYM.2018.8580197](https://doi.org/10.1109/ULTSYM.2018.8580197).

[43] J. Jensen, "Field: A program for simulating ultrasound systems", in *10th Nordic-Baltic Conference on Biomedical Imaging*, vol. 34, Supple, 1996, pp. 351–353.

[44] M. van der Ven, J. J. Luime, L. L. van der Velden, J. G. Bosch, J. M. Hazes, and H. J. Vos, "High-frame-rate power Doppler ultrasound is more sensitive than conventional power Doppler in detecting rheumatic vascularisation", *Ultrasound in Medicine & Biology*, vol. 43, no. 9, pp. 1868–1879, 2017. DOI: [10.1016/j.ultrasmedbio.2017.04.027](https://doi.org/10.1016/j.ultrasmedbio.2017.04.027).

[45] B. Meijlink, I. Skachkov, A. F. van der Steen, N. de Jong, and K. Kooiman, "The preparation of chicken *ex ovo* embryos and chorioallantoic membrane vessels as *in vivo* model for contrast-enhanced ultrasound imaging and microbubble-mediated drug delivery studies", *Journal of Visualized Experiments*, vol. 2021, pp. 1–27, 168 2021. DOI: [10.3791/62076](https://doi.org/10.3791/62076).

[46] B. W. Ossenkoppele, B. Luijten, D. Bera, N. de Jong, M. D. Verweij, and R. J. G. van Sloun, "Improving Lateral Resolution in 3-D Imaging With Micro-beamforming Through Adaptive Beamforming by Deep

Learning”, *Ultrasound in Medicine & Biology*, vol. 49, no. 1, pp. 237–255, 2023. DOI: [10.1016/j.ultrasmdbio.2022.08.017](https://doi.org/10.1016/j.ultrasmdbio.2022.08.017).

[47] D. P. Kingma and J. L. Ba, “Adam: A method for stochastic optimization”, *3rd International Conference on Learning Representations, ICLR 2015 - Conference Track Proceedings*, pp. 1–15, 2015. DOI: [10.48550/arXiv.1412.6980](https://doi.org/10.48550/arXiv.1412.6980).

[48] H. W. Kuhn, “The Hungarian method for the assignment problem”, *Naval research logistics quarterly*, vol. 2, no. 1-2, pp. 83–97, 1955. DOI: [10.1002/nav.3800020109](https://doi.org/10.1002/nav.3800020109).

[49] N. Bottenus, B. C. Byram, and D. Hyun, “Histogram Matching for Visual Ultrasound Image Comparison”, vol. 68, pp. 1487–1495, 5 2021. DOI: [10.1109/TUFFC.2020.3035965](https://doi.org/10.1109/TUFFC.2020.3035965).

[50] D. Hyun, G. B. Kim, N. Bottenus, and J. J. Dahl, “Ultrasound Lesion Detectability as a Distance Between Probability Measures”, *IEEE Transactions on Ultrasonics, Ferroelectrics, and Frequency Control*, vol. 69, no. 2, pp. 732–743, 2022. DOI: [10.1109/TUFFC.2021.3138058](https://doi.org/10.1109/TUFFC.2021.3138058).

[51] C. M. Sparrow, “On spectroscopic resolving power”, *The Astrophysical Journal*, vol. 44, p. 76, 1916.

[52] T. S. Stevens, E. B. Herbst, B. Luijten, B. W. Ossenkoppele, T. J. Voskuil, S. Wang, J. Youn, C. Errico, M. Mischi, *et al.*, “A Hybrid Deep Learning Pipeline for Improved Ultrasound Localization Microscopy”, in *2022 IEEE International Ultrasonics Symposium (IUS)*, 2022, pp. 1–4. DOI: [10.1109/IUS54386.2022.9958562](https://doi.org/10.1109/IUS54386.2022.9958562).

7

DISCUSSION AND RECOMMENDATIONS

This chapter discusses the contributions made in the thesis, puts their applications and limitations in context and notes recommendations for future work.

7.1. A HIGH-FRAME-RATE 3D-ICE TRANSDUCER FOR EWI

The first three chapters of this thesis focused on the development of a transducer for high-frame-rate 3D-ICE. Chapter 2 described the design of an imaging scheme and transducer layout aiming to enable high-frame-rate volumetric acquisitions suitable for electromechanical wave imaging. Chapters 3 and 4 described the development and testing of two consecutively realized prototypes of the high-frame-rate 3D-ICE transducer. Successful high-frame-rate volumetric imaging with the 3D-ICE prototype was realized. However, further steps need to be taken to realize diagnostically relevant imaging. Some of the needed steps include further research and developments in the electromechanical wave imaging technique in general, while others relate more specifically to the high-frame-rate 3D-ICE transducer.

7.1.1. ELECTROMECHANICAL WAVE IMAGING

In Chapter 2 it was proposed that electromechanical wave imaging with a high-frame-rate 3D-ICE transducer could provide an atrial map that can be used for localization of the arrhythmogenic sites. Such a map is useful in planning the ablation procedure and in assessing the ablation treatment. Currently, electroanatomical mapping during atrial ablation procedures is realized by introducing another catheter or set of catheters specifically for electroanatomical mapping. However, the various existing electroanatomical methods have disadvantages, including long procedure times due to the need for point-by-point mapping, the need for ionizing radiation to guide the electroanatomical mapping and only providing a superficial mapping of the endocardial surface. The electromechanical activation that EWI provides could be used in a similar manner as

an electroanatomical map. With EWI the electrical activation is not directly measured, but an anatomical map is made of the onset of the muscle contraction, which is a direct result of the electrical activation. There exists an electromechanical delay between the electrical activation and the onset of muscle contraction, which is not constant throughout the heart [1]. However, several studies have already shown that electromechanical activation maps recorded with EWI, have a strong correlation with recorded electrical activation and thus strongly reflect the electrical behavior of the myocardium [2–5].

While most studies of EWI so far were based on 2D images or 3D renders acquired by the interpolation of multiple 2D views [6], some 3D recordings have been made in Langendorff perfused heart set-ups [7], in open-chest canines and transthoracically in humans [8]. In these studies, the importance of using high-frame-rate 3D imaging to capture the dynamic 3D contraction movement was noted as well. 2D EWI has been performed transthoracically in humans for the atrium during atrial arrhythmias [9, 10]. For the atrium specifically, 3D EWI has been demonstrated transthoracically in humans during sinus rhythm [8] and 3D rendered transthoracic EWI has been demonstrated for the localization of two types of regular arrhythmias [11]. However, in general more research is needed to evaluate whether the use of EWI can lead to specific diagnoses for individual patients. Specifically in the context of a 3D-ICE probe, it needs to be determined whether 3D EWI can improve treatment planning for atrial fibrillation and how it could enhance or replace parts of the current clinical routine.

So far EWI has been studied with non-invasive transthoracic imaging. However, when EW images are acquired by ICE the imaging depth and thus also the attenuation is greatly reduced. As such, a higher central frequency can be used, thereby realizing EW images with better spatial resolution in the atrium. Furthermore, compared to transthoracic ultrasound, unwanted reflections from the patient's ribs and lungs can be avoided. The advantages and challenges of EWI with HFR ICE need to be evaluated further. EWI of a Langendorff-perfused heart with high-frame-rate ICE probes is a next step that is of great interest. While initial evaluations with HFR 2D-ICE probes could provide some verification of the technique, the availability of within-heartbeat HFR 3D-ICE will be needed to gain further insight into the possibilities to generate EWI maps for localizing arrhythmias.

The development of EWI is not only interesting from the perspective of providing a clinical tool to improve the localization and treatment of cardiac arrhythmias. EWI also has the potential to fill the gap that currently exists in available methods for mapping mechanical aspects of cardiac disease. By evaluating electrical function with an electrical mapping system and using high-frame-rate 3D ultrasound to evaluate the mechanical contraction, the link between electrical and mechanical factors in cardiac disease can be studied further [8].

7.1.2. HIGH-FRAME-RATE 3D-ICE CATHETER

Realizing a high-frame-rate 3D-ICE transducer requires a careful evaluation of trade-offs to come up with a design that tackles the data rate challenge and realizes sufficient image quality with a very limited number of acquisitions per volume, while staying within the additional constraints of transducer size and power dissipation. In Chapter 2 a transducer and imaging scheme were proposed for a high-frame-rate 3D-ICE probe that

would fulfill the requirements for EWI of atrial fibrillation. The proposed solution consisted of 1D micro-beamforming in the elevation direction to reduce channel count and data rate, while using transmit beams that have a narrow divergence along the direction of micro-beamforming to suppress grating lobes. Their divergence along the azimuth direction is wide enough to span the intended field of view. By transmitting the fan-shaped beams in only 7 elevational directions, the desired 1 kHz frame rate is achieved. The combination of the data received from the 7 angles was designed to further suppress grating lobes. The divergence angle and frame rate were optimized to achieve a high spatial resolution with a low level of so-called axial lobes or secondary pulses. Chapter 4 showed that the prototype transducer can achieve the desired transmit beamforming flexibility, the needed micro-beamforming and that 3D imaging at the desired 1kHz frame rate is possible, while cable count can be reduced to a realistic number for a catheter-based probe. However, there are some limitations in the current probe that should be addressed in subsequent iterations of a HFR 3D-ICE device.

First of all, the realized 16 x 18 element array constitutes a full prototype in the elevational direction, but is only a quarter of the final intended size in the azimuth direction. The main bottleneck to realize a full design was the development of the data connection to the mainframe. The time and cost needed to develop a dedicated data connection solution for the full-sized prototype did not fit within the constraints of the project. The smaller size results in a lower SNR and smaller azimuthal resolution than for a full prototype. From the successful functionality demonstrated with the smaller prototype, it is recommended to develop a full-sized prototype. Placing this subsequent prototype including the cable connections in a protective housing would make it more suitable for use in a range of experimental settings.

A slightly less obvious result of having a smaller than full-sized transducer is the fact that the intended diverging wave cannot be generated with exactly the same transmit delay strategy. However, the 7 steered transmit beams can be generated in a somewhat less ideal way, with a dual virtual source strategy. Alternatively, the same single virtual source strategy can be used and either the azimuthal or elevational width of the beam can be slightly adjusted. Furthermore, the center frequency and desired divergence angle were chosen based on the values that minimized the effect of axial lobes while having a relatively high center frequency. With a different sized transducer and slightly different center frequency from the actual prototype the intended azimuthal divergence angle might not be optimal for suppressing unwanted axial lobes. Although this might seem like a small technical detail and practically this just means that some more settings can be evaluated for the best imaging setting in further experiments, it also illustrates that once a transducer layout and imaging scheme is carefully optimized, small changes will impact the optimization efforts.

The imaging requirements for EWI with a 3D-ICE probe were based on properties of the electromechanical wave and experience from previous research on EWI. The proposed HFR 3D-ICE transducer design would achieve an azimuthal lateral resolution that is likely sufficient for EWI along the full imaging depth. In the elevational direction the lateral resolution would be worse than the 5 mm value that was the initial aim of the design, for depths greater than approximately half the desired imaging depth. This should however be considered in light of the fact that only a few studies have been done with

3D-EWI, and the studies that were performed by spatially interpolating a few 2D planes rather than using a single 2D plane already provided valuable extra information on the electromechanical wave [3, 6]. The desired frame rate of 1 kHz was achieved, thereby resulting in a probe that outperforms current 3D-ICE designs in terms of frame rate. However, this desired value is not a requirement that is set in stone. Some research on EWI suggests that this rate is only needed for local motion detection and that interleaving techniques can be used to reduce the needed frame rate, however it is still unknown whether that would be the case for atrial arrhythmia mapping. Clearly, further experimental research on EWI is required to get a more definitive insight into the lateral resolution and frame rate that are needed to provide valuable clinical information. In the meantime, devices still need to be developed based on the best known information of the requirements, to have the tools to do further research with.

Besides its capability for EWI, the 3D-ICE probe is designed such that it can also operate in different imaging modes. Transmit delay patterns can be generated to transmit diverging or plane waves over a larger number of angles, such that higher image quality at a lower frame rate can be realized through coherent compounding. Focused transmits are also possible. In this way, the probe can be used to produce higher-quality images for image guidance during cardiac interventional procedures as well. Furthermore, the 1kHz frame rate does not just enable EWI, but also other ultrafast ultrasound imaging applications that benefit from 3D imaging.

Integrating an array of matrix elements on an ASIC has the advantage of an improved SNR compared to a sparse array, more flexibility in the transmit scheme than a row-column array and fewer imaging artifacts than either a sparse or row-column array. However, integrating transducer elements directly on an ASIC has the disadvantage that silicon is far from an ideal backing material for the transducer elements. The thin layer interfacing the PZT elements of the prototype with the ASIC provides little damping and the ASIC itself also has a low acoustic attenuation. Direct reflections cause ringing in the transmit profile and a reduced bandwidth of the transducer. Furthermore, acoustic energy propagates through the ASIC as Lamb waves [12] that excite neighboring elements. This unwanted crosstalk also negatively impacts the directivity pattern of the array [13, 14]. To prevent the ASIC from having a negative impact on image quality, several solutions have been proposed, including the use of a high impedance backing to force the PZT elements to vibrate in quarter-wavelength mode [15, 16], a very thick interposer layer with highly attenuating conductive material [17], or a differently designed interposer layer with lower thickness [14]. There is no agreement yet on the optimal solution and further development is needed to determine the best way to minimize negative acoustic effects from integrating PZT elements on an ASIC.

7.2. DEEP LEARNING-BASED BEAMFORMING FOR 3D US

Chapter 5 showed that the lateral resolution of volumetric ultrasound images can be improved by using deep learning in the beamforming process. This was shown specifically for a matrix array that applies on-chip micro-beamforming, as is employed for channel count reduction in the 3D-ICE prototype. The training targets were formed by volumetric images acquired with a larger aperture array, which inherently has a better lateral resolution. Only a small amount of training data was required and the training data can

consist entirely of simple simulations. It was possible to use only a modest amount of training data, because the ABLE method replaces only a critical part of the image reconstruction process rather than replacing it completely with a neural network [18, 19]. In general, the need for massive amounts of data and computational resources to train highly parameterized deep neural networks can be avoided by not blindly replacing a complete process with a generic neural network. When a model-based deep learning approach is used, the benefit of learning from data can be obtained while using a limited amount of data by also using knowledge of the specific application, realizing a hybrid model-based deep learning solution [18, 20–22].

In light of the desire to realize high-quality imaging with the small aperture 3D-ICE array, it is promising that the result from Chapter 5 shows that adaptive beamforming by deep learning (ABLE) can be used to improve the lateral resolution of miniature arrays that employ micro-beamforming. However, it remains to be investigated how the improved lateral resolution in the acquired images will translate to EWI specifically. It is recommended that further research is done in the development of deep learning-based processing methods specifically aimed at EWI, where a correlation-based displacement estimation is extracted from the RF data.

Another aspect in the development of matrix arrays where the application of deep learning seems opportune is for the suppression of grating and axial lobes arising from insufficient spatial sampling. Deep learning methods for suppressing grating lobes have been investigated in the context of periodic sparse arrays aimed at reducing the channel count in receive, however *in vivo* results indicate that further improvement of existing techniques is required [23].

In Chapters 5 and 6, deep learning-based beamformers were used to improve the image quality of volumetric ultrasound images, and their performance was compared against the linear DAS beamformer and other common adaptive beamforming methods. Recently, an important concern was raised regarding the comparison of adaptive beamformers. Image quality metrics that have been commonly used to evaluate image contrast, such as CR and CNR, cannot directly be used to compare adaptive beamformers [24, 25]. These metrics can be changed by a simple dynamic range transformation, an operation that can change the apparent contrast of the image without altering the image in such a way that it provides new information or improves the ability of detecting lesions. For an adaptive beamformer, part of an apparent improvement in these metrics can be due to a trivial dynamic range transformation. The GCNR metric, which was recently proposed to circumvent this problem [25], was used for the quantitative evaluation of contrast in Chapter 5. In Chapter 6 histogram matching [26] was used to achieve a fair qualitative comparison of the resolution of *in vivo* images reconstructed with different beamforming methods. These new tools provide improved ways to qualitatively and quantitatively compare ultrasound image reconstruction methods. Still these newer approaches for fair image comparison require careful application and avenues remain open for the metrics to be fooled. Thus, further development of robust metrics to quantitatively evaluate images are required. This is especially the case for resolution. Although criteria exist that define resolution in a way that is resistant to dynamic range stretching, these are not practically suited for the evaluation of *in vivo* images.

A concern that has been raised towards the application of deep learning-based beam-

formers in commercial systems is dealing with user-based preferences. A clinician may often have a set of preferred post-processing settings that are selected on the ultrasound system. After building years of experience evaluating images with a certain level of for example speckle, images with a different characteristic may not be directly preferred by the user. Several strategies can be considered to circumvent this problem, such as allowing the user to select only regional enhancements. Other methods that have been proposed are the use of switchable CycleGAN architecture to allow the user to tune the level of enhancement [27].

A general concern in the application of deep learning is unwanted bias. The risk of introducing unwanted bias in machine/deep learning algorithms has received significant attention with their increased use across many application domains. In the wider media, reports on bias of deep learning have particularly focused on cases where bias leads to prejudice and unfair and unethical treatment of groups of people. In the field of medical imaging, effort is undertaken to identify and address systematic mathematical bias, which leads to differences between the expected performance and the observed performance of deep learning in the clinic [28, 29]. Minimizing unwanted bias is essential for the wider adoption of deep learning in the medical field. However, there is not one single place or phase where bias is introduced or can be mitigated. Instead, bias can result from different steps in the development process, including the data collection, data handling, model development and selection or use of performance metrics [28, 30, 31].

In Chapters 5 and 6 the performance of ABLE and neural MAP was evaluated on in silico, in vitro and in vivo data. However, the limited availability of in vivo data meant that in Chapter 5 in vivo performance was only evaluated on cardiac images of a porcine heart and in Chapter 6 only on a chicken embryo with CAM. Having a wider set of images available that closely resembles the distribution of images in the target application is the ideal situation, but can be challenging to realize in some situations, e.g. when considering in vivo data collection with a novel prototype device. Although the in vivo population was small, the risk of introducing bias by overfitting to a small population was mitigated by the use of in silico data in the training set. Furthermore, the small receptive field of the neural network in the ABLE implementation (only a few voxels) prevents the algorithm from forming a reliance on recognizing large structures in the image data. This means that the risk of overfitting to the specific structures present in the training data is mitigated. Bias can also be introduced by the objective function. As an example, for ultrasound images, which have a large dynamic range, the (signed)-mean-squared-logarithmic error is more suitable than the mean-square-error. The choice of evaluation metrics can also result in bias in deep learning models when an incomplete set of metrics is used or when the metrics don't reflect practical improvement well. Future research in improving performance metrics for ultrasound imaging will help prevent bias in the selection of deep learning models and image processing techniques in general.

REFERENCES

- [1] E. Kovacheva, L. Baron, O. Dössel, and A. Loewe, "Electro-Mechanical Delay in the Human Heart: A Study on a Simple Geometry", in *2018 Computing in Cardiology Conference (CinC)*, IEEE, vol. 45, 2018, pp. 1–4. DOI: [10.22489/CinC.2018.199](https://doi.org/10.22489/CinC.2018.199).

[2] J. Provost, W.-N. Lee, K. Fujikura, and E. E. Konofagou, "Imaging the electromechanical activity of the heart *in vivo*", *Proceedings of the National Academy of Sciences*, vol. 108, no. 21, pp. 8565–8570, 2011. DOI: [10.1073/pnas.1011688108](https://doi.org/10.1073/pnas.1011688108).

[3] A. Costet, E. Wan, E. Bunting, J. Grondin, H. Garan, and E. Konofagou, "Electromechanical wave imaging (EWI) validation in all four cardiac chambers with 3D electroanatomic mapping in canines *in vivo*", *Physics in Medicine & Biology*, vol. 61, no. 22, p. 8105, 2016. DOI: [10.1088/0031-9155/61/22/8105](https://doi.org/10.1088/0031-9155/61/22/8105).

[4] J. Grondin, A. Costet, E. Bunting, A. Gambhir, H. Garan, E. Wan, and E. E. Konofagou, "Validation of electromechanical wave imaging in a canine model during pacing and sinus rhythm", *Heart Rhythm*, vol. 13, no. 11, pp. 2221–2227, 2016. DOI: [10.1016/j.hrthm.2016.08.010](https://doi.org/10.1016/j.hrthm.2016.08.010).

[5] J. Provost, V. Gurev, N. Trayanova, and E. E. Konofagou, "Mapping of cardiac electrical activation with electromechanical wave imaging: an *in silico*–*in vivo* reciprocity study", *Heart Rhythm*, vol. 8, no. 5, pp. 752–759, 2011. DOI: doi.org/10.1016/j.hrthm.2010.12.034.

[6] L. Melki, C. S. Grubb, R. Weber, P. Nauleau, H. Garan, E. Wan, E. S. Silver, L. Liberman, and E. E. Konofagou, "Localization of accessory pathways in pediatric patients with Wolff-Parkinson-White syndrome using 3D-rendered electromechanical wave imaging", *JACC: Clinical Electrophysiology*, vol. 5, no. 4, pp. 427–437, 2019. DOI: [10.1016/j.jacep.2018.12.001](https://doi.org/10.1016/j.jacep.2018.12.001).

[7] J. Christoph, M. Chebbok, C. Richter, J. Schröder-Schetalig, P. Bittihn, S. Stein, I. Uzelac, F. H. Fenton, G. Hasenfuß, *et al.*, "Electromechanical vortex filaments during cardiac fibrillation", *Nature*, vol. 555, no. 7698, pp. 667–672, 2018. DOI: [10.1038/nature26001](https://doi.org/10.1038/nature26001).

[8] J. Grondin, D. Wang, C. S. Grubb, N. Trayanova, and E. E. Konofagou, "4D cardiac electromechanical activation imaging", *Computers in biology and medicine*, vol. 113, p. 103382, 2019. DOI: doi.org/10.1016/j.combiomed.2019.103382.

[9] J. Provost, A. Costet, E. Wan, A. Gambhir, W. Whang, H. Garan, and E. E. Konofagou, "Assessing the atrial electromechanical coupling during atrial focal tachycardia, flutter, and fibrillation using electromechanical wave imaging in humans", *Computers in biology and medicine*, vol. 65, pp. 161–167, 2015. DOI: [10.1016/j.combiomed.2015.08.005](https://doi.org/10.1016/j.combiomed.2015.08.005).

[10] J. Provost, A. Gambhir, J. Vest, H. Garan, and E. E. Konofagou, "A clinical feasibility study of atrial and ventricular electromechanical wave imaging", *Heart Rhythm*, vol. 10, no. 6, pp. 856–862, 2013. DOI: [10.1016/j.hrthm.2013.02.028](https://doi.org/10.1016/j.hrthm.2013.02.028).

[11] C. S. Grubb, L. Melki, D. Y. Wang, J. Peacock, J. Dizon, V. Iyer, C. Sorbera, A. Biviano, D. A. Rubin, *et al.*, "Noninvasive localization of cardiac arrhythmias using electromechanical wave imaging", *Science translational medicine*, vol. 12, no. 536, eaax6111, 2020. DOI: [10.1126/scitranslmed.aax611](https://doi.org/10.1126/scitranslmed.aax611).

[12] M. Shabanimotlagh, V. Daeichin, S. B. Raghunathan, P. Kruizinga, H. J. Vos, J. G. Bosch, M. Pertij, N. De Jong, and M. Verweij, "Optimizing the directivity of piezoelectric matrix transducer elements mounted on an ASIC", in *IEEE International Ultrasonics Symposium, IUS*, 2017, pp. 5–8. DOI: [10.1109/ULTSYM.2017.8091752](https://doi.org/10.1109/ULTSYM.2017.8091752).

[13] M. Shabanimotlagh, "Ultrasound Matrix Transducers for High Frame Rate 3D Medical Imaging", Ph.D. dissertation, Delft University of Technology, 2018. DOI: [10.4233/uuid:7ce26659-91fa-45a0-bfdf-7223375fed69](https://doi.org/10.4233/uuid:7ce26659-91fa-45a0-bfdf-7223375fed69).

[14] D. S. Dos Santos, F. Fool, M. Mozaffarzadeh, M. Shabanimotlagh, E. Noothout, T. Kim, N. Rozsa, H. J. Vos, J. G. Bosch, *et al.*, "A Tiled Ultrasound Matrix Transducer for Volumetric Imaging of the Carotid Artery", *Sensors*, vol. 22, no. 24, p. 9799, 2022. DOI: [10.3390/s22249799](https://doi.org/10.3390/s22249799).

[15] D. Wildes, W. Lee, B. Haider, S. Cogan, K. Sundaresan, D. M. Mills, C. Yetter, P. H. Hart, C. R. Haun, *et al.*, "4-D ICE: A 2-D Array Transducer with Integrated ASIC in a 10-Fr Catheter for Real-Time 3-D Intracardiac Echocardiography", *IEEE Transactions on Ultrasonics, Ferroelectrics, and Frequency Control*, vol. 63, no. 12, pp. 2159–2173, 2016. DOI: [10.1109/TUFFC.2016.2615602](https://doi.org/10.1109/TUFFC.2016.2615602).

[16] S. Lee, K. Choi, K. Lee, Y. Kim, and S. Park, "A quarter-wavelength vibration mode transducer using clamped boundary backing layer", 2012.

[17] R. Wodnicki, D. N. Stephens, Q. Zhou, K. W. Ferrara, H. Kang, R. Chen, N. E. Cabrera-Munoz, H. Jung, L. Jiang, *et al.*, "Co-Integrated PIN-PMN-PT 2-D Array and Transceiver Electronics by Direct Assembly Using a 3-D Printed Interposer Grid Frame", *IEEE Transactions on Ultrasonics, Ferroelectrics, and Frequency Control*, vol. 67, no. 2, pp. 387–401, 2020. DOI: [10.1109/TUFFC.2019.2944668](https://doi.org/10.1109/TUFFC.2019.2944668).

[18] B. Luijten, N. Chennakeshava, Y. C. Eldar, M. Mischi, and R. J. G. van Sloun, "Ultrasound Signal Processing: From Models to Deep Learning", *Ultrasound in medicine & biology*, 2023. DOI: [10.1016/j.ultrasmdbio.2022.11.003](https://doi.org/10.1016/j.ultrasmdbio.2022.11.003).

[19] B. Luijten, R. Cohen, F. J. De Bruijn, H. A. Schmeitz, M. Mischi, Y. C. Eldar, and R. J. Van Sloun, "Adaptive Ultrasound Beamforming Using Deep Learning", *IEEE Transactions on Medical Imaging*, vol. 39, no. 12, pp. 3967–3978, 2020. DOI: [10.1109/TMI.2020.3008537](https://doi.org/10.1109/TMI.2020.3008537).

[20] N. Shlezinger, J. Whang, Y. C. Eldar, and A. G. Dimakis, "Model-based deep learning", *Proceedings of the IEEE*, pp. 1–35, 2023. DOI: [10.1109/JPROC.2023.3247480](https://doi.org/10.1109/JPROC.2023.3247480).

[21] J. Youn, B. Luijten, M. Schou, M. B. Stuart, Y. C. Eldar, R. J. Van Sloun, and J. A. Jensen, "Model-based Deep Learning on Ultrasound Channel Data for Fast Ultrasound Localization Microscopy", *IEEE International Ultrasonics Symposium, IUS*, pp. 21–24, 2021. DOI: [10.1109/IUS52206.2021.9593435](https://doi.org/10.1109/IUS52206.2021.9593435).

[22] R. J. G. Van Sloun, R. Cohen, and Y. C. Eldar, "Deep learning in ultrasound imaging", *Proceedings of the IEEE*, vol. 108, no. 1, pp. 11–29, 2019. DOI: [10.1109/JPROC.2019.2932116](https://doi.org/10.1109/JPROC.2019.2932116).

[23] V. Kumar, P.-Y. Lee, B.-H. Kim, M. Fatemi, and A. Alizad, "Gap-filling method for suppressing grating lobes in ultrasound imaging: Experimental study with deep-learning approach", *IEEE Access*, vol. 8, pp. 76 276–76 286, 2020. DOI: [10.1109/ACCESS.2020.2989337](https://doi.org/10.1109/ACCESS.2020.2989337).

[24] O. M. H. Rindal, A. Austeng, A. Fatemi, and A. Rodriguez-Molares, "The Effect of Dynamic Range Alterations in the Estimation of Contrast", *IEEE Transactions on Ultrasonics, Ferroelectrics, and Frequency Control*, vol. 66, no. 7, pp. 1198–1208, 2019. DOI: [10.1109/TUFFC.2019.2911267](https://doi.org/10.1109/TUFFC.2019.2911267).

[25] A. Rodriguez-Molares, O. M. H. Rindal, J. D'Hooge, S. E. Masoy, A. Austeng, M. A. Lediju Bell, and H. Torp, "The Generalized Contrast-to-Noise Ratio: A Formal Definition for Lesion Detectability", *IEEE Transactions on Ultrasonics, Ferroelectrics, and Frequency Control*, vol. 67, no. 4, pp. 745–759, 2020. DOI: [10.1109/TUFFC.2019.2956855](https://doi.org/10.1109/TUFFC.2019.2956855).

[26] N. Bottensus, B. C. Byram, and D. Hyun, "Histogram Matching for Visual Ultrasound Image Comparison", vol. 68, pp. 1487–1495, 5 2021. DOI: [10.1109/TUFFC.2020.3035965](https://doi.org/10.1109/TUFFC.2020.3035965).

[27] J. Huh, S. Khan, S. Choi, D. Shin, J. E. Lee, E. S. Lee, and J. C. Ye, "Tunable image quality control of 3-d ultrasound using switchable cyclegan", *Medical Image Analysis*, vol. 83, p. 102 651, 2023. DOI: <https://doi.org/10.1016/j.media.2022.102651>.

[28] P. Rouzrokh, B. Khosravi, S. Faghani, M. Moassefi, D. V. Vera Garcia, Y. Singh, K. Zhang, G. M. Conte, and B. J. Erickson, "Mitigating bias in radiology machine learning: 1. Data handling", *Radiology: Artificial Intelligence*, vol. 4, no. 5, e210290, 2022. DOI: [10.1148/ryai.210290](https://doi.org/10.1148/ryai.210290).

[29] J. S. Suri, M. Bhagawati, S. Paul, A. Protogerou, P. P. Sfikakis, G. D. Kitas, N. N. Khanna, Z. Ruzsa, A. M. Sharma, *et al.*, "Understanding the bias in machine learning systems for cardiovascular disease risk assessment: The first of its kind review", *Computers in biology and medicine*, p. 105 204, 2022. DOI: [10.1016/j.combiomed.2021.105204](https://doi.org/10.1016/j.combiomed.2021.105204).

[30] G. Varoquaux and V. Cheplygina, "Machine learning for medical imaging: methodological failures and recommendations for the future", *NPJ digital medicine*, vol. 5, no. 1, p. 48, 2022. DOI: [10.1038/s41746-022-00592-y](https://doi.org/10.1038/s41746-022-00592-y).

[31] J. S. Baxter and P. Jannin, *Bias in machine learning for computer-assisted surgery and medical image processing*, 2022. DOI: [10.1080/24699322.2021.2013619](https://doi.org/10.1080/24699322.2021.2013619).

A

SYSTEM IDENTIFICATION OF ANKLE JOINT DYNAMICS BASED ON PLANE-WAVE ULTRASOUND MUSCLE IMAGING

This appendix has been published as:

Boudewine W. Ossenkoppela, Verya Daeichin, Karen E. Rodriguez Hernandez, Nicolaas de Jong, Martin D. Verweij, Alfred C. Schouten, Winfred Mugge, System identification of ankle joint dynamics based on plane-wave ultrasound muscle imaging, 2019 41st Annual International Conference of the IEEE Engineering in Medicine and Biology Society (EMBC), 2019, pp. 2111-2114

Improved treatment of posture and movement disorders requires a better understanding of human neuromuscular control. Joint dynamics can be assessed using robotic manipulators and system identification. Due to tendon compliance, joint angle and muscle fiber stretch are not proportional. This study uses plane-wave ultrasound imaging to investigate the dynamic relation between ankle joint angle and muscle length. The first goal is to determine the feasibility of using ultrasound imaging with system identification; the second goal is to assess the relation between ankle and muscle stretch, and reflex size. Transient and continuous ankle joint motions were applied, while soleus and gastrocnemius muscle stretches were assessed with ultrasound imaging and an image tracking algorithm. For small (1° SD) continuous motions, ankle angle and muscle length are proportional during a relax task. However, during an active position task muscle length measurements were too noisy to make this assessment. For transient perturbations with a high velocity ($> 90^\circ/\text{s}$) the muscle length showed oscillations that were not present in the ankle angle, demonstrating a non-proportional relationship and muscle-tendon interaction. The gastrocnemius velocity predicted the size of the short-latency reflex better than the ankle joint velocity. Concluding, plane-wave ultrasound muscle imaging is feasible for system identification experiments and shows that muscle length and ankle angle are proportional during a relax task with small continuous perturbations.

A.1. INTRODUCTION

Many daily activities, such as standing or driving on a bumpy road, require posture maintenance. Mechanisms to resist perturbations are co-activation of antagonistic muscles and proprioceptive reflexes, originating from muscle spindles and Golgi tendon organs. Posture control experiments use both transient [1] and continuous perturbations [2]. Transients offer a straightforward assessment by isolating the instantaneous (mechanics) from the delayed (reflex) response. Continuous perturbations allow to study adaptation of reflexive and visco-elastic properties to different circumstances.

With system identification the joint dynamics can be expressed in a Frequency Response Function (FRF) from the applied torque to the measured joint angle, i.e. admittance. Motor control experiments, system identification and modelling are used to improve the understanding of the relevant structures and their interaction in posture maintenance.

The first goal of this study is to determine the feasibility of measuring muscle length changes using plane-wave ultrasound imaging during continuous and transient perturbations. The second goal is to assess the relation between ankle rotation and muscle stretch, and their relation with the reflex response.

JOINT ANGLE AND MUSCLE STRETCH

Some models represent muscle length as ankle angle filtered by an elastic tendon, others assume an infinite tendon stiffness. Muscle spindles are sensitive to muscle stretch and stretch velocity. As muscle spindle stretch is derived from the joint angle, modelling muscle-tendon interaction affects the estimated muscle spindle contribution. Therefore, this study aims to verify if muscle stretch can be assumed to be proportional to ankle angle during system identification experiments.

Following transient perturbations, EMG signals show a short latency stretch reflex

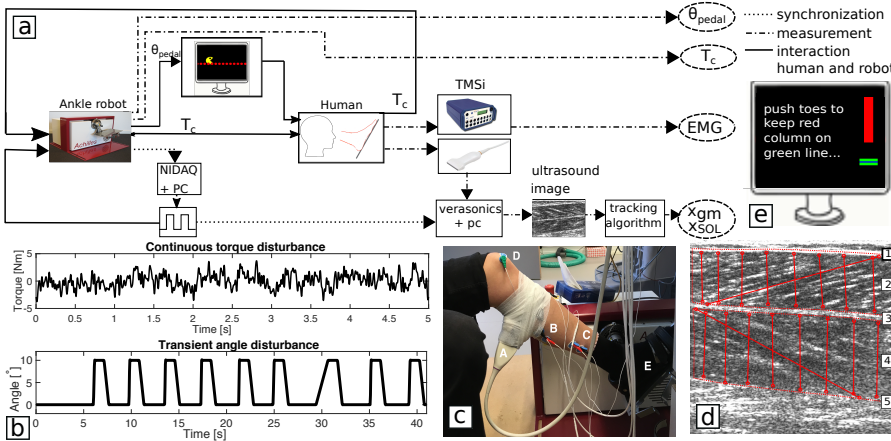


Figure A.1: a) Experimental setup. Human and manipulator interact through contact torque T_c . Onscreen feedback for Experiment 1: 'Pacman' shows the low-pass filtered joint angle and red dots the required angle. b) Top: 5s segment of the 30s continuous torque disturbance of Experiment 1. Bottom: Example of a transient position disturbance applied in Experiment 2. c) Attachment of ultrasound probe (A), EMG electrodes on GM (B), SOL (C) and ground electrode on knee cap (D). The foot is strapped on the pedal (E). d) ROIs and tracking lines in an ultrasound image. Proximal aponeurosis GM (1), ROI GM (2), distal aponeurosis GM and distal aponeurosis SOL(3), ROI SOL (4), proximal aponeurosis SOL(5). e) Onscreen feedback of Experiment 2. A blue bar indicates the required torque, with $\pm 5\%$ margin in green. The red column indicates the low-pass filtered torque.

response (M1) and a long latency response (M2). With transient perturbations, joint velocity correlates with M1 amplitude [3]. Since muscle stretch is a more direct measure of muscle spindle input, it is hypothesized that muscle stretch velocity correlates stronger with M1 magnitude than ankle joint velocity.

A.2. METHOD

Eight healthy participants (5 women) aged 24-27 volunteered: four received small amplitude continuous perturbations (Experiment 1) and four received transient perturbations (Experiment 2). All participants gave informed consent and the study was approved by the human research ethics committee of the Delft University of Technology.

ACHILLES

A single-axis ankle manipulator (Moog, Nieuw-Vennep, The Netherlands) applied the perturbations and recorded torque and angle at 1024Hz. Participants were seated with their left foot straight (0°) and 45° knee flexion.

ELECTROMYOGRAPHY

A TMSi amplifier (Porti-7) recorded EMG signals at 1024Hz. Surface electrodes were positioned according to the SENIAM guidelines on the tibialis anterior (TA), gastrocnemius medialis (GM), gastrocnemius lateralis (GL) and soleus (SOL) muscles.

A

A**ULTRASOUND**

Images were recorded with a Verasonics Vantage 256 ultrasound system and a Philips L12-5 50mm probe operating at a centre frequency of 7.8MHz and an imaging depth of 50mm. Ultrafast ultrasound imaging uses unfocused plane-waves instead of conventional line-by-line acquisition, enabling a high temporal resolution ($>k\text{Hz}$) [4]. In Experiment 1, ultrasound images were recorded at 130Hz for 23s and in Experiment 2 at 100Hz for 30s. The probe was fastened to the leg with an encasing of clay, Velcro straps and a self-adhesive bandage (Fig. A.1c).

DATA RECORDING

The manipulator sent a TTL signal to the TMSi and NIDAQ 6211 USB device, which sent a square wave with a pulse frequency equal to the desired ultrasound frame rate to trigger the ultrasound, see Fig. A.1a.

A.2.1. EXPERIMENT 1: CONTINUOUS**SIGNAL**

The signal had equal power at 40 logarithmically spaced frequencies between 0.2Hz and 40Hz and a random phase. From 10,000 realizations, one 5s segment was chosen that had no outliers while having a distribution closest to a normal distribution, see Fig. A.1b. Six repetitions formed a 30s disturbance signal.

PROCEDURE

To ensure approximately linear dynamics during the position task, the disturbance amplitude was scaled for every participant to achieve small ankle movements (1° SD). To attain similar movements during the relax task, the virtual stiffness of the manipulator was increased. Participants performed 4 repetitions of the position task followed by 4 repetitions of the relax task, with 10-minute breaks between repetitions. During position tasks a 3Nm bias torque was applied to ensure constant contraction of the plantarflexor muscles. To allow sufficient time to achieve the initial position, disturbances started after 13s.

TASK

Participants were instructed not to intervene with disturbances during the relax task. For the position task, they were instructed to keep their foot in a constant angle, while performance feedback was given onscreen (Fig. A.1a).

A.2.2. EXPERIMENT 2: TRANSIENT**SIGNAL**

The transient disturbance consisted of nine Ramp-and-Hold (RaH) signals, see Fig. A.1b. The first two RaHs were used to familiarize the participant with the task. Of the subsequent seven ramps, one had a velocity of $8^\circ/\text{s}$ and two ramps each had velocities of 90, 150 and $200^\circ/\text{s}$. The order was randomized and the time interval between RAHs varied ($2.5 \pm 0.29\text{s}$). The return velocity was $20^\circ/\text{s}$.

PROCEDURE

Participants first performed 4 repetitions of the relax task with no torque requirement, then practiced the active task until they consistently maintained the required torque level of 4Nm, and finally, performed 4 repetitions of the active task. Breaks between repetitions were 10 minutes.

TASK

Participants were instructed not to intervene with the disturbances during the relax task. For the active task they were instructed to contract their muscles such that the onscreen torque level was reached (Fig. A.1e), but not to intervene with the disturbance.

A.2.3. DATA PROCESSING

IMAGE PROCESSING

Images were processed with the automatic tracking algorithm *Ultratrack* [5]. The algorithm is based on a Lucas-Kanade optical flow algorithm with affine optic flow extension. It tracks the complete muscle region, making it suitable for tracking larger and faster movements in which complex muscle deformations occur that can cause small regions to move out of the imaging plane. Regions of interest (ROI) for the GM and SOL were marked on the first frame, see Fig. A.1d. In each ROI, a muscle fascicle was marked as well as eight points on each aponeurosis, which form vertical lines in the image. The relative movement between the eight markers on the upper and lower aponeuroses were averaged and used to determine the relative muscle stretch along the aponeurosis.

EXPERIMENT 1: CONTINUOUS

The first and last 5s segments were eliminated to remove onset and termination effects, leaving 16 segments per participant. Recordings were transformed to the frequency domain after which the cross-spectral densities $\hat{S}_{\theta D}(f)$, $\hat{S}_{TD}(f)$, $\hat{S}_{x_{GM}D}(f)$ and $\hat{S}_{x_{SOL}D}(f)$ were determined. Here $D(f)$ is the applied torque disturbance, $T_c(f)$ the torque on the pedal and $x_{GM}(f)$ and $x_{SOL}(f)$ are the contractile element lengths of the GM and SOL muscles. Spectral densities were averaged per participant over the different trials. A closed-loop identification method was used to estimate the admittances $\hat{H}_{\theta T}(f)$, $\hat{H}_{x_{GM}T}(f)$, $\hat{H}_{x_{SOL}T}(f)$, $\hat{H}_{x_{GM}\theta}(f)$ and $\hat{H}_{x_{SOL}\theta}(f)$ by division of the spectral densities [2]. The coherence $\hat{\gamma}_{\theta D}^2(f)$ between D and θ , $\hat{\gamma}_{x_{GM}D}^2(f)$ between D and x_{GM} and $\hat{\gamma}_{x_{SOL}D}^2(f)$ between D and x_{SOL} were determined to check linearity. A coherence value of 1 indicates a linear noise-free relation. FRFs and coherences were only evaluated at the frequencies where the torque disturbance had power.

EXPERIMENT 2: TRANSIENT

Ultrasound images were analyzed with the tracking algorithm per individual ramp. For the EMG recordings 50Hz power line interference was removed, the signal was high-pass filtered (1Hz cut-off, third-order Butterworth), rectified and smoothed with a low-pass filter (80Hz cut-off, third-order Butterworth [1]). RaH segments were removed from the analysis if the torque was not within 10% of the required torque in the 100ms before ramp onset. Trials were also excluded if the EMG peak after the ramp was not larger than the mean plus 3 times the standard deviation of the baseline EMG which was determined - 500 to -100ms before the ramp onset or if a large EMG peak (within 2 standard deviations

A

of the reflex peak) was present in the 100ms before the ramp onset. The M1 and M2 response were then quantified by the area under the EMG signal at a window of 40-65ms and 70-110ms respectively and normalized with respect to the baseline EMG.

STATISTICS

The Pearson correlation coefficient was used to examine relationships between muscle velocity, disturbance velocity and reflex size. Significance level: $p < 0.05$.

A.3. RESULTS

A.3.1. EXPERIMENT 1: CONTINUOUS FEASIBILITY

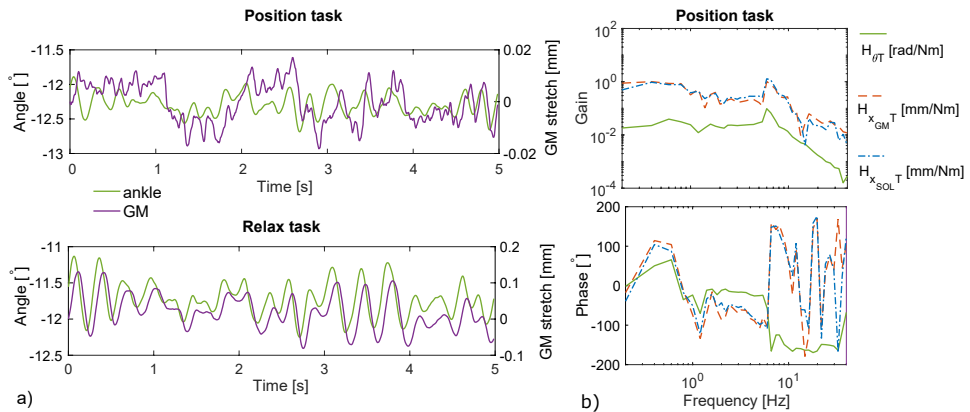


Figure A.2: Experiment 1: a) Typical average ankle angle and GM contractile length during a position and relax task. b) Typical results for frequency response functions during the position task showing similar shapes.

Fig. A.2 shows the ankle angle and contractile length of the GM averaged over all 16 data segments for a typical subject. During the relax task the contractile length of the GM oscillates in a similar pattern as the ankle angle and the trajectory is only slightly less smooth than the ankle angle. During the position task the x_{GM} has small high-frequent oscillations that are not present in the ankle angle. The same was observed for the x_{SOL} recording (not shown).

PROPORTIONALITY

Fig. A.2 shows that ankle angle is not proportional to muscle length during the position task.

Frequency domain identification: Fig. A.2 shows typical results for frequency response functions $\hat{H}_{\theta T}$, $\hat{H}_{x_{GM} T}$, $\hat{H}_{x_{SOL} T}$ and coherences $\hat{\gamma}_{\theta D}^2$, $\hat{\gamma}_{x_{GM} D}^2$ and $\hat{\gamma}_{x_{SOL} D}^2$ for the position task. Before calculating the FRFs x_{SOL} and x_{GM} recordings were detrended to correct for drift and 16 out of 64 segments of the position task were removed as they showed 'jumps'. Fig. A.3 shows that overall $\hat{H}_{x_{GM} \theta}$ and $\hat{H}_{x_{SOL} \theta}$ are not constant across all frequencies, indicating that muscle length is not proportional to ankle angle. Yet, at frequencies where $\hat{\gamma}_{x_{GM} D}^2$ and $\hat{\gamma}_{x_{SOL} D}^2$ are relatively high, $\hat{H}_{x_{GM} \theta}$ and $\hat{H}_{x_{SOL} \theta}$ are relatively

straight especially for the relax task. The coherence of the muscle length is much lower than that of the ankle angle, which, averaged over all frequencies and participants, is 0.98 during the relax task and 0.89 during the position task. $\hat{\gamma}_{x_{GM}D}^2$ and $\hat{\gamma}_{x_{SOL}D}^2$ are higher during the relax task than the position task especially from 1-4Hz.

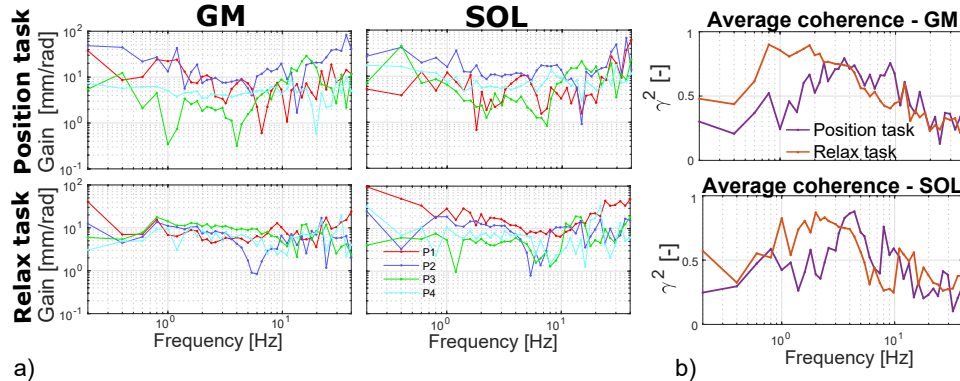


Figure A.3: a) Experiment 1: Top and Bottom) If θ_{pedal} is proportional to x_{SOL} and x_{GM} then $\hat{H}_{x_{GM}\theta}$ and $\hat{H}_{x_{SOL}\theta}$ would be constant across all frequencies (colours represent subjects). b) Average coherence for each muscle.

A.3.2. EXPERIMENT 2: TRANSIENT FEASIBILITY

Fig. A.4 a) shows a large dissimilarity between ankle angle and contractile element length trajectories.

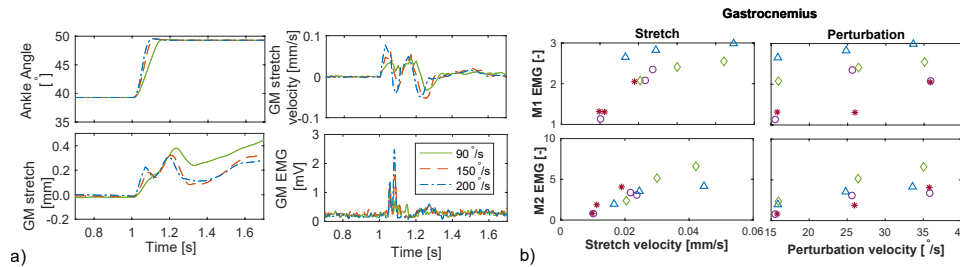


Figure A.4: a) Experiment 2: Response of a typical subject to RaH perturbations of different velocities during an active task, averaged over the included trials. GM contractile length shows oscillations not present in the ankle angle recording. Larger perturbation velocity corresponds with a larger GM stretch velocity and with higher peaks in the EMG trajectories. b) Experiment 2: Average GM stretch velocity and perturbation velocity at 0.014s after perturbation onset plotted against the average M1 and M2 responses during the active task. Every symbol represents a participant. For a perfect correlation the symbols would lie on a straight line.

PROPORTIONALITY

Fig. A.4 a) shows that muscle length is not proportional to ankle angle during an active task, as oscillations in the GM length are missing in the ankle angle. The same was

Table A.1: Correlations and (p - value)

A

	GM Active	SOL Active	GM Passive	SOL Passive
Stretch Vel. - M1	0.664 (0.018)	0.441 (0.151)	0.323 (0.306)	0.492 (0.104)
Stretch Vel. - M2	0.893 (0.000)	0.540 (0.070)	0.746 (0.005)	0.444 (0.148)
Pert. Vel. - M1	0.402 (0.195)	0.430 (0.163)	0.556 (0.061)	0.585 (0.046)
Pert. Vel. - M2	0.760 (0.004)	0.903 (0.000)	0.697 (0.012)	0.277 (0.383)

observed for the relax task and the soleus muscle (not shown).

REFLEXES

Fig. A.4 a) shows the averaged ramp responses for a typical subject. Higher ramp velocity corresponds with a larger muscle velocity directly after ramp onset (0.014s after the disturbance) and a larger EMG peak. Fig. A.4 b) shows the relationship of M1 and M2 with muscle stretch and perturbation velocity for all participants during the active task. M1 has a strong and significant correlation with GM muscle stretch velocity whereas no significant correlation is found with perturbation velocity (Table A.1). For the active condition, M2 has a strong and significant correlation with stretch and perturbation velocity. For the soleus only a strong correlation is found between perturbation velocity and M2. For the relax task, a weak correlation is found between perturbation velocity and the M1 response of the soleus. Stronger correlations are found between perturbation velocity and M2 of the GM and between GM stretch velocity and M2.

A.4. DISCUSSION

FEASIBILITY

Plane-wave ultrasound has been used before to image skeletal muscle [4]. In contrast to this study, local instead of global muscle displacement was recorded and electrical stimulation was used instead of mechanical perturbations. The high coherence between disturbance torque and pedal angle indicates that these measurements have a low noise level. The lower coherence of muscle length, especially during the position task, may be caused by non-linear behaviour or noise in the muscle imaging. Drift was observed in some muscle length recordings. This can be due to error accumulation of the tracking algorithm, or be the behaviour of the muscle. If a subject slowly increases the level of co-activation, this will reduce muscle length.

REFLEX PREDICTION

The M1 response originates from the monosynaptic Ia afferent reflex pathway, where the Ia afferent provides feedback on muscle stretch velocity. This study found a strong correlation between muscle stretch velocity of the GM and the size of M1. However, Cronin et al. [6] previously found a weak correlation between muscle stretch velocity and the size of M1. Reasons that could explain this discrepancy are differences in measurement intervals after perturbation onset, disturbance parameters and use of change along the aponeurosis instead of fascicle velocity. The origin of the M2 response is still unclear. Nevertheless, the findings of this study align with Thilmann et al. [3] who found an in-

crease in the size of the M2 response of the triceps surae with increased disturbance velocity.

EXPERIMENTAL CONSIDERATIONS

A 0.14s lag of the data in Experiment 2, was corrected by realignment. The use of ultrafast ultrasound imaging with frame rates in the order of kHz was not explored, since RAM storage enabled recording <3000 frames consecutively. However, plane-wave ultrasound imaging allows imaging at >kHz without affecting image quality. Thus, it is possible to investigate the muscle response even shorter after the disturbance onset.

In conclusion, plane-wave ultrasound muscle length measurements in motor control experiments are feasible. With continuous perturbations, system identification on muscle length showed that muscle length and ankle angle are proportional during a relax task. For transient perturbations muscle length and ankle angle were not proportional; a stronger correlation was found between reflex response and gastrocnemius muscle stretch velocity than with ramp velocity.

REFERENCES

- [1] J. Schuurmans, E. De Vlugt, A. C. Schouten, C. G. M. Meskers, J. H. De Groot, and F. C. T. Van Der Helm, "The monosynaptic Ia afferent pathway can largely explain the stretch duration effect of the long latency M2 response", *Exp. Brain Res.*, vol. 193, no. 4, pp. 491–500, 2009. doi: [10.1007/s00221-008-1647-7](https://doi.org/10.1007/s00221-008-1647-7).
- [2] F. C. T. Van Der Helm, A. C. Schouten, E. De Vlugt, and G. G. Brouwn, "Identification of intrinsic and reflexive components of human arm dynamics during postural control", *J. Neurosci. Methods*, vol. 119, no. 1, pp. 1–14, 2002. doi: [10.1016/S0165-0270\(02\)00147-4](https://doi.org/10.1016/S0165-0270(02)00147-4).
- [3] A. F. Thilmann, M. Schwarz, R. Topper, S. J. Fellows, and J. Noth, "Different mechanisms underlie the long-latency stretch reflex response of active human muscle at different joints.", *J. Physiol.*, vol. 444, pp. 631–643, 1991. doi: [10.1113/jphysiol.1991.sp018898](https://doi.org/10.1113/jphysiol.1991.sp018898).
- [4] T. Deffieux, J. L. Gennisson, M. Tanter, M. Fink, and A. Nordez, "Ultrafast imaging of in vivo muscle contraction using ultrasound", *Applied Physics Letters*, vol. 89, 18 2006. doi: [10.1063/1.2378616](https://doi.org/10.1063/1.2378616).
- [5] D. J. Farris and G. A. Lichtwark, "UltraTrack: Software for semi-automated tracking of muscle fascicles in sequences of B-mode ultrasound images", *Computer methods and programs in biomedicine*, vol. 128, pp. 111–118, 2016. doi: [10.1016/j.cmpb.2016.02.016](https://doi.org/10.1016/j.cmpb.2016.02.016).
- [6] N. J. Cronin, T. Rantalainen, and J. Avela, "Triceps surae fascicle stretch is poorly correlated with short latency stretch reflex size", *Muscle and Nerve*, vol. 52, no. 2, pp. 245–251, 2015. doi: [10.1002/mus.24538](https://doi.org/10.1002/mus.24538).

ACKNOWLEDGEMENTS

After more than four years of the PhD journey, what stands out the most is the number of great people I have had the fortune to meet during this time. Both while working together in specific projects and when working alongside each other on different topics. I want to thank the people I have had the opportunity to work with and the friends and family whose support were also essential in completing this thesis.

First I want to thank my promotores Nico de Jong, Martin Verweij and Ruud van Sloun, for the opportunities you have given me to work on very interesting research in the field of ultrasound, what you have thought me and your support and guidance. Nico, thank you for pushing me to think more experimentally. I also want to thank you for the time you took in helping me at specific points along the way such as teaching me how to approach the rebuttal of a paper and your guidance in the final stages of finishing the thesis.

Martin, thank you for all the discussions about next steps in the project, how to interpret results, what more results are needed, your sharpness in pinpointing what is wrong in a figure. With your extensive knowledge of acoustics you could always point me to an article or often book from your office collection, to find more details about a topic. Ruud, meetings with you always contained a lot of ideas and ended with many new avenues to explore. I also want to thank you for your encouragement and positivity and for the opportunities to be part of everything, including AI meetings and the super-resolution challenge.

It was very enjoyable to be part of a multidisciplinary project and I want to thank everyone in the 3D-ICE team. Hans Bosch, Rik Vos and Michiel Pertijs, it was a very interesting process to get to a prototype. I learned so much from your knowledge and perspectives, and want to thank you for all your feedback. Mehdi, I really enjoyed our discussions and of course working together on all the Field II simulations. I want to thank you for sharing your knowledge of ultrasound imaging when I was just starting out. Yannick, I appreciate how you always brought a lot of ideas, thoroughness and organization and both took the time to explain details of the electronics and ask a lot of questions about the acoustics side. I also enjoyed the time in the lab, doing prototype measurements and investigating problems with the samples. Djalma, you also joined the project at this point and your experience with acoustic measurements and the discussions about the set-up and processing was very valuable.

Emile, with your skill and expertise in fabricating the acoustic array it was possible to realize a successful transducer prototype. Henry, thank you for always being available with answers and advice about lab set-ups, such as helping when our watertight box was not so watertight. Angela, you saved us on another day of measurements with a not so watertight measurement box and I also want to thank you for your help with forms and other issues and your kindness over the years.

Of course, many thanks goes to all the colleagues in Delft, Eindhoven en Rotterdam for the enjoyable work environment. Jack and Albe you were my office mates for many years in Delft and I want to thank you not just for your help and advice on practical matters and frustrations such as PZFlex, courses and forms, but of course also for the shared table tennis, dinners, beers etc. There are many others in the Medical Imaging group I want to thank for sharing fun at conferences, all the interesting research presentations and discussions, the lunch breaks and drinks, including Fabian, Moein, Elango, Agis, Djalma, Rick, Alina, Martijn, Chih-Hsien, Xiufeng, Dion, Baptiste, Chiara, Masja, Paulina, Ayda, Changchun, Caitlin, Yidong, Tarannum, Sabiju. After going to Eindhoven and meeting everyone about twice, Covid-19 happened... Xufei, I was very happy you set-up the digital coffee breaks! Ben, I enjoyed working with you and I learned a lot from you through the discussions on beamforming and your suggestions for things to try in training networks. Jihwan, Tristan, Ben, Thierry working on the challenge together was a lot of fun and I also want to thank you all and the others including Beatrice, Hans, Iris, Nish for discussions at coffee breaks, fun at the IUS conference and AI meetings. Lucy, it was a nice change to get to work a bit with the spiral array at Erasmus MC. We had some frustrating channel connection mysteries, but I enjoyed working together and want to thank you for the discussions on imaging with the spiral array.

I also want to express my gratitude for the support en encouragement from friends and family. Barbara and Stéphanie for listening to all my doubts along the way. Vera, Jildau, Nina and Theresa for sharing the journey of PhD research across different countries. It was always good to hear about your experiences and perspectives. Theresa, thank you for those writing sessions together over Teams and your positive approach to things. Merel and Dirk, it is great to know that I can always rely on my brother and sister. Pap en mam, thank you for always encouraging me to develop myself, always being there for me and encouraging me to keep going! Finally, Jim, my husband, I want to thank you for your love and encouragement throughout this journey :).

CURRICULUM VITÆ

Boudewine Willemine OSSENKOPPELE

11-11-1991 Born in Amersfoort, The Netherlands.

EDUCATION AND EXPERIENCE

2003–2009 Pre-University Education
OSG Erasmus
Almelo, The Netherlands

2009–2010 Foundation Diploma in Liberal Arts
Oxford Brookes University
Oxford, United Kingdom

2010–2015 Bachelor of Science in Aerospace Engineering
Delft University of Technology
Delft, The Netherlands

2015–2018 Master of Science in Mechanical Engineering
Delft University of Technology
Delft, The Netherlands

2018–2023 Ph.D. Candidate Applied Physics
Delft University of Technology
Delft, The Netherlands

2023– Researcher Energy Statistics
Centraal Bureau voor de Statistiek
The Hague, The Netherlands

LIST OF PUBLICATIONS

B. W. Ossenkoppele*, D. S. Dos Santos*, Y. M. Hopf, M. Soozande, E. Noothout, H. J. Vos, J. G. Bosch, M. A. P. Pertij, M. D. Verweij and N. de Jong, "An Ultrasound Matrix Transducer for High-Frame-Rate 3D Intracardiac Echocardiography", *(In preparation for submission in Ultrasound in Medicine & Biology)*,

B. W. Ossenkoppele, B. Luijten, D. Bera, N. de Jong, M. D. Verweij, and R. J. G. van Sloun, "Improving lateral resolution in 3d imaging with micro-beamforming through adaptive beamforming by deep learning", *Ultrasound in Medicine & Biology*, vol. 49, no. 1, pp. 237–255, 2023.

B. Luijten, **B. W. Ossenkoppele**, N. de Jong, M. D. Verweij, Y. C. Eldar, M. Mischi, and R. J. G. van Sloun, "Neural maximum-a-posteriori beamforming for ultrasound imaging", in *ICASSP 2023 - 2023 IEEE International Conference on Acoustics, Speech and Signal Processing (ICASSP)*, 2023, pp. 1–5.

R. J. G. van Sloun, W. M. B. Luijten, and **B. W. Ossenkoppele**, *A computer-implemented method for beamforming of ultrasound channel data*, Patent application, Filed 2022.

B. W. Ossenkoppele, L. Wei, B. Luijten, H. J. Vos, N. De Jong, R. J. Van Sloun, and M. D. Verweij, "3-D contrast enhanced ultrasound imaging of an in vivo chicken embryo with a sparse array and deep learning based adaptive beamforming", in *2022 IEEE International Ultrasonics Symposium (IUS)*, IEEE, 2022, pp. 1–4.

T. S. W. Stevens, E. B. Herbst, B. Luijten, **B. W. Ossenkoppele**, T. J. Voskuil, S. Wang, J. Youn, and C. Errico, M. Mischi, N. Pezzotti and R. J. G. van Sloun, "A Hybrid Deep Learning Pipeline for Improved Ultrasound Localization Microscopy", in *2022 IEEE International Ultrasonics Symposium (IUS)*, 2022, pp. 1–4.

M. Soozande, **B. W. Ossenkoppele**, Y. Hopf, M. A. P. Pertij, M. D. Verweij, N. De Jong, H. J. Vos, and J. G. Bosch, "Imaging Scheme for 3-D High-Frame-Rate Intracardiac Echography: A Simulation Study", *IEEE Transactions on Ultrasonics, Ferroelectrics, and Frequency Control*, vol. 69, no. 10, pp. 2862–2874, 2022.

Y. M. Hopf, **B. W. Ossenkoppele**, M. Soozande, E. Noothout, Z. Chang, C. Chen, H. J. Vos, J. G. Bosch, M. D. Verweij, N. de Jong and M. A. P. Pertij, "A Pitch-Matched Transceiver ASIC With Shared Hybrid Beamforming ADC for High-Frame-Rate 3-D Intracardiac Echocardiography", *IEEE Journal of Solid-State Circuits*, vol. 57, no. 11, pp. 3228–3242, 2022.

* The first and second author contributed equally to this work.

Y. M. Hopf, **B. W. Ossenkoppеле**, M. Soozande, E. Noothout, Z. Chang, H. J. Vos, J. G. Bosch, M. D. Verweij, N. de Jong and M. A. P. Pertijis, “A Compact Integrated High-Voltage Pulser Insensitive to Supply Transients for 3D Miniature Ultrasound Probes”, *IEEE Solid-State Circuits Letters*, vol. 5, pp. 166–169, 2022.

B. W. Ossenkoppеле, B. Luijten, D. Bera, N. de Jong, R. J. G. van Sloun, and M. D. Verweij, “High resolution fast 3D imaging with deep learning based adaptive beam-forming”, *Proceedings of the 2021 Symposium on Information Theory and Signal Processing in the Benelux*, May 20-21, TU Eindhoven, pp. 142–143,

B. W. Ossenkoppеле, V. Daeichin, K. E. Rodriguez Hernandez, N. De Jong, M. D. Verweij, A. C. Schouten, and W. Mugge, “System identification of ankle joint dynamics based on plane-wave ultrasound muscle imaging”, *Proceedings of the Annual International Conference of the IEEE Engineering in Medicine and Biology Society*, EMBS, pp. 2111–2114, 2019.